

AWARD NUMBER:

W81XWH-13-1-0391

TITLE: MRI-Derived Cellularity Index as a Potential Noninvasive Imaging Biomarker of Prostate Cancer

PRINCIPAL INVESTIGATOR: David S. Karow, MD, PhD

CONTRACTING ORGANIZATION:

University of California, San Diego  
La Jolla, CA 92093

REPORT DATE:

December 2016

TYPE OF REPORT: Final

PREPARED FOR: U.S. Army Medical Research and Materiel Command

Fort Detrick, Maryland 21702-5012

DISTRIBUTION STATEMENT:   Approved for Public Release;  
  Distribution Unlimited

The views, opinions and/or findings contained in this report are those of the author(s) and should not be construed as an official Department of the Army position, policy or decision unless so designated by other documentation.

REPORT DOCUMENTATION PAGE				Form Approved OMB No. 0704-0188	
Public reporting burden for this collection of information is estimated to average 1 hour per response, including the time for reviewing instructions, searching existing data sources, gathering and maintaining the data needed, and completing and reviewing this collection of information. Send comments regarding this burden estimate or any other aspect of this collection of information, including suggestions for reducing this burden to Department of Defense, Washington Headquarters Services, Directorate for Information Operations and Reports (0704-0188), 1215 Jefferson Davis Highway, Suite 1204, Arlington, VA 22202-4302. Respondents should be aware that notwithstanding any other provision of law, no person shall be subject to any penalty for failing to comply with a collection of information if it does not display a currently valid OMB control number. PLEASE DO NOT RETURN YOUR FORM TO THE ABOVE ADDRESS.					
1. REPORT DATE December 2016		2. REPORT TYPE Final		3. DATES COVERED 15 Sep 2013 - 14 Sep 2016	
4. TITLE AND SUBTITLE  MRI-Derived Cellularity Index as a Potential Noninvasive Imaging Biomarker of Prostate Cancer				5a. CONTRACT NUMBER	
				5b. GRANT NUMBER W81XWH-13-1-0391	
				5c. PROGRAM ELEMENT NUMBER	
6. AUTHOR(S)  David S. Karow, MD, PhD  E-Mail: dkarow@ucsd.edu				5d. PROJECT NUMBER	
				5e. TASK NUMBER	
				5f. WORK UNIT NUMBER	
7. PERFORMING ORGANIZATION NAME(S) AND ADDRESS(ES)  University of California, San Diego 9500 Gilman Dr. Dept 621 La Jolla, CA 92093-0621				8. PERFORMING ORGANIZATION REPORT NUMBER	
9. SPONSORING / MONITORING AGENCY NAME(S) AND ADDRESS(ES)  U.S. Army Medical Research and Materiel Command Fort Detrick, Maryland 21702-5012				10. SPONSOR/MONITOR'S ACRONYM(S)	
				11. SPONSOR/MONITOR'S REPORT NUMBER(S)	
12. DISTRIBUTION / AVAILABILITY STATEMENT  Approved for Public Release; Distribution Unlimited					
13. SUPPLEMENTARY NOTES					
14. ABSTRACT Standard magnetic resonance imaging (MRI) of the prostate lacks sensitivity in the diagnosis and staging of prostate cancer (PCa). To improve the operating characteristics of prostate MRI in the detection and characterization of PCa, we developed a novel, enhanced MRI diffusion technique using restriction spectrum imaging (RSI-MRI). This technique leads to greater tumor conspicuity and also more accurate localization due to spatial distortion correction techniques. As of this annual report, we show that these techniques increase our ability to detect extraprostatic extension, improve accuracy of targeted biopsies and we show that our quantitative imaging signal (RSI z-score) correlates with Gleason grade on final histopathology.					
15. SUBJECT TERMS					
16. SECURITY CLASSIFICATION OF: Unclassified			17. LIMITATION OF ABSTRACT  Unclassified	18. NUMBER OF PAGES  82	19a. NAME OF RESPONSIBLE PERSON USAMRMC
a. REPORT  Unclassified	b. ABSTRACT  Unclassified	c. THIS PAGE  Unclassified			19b. TELEPHONE NUMBER (include area code)

## Table of Contents

	<u>Page</u>
<b>1. Introduction .....</b>	<b>1</b>
<b>2. Keywords.....</b>	<b>1</b>
<b>3. Overall Project Summary.....</b>	<b>2</b>
<b>4. Key Research Accomplishments .....</b>	<b>3</b>
<b>5. Conclusion.....</b>	<b>9</b>
<b>6. Publications, Abstracts, and Presentations.....</b>	<b>9</b>
<b>7. Inventions, Patents and Licenses .....</b>	<b>10</b>
<b>8. Reportable Outcomes.....</b>	<b>10</b>
<b>9. Other Achievements.....</b>	<b>10</b>
<b>10. References .....</b>	<b>11</b>
<b>11. Appendices .....</b>	<b>11</b>

**Introduction:**

Enhanced MRI imaging techniques called restriction spectrum imaging (RSI) has been utilized to identify glioblastoma multiforme (GBM) brain tumors (1). The output from these techniques has been termed the tumor 'RSI cellularity index' and provides significantly greater accuracy in distinguishing brain tumor from normal tissue than traditional imaging measures. The RSI tumor signal was noted to be 10-fold greater than conventional imaging measures (1-2). In addition, these imaging techniques are corrected for spatial distortions that allows for more accurate localization of the tumor signal (3). In prostate cancer, increasing Gleason score correlates with loss of normal gland formation, loss of peripheral gland tubular structure and increased cellularity. Therefore, we hypothesize that the RSI cellularity index will correlate with higher tumor grade based on Gleason score and will provide significantly greater accuracy in discriminating aggressive tumor from benign and indolent lesions when compared to current imaging techniques. Based on its prior ability to discriminate between brain tumors and adjacent normal tissue with high accuracy and high signal to noise, we hypothesize that the RSI cellularity index will perform similarly in prostate tissue. We propose a non-invasive (without endorectal coil or IV contrast), rapid imaging test based on these procedures. The goal of the current research is to test whether that objective is feasible.

**Keywords:**

DCE = dynamic contrast enhancement

DWI = diffusion weighted imaging

ADC = apparent diffusion coefficient

RSI = restriction spectrum imaging

CI = cellularity index

EPI = echo planar imaging

Prostate cancer screening

Prostate cancer staging

Non-invasive imaging



## **Overall Project Summary:**

### **Specific Aim 1:**

All aspects of Specific Aim 1 were accomplished. Existing pulse sequences at UCSD were modified for signal optimization in patients. Post-processing techniques for displaying and analyzing RSI data were developed and optimized. The whole mount sectioning protocol for prostate specimens at UCSD was optimized. Local IRB approval was obtained under HRPP#071983, which was also accepted by the DoD.

### **Specific Aim 2:**

Major Tasks 2 and 3 include data collection and analysis. MR imaging with an endorectal coil for 85 patients, without an endorectal coil for 10 patients, and TIFFs of whole-mount pathology slides for 28 patients, were anonymously transferred to UCSD from UCLA for analysis. In parallel we collected imaging and pathology data at UCSD without an endorectal coil using similar imaging and pathology techniques. All imaging evaluated from UCSD and UCLA have RSI techniques incorporated. As noted below we imaged 925 patients at UCSD with 104 specimens using whole mount pathology sections. We collected 125% of our goal of 150 patients with whole mount pathology sections. Analysis of these UCLA data resulted in four published manuscripts (White et al, Cancer Research 2014; Rakow-Penner et al, PCAN 2015, Rakow-Penner et al, MRI 2015; Liss et al, Frontiers in Oncology 2015). In summary, all tasks and subtasks of Aim 2 have been completed.

### **Specific Aim 3:**

Major Tasks 4 and 5 include data collection and analysis. Imaging using RSI was implemented as part of the patient standard of care at UCSD, both for screening and for pre-operative MRI. All patients undergoing pre-operative MRI at UCSD are scanned using the modified imaging protocol without an endorectal coil, resulting in 925 scans at UCSD during the covered grant period. Prostate tissue is obtained from each prostatectomy patient and processed using the optimized whole mount sectioning protocol. 104 patients at UCSD underwent prostatectomy with subsequent whole-mount pathology during the covered grant period. Our stated goal in the SOW was to collect imaging and whole mount path data from 75 patients by month 17, and we have exceeded that goal. Analysis of these UCSD data has resulted in three published manuscripts (McCammack et al., PCAN 2016; McCammack et al., 2016 Abdominal Radiology; Yamin et al., 2016 Clinical Cancer Research). In summary, all tasks and subtasks of Aim 3 have been completed.

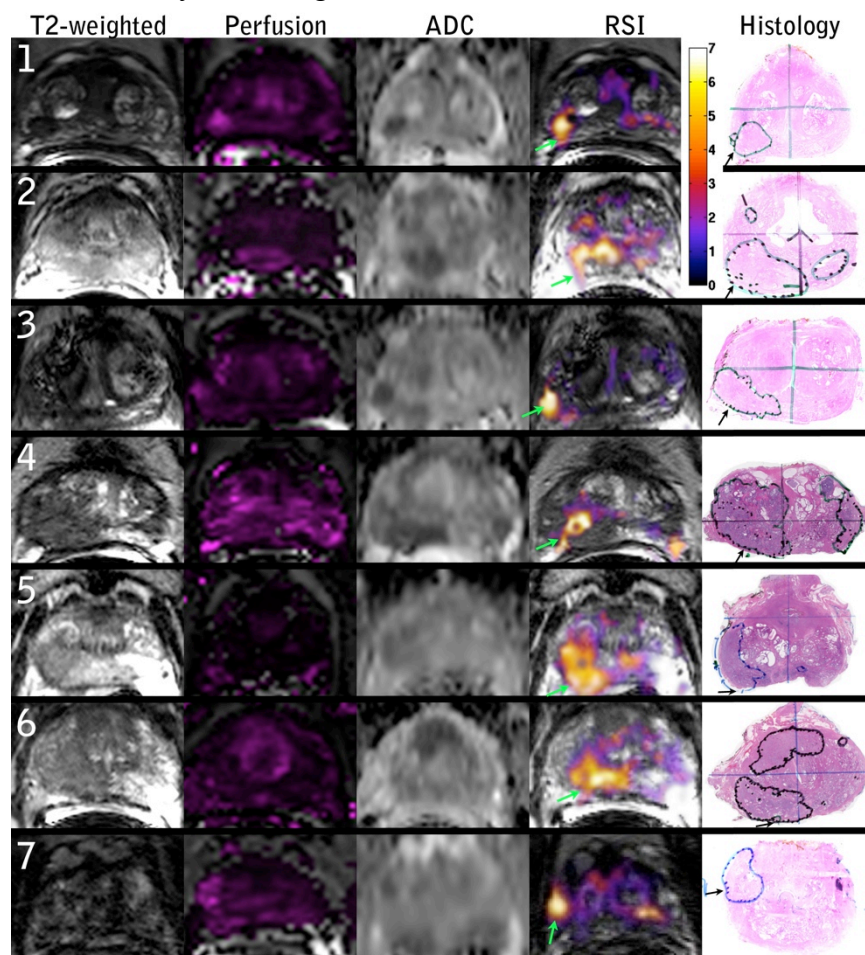
## Key Research Accomplishments:

1) We have identified spatial distortion in conventional diffusion weighted imaging and, using RSI, we are able to correct for it. This table summarizes the results for 28 patients. The results show that distortions of tumor signal can be as great as 1.3 cm if left uncorrected.

Table 2. Distortion distance of the whole prostate and tumor regions of interest due to B0 inhomogeneity		
	Mean (standard deviation) (mm)	Maximum distortion (mm)
Whole prostate distortion	3.2 (2.2)	12
Tumor ROI distortion	3.2 (2.4)	13

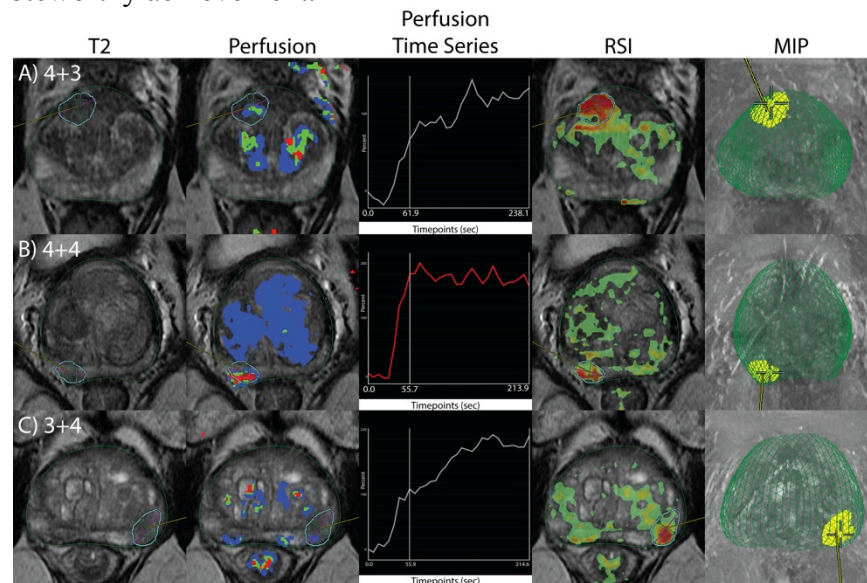
(Rakow-Penner et al, MRI, 2015)

2) As a result of the correction for distortion, RSI has improved our detection of extra prostatic extension by more accurately localizing tumor location.



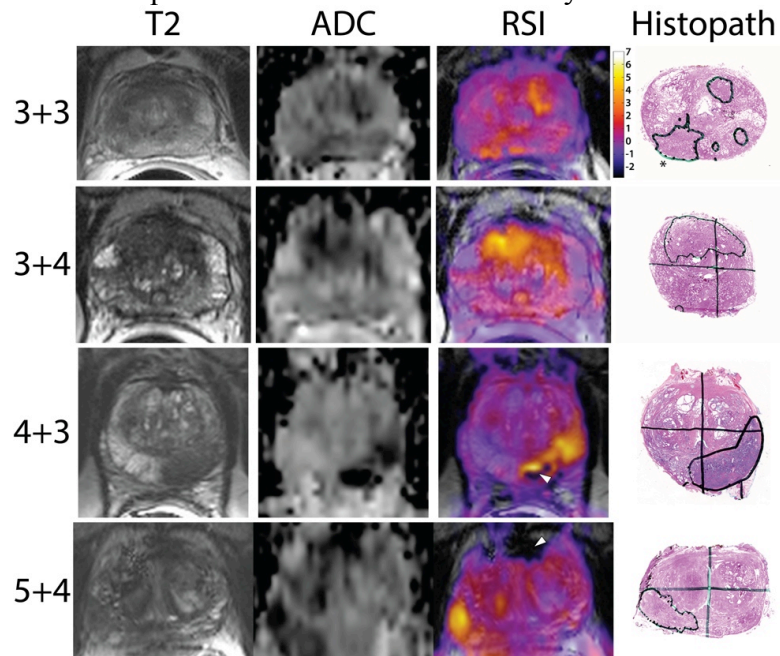
MR imaging and whole mount pathology for 7 prostate cancer patients. Column 1: T2 – weighted images, column 2: Perfusion  $K_{trans}$  maps, column 3: standard apparent diffusion coefficient (ADC) maps ( $b = 0, 100, 400, \text{ and } 800 \text{ s/mm}^2$ ), column 4: RSI z-score maps, column 5: whole mount pathology with tumor and area of EPE identified. Color bar represents zscores from 0 to 7 for the RSI maps. (Rakow-Penner et al, PCAN, 2015)

3) RSI imaging has also been implemented as part of the work flow for defining tumor regions of interest for targeted biopsy using Dynacad and UroNav MR-fused ultrasound targeted biopsy software. Due to increased conspicuity of the RSI signal compared to perfusion (DCE) and conventional DWI, as well as correction of spatial distortions, we are able to localize small tumors with accuracy as illustrated below. While this was not an Aim of the DoD proposal, this is certainly a noteworthy achievement.

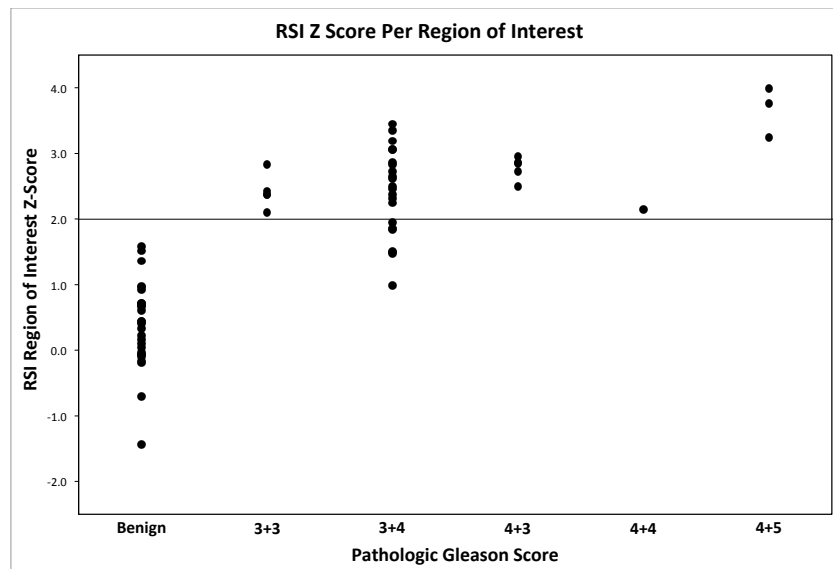


Images from three patients who underwent targeted biopsy. The first column demonstrates the T2 map with the ROI drawn to guide the MR-fused ultrasound guided biopsy. The second column displays the Dynacad perfusion maps, where red signifies rapid intense enhancement with washout, green signifies rapid intense enhancement with plateau washout and blue signifies gradual enhancement. The third column demonstrates the perfusion curves for the location identified by the crosshair in the other images. The fourth column illustrates a heatmap based on the RSI overlaid on T2 images, with red regions correlating to the areas of greatest restricted diffusion. The fifth column shows maximum intensity projections of the prostate boundary (green) and ROI for targeting (yellow). A) Patient with three negative previous biopsies. The targeted biopsy found Gleason 4+3 cancer. B) Patient with previous incomplete radiation therapy for response to low-grade cancer. Targeted biopsy found Gleason 4+4 cancer. C) Patient with previous biopsy demonstrating low-grade cancer. Targeted biopsy found Gleason 3+4 cancer.

4) Quantitatively, we have shown RSI to be at least as good as ADC in detecting high-grade cancer. Our results suggest that the RSI z-score may accurately predict Gleason grade. The RSI z-score is a quantitative measure of cellularity.



Representative images showing RSI z-score maps across Gleason scores. The y-axis shows the pathologic Gleason score with the x-axis designating the MRI sequence. The last column displays the whole mount pathology with the corresponding cancer region of interest circled in black. The star 3+3 pathologic figure represents the lesion with 3+3 prostate cancer while the other lesions are 4+3. White arrows in the 4+3 and 5+4 RSI indicate regions where the ADC is dark and would be suspicious for tumor, but the RSI reveals these are regions with signal void and are unlikely to be cancerous. Color bar represents z-scores from -2.8 to 7 for the RSI maps. (Liss et al, Frontiers in Oncology, 2015)



RSI z-score value grouped by pathologic Gleason score for 28 patients: The y-axis represents the RSI z-score derived from a given region of interest. The x-axis demonstrates the pathological Gleason scores in increasing levels of aggressiveness from left to right. Each data point represents one region of interest corresponding to a location on the whole mount prostatectomy specimen contoured by a GU pathologist (Liss et al, Frontiers in Oncology, 2015).

5) Statistical comparison of RSI z-score with traditional imaging (ADC and Ktrans) revealed that RSI-MRI significantly improves upon current non-invasive prostate cancer imaging and may potentially enhance its diagnosis and characterization.

Test	AUC (%)	<i>P</i> *	Maximum Accuracy (%)	Cutoff Value
RSI z-score	93.6 (87.6-99.7)	1	87.5	0.47
ADC values	84.8 (75.4-94.3)	0.04	79.7	1253 mm <sup>2</sup> /s
$K^{trans}$	79.2 (67.7-90.6)	0.03	78.1	0.85 mL/g/min
$k_{ep}$	74.0 (61.6-86.4)	0.007	70.3	3.66 min <sup>-1</sup>
$v_e$	77.9 (66.8-89.1)	0.02	71.9	0.29 mL/g

Effectiveness of quantitative imaging features in the differentiation of prostate cancer from normal gland. \*Each *P* value compares the individual term AUC to RSI AUC. (McCammack et al, PCAN, 2016)

Test	$\rho$	<i>P</i>
RSI z-score	0.53	0.002
ADC values	-0.42	0.01
PSA	0.36	0.04
$K^{trans}$	0.18	0.30
$k_{ep}$	0.18	0.32
$v_e$	0.19	0.30

Spearman rank-order correlation with post-prostatectomy GS results. (McCammack et al., PCAN, 2016)

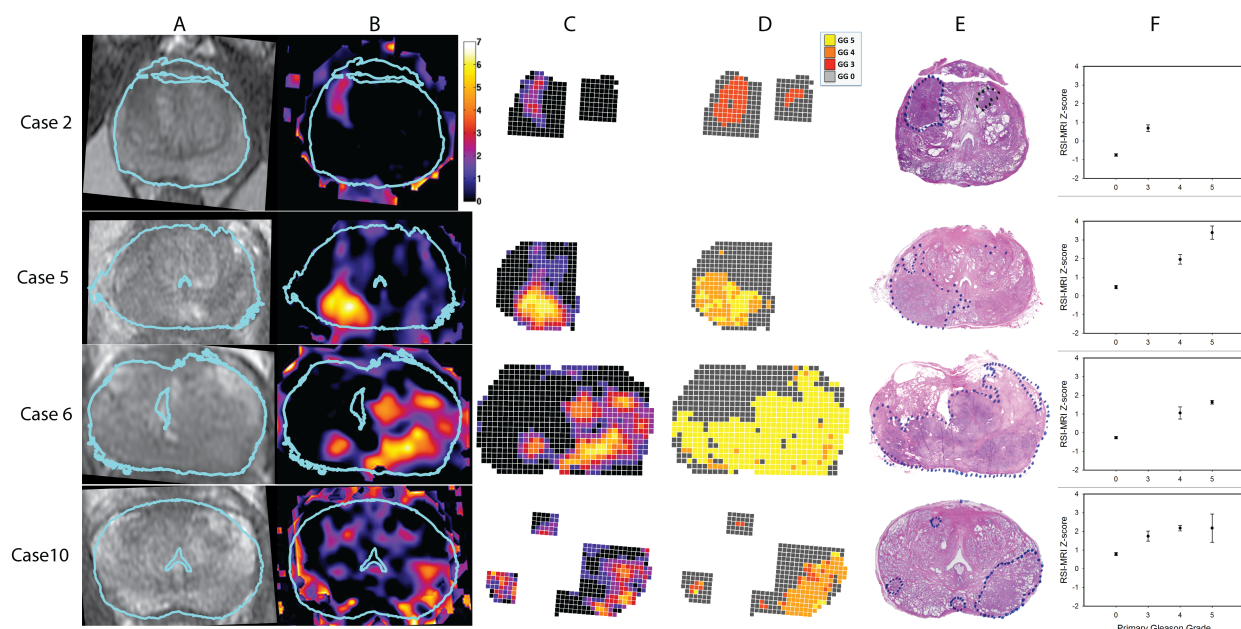
6) Evaluation of clinical radiologist-based ROC performance analysis of conventional multiparametric MRI (MP-MRI) versus RSI showed that inclusion of RSI with MP-MRI allows readers to better detect prostate cancer than does MP-MRI alone, and RSI with T2 in isolation achieves similar prostate cancer detection compared to MP-MRI.

Reader	MP-MRI	MP-MRI+RSI	$P^*$	RSI+T2	$P^\Phi$
<b>Sextant-based Analysis</b>					
<b>All PCa</b>					
Reader 1	0.63 (0.65)	0.68 (0.70)	<0.001	0.61 (0.60)	0.39
Reader 2	0.58 (0.60)	0.64 (0.68)	<0.001	0.63 (0.64)	<0.001
Reader 3	0.61 (0.63)	0.66 (0.68)	0.001	0.58 (0.58)	0.08
Combined	0.61 (0.63)	0.66 (0.69)	<0.001	0.61 (0.61)	0.85
<b>High grade PCa</b>					
Reader 1	0.71 (0.69)	0.80 (0.79)	0.01	0.73 (0.69)	0.62
Reader 2	0.66 (0.66)	0.75 (0.77)	0.01	0.74 (0.72)	0.03
Reader 3	0.72 (0.72)	0.79 (0.78)	0.04	0.66 (0.62)	0.08
Combined	0.70 (0.69)	0.78 (0.78)	<0.001	0.71 (0.68)	0.62

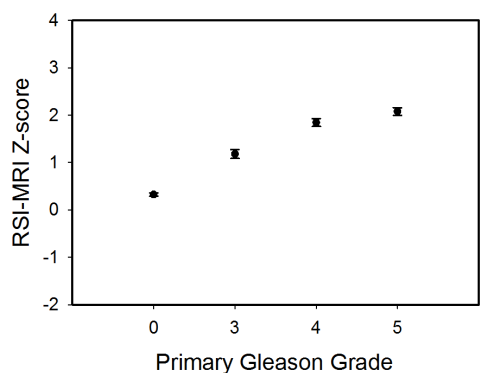
Covariance of reader findings with pathology findings from biopsy and/or prostatectomy using MP-MRI, MP-MRI+RSI, and RSI+T2 in isolation. Data in parentheses represents data using prostatectomy data alone;  $P^*$  is based on the comparison between readers' findings using MP-MRI versus MP-MRI plus RSI to predict high grade cancer;  $P^\Phi$  denotes comparison between readers' findings using MP-MRI and RSI plus T2 to predict high grade cancer. (McCammack et al., Abdominal Radiology, 2016)



7) Evaluation of RSI-MRI at voxel-level resolution shows an ability of RSI-MRI to differentiate among benign, low-grade and high-grade prostate cancer, allowing for detecting of intratumor variation in cancer grade using non-invasive diffusion-weighted imaging.



**T2, RSI-MRI, Gleason grade, and H&E: Cases 2, 5, 6, and 10.** A) T2-weighted MR images, after in-plane affine transformation to correspond to the histopathology slides, B) RSI-MRI color coded z-score maps, C) “Digital prostate map” grid overlay color-coded for RSI-MRI z-score, D) “Digital prostate map” grid overlay color-coded for Gleason grade, E) H&E-stained WM histopathological prostate section with tumor area(s) outlined, F) Plots for each case of the mean RSI-MRI signal corresponding to each histological Gleason grade based on voxel-level analysis. Error bars represent the standard errors of the mean. Blue outline in A&B indicates the correspondence of the histopathology slide to the MR image. Abbreviations: H&E, haematoxylin & eosin; MR, magnetic resonance; RSI, restriction spectrum imaging; WM, whole mount. (Yamin et al., Clinical Cancer Research, 2016)



**RSI-MRI mean z-score grouped by pathologic Gleason grade.** Mean RSI-MRI cellularity index represented as a z-score corresponding to histological Gleason grade using data from all voxels graded in all cases. Error bars represent the standard errors of the mean. (Yamin et al., Clinical Cancer Research, 2016)

8) A review of RSI in the detection, *in vivo* characterization, localization, and targeting of prostate cancer was published in the Journal of Magnetic Resonance Imaging.

## Conclusion:

- We have identified the distortions in RSI and conventional diffusion weighted imaging and corrected for them in our postprocessing stream. This has increased our ability to detect extraprostatic extension and helped to increase the accuracy of targeted biopsies.
- We have optimized and implemented a non-invasive imaging measure of Gleason grade (RSI z –score) that is at least as good as standard ADC, and may significantly improve upon current non-invasive imaging, potentially enhancing the diagnosis and characterization of prostate cancer.
- Clinical radiologist-based ROC performance of RSI with T2 vs conventional multiparametric MRI is similar, and inclusion of RSI with MP-MRI improves readers ability to detect prostate cancer.
- All RSI cases scanned at UCSD have been performed without an endorectal coil and with sequences of less than 10 minutes, indicating the feasibility of using this protocol clinically on a non-invasive screening basis.

## Publications, Abstracts and Presentations:

White, N.S., McDonald, C.R., Farid, N., Kuperman J., **Karow, D.**, Schenker-Ahmed, N.M., Bartsch, H., Rakow-Penner, R., Holland, D., Shabaik, A., Bjornerud, A., Hope, T., Hattangadi-Gluth, J., Liss, M., Parsons, J.K., Chen, C.C., Raman, S., Margolis, D., Reiter, R.E., Marks, L., Kesari, S., Mundt, A.J., Kane, C.J., Carter, B.S., Bradley, W.G., and Dale, A.M. Diffusion-Weighted Imaging in Cancer: Physical Foundations and Applications of Restriction Spectrum Imaging. *Cancer Research*. 74:4638-4652, 2014.

Rakow-Penner, R.A., White, N.S., Parsons, J.K., Choi, H.W., Liss, M.A., Kuperman, J.M., Schenker-Ahmed, N., Bartsch, H., Mattrey, R.F., Bradley, W.G., Shabaik, A., Huang, J., Margolis, D.J., Raman, S.S., Marks, L., Kane, C.J., Reiter, R.E., **\*Karow, D.S.** and Dale, A.M. Novel Technique for Characterizing Prostate Cancer Utilizing MRI Restriction Spectrum Imaging: Proof of Principle and Initial Clinical Experience with Extra-Prostatic Extension. *Prostate Cancer Prostatic Diseases*. 18:81-85, 2015. **\*Corresponding author**.

Rakow-Penner, R.A., White, N.S., Margolis, D.J.A., Parsons, J.K., Schenker-Ahmed, N., Kuperman, J.M., Bartsch, H., Choi, H.W., Bradley, W.G., Shabaik, A., Huang, J., Liss, M.A., Marks, L., Kane, C.J., Reiter, R.E., Raman, S.S., **\*Karow, D.S.** and Dale, A.M. Prostate diffusion imaging with distortion correction. *Magnetic Resonance Imaging*. 33(9):1178-1181, 2015. **\*Corresponding author**.

Liss, M.A., White, N.S., Parsons, J.K., Schenker-Ahmed, N., Rakow-Penner, R.A., Kuperman, J.M., Bartsch, H., Choi, H.W., Mattrey, R.F., Bradley, W.G., Shabaik, A., Huang, J., Margolis, D.J., Raman, S.S., Marks, L., Kane, C.J., Reiter, R.E., Dale, A.M., and **D.S. Karow**. MRI-derived Restriction Spectrum Imaging Cellularity Index is Associated with High Grade Prostate Cancer on Radical Prostatectomy Specimens. *Frontiers in Oncology*. 5:30, 2015.

McCammack, K.C., Kane, C.J., Parsons, J.K., White, N.S., Schenker-Ahmed, N.M., Kuperman, J.M., Bartsch, H., Desikan, R.S., Rakow-Penner, R.A., Adams, D., Liss, M.A., Mattrey, R.F., Bradley, W.G., Margolis, D.J.A., Raman, S.S., Shabaik, A., Dale, A.M., and **\*D.S. Karow**. *In*



*vivo* prostate cancer detection and grading using Restriction Spectrum Imaging-MRI. Prostate Cancer Prostatic Diseases. 19:168-173, 2016. **\*Corresponding author.**

McCammack, K.C., Schenker-Ahmed, N.M., White, N.S., Best, S.R., Marks, R.M., Heimbinger, J., Kane, C.J., Parsons, J.K., Kuperman, J.M., Bartsch, H., Desikan, R.S., Rakow-Penner, R.A., Liss, M.A., Margolis, D.J.A., Raman, S.S., Shabaik, A., Dale, A.M., and **\*D.S. Karow**. Restriction spectrum imaging improves MRI-based prostate cancer detection. Abdominal Radiology. 41(4):946-953, 2016. **\*Corresponding author.**

Yamin, G., Schenker-Ahmed, N.M., Shabaik, A., Adams, D., Bartsch, H., Kuperman, J., White, N.S., Rakow-Penner, R.A., McCammack, K., Parsons, J.K., Kane, C.J., Dale, A.M. and **\*D.S. Karow**. Voxel level radiologic-pathologic validation of Restriction Spectrum Imaging cellularity index with Gleason grade in prostate cancer. Clinical Cancer Research. 22(11):2668-2674. **\*Corresponding author.**

Brunsing, Ryan L, Natalie M Schenker-Ahmed, Nathan S White, J Kellogg Parsons, Christopher Kane, Joshua Kuperman, Hauke Bartsch, Andrew Karim Kader, Rebecca Rakow-Penner, Tyler M. Seibert, Daniel Margolis, Steven S. Raman, Carrie R. McDonald, Nikdokht Farid, Santosh Kesari, Donna Hansel, Ahmed Shabaik, Anders M. Dale, **\*David S. Karow**. 2016. "Restriction Spectrum Imaging : An Evolving Imaging Biomarker in Prostate MRI." *Journal of Magnetic Resonance Imaging*, 1–14. doi:10.1002/jmri.25419. **\*Corresponding author.**

**Inventions, Patents and Licenses:**

None

**Reportable Outcomes:**

None

**Other Achievements:**

None

## References:

- (1) White, N. S., McDonald, C. R., Farid, N. et al.: Improved conspicuity and delineation of high-grade primary and metastatic brain tumors using "restriction spectrum imaging": quantitative comparison with high B-value DWI and ADC. *AJNR Am J Neuroradiol*, **34**: 958, 2013
- (2) White, N. S., Leergaard, T. B., D'Arceuil, H. et al.: Probing tissue microstructure with restriction spectrum imaging: Histological and theoretical validation. *Hum Brain Mapp*, **34**: 327, 2013
- (3) Holland, D., Kuperman, J. M., Dale, A. M.: Efficient correction of inhomogeneous static magnetic field-induced distortion in Echo Planar Imaging. *Neuroimage*, **50**: 175, 2010

## Appendices:

- White, N. S., C. R. McDonald, N. Farid, J. Kuperman, D. Karow, N. M. Schenker-Ahmed, H. Bartsch, et al. 2014. "Diffusion-Weighted Imaging in Cancer: Physical Foundations and Applications of Restriction Spectrum Imaging." *Cancer Research* 74 (17): 4638–52. doi:10.1158/0008-5472.CAN-13-3534.
- Rakow-Penner, Rebecca A., N S White, J K Parsons, H W Choi, M a Liss, J M Kuperman, N Schenker-Ahmed, et al. 2015. "Novel Technique for Characterizing Prostate Cancer Utilizing MRI Restriction Spectrum Imaging: Proof of Principle and Initial Clinical Experience with Extraprostatic Extension." *Prostate Cancer and Prostatic Disease* 18 (1). Nature Publishing Group: 81–85. doi:10.1038/pcan.2014.50.
- Rakow-Penner, Rebecca A., Nathan S. White, Daniel J.a. Margolis, J. Kellogg Parsons, Natalie Schenker-Ahmed, Joshua M. Kuperman, Hauke Bartsch, et al. 2015. "Prostate Diffusion Imaging with Distortion Correction." *Magnetic Resonance Imaging*. Elsevier B.V., 0–3. doi:10.1016/j.mri.2015.07.006.
- Liss, Michael A., Nathan S. White, J. Kellogg Parsons, Natalie M. Schenker-Ahmed, Rebecca Rakow-Penner, Joshua M. Kuperman, Hauke Bartsch, et al. 2015. "MRI-Derived Restriction Spectrum Imaging Cellularity Index Is Associated with High Grade Prostate Cancer on Radical Prostatectomy Specimens." *Frontiers in Oncology* 5 (February): 1–8. doi:10.3389/fonc.2015.00030.
- McCammack, Kevin C, Christopher J. Kane, J. Kellogg Parsons, Nathan S. White, Natalie M. Schenker-Ahmed, Joshua M. Kuperman, Hauke Bartsch, et al. 2016. "In Vivo Prostate Cancer Detection and Grading Using Restriction Spectrum Imaging-MRI." *Prostate Cancer and Prostatic Diseases* 19: 168–73.
- McCammack, Kevin C., Natalie M. Schenker-Ahmed, Nathan S. White, Shaun R. Best, Robert M. Marks, Jared Heimbigner, Christopher J. Kane, et al. 2016. "Restriction Spectrum Imaging Improves MRI-Based Prostate Cancer Detection." *Abdominal Radiology*. Springer US, 1–8. doi:10.1007/s00261-016-0659-1.
- Yamin, G.\*, N. M. Schenker-Ahmed\*, A. Shabaik, D. Adams, H. Bartsch, J. Kuperman, N. S. White, et al. 2016. "Voxel Level Radiologic-Pathologic Validation of Restriction Spectrum Imaging Cellularity Index with Gleason Grade in Prostate Cancer." *Clinical*

*Cancer Research* 22 (11): 2668–74. doi:10.1158/1078-0432.CCR-15-2429. \*equal contribution

- Brunsing, Ryan L\*, Natalie M Schenker-Ahmed\*, Nathan S White, J Kellogg Parsons, Christopher Kane, Joshua Kuperman, Hauke Bartsch, et al. 2016. “Restriction Spectrum Imaging : An Evolving Imaging Biomarker in Prostate MRI.” *Journal of Magnetic Resonance Imaging*, 1–14. doi:10.1002/jmri.25419. \*equal contribution

## Diffusion-Weighted Imaging in Cancer: Physical Foundations and Applications of Restriction Spectrum Imaging

Nathan S. White<sup>1</sup>, Carrie R. McDonald<sup>2</sup>, Niky Farid<sup>1</sup>, Josh Kuperman<sup>1</sup>, David Karow<sup>1</sup>, Natalie M. Schenker-Ahmed<sup>1</sup>, Hauke Bartsch<sup>1</sup>, Rebecca Rakow-Penner<sup>1</sup>, Dominic Holland<sup>1</sup>, Ahmed Shabaik<sup>3</sup>, Atle Bjørnerud<sup>4</sup>, Tuva Hope<sup>5</sup>, Jona Hattangadi-Gluth<sup>6</sup>, Michael Liss<sup>7</sup>, J. Kellogg Parsons<sup>7</sup>, Clark C. Chen<sup>8</sup>, Steve Raman<sup>9</sup>, Daniel Margolis<sup>9</sup>, Robert E. Reiter<sup>10</sup>, Leonard Marks<sup>10</sup>, Santosh Kesari<sup>11</sup>, Arno J. Mundt<sup>6</sup>, Christopher J. Kane<sup>7</sup>, Bob S. Carter<sup>8</sup>, William G. Bradley<sup>1</sup>, and Anders M. Dale<sup>1,11</sup>

### Abstract

Diffusion-weighted imaging (DWI) has been at the forefront of cancer imaging since the early 2000s. Before its application in clinical oncology, this powerful technique had already achieved widespread recognition due to its utility in the diagnosis of cerebral infarction. Following this initial success, the ability of DWI to detect inherent tissue contrast began to be exploited in the field of oncology. Although the initial oncologic applications for tumor detection and characterization, assessing treatment response, and predicting survival were primarily in the field of neurooncology, the scope of DWI has since broadened to include oncologic imaging of the prostate gland, breast, and liver. Despite its growing success and application, misconceptions about the underlying physical basis of the DWI signal exist among researchers and clinicians alike. In this review, we provide a detailed explanation of the biophysical basis of diffusion contrast, emphasizing the difference between hindered and restricted diffusion, and elucidating how diffusion parameters in tissue are derived from the measurements via the diffusion model. We describe one advanced DWI modeling technique, called restriction spectrum imaging (RSI). This technique offers a more direct *in vivo* measure of tumor cells, due to its ability to distinguish separable pools of water within tissue based on their intrinsic diffusion characteristics. Using RSI as an example, we then highlight the ability of advanced DWI techniques to address key clinical challenges in neurooncology, including improved tumor conspicuity, distinguishing actual response to therapy from pseudoresponse, and delineation of white matter tracts in regions of peritumoral edema. We also discuss how RSI, combined with new methods for correction of spatial distortions inherent in diffusion MRI scans, may enable more precise spatial targeting of lesions, with implications for radiation oncology and surgical planning.

**See all articles in this *Cancer Research* section, "Physics in Cancer Research."**

*Cancer Res*; 74(17): 4638–52. ©2014 AACR.

### Introduction

Diffusion-weighted imaging (DWI) is increasingly used as an imaging biomarker for the detection and characterization of primary and metastatic brain tumors as well as for prognostic

cation and monitoring treatment response in this patient population. The unique ability of this technique to probe the underlying structure of brain tissue at a cellular level makes it well poised to answer questions about tumor biology, as well as the microstructure of peritumoral white matter. The greatest enthusiasm to date has surrounded the ability of DWI to estimate tumor cellularity on the basis of quantitative images of diffusion, namely apparent diffusion coefficient (ADC) maps. In particular, numerous investigators have shown a negative correlation between tumor ADC values and cellularity (1–3), which is commonly attributed to increased restricted diffusion imposed by tumor cells. Following this logic, ADC has been used with varying success to characterize and grade primary and metastatic brain tumors (3–9), to assess tumor response to therapy (10–12), and to predict survival in patients with malignant tumors (13–17). However, confusion about the true biophysical basis of the DWI signal abounds, and awareness of the limitations of the existing approaches has led to the development of advanced DWI methods that extend beyond the tensor model. These methods include high-angular diffusion imaging techniques, such as diffusion spectrum imaging (DSI; ref. 18) and

<sup>1</sup>Department of Radiology, University of California, San Diego, San Diego, California. <sup>2</sup>Department of Psychiatry, University of California, San Diego, San Diego, California. <sup>3</sup>Department of Pathology, University of California, San Diego, San Diego, California. <sup>4</sup>Department of Physics, University of Oslo, Oslo, Norway. <sup>5</sup>Department of Circulation and Medical Imaging, Norwegian University of Science and Technology, Trondheim, Norway. <sup>6</sup>Department of Radiation Oncology, University of California, San Diego, San Diego, California. <sup>7</sup>Department of Urology, University of California, San Diego, San Diego, California. <sup>8</sup>Center for Theoretical and Applied Neuro-Oncology, Division of Neurosurgery, University of California, San Diego, San Diego, California. <sup>9</sup>Department of Radiology, University of California, Los Angeles, Los Angeles, California. <sup>10</sup>Department of Urology, University of California, Los Angeles, Los Angeles, California. <sup>11</sup>Department of Neurosciences, University of California, San Diego, San Diego, California.

**Corresponding Author:** N.S. White, University of California, San Diego, 9500 Gilman Drive #0841, La Jolla, CA 92093-0841. Phone: 858-534-8259; Fax: 858-534-1078; E-mail: nswhite@ucsd.edu

doi: 10.1158/0008-5472.CAN-13-3534

©2014 American Association for Cancer Research.

Q-ball imaging (19), as well as methods to probe non-Gaussian diffusion, including biexponential (20, 21), stretched exponential (22), and kurtosis imaging (23), and methods to study perfusion-related effects at low  $b$ -values, such as intravoxel incoherent motion (IVIM; ref. 24). Although these techniques often provide a better characterization of tissue architecture than traditional models, the relationship of these measures to the underlying pathophysiology of tumors is largely unknown.

Advances in magnetic resonance (MR) technology are now creating even more possibilities, increasing excitement in the field by broadening the potential applications of DWI within cancer diagnosis and treatment. Newer scanners with improved gradient performance allow for higher  $b$ -values with shorter diffusion and echo times. In addition, improved coil technology and higher field strength provide better signal-to-noise ratio (SNR). With these MR advancements, it has become possible to develop new, innovative DWI methods that provide more direct measures of tumor cellularity by leveraging the intrinsic contrast of tumor cells relative to other tissues. Such direct measures address a top challenge posed by the NCI to develop *in vivo* imaging methods that portray tumor "cytotypes," i.e., imaging methods that can probe the identity, quantity, and location of different cells that make up a tumor and its microenvironment (NIH RFA-CA-13-020). However, the successful application of such methods requires not only advanced MR technology and an appreciation of the clinical challenges in neurooncology, but also an exquisite understanding of the physical basis of the DWI signal and its current limitations.

The purpose of this review is to provide a detailed explanation of the biophysical basis of diffusion contrast and to demonstrate what is known about how it reflects tissue microstructure in the context of key clinical dilemmas in neurooncology. We begin with a basic introduction of how diffusion measurements are derived from DWI and then follow with a review of the biophysical properties of water diffusion in tissue. We then describe how diffusion parameters in tissue are derived from the measurements via fitting of the diffusion model to observed data. For this review, we focus on one advanced DWI modeling technique called restriction spectrum imaging (RSI), which provides a general framework for estimating tissue properties from DWI data and addresses the NCI challenge for more direct, *in vivo* imaging of tumor cells. We also address the power of multispectral imaging, highlighting the importance of combining advanced DWI methods such as RSI with other imaging modalities (i.e., MRI perfusion, PET) to optimize the detection and monitoring of brain tumors. Although the primary focus of this review is on the application of RSI to neurooncology, the same methods are equally applicable to other applications of oncologic imaging, such as prostate, liver, and breast cancer, and we briefly present some preliminary data in prostate cancer at the end of "clinical applications."

## Principles of Diffusion MRI

### The diffusion experiment

While early diffusion measurements using nuclear magnetic resonance (NMR) in biologic tissue were made in the 1960s and 1970s, it was not until the mid 1980s that the basic principles of DWI emerged (25–27). All MRI techniques, including DWI, rely

on the fundamental principle that water hydrogen nuclei become magnetized when placed in a strong static magnetic field. MRI contrast is formed by perturbing this magnetization using electromagnetic waves and then allowing the magnetization to "relax" back to an equilibrium state. Tissue relaxation times—namely, the spin–lattice ( $T_1$ ) and spin–spin ( $T_2$ ) relaxation times—form the fundamental basis of soft tissue contrast and anatomic imaging with MRI. DWI is an MRI technique that adds additional sensitivity to the intrinsic random thermal displacements of water molecules that take place during the MRI experiment as part of the natural diffusion process. A pair of pulsed magnetic field gradients are turned on and off in succession (with duration  $\delta$ ) to magnetically "label" and "refocus" the spin phase of hydrogen nuclei, depending on where they reside physically in the gradient field (Fig. 1). The second refocusing pulse is applied some finite time  $\Delta$  after the first pulse in an effort to realign the spin phases of stationary nuclei. Thus, any residual spin phase left after the application of the refocusing pulse can be attributed to the diffusion of water along the orientation of the field gradient during the effective diffusion time of the experiment  $T_d$ , defined here as  $\Delta - (\delta/3)$ . The net phase dispersion due to diffusion causes an attenuation of the measured signal and a decrease in the voxel intensity. Stejskal and Tanner (28) were some of the pioneers of the pulsed field gradient experiment and provided the mathematic framework to relate the diffusion coefficient to the experimental variables. To date, the Stejskal Tanner pulse sequence remains the gold standard method for measuring diffusion in the clinic and forms the basis of quantitative mapping of tumor cellularity with ADC, as discussed below.

### Biophysics of water diffusion in tissue

In this section, we provide a basic review of the three principal physical modes of diffusion in tissue: free, hindered, and restricted.

**Free diffusion.** Free water diffusion describes the random (Brownian) motion of water molecules due to thermal agitation, in the absence of any obstacles. The displacement distribution of free water molecules is time dependent and Gaussian and obeys a statistical law established by Einstein in 1905. Along a single direction in space, the average molecular excursion of water molecules is proportional to the square root of diffusion time  $T_d$ . Mathematically, this can be expressed as  $s = (2DT_d)^{1/2}$ , where  $s$  is the root-mean-squared distance and  $D$  is the diffusion coefficient (Fig. 2A). For free water at brain temperatures (37°C), the diffusion coefficient is approximately  $3 \mu\text{m}^2/\text{ms}$  (29), which translates to a distance of approximately  $17 \mu\text{m}$  in 50 milliseconds. In brain tissue, however, water molecules are constantly bouncing off and interacting with various tissue elements such as cell membranes and macromolecules. The net result is a decrease in diffusion mobility of water and a displacement distribution that no longer follows a single Gaussian distribution. Generally speaking, tissue elements impede water diffusion both through diffusion hindrance and restriction. Hindered and restricted diffusion are two distinct processes that result from fundamentally different behavior of spins within the intra- and extracellular tissue compartments, as described next.

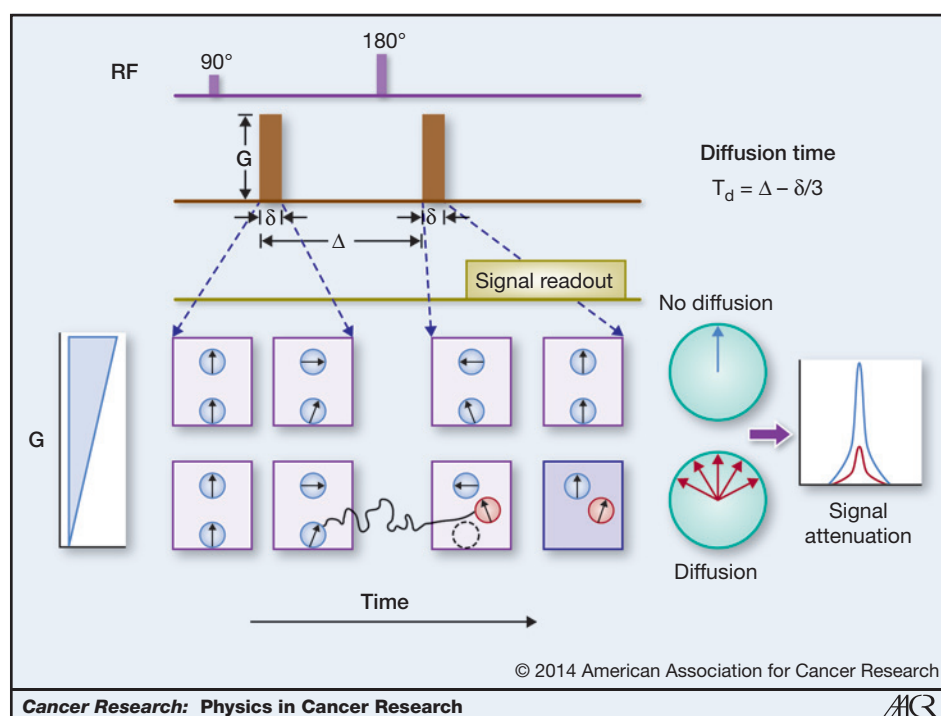


Figure 1. The diffusion experiment. Sensitivity to the random molecular displacements (Brownian motion) of water molecules is achieved through the use of two magnetic field gradient pulses with amplitude  $G$ , duration  $\delta$ , and separation  $\Delta$ . During the first pulse, the initial positions of water molecules (spins) are encoded with a phase offset, depending on their spatial location in the gradient field. The second pulse is then applied after some finite delay  $\Delta$  to realign the spin phases. In this way, if water molecules diffuse to a different physical location along the gradient field direction, refocusing will be imperfect and a net phase dispersion will result. This phase dispersion causes an attenuation of the magnitude signal and a decrease (darkening) of the measurement voxel in the reconstructed image.

**Hindered diffusion.** Hindered diffusion refers to the delay of passage of small molecules as they navigate around cellular obstacles, as in brain extracellular space (ECS; Fig. 2B). There is a long history (30) of quantifying the degree of hindrance to diffusion in the ECS compared with that of a free medium by the tortuosity  $\lambda$  (31), defined simply as the square root of the ratio of the free (or intrinsic) extracellular diffusion coefficient  $D_{\text{extra}}$  to the measured or ADC for extracellular water  $\text{ADC}_{\text{extra}}$ :  $\lambda = (D_{\text{extra}}/\text{ADC}_{\text{extra}})^{1/2}$ . As such, tortuosity simply reflects the degree to which the ECS slows diffusion relative to free water. Extensive experimental studies using real-time iontophoresis (RTI) using the cation tetramethylammonium (TMA) indicate that diffusion through tortuous ECS in normal brain is generally slowed by a factor of about 2.6, corresponding to  $\lambda$  of about 1.6 (31). Although there may be several factors that ultimately contribute to the delay of passage of water molecules in brain ECS (such as the composition of the extracellular matrix and the transient trapping or binding of water molecules to cell surfaces; see ref. 32), perhaps the greatest contribution is ECS geometry (dictated by the extracellular volume fraction  $\alpha$  and shape of cells). As  $\alpha$  decreases, due to, for example, cell swelling or greater cell packing density (cellularity), water molecules must travel more circuitous paths around cellular obstructions and tortuosity increases. The maximum theoretical tortuosity due to geometry can be quantified as the ratio of the distance though the center of a spherical cell to the distance around the periphery of the cell or  $\lambda_g = \pi/2 = 1.57$  (Fig. 2, inset). However, more complex simulations over a wide variety of packed cellular objects indicate that the maximum tortuosity due to geometry is no greater than 1.22 (33). In tumor ECS (or "tumor interstitium"), both tortuosity and volume fraction  $\alpha$  are generally higher. For example, in anaplastic astrocytomas and glioblas-

tomas, the average  $\alpha$  was measured to be as high as 0.47 to 0.49, with  $\lambda$  around 1.67 to 1.77 (34). Increased  $\alpha$  has been associated with necrosis and/or vasogenic edema, whereas increased  $\lambda$  may result from either astrogliosis, commonly observed in tumor tissue, or to changes in the extracellular matrix (32, 34). In summary, while it is often suggested that the low ADC observed in high-grade tumors results from increased packing density (cellularity) of cells due to greater hindrance imposed on extracellular water diffusion, from a physical perspective, cellular crowding can only mildly reduce the effective diffusion coefficient in tumors ( $\lambda$  increases only narrowly with decreasing  $\alpha$ ). Therefore, it stands to reason that a major component in decreased ADC in tumors, especially at high  $b$ -values, is restricted diffusion within the cellular compartments themselves, described next.

**Restricted diffusion.** Restricted diffusion is a term classically used (35) to describe the trapping of water molecules within an enclosed compartment (i.e., as defined by the cell plasma membrane) such that the net distance traveled is restricted or confined by the compartment dimensions. Although the term "restricted diffusion" is often used in the clinical literature to refer to any reported decrease in ADC, the physics of restricted diffusion is fundamentally different from hindered or free water diffusion. Specifically, for restricted diffusion, the net squared displacement of water molecules is sublinear in time and therefore non-Gaussian (Fig. 2C). In addition, the time evolution of net displacements strongly depends on the size and shape of the restricting compartment as well as the intrinsic intracellular diffusivity  $D_{\text{intra}}$ . In contradistinction to hindered extracellular water, where  $\text{ADC}_{\text{extra}}$  is independent with diffusion time  $T_d$ , the effective diffusion coefficient for intracellular water (or  $\text{ADC}_{\text{intra}}$ ) decreases with



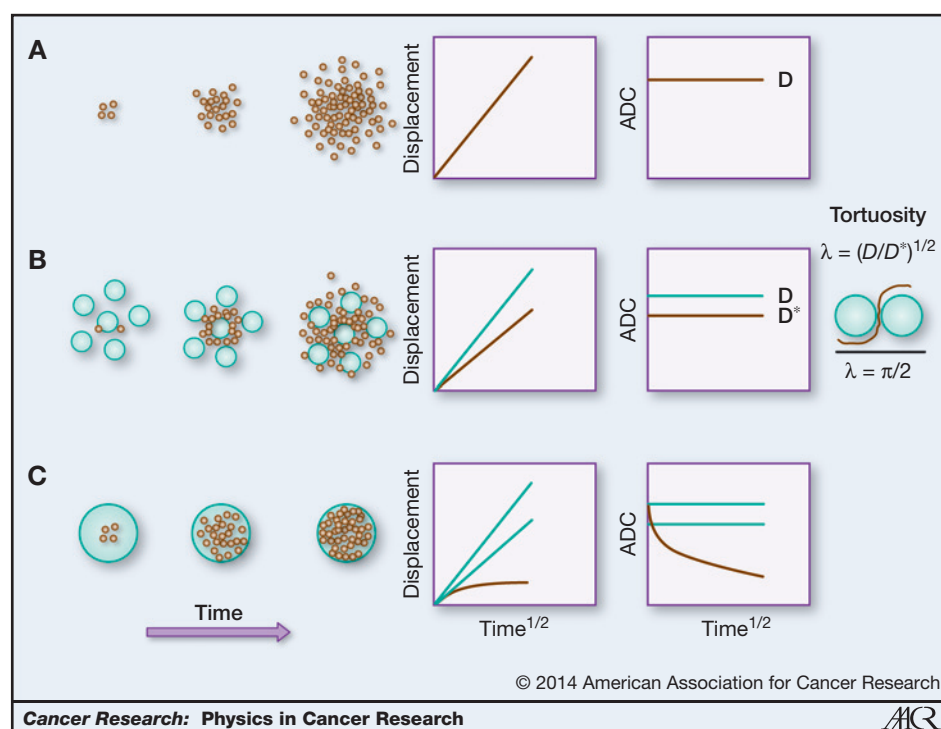


**Figure 2.** The three principal modes of diffusion in tissue. A, free diffusion; in free water, the average molecular excursion along a single dimension in space in terms of the root-mean-squared distance  $s$  increases linearly with the square root of diffusion time  $s = (2DT_d)^{1/2}$  with a slope that depends on the intrinsic diffusivity  $D$ . B, hindered diffusion; for hindered water in brain ECS, the net displacements remain linear with the square root of diffusion time (i.e., Gaussian), but the effective diffusion coefficient  $D^*$  (or ADC) is reduced compared with  $D$  due to tortuosity of the ECS. The theoretical maximum reduction in  $D^*$  (or ADC) that can be expected due to crowding of small spherical cells in the ECS is given by the tortuosity limit  $\pi/2$  or 40% (35). C, restricted diffusion; in restricted intracellular diffusion, the net distance traveled by water molecules is limited by the compartment dimensions, leading to a sublinear time evolution of the net squared displacement and a decreased ADC. The ADC of restricted intracellular water decreases with diffusion time as a larger proportion of the spins "bounce off" the plasma membrane.

$T_d$  over a finite range as a larger proportion of the spins "bounce off" the plasma membrane.

It is important to note that restricted (or non-Gaussian) diffusion must be discussed within the context of diffusion time, permeability, and the size of the restricting cellular compartments. For instance, in the short-time limit ( $T_d < 1$  ms), diffusion is largely unrestricted and dictated by the intrinsic diffusivity of the medium ( $ADC_{intra} \sim D_{intra}$ ), except for a small minority of spins located in close proximity to cell membranes or other barriers. Conversely, in the long-time limit ( $T_d > 1$  s), much greater than the average residence time for water within intra- and extracellular compartments, diffusion is dominated by exchange and can be accounted for by a single apparent tensor, reflecting the effective medium approximation of the tissue ( $ADC_{intra} \sim ADC_{tissue}$ ). In the intermediate-time regimen, relevant to typical clinical DWI acquisitions ( $T_d \sim 50$ – $100$  ms), the diffusion time is short relative to exchange between intra- and extracellular compartments through the plasma membrane (36), but long enough for water molecules to repeatedly come in contact with and "bounce off" the plasma membrane. In this case, the intracellular spins approach a "fill-up" regimen, where the displacements of spins are physically restricted by the plasma membrane and, therefore, dictated by the size and shape of the cellular compartment. Note that in the intermediate-time regimen, diffusion in the ECS remains hin-

dered and behaves according to a classic Gaussian model, where the tortuosity is a function of packing density and extracellular volume fraction (31). Therefore, the total water signal in the intermediate-time regimen reflects a superpositioning of hindered and restricted water, leading to a non-monoexponential signal decay at high  $b$ -value. As we see below, separating the restricted water fraction from hindered and free water fraction provides a more sensitive and specific biomarker for tumor cellularity compared with traditional ADC.

### Diffusion models

Diffusion models form the fundamental basis through which quantitative information about the underlying tissue microstructure can be gleaned from DWI signals. The typical millimetric scale at which DWI measurements are made (i.e., voxel size) is large compared with the micrometric scale of the underlying physical diffusion process, and, therefore, the goal of the diffusion model is to bridge the gap such that inference can be drawn on a scale much smaller than the voxel dimensions. One of the advantages of DWI over other MRI techniques is that the physical scale probed by the measurements can be adjusted by the experimental variables, namely the diffusion time ( $T_d$ ) and diffusion-weighting factor ( $b$ -value). As we see, this forms the fundamental basis through which more advanced multiscale, or non-Gaussian, diffusion models offer

insight into compartmental diffusion in cancer and improved imaging biomarkers for tumors. We begin this section with brief introduction of the classic ADC and tensor model for Gaussian diffusion and follow it with a more detailed introduction to RSI, a technique developed in our laboratory for probing tissue microstructure in greater detail.

**ADC.** As a departure from earlier studies in which efforts were made to measure the true diffusion process in biologic systems (37), it was suggested in the mid 1980s (24) to model the complex diffusion in tissue using the free (Gaussian) diffusion equation, but replace the intrinsic diffusion coefficient  $D$  with a global statistical parameter called ADC. The ADC concept has since been used extensively in the literature as well as clinical oncology as a surrogate marker of tumor cellularity (1–3). In practice, the ADC is estimated by combining the experimental variables (i.e., the magnitude, duration, and temporal spacing of the diffusion gradients) into a single parameter called the diffusion-weighting factor, or  $b$ -value (24), and comparing the signal attenuation at one or more nonzero  $b$ -values with the baseline signal measured without diffusion weighting (i.e., with a  $b$ -value of zero). For Gaussian diffusion, the signal attenuation decays exponentially with the product of the  $b$ -value and ADC, and, therefore, the ADC reflects the slope of the best fit line to the log signal as a function of  $b$ -value. The diffusion tensor model (DTI) extends the ADC concept to three-dimensional space, allowing for different ADCs along and perpendicular to the principal axis of diffusion (38).

The main limitation of the ADC and tensor model as imaging biomarkers for tumors is their strict dependence on a single Gaussian function for the displacement distribution of water molecules within cancer tissue and, therefore, a monoexponential dependence on the  $b$ -value. Although a single Gaussian assumption may be appropriate for data collected over a fairly narrow range of  $b$ -values (up to about 1,000 s/mm<sup>2</sup>), the inferences that can be drawn are limited by lack of specificity. For example, numerous investigators have shown a negative correlation between the tumor ADC values and cellularity (1–3), which is commonly attributed to increased restricted diffusion imposed by tumor cells. However, despite increased restricted diffusion, tumor ADC values rarely fall below that of normal appearing white matter (NAWM). This is true even in highly cellular tumors that originate in white matter, such as glioblastoma multiforme (GBM) and primary CNS lymphoma (39). One explanation for higher than expected ADC values in these tumors is the presence of vasogenic edema and focal necrosis within the tumor itself, which increases the ADC through reduced hindrance imposed on the extracellular water (40, 41). Thus, increased ADC due to edema and necrosis will offset reduced ADC imposed by tumor cells, resulting in lesions that are difficult to discern from NAWM on the basis of the ADC alone. This effect becomes more pronounced as the  $b$ -value is reduced because of increasing sensitivity to the fast, hindered water fraction.

**RSI.** Over the past decade or so, advances in DWI acquisition and gradient hardware have made it possible to probe a whole new regimen of water diffusion in cancer tissue beyond what was previously possible on clinical MRI scanners. Specifically, the application of strong magnetic field gradient

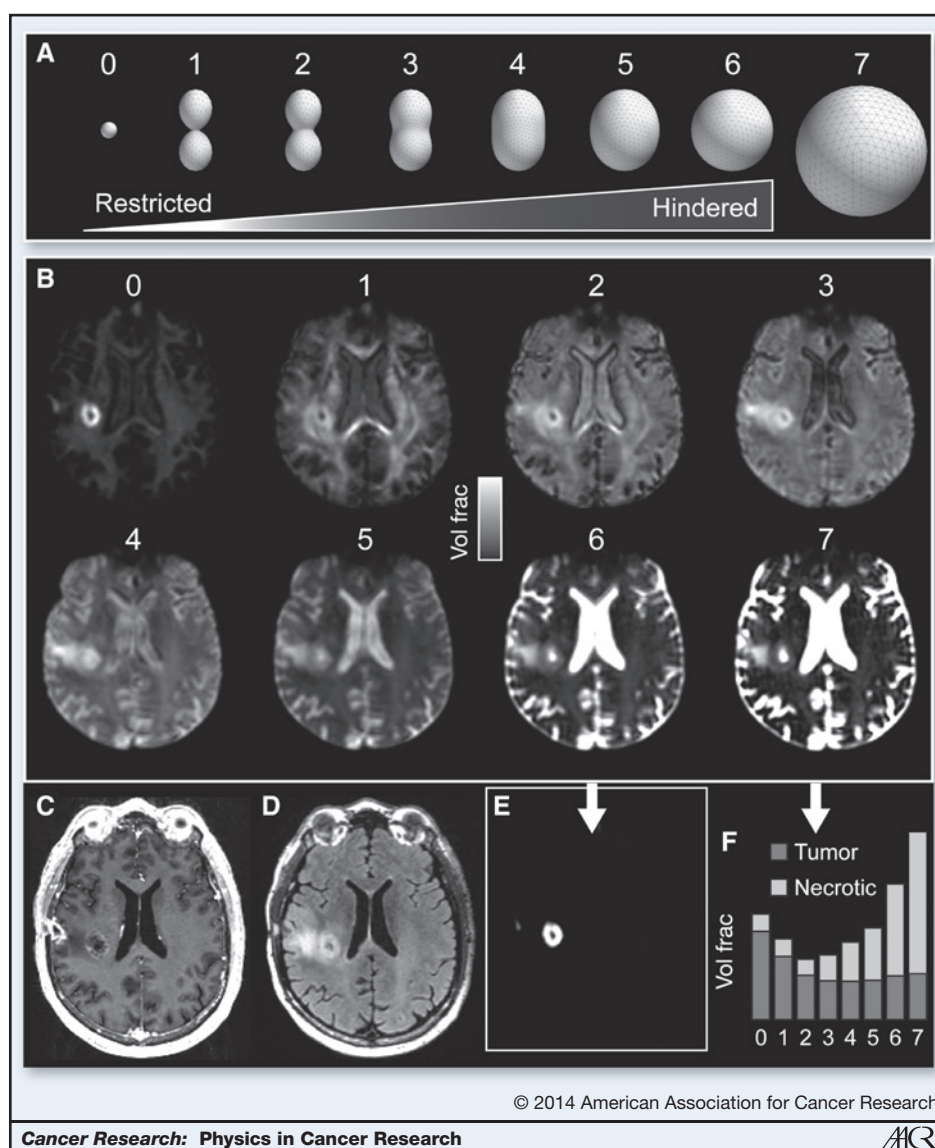
pulses has allowed a much greater range of  $b$ -values, diffusion directions, and diffusion times to be acquired during a clinical acquisition. As a result, diffusion signals can be made specific to pools of water with very low effective diffusion coefficients, well below the tortuosity limit for ECS water, likely originating from restricted water trapped within the cells themselves (42). Numerous promising methods are emerging to capture and model complex non-Gaussian diffusion in tissue, including biexponential (20, 21), stretched exponential (22), and kurtosis models (23), as well as methods to study perfusion-related effects in DWI data at low  $b$ -values, such as IVIM (24). The application and description of many of these techniques for neurooncology applications can be found in an excellent review provided by Maier and colleagues (39). Moreover, techniques are emerging to probe diffusion spectra at ultra-short diffusion times on clinical systems using oscillating gradients (43), which hold promise for probing intracellular structures and alterations in cancer (44). For this review, we focus on one particular technique developed in our laboratory called RSI. Over the last few years, RSI has gained increased recognition as an important tool in oncology that overcomes many of the limitation of traditional DWI and ADC.

RSI is a general framework for modeling diffusion signals collected across a broad range of experimental parameters and relating these signals to underlying tissue parameters (e.g., size and shape/orientation of hindered and restricted water compartments) using a linear mixture model (45). The ultimate goal of RSI is to enable quantitative estimates of tissue microstructure based on noninvasive imaging. To achieve this, the diffusion signal is modeled as reflecting a mixture of components, where each component describes the signal dependence on specific tissue properties (e.g., cell size, density, orientation, etc.) as a function of the experimental (protocol) settings (e.g.,  $b$ -value, diffusion time, echo time, etc.). The total signal becomes the weighted sum of these components, and the goal is to determine the individual weights. This is achieved through the application of generalized linear estimation techniques (45, 46). As such, the RSI framework is designed to strike a balance between model complexity and interpretability by minimizing *a priori* assumptions on microstructure while preserving biophysical interpretability of the resulting estimates.

Our current clinical implementation of RSI acquires data with  $b$ -values of 500, 1,500, and 4,000 s/mm<sup>2</sup> and multiple diffusion directions at each  $b$ -value at a fixed intermediate diffusion time (~90 ms), where intracellular spins would be expected to be in the fill-up regimen. The RSI design matrix includes a distribution (or "spectrum") of effective diffusion pools spanning hindered and restricted length scales with both isotropic and anisotropic geometries. In Fig. 3, we illustrate both a schematic for the RSI spectrum model and the resultant fit of the model to data collected in a 51 year-old patient with right frontal GBM before surgical intervention (47). Note the separation of diffusion components in different tissue types, with the primary lesion exhibiting a large volume fraction of spherically restricted water, likely stemming from water trapped within cancer cells. Also note the large fraction of free and hindered water in areas of necrosis and edema. The volume fraction of spherically restricted water (either with or



**Figure 3.** RSI analysis of a 51 year old male with right frontal GBM. A, illustration of the RSI "spectrum" model used to fit the multi- $b$ -value, multidirection DWI data. Scales 0–2 and 3–6 correspond to restricted and hindered diffusion, respectively. Scales 0, 6, and 7 are isotropic, whereas scales 1–5 are anisotropic (i.e., oriented). B, RSI-derived ( $T_2$ -weighted) volume fraction maps for each scale in A. C,  $T_1$ -weighted postcontrast (D)  $T_2$ -weighted FLAIR (E) RSI-derived "cellularity map" (RSI-CM) corresponding to a weighted ("beamformed") linear combination of scales 0–7 showing maximal sensitivity and specificity to spherically restricted diffusion (scale 0). F, bar plot of volume fractions for two representative voxels in tumor and necrotic tissue, respectively.



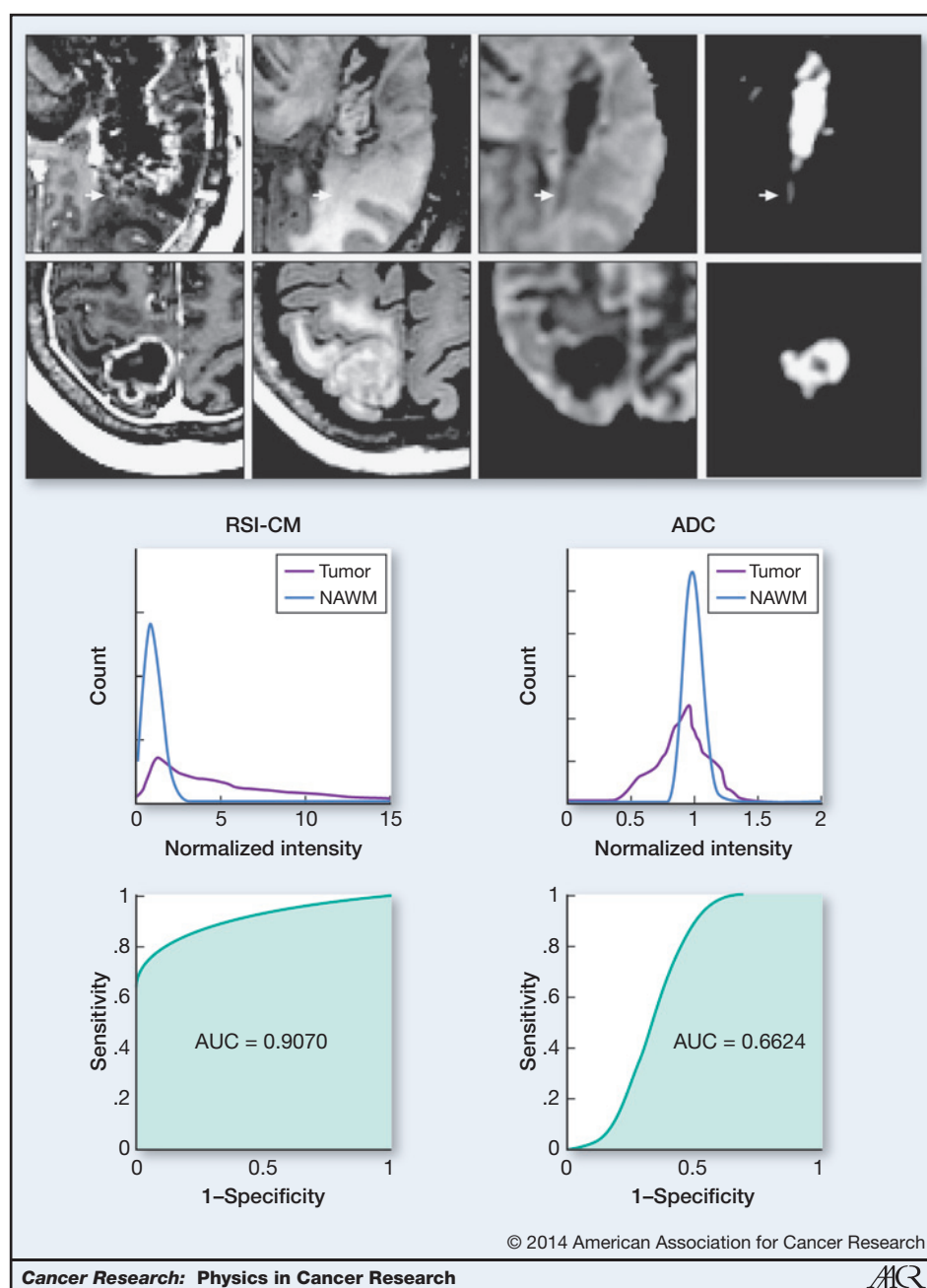
without additional filtering of white matter signal using a technique called "beamforming"; ref. 48) has been coined the RSI cellularity index or cellularity map (47, 49–51). In addition, the signal from the restricted anisotropic component can be used to map the density and orientation of surrounding white matter tracts (50).

In summary, advanced DWI methods such as RSI that acquire data over an extended  $b$ -value range provide the ability to quantify complex non-Gaussian diffusion in tissue (21–23, 45, 52). Although these emerging techniques offer a new class of cancer imaging biomarkers, there remain many unanswered questions and tremendous opportunity for further advancing the field. Of particular importance is to understand exactly how parameters of the diffusion model relate to specific properties of cancer tissue, such as tumor cell size, density, and nuclear volume fraction. How specific are these biomarkers to tumor cells versus healthy or inflammatory cells? Can these new imaging biomarkers characterize tumor cytotypes and

address a top challenge posed by the NCI to develop *in vivo* imaging methods that can probe the identity, quantity, and location of different cells that make up a tumor and its microenvironment? (NIH RFA-CA-13-020). Finally, to what extent can these new imaging biomarkers help solve current clinical dilemmas in oncology such as distinguishing tumor recurrence from radiation injury? Answering these questions will undoubtedly require both advances in diffusion modeling, simulation, and MRI hardware and software [such as the latest ultra-high performance ("connectome") MRI scanners; ref. 53] together with improved quantitative histology, multimodal image registration, and validation procedures.

### Clinical Applications of RSI

Because of its ability to isolate areas of truly restricted diffusion by separating and removing the hindered diffusion signal, RSI offers a more direct measure of tumor cells than other diffusion-weighted methods. Within the past year, we



have shown that by identifying areas of restricted diffusion, RSI can be applied clinically to (i) improve tumor conspicuity in patients with high-grade primary and metastatic brain tumors (47), (ii) facilitate the interpretation of tumor response on imaging following antiangiogenic treatments that significantly reduce edema (49), and (iii) improve the ability to visualize white matter pathways coursing through regions of peritumoral edema relative to standard DTI (50). In the following sections, we describe each of these clinical applications in further detail. In addition, we describe a clinical scenario in which RSI lacks specificity and a multispectral imaging approach is warranted.

#### Improved conspicuity of high-grade tumors with RSI

As described in the Introduction, ADC is frequently used as a marker of tumor cellularity in patients with high-grade tumors (1–3). Areas of tumor are associated with decreased ADC relative to surrounding tissue (40). However, concomitant edema and tumor-related necrosis increase ADC values, thereby directly opposing the reduction in ADC associated with tumor (54, 55). This offset presents a diagnostic challenge by diminishing the conspicuity of tumor on ADC maps. Because RSI isolates areas of spherically restricted diffusion, we tested whether it could provide increased conspicuity and delineation of tumor margins relative to standard and high *b*-value ADC

(47). To accomplish this, RSI was performed in ten presurgical patients: four with GBM, three with primary CNS lymphoma, and three with metastatic brain tumors. Tumor conspicuity, edema conspicuity, and relative sensitivity to edema were quantified for RSI cellularity maps (RSI-CM), high  $b$ -value DWI ( $b = 4,000$ ), and ADC, and these values were compared in manually drawn volumes of interest. Receiver operating characteristic (ROC) curves were used to evaluate the sensitivity and specificity of each method for delineating tumor from NAWM. In addition to visible differences in conspicuity (Fig. 4), ROC curves revealed greater sensitivity and specificity for delineating tumor from NAWM with RSI-CM (AUC = 0.91) compared with both high  $b$ -value DWI (AUC = 0.77) and ADC (AUC = 0.66). In addition, the relative sensitivity to edema was greater for high  $b$ -value DWI and ADC compared with RSI, reflecting RSI's ability to suppress the fast diffusion component associated with edema. Furthermore, greater heterogeneity of the diffusion signal within the tumor was observed on the RSI-CMs compared with DWI and ADC, as evidenced by a broader

histogram distribution. This may represent the intrinsic heterogeneity of tumor cellularity both within and across tumor types. These data demonstrate one promising application of RSI, i.e., improved conspicuity and delineation of high-grade tumors compared with traditional DWI models and underscore the possibility that RSI may prove helpful in delineating tumor cytotypes and infiltrating disease in peritumoral edema.

#### RSI in the context of antiangiogenic treatment

Antiangiogenic therapies, such as bevacizumab, are increasingly used in the treatment of recurrent high-grade gliomas. However, these agents decrease permeability of the blood-brain barrier and, therefore, decrease contrast enhancement and edema in patients with high-grade gliomas in a manner that may not correlate with actual tumor response—a phenomenon known as pseudoresponse (56). Given this imaging challenge, we evaluated the ability of RSI to improve conspicuity within regions of the tumor compared with ADC in patients treated with bevacizumab and to further demonstrate

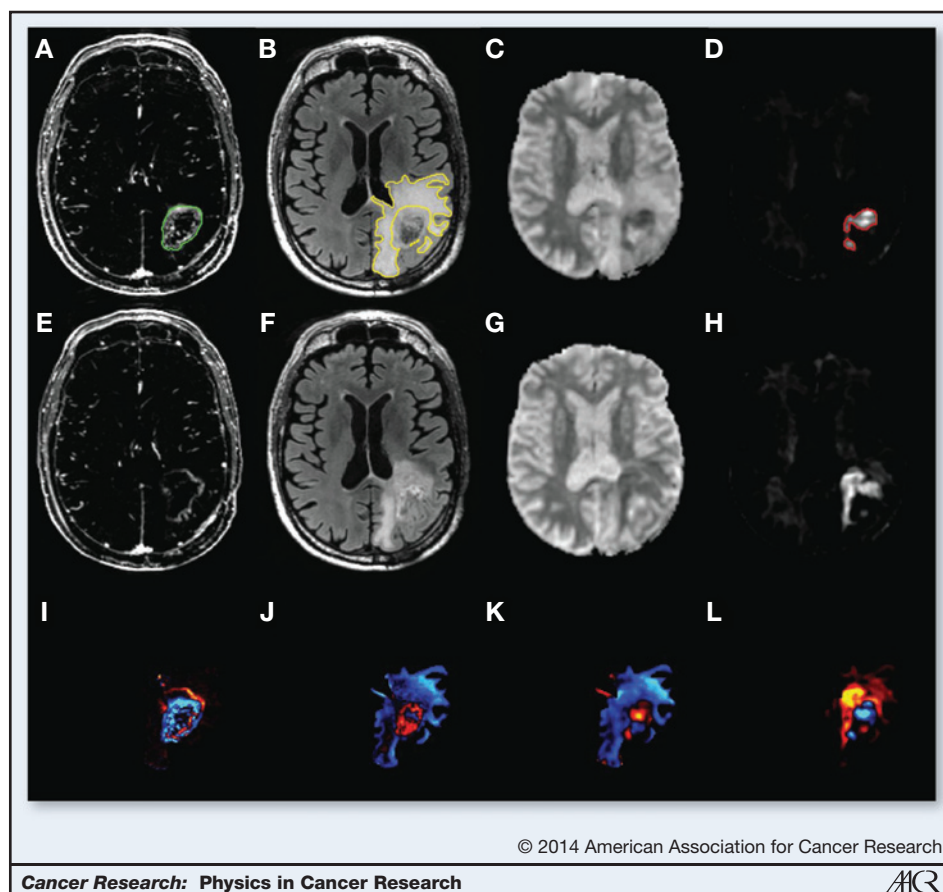


**Figure 5.** A 67 year old male with left parietal GBM status postresection and chemoradiation. Top, the T<sub>1</sub> postcontrast – T<sub>1</sub> precontrast (A), FLAIR (B), ADC (C), and RSI-CMs (D) before the start of bevacizumab; middle, T<sub>1</sub> postcontrast – T<sub>1</sub> precontrast (E), FLAIR (F), ADC (G), and RSI-CMs (H) after initiation of bevacizumab. Arrowheads, contrast-enhancing region (green), the surrounding region of FLAIR hyperintensity (yellow), and the region of restricted diffusion on RSI-CMs (red). Although there is a decrease in contrast enhancement and surrounding FLAIR hyperintensity after initiation of bevacizumab, the region of restricted diffusion increases and becomes more confluent, suggesting worsening residual/recurrent tumor. Moreover, this increase in the region of restricted diffusion is much more conspicuous on the RSI-CMs compared with the ADC. Bottom row depicts these changes on "change maps" (change in T<sub>1</sub> postcontrast – precontrast; I), change in FLAIR (J), change in ADC (K), and change in the RSI-CMs (L), with red-yellow indicating an increase in signal intensity and blue-cyan indicating a decrease in signal intensity. Of note, on the ADC change map (K), the area of increased restricted diffusion is essentially masked by the decreased signal intensity within the region of surrounding FLAIR hyperintensity.



that RSI is minimally affected by bevacizumab-induced reductions in edema (49). RSI-CMs and DWI were available for a series of patients with recurrent gliomas at baseline and following initiation of bevacizumab. Results showed that all patients exhibited sharp decreases in contrast enhancement and edema following treatment (i.e., pseudoresponse). Bevacizumab-induced decreases in edema had a greater effect on ADC than on the RSI-CMs, with the relative sensitivity to changes in edema being more than 20 times higher on ADC than on RSI-CMs (Fig. 5). These data provide additional evidence that RSI is less influenced by changes in edema compared with ADC, which may confer an advantage of RSI for interpreting true tumor response in the setting of anti-angiogenic treatment. However, this study did not include clinical follow-up. Thus, whether RSI has greater predictive validity than ADC is of key importance and requires additional investigation.

#### RSI for improved delineation of white matter tracts

There is increasing enthusiasm for the use of DTI and tractography in neurosurgical planning (57–64), and there is some evidence that tractography-guided neuronavigation can be used to minimize neurologic morbidity (60, 65, 66). However, the ability to resolve white matter structure in peritumoral regions that include edema has remained a challenge (39, 67). We applied the same logic as in the previous examples and tested the ability of RSI to provide better visualization and quantification of white matter tracts in regions that include edema (50). In this example, isolating the slow, restricted compartment yields a better estimate of "tubularity" (i.e.,

models the cylindrically restricted diffusion within axons; Fig. 3B, scale 1; ref. 45). This increases the sharpness of the estimates, allowing for better delineation of fiber tract orientation. In a series of ten patients with high-grade gliomas, we were able to demonstrate that RSI yielded higher fractional anisotropy (FA) estimates in regions of edema relative to standard DTI. Furthermore, at follow-up when the edema had resolved in most patients, FA estimates increased with DTI, but remained stable with RSI, indicating that FA estimates based on DTI were artificially suppressed by the edema. Tractography performed within regions of edema revealed superior ability of RSI to track fibers through areas of significant edema relative to standard DTI (Fig. 6). These data address yet another important and growing application of diffusion imaging within the field of neurooncology (i.e., surgical planning) and speak to the advantage of using advanced DWI models for revealing the anatomic structure of peritumoral white matter. An important caveat to mention is that it is well known that gliomas grow via an infiltrative pattern and that there is often nonenhancing infiltrating tumor surrounding the enhancing portion of a high-grade glioma (68). Further investigation is required to determine whether RSI or other advanced DWI methods will prove useful for detecting these areas of tumor infiltration.

#### Importance of a multispectral imaging approach

Despite the many recent advancements in MR technology and DWI methods, no single modality has emerged as the "holy grail" of tumor imaging. Thus, most diagnostic challenges in neurooncology are best addressed using a multispectral

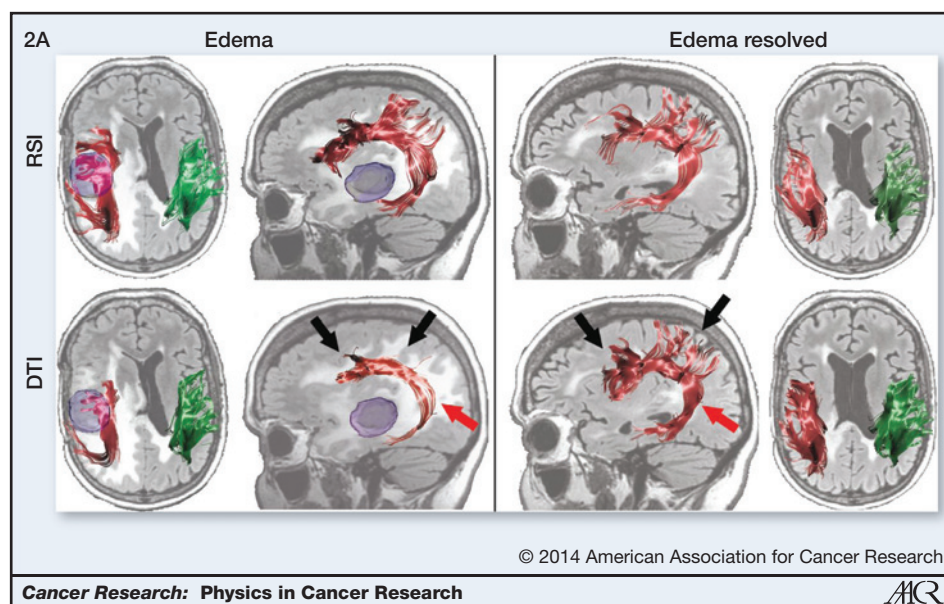
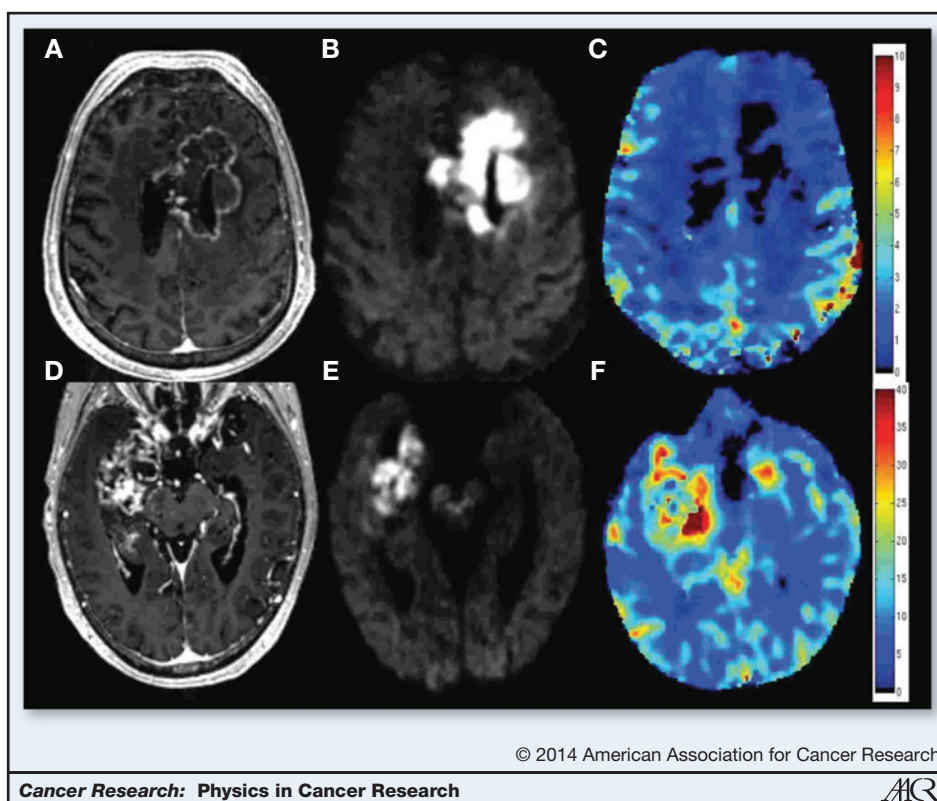


**Figure 6.** Streamline tractography of the superior longitudinal fasciculus for a 58 year old female with a right temporal lobe GBM projected onto baseline and follow-up FLAIR images. Left, RSI and DTI-based tractography at baseline in regions of edema; right, data obtained using the same tractography algorithm once the edema had mostly resolved. The ipsilateral (red) and contralateral (green) 3D renditions of the superior longitudinal fasciculus are superimposed on axial and sagittal FLAIR slices collected at each time point. The GBM is shown in blue in the preoperative image. With RSI, the superior longitudinal fasciculus appears very similar at baseline and at follow-up. However, with DTI, the superior longitudinal fasciculus appears thinner and truncated at baseline in regions of edema. Black arrows, frontal and parietal regions of the superior longitudinal fasciculus that terminate completely in regions of edema; red arrow, sparse streamlines in the temporal portion of the superior longitudinal fasciculus. These streamlines are "recovered" using DTI once the edema resolves.

**Figure 7.** Comparison of a 55 year old male with GBM treated with chemoradiation and bevacizumab (top) and a 66 year old male with GBM before any treatment (bottom). T<sub>1</sub> postcontrast images (A and D), RSI maps (B and E), and rCBV maps (C and F) are shown. Degree and homogeneity of restricted diffusion is greater in the patient treated with bevacizumab than in the pretreatment GBM control (images scaled identically with same window and level), whereas rCBV in the region of restricted diffusion is remarkably low in the patient treated with bevacizumab—lower than in the GBM control and lower than in the NAWM.



imaging approach. One particular challenge occurs following treatment with concurrent bevacizumab and radiotherapy, with a subset of patients developing regions of marked and persistent restricted diffusion that do not seem to reflect an aggressive tumor (69–71). Although the etiology of these lesions remains uncertain, pathologic confirmation in several patients has revealed atypical gelatinous necrosis. We have coined this abnormality bevacizumab-related imaging abnormality (BRIA) and have observed that the BRIA signal on RSI is quantitatively similar to that seen in a tumor (51). This illustrates a clinical scenario in which RSI lacks specificity and a multispectral imaging approach is warranted. Thus, we explored whether using RSI in combination with perfusion imaging could help to differentiate BRIA from recurrent tumor. In a series of patients, we show that these techniques are complementary in that RSI is superior to rCBV for differentiating pathology from NAWM, whereas rCBV is superior for differentiating BRIA from tumor (Fig. 7). Thus, the combination of high RSI signal and low rCBV provides a distinct imaging signature of the BRIA phenomenon. Because of the increasing use of antiangiogenic agents, imaging methods that increase our understanding of both pseudoresponse and BRIA are of high importance. These data highlight an important example in which RSI lacks specificity in its current instantiation, and information from complementary imaging modalities is essential.

#### RSI for improved detection of other solid organ tumors

Although this review is primarily focused on neurooncology applications, quantitative imaging is equally relevant to other

solid organ tumors. For example, multiparametric MRI has been explored in a variety of applications, including discrimination between indolent and aggressive disease in prostate cancer. Routine  $T_2$ -weighted imaging of the prostate is the most sensitive way to evaluate anatomic detail, but is limited for disease detection, with sensitivity of around 70% and specificity of 55% (72). Functional MR techniques enhance detection, grading, and staging of prostate cancer through the use of dynamic contrast enhancement (DCE), DWI, and MR spectroscopic imaging. DCE requires intravenous administration of a  $T_1$ -shortening agent with the chief limitation being that the maximum contrast enhancement between malignant and nonaggressive disease is small (73). MR spectroscopic imaging increases specificity (74, 75), but is technically challenging and can add significantly to scan time.

Multiple studies have shown that DWI improves sensitivity and specificity in the diagnosis of prostate cancer by increasing tumor conspicuity on DWI or quantitative ADC maps. However, hemorrhage, inflammatory processes, and benign nodules in the transitional zone can all exhibit lower ADC values, leading to false positives (76). DWI can also suffer from severe spatial distortion, limiting its coregistration to anatomic images, which is necessary for tumor localization.

Increasing Gleason score correlates with loss of normal gland formation, loss of peripheral gland tubular structure, and increased cellularity (77). We hypothesize, therefore, that RSI cellularity will correlate with higher tumor grade, as measured by Gleason score, and will provide significantly greater accuracy in discriminating aggressive tumors from

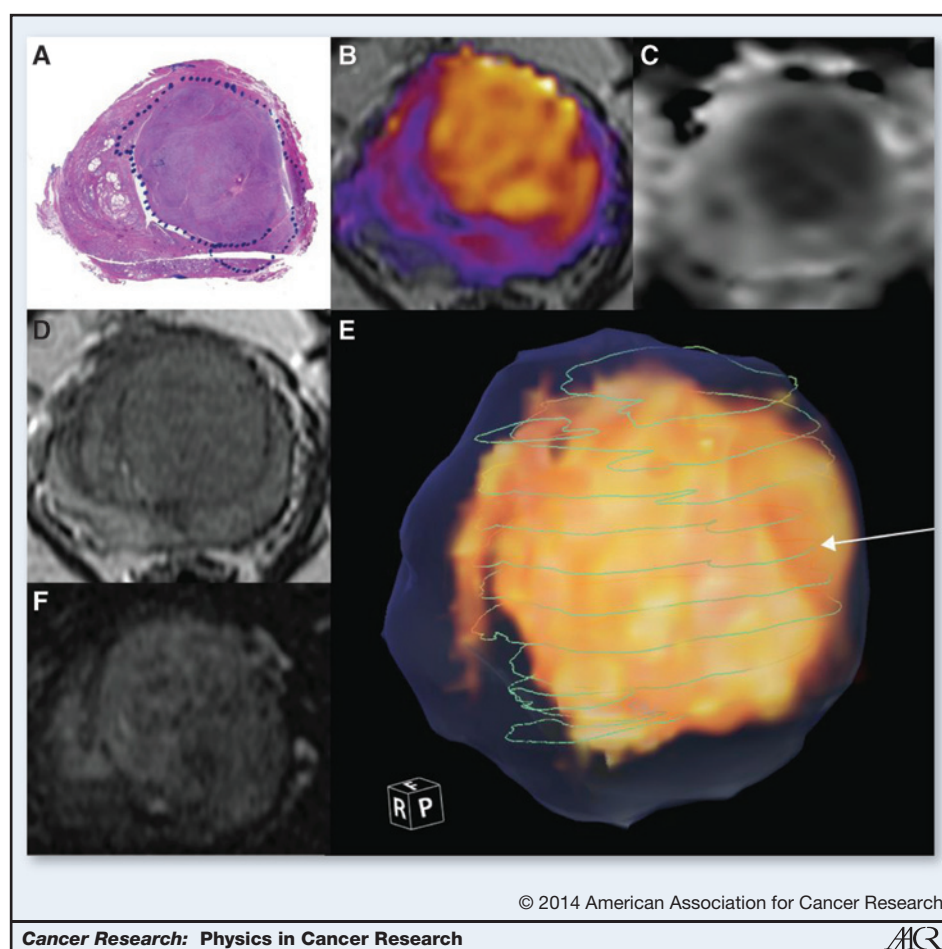


**Figure 8.** Gleason 3+4. A, histology section stained with hematoxylin and eosin. Blue dotted line, the boundary of the tumor. B, RSI cellularity map, color-coded and overlaid on T<sub>2</sub>. C, ADC image. D, T<sub>2</sub> image. E, 3D volume rendering of the RSI (in yellow), the whole extent of the prostate as traced on T<sub>2</sub> images (translucent blue), and green lines indicating the boundary of the tumor on each of the whole-mount histologic sections that were compared with the RSI. The white arrow indicates the line corresponding to the histology section shown in A. F, raw perfusion data.

benign and indolent lesions when compared with current functional or anatomic imaging techniques.

Our preliminary data are encouraging. Figure 8 shows a patient with Gleason 3+4 = 7 disease. RSI cellularity map is shown color-coded and fused with the T<sub>2</sub> after spatial distortion correction and registration. Note the correspondence of RSI cellularity with the histopathology slice. T<sub>2</sub> and perfusion images are not as conspicuous, with much less contrast-to-noise ratio. This represents an example case in which conventional imaging is not as diagnostic.

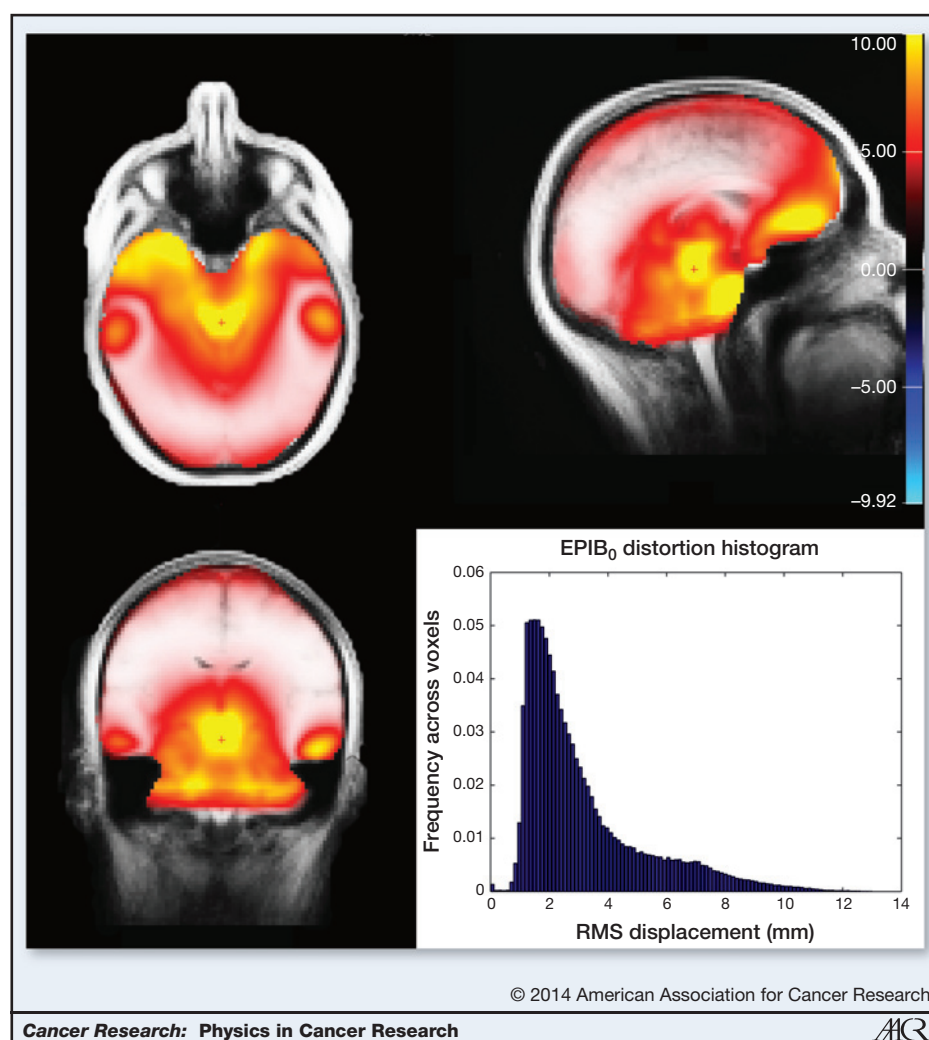
#### Importance of spatial distortion correction for accurate image-guided intervention

One of the main limitations of diffusion imaging in general is nonlinear spatial distortion of the images due to a number of factors, including gradient nonlinearities, eddy currents, and B<sub>0</sub> field inhomogeneities. Although distortions due to nonlinearities of the gradient fields are commonly corrected for by software on the scanner console, B<sub>0</sub> field inhomogeneities are not, despite being the dominant source of spatial inaccuracy in DWI. The magnitude of B<sub>0</sub> distortions varies depending on a number of factors, including field strength, positioning of the subject within the scanner, and subject-specific anatomy. The typical pattern of B<sub>0</sub> distortion on 3T systems is illustrated

in Fig. 9, along with the total whole-brain histogram of root mean square (RMS) displacements. As illustrated in the figure, on average (based scans from on 40 subjects) the typical (mode) distortion magnitude is approximately 2 mm, with a substantial proportion of voxels displaced more than 6 mm. Such distortions are of particular concern when images are used for image-guided intervention, including surgery, biopsy, or radiation dose planning. Although methods for correcting B<sub>0</sub> distortions have existed for some time (78–80), they are typically used only in research studies and not in clinical practice, primarily due to the additional scan time required to acquire the B<sub>0</sub> field maps required for standard correction methods. The method introduced by Holland and colleagues (81) overcomes this limitation by requiring only a single additional TR (2–3 seconds), using the reverse phase–encode polarity method (79, 82, 83). Moreover, this additional volume acquisition can be integrated directly in the native DWI protocol without changing the pulse sequence. Combined with efficient post-processing methods to estimate the distortion field (81), the reverse phase–encode polarity technique provides a much needed clinical solution for accurate spatial distortion correction of DWI data. The RSI technique incorporates this procedure as part of standard preprocessing of data, and all the data presented in this review has been corrected in this manner.



**Figure 9.** Three-plane map and histogram of the RMS displacement of voxels (in mm) due to  $B_0$  distortions for axially acquired EPI images (A/P phase encoding) from EPI scans of a 40 normal healthy subjects.



## Discussion and Conclusion

The field of MR imaging is rapidly evolving, leading to new and exciting possibilities within neurooncology, urologic oncology, and beyond. In particular, the development of advanced DWI methods has allowed for improved visualization and detection of tumor cells and, thus, has great potential for better understanding of tumor biology. Numerous clinical applications of this powerful technique have already been demonstrated, including tumor characterization and grading, prognostication, early prediction of response to therapy and survival, distinguishing tumor from treatment-related confounds, detecting microinfiltration, and guiding neurosurgical and radiation planning (84). However, future advances in the field will require a fundamental understanding of the underlying DWI signal coupled with validation of diffusion contrast in unique tumor-related pathologies. In addition to improved detection of tumors, advanced diffusion methods such as RSI may also provide quantitative characterization of cellular properties such as cell size, permeability, and nuclear volume fraction, based on signal variation as a function of diffusion

time and echo time (42). Validation of these measures will likely be borne out of translational efforts that include both preclinical and clinical studies in which histologic specimens are carefully coregistered to *in vivo* imaging. The need for targeted biopsies based on advanced DWI, precise coregistration of DWI with other imaging modalities, and careful corrections for geometric distortions will all be pivotal to providing the spatial precision needed to achieve such validation. These requirements underscore the need for a multidisciplinary approach to this validation including experts in the fields of oncology, surgery, pathology, and radiology. Through this collaboration, not only will current applications of DWI be further improved, but new possibilities will also be created that will ultimately lead to better care for patients suffering from cancer.

## Disclosure of Potential Conflicts of Interest

D. Holland has ownership interest in patent #8,160,319 (reducing distortion in magnetic resonance images). A. Bjørnerud is a board member of NordicNeuroLab AS. D. Margolis received a commercial research grant from Siemens Medical Systems. A.M. Dale received a commercial research grant from General Electric Healthcare and has ownership interest (including

patents) in CorTech Labs, Inc. No potential conflicts of interest were disclosed by the other authors.

## Acknowledgments

The authors thank the patients at University of California, San Diego, Neuro-Oncology Program for their generous participation.

## References

- Sugahara T, Korogi Y, Kochi M, Ikushima I, Shigematu Y, Hirai T, et al. Usefulness of diffusion-weighted MRI with echo-planar technique in the evaluation of cellularity in gliomas. *J Magn Reson Imaging* 1999;9:53–60.
- Chen J, Xia J, Zhou YC, Xia LM, Zhu WZ, Zou ML, et al. [Correlation between magnetic resonance diffusion weighted imaging and cell density in astrocytoma]. *Zhonghua Zhong Liu Za Zhi* 2005;27:309–11.
- Guo AC, Cummings TJ, Dash RC, Provenzale JM. Lymphomas and high-grade astrocytomas: comparison of water diffusibility and histologic characteristics. *Radiology* 2002;224:177–83.
- Hilario A, Ramos A, Perez-Nunez A, Salvador E, Millan JM, Lagares A, et al. The added value of apparent diffusion coefficient to cerebral blood volume in the preoperative grading of diffuse gliomas. *AJNR Am J Neuroradiol* 2012;33:701–7.
- Server A, Kulle B, Maehlen J, Josefsen R, Schellhorn T, Kumar T, et al. Quantitative apparent diffusion coefficients in the characterization of brain tumors and associated peritumoral edema. *Acta Radiol* 2009;50:682–9.
- Toh CH, Castillo M, Wong AM, Wei KC, Wong HF, Ng SH, et al. Primary cerebral lymphoma and glioblastoma multiforme: differences in diffusion characteristics evaluated with diffusion tensor imaging. *AJNR Am J Neuroradiol* 2008;29:471–5.
- Wang W, Steward CE, Desmond PM. Diffusion tensor imaging in glioblastoma multiforme and brain metastases: the role of p, q, L, and fractional anisotropy. *AJNR Am J Neuroradiol* 2009;30:203–8.
- Wang S, Kim S, Chawla S, Wolf RL, Zhang WG, O'Rourke DM, et al. Differentiation between glioblastomas and solitary brain metastases using diffusion tensor imaging. *Neuroimage* 2009;44:653–60.
- Yamasaki F, Kurisu K, Satoh K, Arita K, Sugiyama K, Ohtaki M, et al. Apparent diffusion coefficient of human brain tumors at MR imaging. *Radiology* 2005;235:985–91.
- Tomura N, Narita K, Izumi J, Suzuki A, Anbai A, Otani T, et al. Diffusion changes in a tumor and peritumoral tissue after stereotactic irradiation for brain tumors: possible prediction of treatment response. *J Comput Assist Tomogr* 2006;30:496–500.
- Schminda KM. Diffusion-weighted MRI as a biomarker for treatment response in glioma. *CNS Oncol* 2012;1:169–80.
- Babsky AM, Hekmatyar SK, Zhang H, Solomon JL, Bansal N. Predicting and monitoring response to chemotherapy by 1,3-bis(2-chloroethyl)-1-nitrosourea in subcutaneously implanted 9L glioma using the apparent diffusion coefficient of water and <sup>23</sup>Na MRI. *J Magn Reson Imaging* 2006;24:132–9.
- Oh J, Henry RG, Pirzkall A, Lu Y, Li X, Catalaa I, et al. Survival analysis in patients with glioblastoma multiforme: predictive value of choline-to-N-acetylaspartate index, apparent diffusion coefficient, and relative cerebral blood volume. *J Magn Reson Imaging* 2004;19:546–54.
- Pope WB, Lai A, Mehta R, Kim HJ, Qiao J, Young JR, et al. Apparent diffusion coefficient histogram analysis stratifies progression-free survival in newly diagnosed bevacizumab-treated glioblastoma. *AJNR Am J Neuroradiol* 2011;32:882–9.
- Nakamura H, Murakami R, Hirai T, Kitajima M, Yamashita Y. Can MRI-derived factors predict the survival in glioblastoma patients treated with postoperative chemoradiation therapy? *Acta Radiol* 2013;54:214–20.
- Pope WB, Mirsadraei L, Lai A, Eskin A, Qiao J, Kim HJ, et al. Differential gene expression in glioblastoma defined by ADC histogram analysis: relationship to extracellular matrix molecules and survival. *AJNR Am J Neuroradiol* 2012;33:1059–64.
- Saksena S, Jain R, Narang J, Scarpace L, Schultz LR, Lehman NL, et al. Predicting survival in glioblastomas using diffusion tensor imaging metrics. *J Magn Reson Imaging* 2010;32:788–95.
- Wedeen VJ, Hagmann P, Tseng WY, Reese TG, Weisskoff RM. Mapping complex tissue architecture with diffusion spectrum magnetic resonance imaging. *Magn Reson Med* 2005;54:1377–86.
- Tuch DS. Q-ball imaging. *Magn Reson Med* 2004;52:1358–72.
- Maier SE, Bogner P, Bajzik G, Mamata H, Mamata Y, Repa I, et al. Normal brain and brain tumor: multicomponent apparent diffusion coefficient line scan imaging. *Radiology* 2001;219:842–9.
- Mulkern RV, Gudbjartsson H, Westin CF, Zengingonul HP, Gartner W, Guttmann CR, et al. Multi-component apparent diffusion coefficients in human brain. *NMR Biomed* 1999;12:51–62.
- Bennett KM, Schminda KM, Bennett RT, Rowe DB, Lu H, Hyde JS. Characterization of continuously distributed cortical water diffusion rates with a stretched-exponential model. *Magn Reson Med* 2003;50:727–34.
- Jensen JH, Helpert JA, Ramani A, Lu H, Kaczynski K. Diffusional kurtosis imaging: the quantification of non-gaussian water diffusion by means of magnetic resonance imaging. *Magn Reson Med* 2005;53:1432–40.
- Le Bihan D, Breton E, Lallemand D, Grenier P, Cabanis E, Laval-Jeantet M. MR imaging of intravoxel incoherent motions: application to diffusion and perfusion in neurologic disorders. *Radiology* 1986;161:401–7.
- Merboldt K-D, Hanicke W, Frahm J. Self-diffusion NMR imaging using stimulated echoes. *J Magn Reson* 1985;64:479–86.
- Le Bihan D, Breton E. Imagerie de diffusion *in-vivo* par résonance. *C R Acad Sci* 1985;301:1109–12.
- Taylor DG, Bushell MC. The spatial mapping of translational diffusion coefficients by the NMR imaging technique. *Phys Med Biol* 1985;30:345–9.
- Stejskal EO, Tanner JE. Spin diffusion measurements: Spin echoes in the presence of a time-dependent field gradient. *J Chem Phys* 1965;42:288–92.
- Le Bihan D. Looking into the functional architecture of the brain with diffusion MRI. *Nat Rev Neurosci* 2003;4:469–80.
- Harris EJ, Burn GP. The transfer of sodium and potassium ions between muscle and the surrounding medium. *Trans Faraday Soc* 1949;45:508–28.
- Nicholson C. Diffusion and related transport mechanisms in brain tissue. *Rep Prog Phys* 2001;64:815.
- Sykova E, Nicholson C. Diffusion in brain extracellular space. *Physiol Rev* 2008;88:1277–340.
- Tao L, Nicholson C. Maximum geometrical hindrance to diffusion in brain extracellular space surrounding uniformly spaced convex cells. *J Theor Biol* 2004;229:59–68.
- Vargova L, Homola A, Zamecnik J, Tichy M, Benes V, Sykova E. Diffusion parameters of the extracellular space in human gliomas. *Glia* 2003;42:77–88.
- Le Bihan D. Molecular diffusion, tissue microdynamics and microstructure. *NMR Biomed* 1995;8:375–86.
- Stanisz GJ. Diffusion MR in biological systems: tissue compartments and exchange. *Isr J Chem* 2003;43:33–44.
- Tanner JE. Transient diffusion in a system partitioned by permeable barriers. Application to NMR measurements with a pulsed field gradient. *J Chem Phys* 1978;69:1748–54.
- Basser PJ, Mattiello J, LeBihan D. MR diffusion tensor spectroscopy and imaging. *Biophys J* 1994;66:259–67.
- Maier SE, Sun Y, Mulkern RV. Diffusion imaging of brain tumors. *NMR Biomed* 2010;23:849–64.

## Grant Support

This study was supported by grants R01AG031224, R01EB000790, and RC2 DA29475 (A.M. Dale).

Received December 9, 2013; revised April 1, 2014; accepted May 19, 2014; published online September 2, 2014.



40. Chenevert TL, Sundgren PC, Ross BD. Diffusion imaging: insight to cell status and cytoarchitecture. *Neuroimaging Clin N Am* 2006;16: 619–32, viii–ix.
41. Nicholson C. Factors governing diffusing molecular signals in brain extracellular space. *J Neural Transm* 2005;112:29–44.
42. White NS, Dale AM. Distinct effects of nuclear volume fraction and cell diameter on high b-value diffusion MRI contrast in tumors. *Mag Res Med* 2013 Dec 19. [Epub ahead of print].
43. Gore JC, Xu J, Colvin DC, Yankeelov TE, Parsons EC, Does MD. Characterization of tissue structure at varying length scales using temporal diffusion spectroscopy. *NMR Biomed* 2010;23: 745–56.
44. Xu J, Li K, Smith RA, Waterton JC, Zhao P, Chen H, et al. Characterizing tumor response to chemotherapy at various length scales using temporal diffusion spectroscopy. *PLoS ONE* 2012;7:e41714.
45. White NS, Leergaard TB, D'Arceuil H, Bjaalie JG, Dale AM. Probing tissue microstructure with restriction spectrum imaging: histological and theoretical validation. *Hum Brain Mapp* 2013;34: 327–46.
46. White NS, Dale AM. Optimal diffusion MRI acquisition for fiber orientation density estimation: an analytic approach. *Hum Brain Mapp* 2009;30:3696–703.
47. White NS, McDonald CR, Farid N, Kuperman JM, Kesari S, Dale AM. Improved conspicuity and delineation of high-grade primary and metastatic brain tumors using "restriction spectrum imaging": quantitative comparison with high B-value DWI and ADC. *AJNR Am J Neuroradiol* 2013;34:958–64, S1.
48. White NS, Kuperman J, McDonald CR, Farid N, Kasai K, Shankaranarayanan A, et al. Restriction Spectrum Imaging of Glioblastoma Multiform: Comparison with ADC. In: *Proceedings of the 20th Annual Meeting ISMRM*; 2012; Melbourne, Australia.
49. Kothari PD, White NS, Farid N, Chung R, Kuperman JM, Girard HM, et al. Longitudinal restriction spectrum imaging is resistant to pseudoresponse in patients with high-grade gliomas treated with bevacizumab. *AJNR Am J Neuroradiol* 2013;34:1752–7.
50. McDonald CR, White NS, Farid N, Lai G, Kuperman JM, Bartsch H, et al. Recovery of white matter tracts in regions of peritumoral FLAIR hyperintensity with use of restriction spectrum imaging. *AJNR Am J Neuroradiol* 2013;34:1157–63.
51. Farid N, Almeida-Freitas DB, White NS, McDonald CR, Muller KA, Vandenberg SR, et al. Restriction-spectrum imaging of bevacizumab-related necrosis in a patient with GBM. *Front Oncol* 2013;3: 258.
52. Parsons EC, Does MD, Gore JC. Temporal diffusion spectroscopy: theory and implementation in restricted systems using oscillating gradients. *Magn Reson Med* 2006;55:75–84.
53. McNab JA, Edlow BL, Witzel T, Huang SY, Bhat H, Heberlein K, et al. The Human Connectome Project and beyond: initial applications of 300 mT/m gradients. *Neuroimage* 2013;80:234–45.
54. Castillo M, Smith JK, Kwok L, Wilber K. Apparent diffusion coefficients in the evaluation of high-grade cerebral gliomas. *Am J Neuroradiol* 2001;22:60–4.
55. Stadnik TW, Chaskis C, Michotte A, Shabana WM, van Rompaey K, Luytjaert R, et al. Diffusion-weighted MR imaging of intracerebral masses: comparison with conventional MR imaging and histologic findings. *Am J Neuroradiol* 2001;22:969–76.
56. Jain RK. Normalization of tumor vasculature: an emerging concept in antiangiogenic therapy. *Science* 2005;307:58–62.
57. Kamada K, Todo T, Masutani Y, Aoki S, Ino K, Takano T, et al. Combined use of tractography-integrated functional neuronavigation and direct fiber stimulation. *J Neurosurg* 2005;102:664–72.
58. Nimsky C, Ganslandt O, Hastreiter P, Wang R, Benner T, Sorensen AG, et al. Preoperative and intraoperative diffusion tensor imaging-based fiber tracking in glioma surgery. *Neurosurgery* 2005;56:130–7; discussion 8.
59. Mori S, Frederiksen K, van Zijl PC, Stieltjes B, Kraut MA, Solaiyappan M, et al. Brain white matter anatomy of tumor patients evaluated with diffusion tensor imaging. *Ann Neurol* 2002;51:377–80.
60. Yu CS, Li KC, Xuan Y, Ji XM, Qin W. Diffusion tensor tractography in patients with cerebral tumors: a helpful technique for neurosurgical planning and postoperative assessment. *Eur J Radiol* 2005;56: 197–204.
61. Kamada K, Houkin K, Takeuchi F, Ishii N, Ikeda J, Sawamura Y, et al. Visualization of the eloquent motor system by integration of MEG, functional, and anisotropic diffusion-weighted MRI in functional neuronavigation. *Surg Neurol* 2003;59:352–61.
62. Duffau H, Thiebaut de Schotten M, Mandonnet E. White matter functional connectivity as an additional landmark for dominant temporal lobectomy. *J Neurol Neurosurg Psychiatry* 2008;79: 492–5.
63. Nimsky C, Ganslandt O, von Keller B, Fahlbusch R. Preliminary experience in glioma surgery with intraoperative high-field MRI. *Acta Neurochir Suppl* 2003;88:21–9.
64. Nimsky C, Grummich P, Sorensen AG, Fahlbusch R, Ganslandt O. Visualization of the pyramidal tract in glioma surgery by integrating diffusion tensor imaging in functional neuronavigation. *Zentralbl Neurochir* 2005;66:133–41.
65. Sun GC, Chen XL, Zhao Y, Wang F, Hou BK, Wang YB, et al. Intraoperative high-field magnetic resonance imaging combined with fiber tract neuronavigation-guided resection of cerebral lesions involving optic radiation. *Neurosurgery* 2011;69:1070–84.
66. Bello L, Gambini A, Castellano A, Carrabba G, Acerbi F, Fava E, et al. Motor and language DTI fiber tracking combined with intraoperative subcortical mapping for surgical removal of gliomas. *Neuroimage* 2008;39:369–82.
67. Kinoshita M, Yamada K, Hashimoto N, Kato A, Izumoto S, Baba T, et al. Fiber-tracking does not accurately estimate size of fiber bundle in pathological condition: initial neurosurgical experience using neuronavigation and subcortical white matter stimulation. *Neuroimage* 2005;25:424–9.
68. Kesari S. Understanding glioblastoma tumor biology: the potential to improve current diagnosis and treatments. *Semin Oncol* 2011;38 Suppl 4:S2–10.
69. Mong S, Ellingson BM, Nghiemphu PL, Kim HJ, Mirsadraei L, Lai A, et al. Persistent diffusion-restricted lesions in bevacizumab-treated malignant gliomas are associated with improved survival compared with matched controls. *AJNR Am J Neuroradiol* 2012; 33:1763–70.
70. Jeyaretna DS, Curry WT Jr, Batchelor TT, Stemmer-Rachamimov A, Plotkin SR. Exacerbation of cerebral radiation necrosis by bevacizumab. *J Clin Oncol* 2011;29:e159–62.
71. Rieger J, Bahr O, Muller K, Franz K, Steinbach J, Hattingen E. Bevacizumab-induced diffusion-restricted lesions in malignant glioma patients. *J Neurooncol* 2010;99:49–56.
72. Kirkham AP, Emberton M, Allen C. How good is MRI at detecting and characterising cancer within the prostate? *Eur Urol* 2006;50:1163–74.
73. Bonekamp D, Macura KJ. Dynamic contrast-enhanced magnetic resonance imaging in the evaluation of the prostate. *Top Magn Reson Imaging* 2008;19:273–84.
74. Kurhanewicz J, Vigneron DB, Hricak H, Narayan P, Carroll P, Nelson SJ. Three-dimensional H-1 MR spectroscopic imaging of the *in situ* human prostate with high (0.24–0.7-cm<sup>3</sup>) spatial resolution. *Radiology* 1996;198:795–805.
75. Weinreb JC, Blume JD, Coakley FV, Wheeler TM, Cormack JB, Sotito CK, et al. Prostate cancer: sextant localization at MR imaging and MR spectroscopic imaging before prostatectomy—results of ACRIN prospective multi-institutional clinicopathologic study. *Radiology* 2009; 251:122–33.
76. Yoshimitsu K, Kiyoshima K, Irie H, Tajima T, Asayama Y, Hirakawa M, et al. Usefulness of apparent diffusion coefficient map in diagnosing prostate carcinoma: correlation with stepwise histopathology. *J Magn Reson Imaging* 2008;27:132–9.
77. Langer DL, van der Kwast TH, Evans AJ, Plotkin A, Trachtenberg J, Wilson BC, et al. Prostate tissue composition and MR measurements: investigating the relationships between ADC, T2, K(trans), v(e), and corresponding histologic features. *Radiology* 2010;255: 485–94.
78. Jezzard P, Balaban RS. Correction for geometric distortion in echo planar images from B(o) field variations. *Magn Reson Med* 1995;34: 65–73.

79. Andersson JLR, Skare S, Ashburner J. How to correct susceptibility distortions in spin-echo echo-planar images: application to diffusion tensor imaging. *Neuroimage* 2003;20:870–88.
80. Robson MD, Gore JC, Constable RT. Measurement of the point spread function in MRI using constant time imaging. *Magn Reson Med* 1997;38:733–40.
81. Holland D, Kuperman JM, Dale AM. Efficient correction of inhomogeneous static magnetic field-induced distortion in Echo Planar Imaging. *Neuroimage* 2010;50:175–83.
82. Morgan PS, Bowtell RW, McIntyre DJO, Worthington BS. Correction of spatial distortion in EPI due to inhomogeneous static magnetic fields using the reversed gradient method. *J Magn Reson Imaging* 2004;19:499–507.
83. Chang H, Fitzpatrick JM. A technique for accurate magnetic resonance imaging in the presence of field inhomogeneities. *IEEE Trans Med Imaging* 1992;11:319–29.
84. Gerstner ER, Sorensen AG. Diffusion and diffusion tensor imaging in brain cancer. *Semin Radiat Oncol* 2011;21:141–6.

## ORIGINAL ARTICLE

# Novel technique for characterizing prostate cancer utilizing MRI restriction spectrum imaging: proof of principle and initial clinical experience with extraprostatic extension

RA Rakow-Penner<sup>1</sup>, NS White<sup>1</sup>, JK Parsons<sup>2</sup>, HW Choi<sup>1</sup>, MA Liss<sup>2</sup>, JM Kuperman<sup>1</sup>, N Schenker-Ahmed<sup>1</sup>, H Bartsch<sup>1</sup>, RF Mattrey<sup>1</sup>, WG Bradley<sup>1</sup>, A Shabaik<sup>3</sup>, J Huang<sup>4</sup>, DJA Margolis<sup>5</sup>, SS Raman<sup>5</sup>, L Marks<sup>6</sup>, CJ Kane<sup>2</sup>, RE Reiter<sup>6</sup>, DS Karow<sup>1</sup> and AM Dale<sup>1</sup>

**BACKGROUND:** Standard magnetic resonance imaging (MRI) of the prostate lacks sensitivity in the diagnosis and staging of prostate cancer (PCa). To improve the operating characteristics of prostate MRI in the detection and characterization of PCa, we developed a novel, enhanced MRI diffusion technique using restriction spectrum imaging (RSI-MRI).

**METHODS:** We compared the efficacy of our novel RSI-MRI technique with standard MRI for detecting extraprostatic extension (EPE) among 28 PCa patients who underwent MRI and RSI-MRI prior to radical prostatectomy, 10 with histologically proven pT3 disease. RSI cellularity maps isolating the restricted isotropic water fraction were reconstructed based on all *b*-values and then standardized across the sample with z-score maps. Distortion correction of the RSI maps was performed using the alternating phase-encode technique.

**RESULTS:** 27 patients were evaluated, excluding one patient where distortion could not be performed. Preoperative standard MRI correctly identified extraprostatic extension in two of the nine pT3 (22%) patients, whereas RSI-MRI identified EPE in eight of nine (89%) patients. RSI-MRI correctly identified pT2 disease in the remaining 18 patients.

**CONCLUSIONS:** In this proof of principle study, we conclude that our novel RSI-MRI technology is feasible and shows promise for substantially improving PCa imaging. Further translational studies of prostate RSI-MRI in the diagnosis and staging of PCa are indicated.

*Prostate Cancer and Prostatic Disease* (2015) **18**, 81–85; doi:10.1038/pcan.2014.50; published online 6 January 2015

## INTRODUCTION

Multiparametric magnetic resonance imaging (MRI) is an emerging diagnostic tool for the screening, staging and treatment of prostate cancer (PCa).<sup>1–17</sup> However, prostate MRI demonstrates variable sensitivity (49–88%) and specificity (84–89%), which currently limits its clinical utility.<sup>2,3,14</sup>

Standard diffusion-weighted imaging (DWI) improves the operating characteristics of prostate MRI.<sup>2,3,14,16,18,19</sup> DWI detects the diffusivity of microscopic water and subsequently reflects the cellularity and integrity of cells imaged. When combined with T2-weighted imaging and dynamic contrast-enhanced imaging, DWI improves sensitivity and specificity of PCa diagnosis by increasing tumor conspicuity.<sup>2,14,16,18,19</sup>

DWI also suffers from distortion due to magnetic field inhomogeneity<sup>20</sup> and relatively high false-positive rates owing to hemorrhage (for example, from prior biopsy), inflammatory processes and benign nodules in the transitional zone.<sup>21</sup> In order to overcome these challenges and improve magnetic resonance detection of PCa, we have developed a novel, sophisticated diffusion method termed prostate restriction spectrum imaging (RSI) or RSI-MRI.<sup>22,23</sup> By collecting a broader, more extended spectrum of diffusion images,<sup>22</sup> combined with sophisticated modeling of differential water compartments in tissue and correction of spatial

distortion,<sup>24</sup> RSI-MRI theoretically focuses on the signal emanating from the intracellular water compartment of tumor cells and thereby minimizes false-positive signals.<sup>25</sup> A similar RSI technique, recently applied to brain imaging, enhanced the signal of glioblastoma multiforme tumors by 10-fold.<sup>23</sup>

In this pilot clinical study, we determined the clinical utility of our novel prostate RSI-MRI technique to stage PCa by assessing the accuracy of RSI-MRI to detect extraprostatic extension (EPE) of tumor.

## MATERIALS AND METHODS

### Restriction spectrum imaging

In this institutional review board approved study, 28 patients underwent standard T2, perfusion (with Gadolinium) and diffusion protocols at 3 T (Siemens, Erlangen, Germany) with an endorectal coil (Table 1). All imaging was performed at a single institute. The 28 patients had biopsy-proven PCa and an MRI was performed for presurgical planning. The restriction spectrum protocol parameters included *b*-values 0, 800, 1500 and 4000 s mm<sup>−2</sup> in 30 unique diffusion directions for each nonzero *b*-value. RSI cellularity maps isolating the restricted isotropic water fraction<sup>22</sup> were reconstructed based on all *b*-values, and then standardized across the sample with z-score maps. The z-score maps were calculated by (i) measuring the mean and s.d. of normal prostate signal from the raw RSI

<sup>1</sup>Department of Radiology, School of Medicine, University of California San Diego, La Jolla, CA, USA; <sup>2</sup>Department of Urology, School of Medicine, University of California San Diego, La Jolla, CA, USA; <sup>3</sup>Department of Pathology, School of Medicine, University of California San Diego, La Jolla, CA, USA; <sup>4</sup>Department of Pathology, David Geffen School of Medicine, University of California Los Angeles, Los Angeles, CA, USA; <sup>5</sup>Department of Radiology, David Geffen School of Medicine, University of California Los Angeles, Los Angeles, CA, USA and <sup>6</sup>Department of Urology, David Geffen School of Medicine, University of California Los Angeles, Los Angeles, CA, USA. Correspondence: Dr DS Karow, Multimodal Imaging Laboratory, Department of Radiology, School of Medicine, University of California, San Diego, 8950 Villa La Jolla Drive Suite C101, La Jolla, 92037, CA, USA. E-mail: dskarow@ucsd.edu

Received 30 July 2014; revised 21 October 2014; accepted 25 October 2014; published online 6 January 2015

**Table 1.** MRI scan parameters for prostate MRI protocol at 3 T

Pulse sequence	Parameters
T2	Axial 3D TSE T2 (Siemens SPACE, TR/TE 3800-5040/101 ETL 13, 14 cm FOV, 256 × 256 matrix, 1.5 mm contiguous slices)
Diffusion-weighted (standard)	Echo planar, TR/TE 3900/60, 21 × 26 cm FOV, 130 × 160 matrix, 3.6 mm slices, 4 NEX, $b$ -values 0, 100, 400 and 800 s mm <sup>-2</sup>
T1 dynamic perfusion imaging	Siemens TWIST, TR/TE 3.9/1.4 ms, 12° flip angle, 26 × 26 cm FOV, 160 × 160 matrix, 3.6 mm slices, 4.75 s per acquisition over 6 min with 15 s injection delay, image analysis using iCAD Versavue
Restriction spectrum imaging	Spin echo EPI, TR/TE 5500/137, 26 × 26 cm FOV, 128 × 96 matrix, 3.6 mm slices, 30 directions at each $b$ -value, $b$ -values 0, 800, 1500 and 4000 s mm <sup>-2</sup> .

Abbreviation: EPI, Echo planar imaging; FOV, field of view; MRI, magnetic resonance imaging; NEX, number of excitations.

**Table 2.** Radiologic findings—documented diagnostic interpretations in nine patients with biopsy-proven localized prostate cancer

Case	Location	Axial clock face location	Capsular involvement	Technical quality
1	Right peripheral gland	7–8 o'clock	Focal EPE may involve adjacent right neurovascular bundle. Right seminal vesicle invasion.	Excellent, no limitations
2	Right central peripheral basal mid gland	7 o'clock	Intact, no suspicion for involvement	Excellent, no limitations
3	Right peripheral basal mid gland	8 o'clock	Bulges the capsule with a broad base of contact, organ confined disease	Excellent, no limitations
4	Right peripheral gland lesion	6–9 o'clock	Bulges the capsule, suspicious but not definitive for extracapsular extension	Excellent, no limitations
5	Right peripheral gland from apex to base	5–10 o'clock	Blurring and irregularity of right capsule, suspicious for capsular involvement	Limited spectral quality, does not diminish diagnostic confidence
6	Right peripheral base lesion	7 o'clock	Bulges the capsule with a broad base of attachment	Excellent, no limitations
7	Right peripheral mid gland	9–10 o'clock	Bulges the capsule laterally	Hemorrhage limits sensitivity and functional characterization
8	Left peripheral mid gland	3–5 o'clock	Bulges the capsule, no gross extraprostatic extension	Motion and hemorrhage limit evaluation
9	Left peripheral gland	4 o'clock	Intact, no suspicion for involvement	Excellent, no limitations

Abbreviation: EPE, extraprostatic extension.

**Table 3.** Pathologic findings determined from post resection whole-mount pathology in nine patients undergoing radical prostatectomy with histologically proven EPE

Case	Gleason	Location of EPE	Staging	Age	PSA	Surgical margins at site of EPE
1	3+4	Right posterior	pT3bNxMx	61	5.8	Negative
2	3+4	Right posterior	pT3aNOMx	55	2.7	Positive
3	4+5	Right posterior	pT3bpN1Mx	64	8.2	Negative
4	4+3	Right posterior	pT3aN1Mx	64	4.2	Positive
5	4+5	Right posterior	pT3aN1Mx	68	7	Positive
6	4+3	Right posterior	pT3apNOMx	56	10	Positive
7	4+3	Right antero-lateral	pT3apNOMx	67	5.1	Negative
8	4+3	Left posterior	pT3aNOMx	65	5.8	Negative
9	3+4	Right lateral, midline posterior	pT3aNOMx	53	3.9	Negative

Abbreviation: EPE, extraprostatic extension.

cellularity maps across the patient pool, (ii) subtracting this measured mean value from each subjects RSI cellularity map and (iii) dividing by the measured normal prostate s.d. Correction of image distortions in RSI maps due to B0 field inhomogeneities was performed using the alternating phase-encode technique.<sup>24</sup> As per standard clinical protocol, radiology reports were generated by an experienced radiologist for each of the patients blinded to the RSI results (Table 2).

#### Correlation of RSI-MRI with histopathology

Whole-mount histopathology was performed on the 28 enrolled patients who underwent RSI-MRI and subsequent radical prostatectomy. For the 10

radical prostatectomy patients with histologically identified EPE (pT3 disease), presurgical pelvic RSI-MRI imaging was reviewed. Out of 10 patients with histologically identified EPE, 1 patient was excluded due to an error in data collection of the MRI-RSI, where distortion correction was unable to be performed. Thus, a total of nine pT3 patients were used for evaluation in this pilot study.

The area of tumor was identified by an experienced uropathologist (Table 3). Clinical images were reviewed in a nonblinded fashion to verify performance of RSI-MRI (Figure 1), where pathology was available for comparison. Standard MRI (including T2, perfusion and traditional DWI), RSI-MRI and histopathology were compared at a multidisciplinary tumor board consisting of radiologists, urologists and uropathologists. RSI-MRI



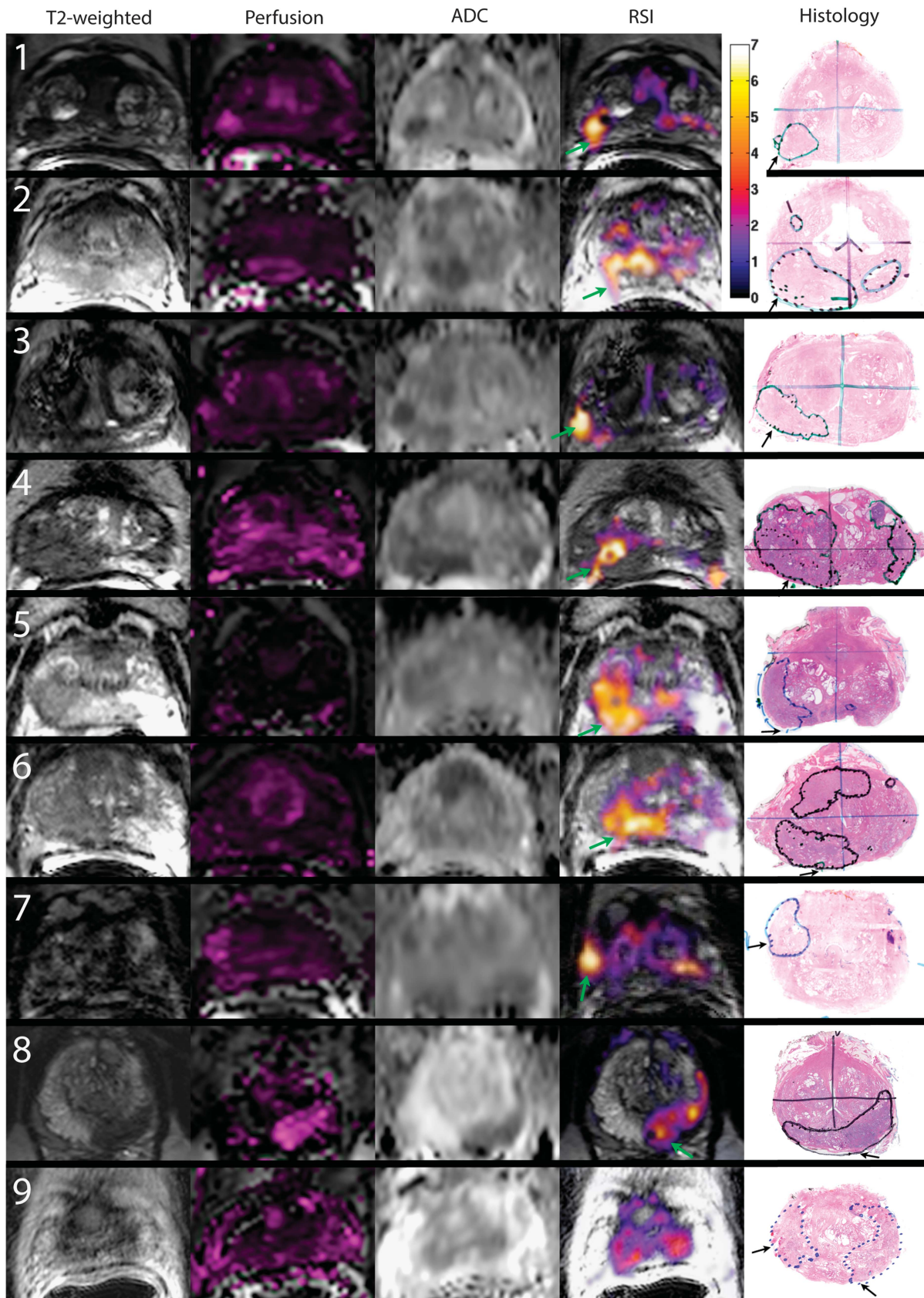


**Figure 1.** MRI and whole-mount pathology for nine prostate cancer patients with EPE. Column 1: T2-weighted images, column 2: perfusion  $K_{trans}$  maps, column 3: standard apparent diffusion coefficient (ADC) maps ( $b = 0, 100, 400$  and  $800 \text{ s mm}^{-2}$ ), column 4: RSI z-score maps and column 5: whole-mount pathology with tumor and area of EPE identified. Color bar represents z-scores from zero to seven for the RSI maps. EPE, extraprostatic extension; MRI, magnetic resonance imaging; RSI, restriction spectrum imaging.



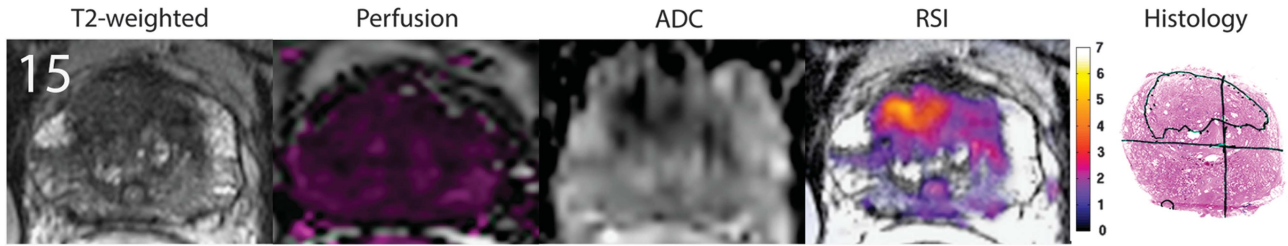


**Figure 2.** MRI and whole-mount pathology for a representative prostate cancer patient without histologically proven EPE. Column 1: T2-weighted image, column 2: perfusion  $K_{trans}$  map, column 3: standard apparent diffusion coefficient (ADC) map ( $b=0, 100, 400$  and  $800 \text{ s mm}^{-2}$ ), column 4: RSI z-score map and column 5: whole-mount pathology with tumor and area of EPE identified. Color bar represents z-scores from zero to seven for the RSI map. EPE, extraprostatic extension; MRI, magnetic resonance imaging; RSI, restriction spectrum imaging.

**Table 4.** Pathologic findings determined from postresection whole-mount pathology in 18 patients undergoing radical prostatectomy without EPE

Case	Gleason	Staging	Age	PSA
10	4+3+5	pT2aN0Mx	62	4.8
11	3+4	pT2NxMx	63	7
12	4+3	pT2cN0Mx	45	6.5
13	3+3	pT2NxMx	71	7.3
14	4+5	pT2N0Mx	62	4.6
15	3+3	pT2cNxMx	59	4.43
16	3+3	pT2N0Mx	61	9.2
17	3+4	pT2cN0Mx	68	6.7
18	3+4	pT2bN0Mx	55	4.7
19	3+4	pT2cNxMx	64	5.8
20	3+4	pT2cN0Mx	61	3.4
21	3+3	pT2cpNxMx	60	6
22	4+3	pT2N0Mx	61	6.6
23	3+4	pT2NxMx	65	5.4
24	3+4	pT2NxMx	50	8.9
25	3+4	pT2aN0Mx	44	2.8
26	3+4	pT2cNxMx	58	3.8
27	3+4	pT2NxMx	53	5.5

Abbreviation: EPE, extraprostatic extension.

images were reviewed to determine if the RSI signal extended beyond the prostatic capsule, defined as the T2-hypointense thin line separating parenchymal tissue from extraprostatic fat and neurovascular structures. RSI maps were spatially corrected and overlaid on standard T2 maps to determine whether the RSI signal was intracapsular or bulging, blurring or grossly extending beyond the capsule. This evaluation was then compared with the preoperative MRI radiology reports to determine whether EPE was suspected without RSI-MRI.

## RESULTS

### Standard MRI

Using the standard preoperative MR protocol (T1 perfusion, T2 and basic diffusion-weighting), patients 1 and 5 demonstrated radiologic findings consistent with capsular involvement and EPE (Table 2). Patient 4's imaging findings were suspicious for EPE but not definitive. Patients 3, 6, 7 and 8 demonstrated standard MR radiologic findings consistent with bulging of the capsule, but no indication of EPE. Patient 2's and patient 9's standard imaging did not indicate the concern for pathology abutting the capsule.

### Restriction spectrum imaging

On analysis of RSI-MRI, eight of nine (89%) patients demonstrated EPE (Figure 1, column 4; Table 3). For eight of the nine patients, the areas of EPE detected on MRI-RSI correlated with the areas encircled on the whole-mount histopathology. Four of eight (50%)

patients with RSI-MRI detected EPE also had positive surgical margins. Two patients (one and three, corresponding to Figure 1 and Table 3) had pT3b disease. In patient 1, MRI-RSI demonstrated seminal vesicle involvement. In patient 3, MRI-RSI did not demonstrate any involvement. For patient 9, a patient with histologically proven EPE, MRI-RSI was concerning for tumor bulging the capsule and possible EPE, but not definitively (and considered negative for EPE on MRI-RSI).

Figure 2 demonstrates a representative patient who did not demonstrate EPE on histology or imaging. Table 4 presents the data from the 18 patients without histologically proven EPE. For the 18 non-EPE patients, MRI-RSI detected the histologically proven area of pT2 disease.

## DISCUSSION

In this pilot clinical study, we demonstrate the potential for our novel prostate RSI-MRI technique to substantially improve upon current imaging-based modalities for the diagnosis and staging of PCa. In our series, RSI-MRI successfully identified pT3 disease in eight of nine (89%) patients, whereas standard MRI accurately identified only two of nine (22%). These data justify further translational studies of RSI-MRI for PCa detection and staging.

RSI-MRI's sensitivity to intracellular diffusivity differentiates it from standard DWI.<sup>22</sup> Extracellular signal emanating from surrounding inflammatory processes and hemorrhage contributes less to the signal detected by RSI-MRI as compared with standard DWI. RSI-MRI minimizes these effects by focusing on the signal emanating from intracellular tumor cells (restricted diffusion within small spherical compartments), with less focus on the extracellular signal (hindered and free water diffusion). RSI-MRI achieves this by collecting diffusion images over an extended  $b$ -value range ( $b=0\text{--}4000 \text{ s mm}^{-2}$ ) and decomposing the relative contribution from separable water compartments within voxels using a linear mixture model framework.<sup>22,23</sup> Standard quantitative diffusion techniques acquire data with  $b$ -values  $< 1000 \text{ s mm}^{-2}$ . In addition, unlike conventional diffusion imaging and apparent diffusion coefficient maps, RSI-MRI maps are distortion corrected and directly overlaid on T2 anatomic images with voxel specific accuracy, permitting more accurate assessment of signal beyond the capsular border. This increases the conspicuity of the EPE.

Current standard MRI prostate protocols lack accurate localization of PCa. RSI-MRI notably improves tumor localization with MRI, potentially rendering MRI more relevant in a variety of clinical scenarios. Presurgical MRI results may provide additional information for clinicians and patients by informing surgical planning (that is, nerve sparing). Other potential applications for RSI-MRI meriting further study include lesion localization for targeting of image-guided biopsies, serial imaging in an active surveillance population and evaluation of posttreatment recurrence following primary radiotherapy.

A challenge in further developing clinical applications of RSI-MRI lies in accurately defining its specificity, sensitivity and positive and negative predictive values. Limitations of this current study included the small number of patients, and the retrospective nonblinded nature of the study. This was necessary for this pilot study for innovative methodological development, but suffers due to potential reader bias. It is also important to note that, although we have included surgical margin data, the MRI-RSI results did not inform surgical technique.

An ongoing, blinded prospective study will allow for more detailed evaluations of the operating characteristics of RSI-MRI relative to standard MRI and its ability to inform clinical care. RSI-MRI is a standardized quantitative technique and can potentially be employed across platforms and institutions. The color bar in Figure 1 illustrates the z-score scale for the RSI maps. As the number of enrollees increase, the z-score threshold range for concern for malignancy can be determined by pooling the variance across patients. One of the challenges of standard diffusion imaging, is that the apparent diffusion coefficient values are not standardized across MRI scanners. The z-score is a standardized statistical method and inherently normalizes across the patient pool. Thus, the z-score is a value that can be compared across different scanners and provides a more robust value for relative comparison.

In summary, in this proof of concept study, we present our initial clinical experience with prostate RSI-MRI. RSI-MRI has the potential to substantially improve the radiological detection and characterization of PCa. Further translational studies will focus on defining its operating characteristics with respect to diagnosis and staging.

## CONFLICT OF INTEREST

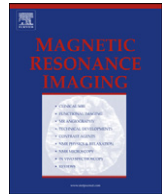
The authors declare no conflict of interest.

## ACKNOWLEDGEMENTS

We would like to thank Brenda Brown for her help on this project. This work was supported by the Department of Defense, Prostate Cancer Research Program W81XWH-13-1-0391, the American Cancer Society—Institutional Research Grant Number 70-002 and the UCSD Clinician Scientist Program.

## REFERENCES

- Turkbey B, Pinto PA, Mani H, Bernardo M, Pang Y, McKinney YL *et al*. Prostate cancer: value of multiparametric MR imaging at 3 T for detection—histopathologic correlation. *Radiology* 2010; **255**: 89–99.
- Isebaert S, Van den Bergh L, Haustermans K, Joniau S, Lerut E, De Wever L *et al*. Multiparametric MRI for prostate cancer localization in correlation to whole-mount histopathology. *J Magn Reson Imaging* 2013; **37**: 1392–1401.
- Haider MA, van der Kwast TH, Tanguay J, Evans AJ, Hashmi A-T, Lockwood G *et al*. Combined T2-weighted and diffusion-weighted MRI for localization of prostate cancer. *AJR Am J Roentgenol* 2007; **189**: 323–328.
- Rastinehad AR, Baccala AA, Chung PH, Proano JM, Kruecker J, Xu S *et al*. D'Amico risk stratification correlates with degree of suspicion of prostate cancer on multiparametric magnetic resonance imaging. *J Urol* 2011; **185**: 815–820.
- Rais-Bahrami S, Turkbey B, Rastinehad AR, Walton-Diaz A, Hoang AN, Siddiqui MM *et al*. Natural history of small index lesions suspicious for prostate cancer on multiparametric MRI: recommendations for interval imaging follow-up. *Diagn Interv Radiol* 2014; **20**: 293–298.
- Abd-Alazeez M, Ahmed HU, Arya M, Charman SC, Anastasiadis E, Freeman A *et al*. The accuracy of multiparametric MRI in men with negative biopsy and elevated PSA level—can it rule out clinically significant prostate cancer? *Urol Oncol* 2014; **32**: 45.e17–22.
- Hoeks CMA, Somford DM, van Oort IM, Vergunst H, Oddens JR, Smits GA *et al*. Value of 3-T multiparametric magnetic resonance imaging and magnetic resonance-guided biopsy for early risk stratification in active surveillance of low-risk prostate cancer: a prospective multicenter cohort study. *Invest Radiol* 2014; **49**: 165–172.
- Stamatakis L, Siddiqui MM, Nix JW, Logan J, Rais-Bahrami S, Walton-Diaz A *et al*. Accuracy of multiparametric magnetic resonance imaging in confirming eligibility for active surveillance for men with prostate cancer. *Cancer* 2013; **119**: 3359–3366.
- Abd-Alazeez M, Kirkham A, Ahmed HU, Arya M, Anastasiadis E, Charman SC *et al*. Performance of multiparametric MRI in men at risk of prostate cancer before the first biopsy: a paired validating cohort study using template prostate mapping biopsies as the reference standard. *Prostate Cancer Prostatic Dis* 2014; **17**: 40–46.
- Turkbey B, Mani H, Aras O, Ho J, Hoang A, Rastinehad AR *et al*. Prostate cancer: can multiparametric MR imaging help identify patients who are candidates for active surveillance? *Radiology* 2013; **268**: 144–152.
- Rais-Bahrami S, Siddiqui MM, Turkbey B, Stamatakis L, Logan J, Hoang AN *et al*. Utility of multiparametric magnetic resonance imaging suspicion levels for detecting prostate cancer. *J Urol* 2013; **190**: 1721–1727.
- Park JJ, Kim CK, Park SY, Park BK, Lee HM, Cho SW. Prostate cancer: role of pretreatment multiparametric 3-T MRI in predicting biochemical recurrence after radical prostatectomy. *Am J Radiol* 2014; **202**: W459–W465.
- Somford DM, Hamoen EH, Fütterer JJ, van Basten JP, Hulsbergen-van de Kaa CA, Vreuls W *et al*. The predictive value of endorectal 3 Tesla multiparametric magnetic resonance imaging for extraprostatic extension in patients with low, intermediate and high risk prostate cancer. *J Urol* 2013; **190**: 1728–1734.
- Lim HK, Kim JK, Kim KA, Cho K-S. Prostate cancer: apparent diffusion coefficient map with T2-weighted images for detection—a multireader study. *Radiology* 2009; **250**: 145–151.
- Tanimoto A, Nakashima J, Kohno H, Shinmoto H, Kuribayashi S. Prostate cancer screening: the clinical value of diffusion-weighted imaging and dynamic MR imaging in combination with T2-weighted imaging. *J Magn Reson Imaging* 2007; **25**: 146–152.
- Donati OF, Jung SI, Vargas HA, Gultekin DH, Zheng J, Moskowitz CS *et al*. Multiparametric prostate MR imaging with T2-weighted, diffusion-weighted, and dynamic contrast-enhanced sequences: are all pulse sequences necessary to detect locally recurrent prostate cancer after radiation therapy? *Radiology* 2013; **268**: 440–450.
- Mazaheri Y, Hricak H, Fine SW, Akin O, Shukla-Dave A, Ishill NM *et al*. Prostate tumor volume measurement with combined T2-weighted imaging and diffusion-weighted MR: correlation with pathologic tumor volume. *Radiology* 2009; **252**: 449–457.
- Miao H, Fukatsu H, Ishigaki T. Prostate cancer detection with 3-T MRI: comparison of diffusion-weighted and T2-weighted imaging. *Eur J Radiol* 2007; **61**: 297–302.
- Giannarini G, Nguyen DP, Thalmann GN, Thoeny HC. Diffusion-weighted magnetic resonance imaging detects local recurrence after radical prostatectomy: initial experience. *Eur Urol* 2012; **61**: 616–620.
- Donato F, Costa DN, Yuan Q, Rofsky NM, Lenkinski RE, Pedrosa I. Geometric distortion in diffusion-weighted MR imaging of the prostate-contributing factors and strategies for improvement. *Acad Radiol* 2014; **21**: 817–823.
- Yoshimitsu K, Kiyoshima K, Irie H, Tajima T, Asayama Y, Hirakawa M *et al*. Usefulness of apparent diffusion coefficient map in diagnosing prostate carcinoma: correlation with stepwise histopathology. *J Magn Reson Imaging* 2008; **27**: 132–139.
- White NS, Leergaard TB, D'Arceuil H, Bjaalie JG, Dale AM. Probing tissue microstructure with restriction spectrum imaging: histological and theoretical validation. *Hum Brain Mapp* 2013; **34**: 327–346.
- White NS, McDonald CR, Farid N, Kuperman JM, Kesari S, Dale AM. Improved conspicuity and delineation of high-grade primary and metastatic brain tumors using 'restriction spectrum imaging': quantitative comparison with high B-value DWI and ADC. *AJNR Am J Neuroradiol* 2012; **34**: 958–964.
- Holland D, Kuperman JM, Dale AM. Efficient correction of inhomogeneous static magnetic field-induced distortion in Echo Planar Imaging. *Neuroimage* 2010; **50**: 175–183.
- White NS, Dale AM. Distinct effects of nuclear volume fraction and cell diameter on high b-value diffusion MRI contrast in tumors. *Magn Reson Med* 2013; **72**: 1435–1443.



## Prostate diffusion imaging with distortion correction☆



Rebecca A. Rakow-Penner<sup>a</sup>, Nathan S. White<sup>a</sup>, Daniel J.A. Margolis<sup>b</sup>, John Kellogg Parsons<sup>c</sup>, Natalie Schenker-Ahmed<sup>a</sup>, Joshua M. Kuperman<sup>a</sup>, Hauke Bartsch<sup>a</sup>, Hyung W. Choi<sup>a</sup>, William G. Bradley<sup>a</sup>, Ahmed Shabaik<sup>d</sup>, Jiaoti Huang<sup>e</sup>, Michael A. Liss<sup>f</sup>, Leonard Marks<sup>g</sup>, Christopher J. Kane<sup>c</sup>, Robert E. Reiter<sup>g</sup>, Steven S. Raman<sup>b</sup>, David S. Karow<sup>a,\*</sup>, Anders M. Dale<sup>a</sup>

<sup>a</sup> Department of Radiology, University of California San Diego School of Medicine

<sup>b</sup> Department of Radiology, University of California Los Angeles Geffen School of Medicine

<sup>c</sup> Department of Urology, University of California San Diego School of Medicine

<sup>d</sup> Department of Pathology, University of California San Diego School of Medicine

<sup>e</sup> Department of Pathology, University of California Los Angeles Geffen School of Medicine

<sup>f</sup> Department of Urology, University of Texas Health Science Center San Antonio

<sup>g</sup> Department of Urology, University of California Los Angeles Geffen School of Medicine

### ARTICLE INFO

#### Article history:

Received 3 February 2015

Revised 9 July 2015

Accepted 19 July 2015

#### Keywords:

Prostate cancer

MRI

Diffusion-weighted imaging

Distortion correction

### ABSTRACT

**Purpose:** Diffusion imaging in the prostate is susceptible to distortion from B0 inhomogeneity. Distortion correction in prostate imaging is not routinely performed, resulting in diffusion images without accurate localization of tumors. We performed and evaluated distortion correction for diffusion imaging in the prostate.

**Materials and methods:** 28 patients underwent pre-operative MRI (T2, Gadolinium perfusion, diffusion at  $b = 800 \text{ s/mm}^2$ ). The restriction spectrum protocol parameters included b-values of 0, 800, 1500, and 4000  $\text{s/mm}^2$  in 30 directions for each nonzero b-value. To correct for distortion, forward and reverse trajectories were collected at  $b = 0 \text{ s/mm}^2$ . Distortion maps were generated to reflect the offset of the collected data versus the corrected data. Whole-mount histology was available for correlation.

**Results:** Across the 27 patients evaluated (excluding one patient due to data collection error), the average root mean square distortion distance of the prostate was 3.1 mm (standard deviation, 2.2 mm; and maximum distortion, 12 mm).

**Conclusion:** Improved localization of prostate cancer by MRI will allow better surgical planning, targeted biopsies and image-guided treatment therapies. Distortion distances of up to 12 mm due to standard diffusion imaging may grossly misdirect treatment decisions. Distortion correction for diffusion imaging in the prostate improves tumor localization.

© 2015 Elsevier Inc. All rights reserved.

## 1. Introduction

In the United States, prostate cancer is the leading cause of cancer in men and the second leading cause of cancer deaths [1]. Multiparametric magnetic resonance imaging (MRI) plays a large role in staging and localizing prostate cancer, with diffusion imaging as a key component [2–16]. Diffusion imaging often increases the conspicuity of prostate cancers and detects them with greater accuracy than T2 or perfusion imaging [5,8,9]. However, standard diffusion sequences with echo planar imaging (EPI) for k-space

sampling suffer from distortion artifacts due to B0 inhomogeneity [17,18]. These distortion artifacts obscure the precise location of concerning findings with this technique. Improved tumor localization with diffusion imaging would enhance MRI's utility in evaluating prostate cancer. Surgical management of prostate cancer often depends on a priori knowledge of tumor extension beyond the prostatic capsule, determining nerve-sparing techniques versus aggressive surgery. In addition, novel techniques and treatments such as MRI-Ultrasound fusion guided biopsies [19] and high-intensity focused ultrasound treatment [20,21], depend on accurate localization of prostate cancer, where a subset may only be detected with diffusion MRI.

Routine standard of care diffusion with EPI does not incorporate correction for B0 inhomogeneity distortions. Techniques for distortion correction for diffusion imaging with EPI exist [22–24] and have been applied in the brain [23,24].

☆ No conflicts of interests.

\* Corresponding author at: Multimodal Imaging Laboratory, 8950 Villa La Jolla Drive Suite C101, La Jolla, CA 92037. Tel./fax: +1 858 534 1078.

E-mail address: [dskarow@ucsd.edu](mailto:dskarow@ucsd.edu) (D.S. Karow).

**Table 1**  
MRI scan parameters.

Pulse sequence	Parameters
T2	Axial 3D TSE T2 (Siemens SPACE) TR/TE 3800–5040/101 ETL 13, 14 cm FOV, 256 × 256 matrix, 1.5 mm contiguous slices, 60 slices
Diffusion-weighted (Standard)	Echoplanar, TR/TE 3900/60, 21 × 26 cm FOV, 130 × 160 matrix, 3.6 mm slices, 4 NEX, b-values of 0, 100, 400, and 800 s/mm <sup>2</sup> , 20 slices, parallel imaging with a factor of 2
T1 Dynamic Perfusion Imaging	Siemens TWIST, TR./TE 3.9/1.4 ms, 12° flip angle, 26 × 26 cm FOV, 160 × 160 matrix, 3.6 mm slices, 4.75 s/acquisition over 6 min with 15 s injection delay, image analysis using iCAD Versavue,
Restriction Spectrum Imaging	Spin echo EPI, TR/TE 5500/137, 26 × 26 cm FOV, 128 × 96 matrix, 3.6 mm slices, 30 directions at each b-value, b-values of 0, 800, 1500, and 4000 s/mm <sup>2</sup> , 60 slices

In this paper, a diffusion MRI technique called Restriction Spectrum Imaging (RSI-MRI) [25–28] was used to evaluate 28 preoperative prostate cancer patients and assess the benefits of correcting for B0 distortion effects. This study is a further evaluation of data used in our initial proof of concept study of RSI-MRI of the prostate [28]. RSI-MRI incorporates distortion correction [23] as part of its image post-processing stream.

## 2. Materials and methods

Preoperative MRI was performed on 28 prostate cancer patients in this IRB approved study. The patients underwent the standard multi-parametric prostate MRI protocol using 3 T MRI systems (TrioTim, Skyra, Siemens, Erlangen, Germany) with an endorectal coil (Medrad, Warrendale, PA) (Table 1): T2 weighted-MRI, dynamic contrast-enhanced (DCE) MRI with gadolinium-based contrast agent, and diffusion-weighted MRI ( $b = 800 \text{ s/mm}^2$ ). In addition, the diffusion protocol included b values of 0, 800, 1500, and 4000 s/mm<sup>2</sup> in 30 unique diffusion directions for each nonzero b-value. The distortion-correction algorithm [23] utilizes the symmetry of the distortion from B0 inhomogeneity (Fig. 1). By collecting images at  $b = 0 \text{ s/mm}^2$  in both the forward and reverse phase encode trajectories, a deformation field map can be calculated and used to correct the entire diffusion data set. For one patient out of the 28 patients, there was an error in the scan parameters for the forward and reverse images, and thus distortion correction could not be performed. This patient was excluded from the evaluation, leaving 27 patients for analysis.

RSI-MRI cellularity maps were reconstructed based on all b-values [25], distortion corrected and then standardized across the sample with z-score maps. The z-score maps were calculated by

**Table 2**  
Distortion distance of the whole prostate and tumor regions of interest due to B0 inhomogeneity.

	Mean (standard deviation) (mm)	Maximum distortion (mm)
Whole prostate distortion	3.2 (2.2)	12
Tumor ROI distortion	3.2 (2.4)	13

(1) measuring the mean and standard deviation of normal prostate signal from the raw cellularity maps across the patient pool, (2) subtracting this measured mean value from each subject's cellularity map, and (3) dividing by the measured normal prostate standard deviation. Distortion maps were also generated to reflect the offset of the collected data in the phase encode direction versus the distortion corrected data. In addition to multi b-value cellularity maps, a low b-value ADC ( $b = 800 \text{ s/mm}^2$ ) map was also generated and distortion-corrected. Whole-mount histopathology was available for correlation. With whole-mount histopathology, the tumor area was identified by an experienced uropathologist.

With the T2 weighted-image, a radiologist delineated a region of interest determined by the prostatic capsule. The region of interest was overlaid on the distortion correction map to measure the mean and standard deviation of the distortion correction in the phase encode direction. This information was used to calculate the root mean square (RMS) distortion distance for the entire prostate in a single slice according to the following relationship:

$$RMS_{\text{distortion}} = 2 \times \sqrt{(\mu_{\text{distortion distance}}^2 + \sigma_{\text{distortion distance}}^2)}$$

where  $\mu_{\text{distortion distance}}$  is the mean distortion distance and  $\sigma_{\text{distortion distance}}$  is the standard deviation of the distortion distance measured on the distortion maps.

Low b-value ADC maps ( $b = 800 \text{ s/mm}^2$ ) were used to define malignant regions of interest, corresponding to tumors identified on whole mount pathology. In some patients, two regions of interest corresponded to tumor. If on the same slice, both of these tumor regions of interest were included in the analysis, for a total of 34 tumor regions of interest in 27 prostates.

## 3. Results

Across the 27 included patients, the average root mean square distortion distance of the prostate was 3.1 mm (standard deviation, 2.2 mm; maximum distortion, 12 mm). When specifically looking at the tumor regions, the average root mean square of the distortion distance of the tumors was similar at 3.1 mm (standard deviation, 2.3 mm; maximum distortion, 13 mm). Results are summarized in Table 2.

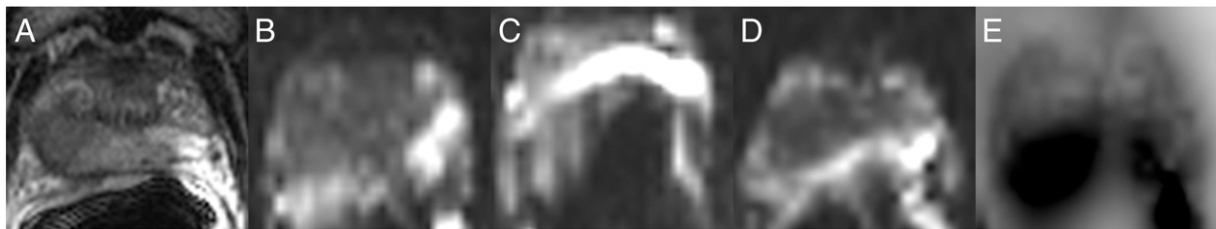


**Fig. 1.** Demonstration of distortion of diffusion MRI with EPI due to B0 inhomogeneity. (A) T2-weighted image of the prostate reflecting the prostate's MR anatomical appearance without distortion. (B) Demonstration of the distortion when the diffusion data are collected only in the forward phase encode direction with an EPI trajectory. (C) Demonstration of the distortion when the diffusion data are collected only in the reverse phase encode direction with an EPI trajectory. (D) Distortion corrected diffusion imaging at  $b = 0$ . (E) Deformation field map.



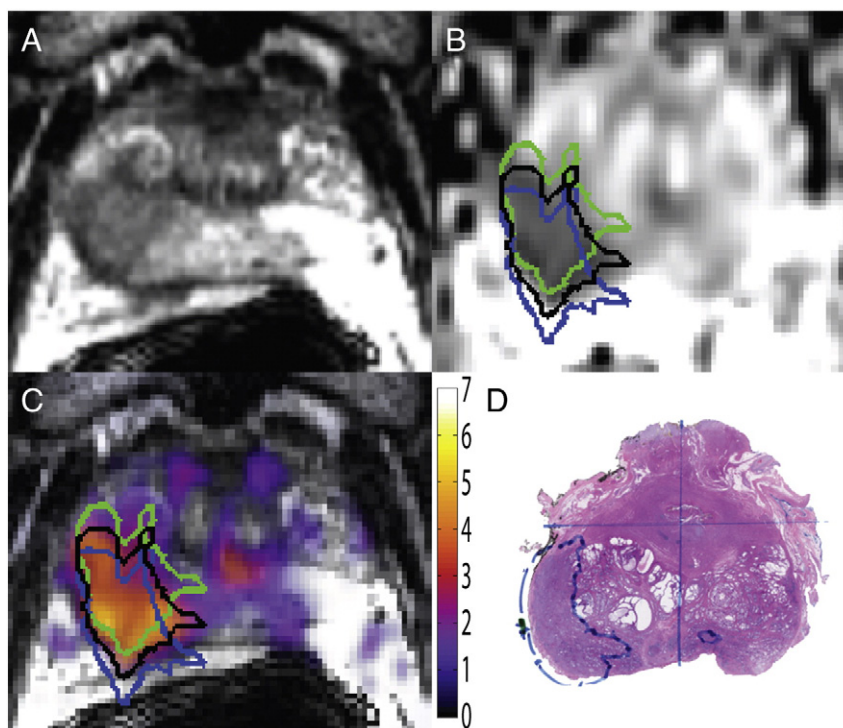


**Fig. 2.** Patient example of the effects of distortion on localizing tumor. (A) T2-weighted image, used as the imaging anatomic gold standard. Note that the tumor is in the right posterior quadrant. (B) Distortion-corrected low b-value ADC map, with the region of low ADC outlined in black. The blue and green ROIs represent the regions of low ADC without distortion correction (blue: in-phase encode direction, green: reverse phase encode direction). (C) RSI-MRI image that incorporates the distortion correction and converts the cellularity map based on multiple b-values to a standardized z-score map, overlaid on the T2-weighted anatomic image. The blue and green ROIs are the regions of RSI signal without distortion correction while the black ROI is distortion corrected. (D) Whole-mount histopathology confirming the location of extraprostatic extension in the right posterior quadrant.

Nine of the 27 patients demonstrated histologically proven extracapsular extension. Standard diffusion MR of the prostate only identified one tumor as definitively demonstrating extracapsular extension. The distortion correction maps demonstrated extracapsular extension in eight of the nine patients.

Fig. 2 shows an example of the calculated offset by 5.5 mm of root mean square distortion. This patient has histologically proven extraprostatic extension. Depending on the phase encode direction, the tumor area may incorrectly be localized anteriorly (thus not identifying extraprostatic extension), or appear to exceed the prostatic capsule in excess.

#### 4. Discussion

Diffusion imaging, because it uses an echo planar trajectory, is sensitive to  $B_0$  inhomogeneity. This manifests as distortion in the phase encode direction. By collecting data in both the forward and reverse phase encoding directions at  $b = 0$ , enough information is collected to correct for the distortion in the phase encode direction. This technique [23] is used to correct for distortion in brain diffusion imaging. Although diffusion imaging in the prostate is becoming the standard of care in prostate MRI protocols, distortion correction has not yet been widely implemented for prostate diffusion imaging. Other distortion minimizing techniques are being evaluated in the prostate but focus on minimizing the distortion rather than correcting for distortion due to  $B_0$  inhomogeneity [29,30].

As demonstrated in this paper, distortion correction improves tumor localization for diffusion imaging. Diffusion imaging is often the best MR technique to detect prostate cancer. With the advent of MRI-ultrasound fusion guided biopsies [19] and high-intensity focused ultrasound treatment [20,21], accurate localization is

necessary. Surgical planning also depends on differentiating between extraprostatic extension of tumor and the tumor remaining within the capsule, a decision that could be made with accurate imaging. Distortion distances of up to 13 mm due to standard diffusion imaging may grossly misdirect treatment decisions and therapies. Distortion correction for diffusion imaging has the potential to improve the standard of care for prostate MRI.

#### Acknowledgements

The authors would like to thank Brenda Brown for her help on this project. Funding: This work was supported by the Department of Defense, Prostate Cancer Research Program W81XWH-13-1-0391, the American Cancer Society–Institutional Research Grant #70-002, NIH-EB-RO1000790, and UCSD Clinician Scientist Program NIH T32-EB005970.

#### References

- [1] Siegel R, Ma J, Zou Z, Jemal A. Cancer statistics. 2014;64:9–29.
- [2] Mazaheri Y, Hricak H, Fine SW, et al. Prostate tumor volume measurement with combined T2-weighted imaging and diffusion-weighted MR: correlation with pathologic tumor volume. *Radiology* 2009;252:449–57. <http://dx.doi.org/10.1148/radiol.2523081423>.
- [3] Tanimoto A, Nakashima J, Kohno H, Shinmoto H, Kuribayashi S. Prostate cancer screening: the clinical value of diffusion-weighted imaging and dynamic MR imaging in combination with T2-weighted imaging. *J Magn Reson Imaging* 2007; 25:146–52. <http://dx.doi.org/10.1002/jmri.20793>.
- [4] Rais-Bahrami S, Siddiqui MM, Turkbey B, et al. Utility of multiparametric magnetic resonance imaging suspicion levels for detecting prostate cancer. *J Urol* 2013;190:1721–7. <http://dx.doi.org/10.1016/j.juro.2013.05.052>.
- [5] Miao H, Fukatsu H, Ishigaki T. Prostate cancer detection with 3-T MRI: comparison of diffusion-weighted and T2-weighted imaging. *Eur J Radiol* 2007;61:297–302. <http://dx.doi.org/10.1016/j.ejrad.2006.10.002>.
- [6] Haider MA, van der Kwast TH, Tanguay J, Evans AJ, Hashmi A-T, Lockwood G, et al. Combined T2-weighted and diffusion-weighted MRI for localization of



- prostate cancer. *AJR Am J Roentgenol* 2007;189:323–8. <http://dx.doi.org/10.2214/AJR.07.2211>.
- [7] Donati OF, Jung SI, Vargas HA, Gultekin DH, Zheng J, Moskowitz CS, et al. Multiparametric prostate MR imaging with T2-weighted, diffusion-weighted, and dynamic contrast-enhanced sequences: are all pulse sequences necessary to detect locally recurrent prostate cancer after radiation therapy? *Radiology* 2013;268:440–50. <http://dx.doi.org/10.1148/radiol.13122149>.
  - [8] Lim HK, Kim JK, Kim KA, Cho K-S. Prostate cancer: apparent diffusion coefficient map with T2-weighted images for detection—a multireader study. *Radiology* 2009;250:145–51. <http://dx.doi.org/10.1148/radiol.2501080207>.
  - [9] Isebaert S, Van den Bergh L, Haustermans K, et al. Multiparametric MRI for prostate cancer localization in correlation to whole-mount histopathology. *J Magn Reson Imaging* 2013;37:1392–401. <http://dx.doi.org/10.1002/jmri.23938>.
  - [10] Rastinehad AR, Baccala AA, Chung PH, et al. D'Amico risk stratification correlates with degree of suspicion of prostate cancer on multiparametric magnetic resonance imaging. *J Urol* 2011;185:815–20. <http://dx.doi.org/10.1016/j.juro.2010.10.076>.
  - [11] Rais-Bahrami S, Türkbey B, Rastinehad AR, et al. Natural history of small index lesions suspicious for prostate cancer on multiparametric MRI: recommendations for interval imaging follow-up. *Diagn Interv Radiol* 2014. <http://dx.doi.org/10.5152/dir.2014.13319>.
  - [12] Abd-Alazeez M, Kirkham A, Ahmed HU, Arya M, Anastasiadis E, Charman SC, et al. Performance of multiparametric MRI in men at risk of prostate cancer before the first biopsy: a paired validating cohort study using template prostate mapping biopsies as the reference standard. *Prostate Cancer Prostatic Dis* 2014; 17:40–6. <http://dx.doi.org/10.1038/pcan.2013.43>.
  - [13] Hoeks CMA, Somford DM, van Oort IM, et al. Value of 3-T multiparametric magnetic resonance imaging and magnetic resonance-guided biopsy for early risk re-stratification in active surveillance of low-risk prostate cancer: a prospective multicenter cohort study. *Investig Radiol* 2014;49:165–72. <http://dx.doi.org/10.1097/RLI.0000000000000008>.
  - [14] Stamatakis L, Siddiqui MM, Nix JW, et al. Accuracy of multiparametric magnetic resonance imaging in confirming eligibility for active surveillance for men with prostate cancer. *Cancer* 2013;119:3359–66. <http://dx.doi.org/10.1002/cncr.28216>.
  - [15] Abd-Alazeez M, Ahmed HU, Arya M, Charman SC, Anastasiadis E, Freeman A, et al. The accuracy of multiparametric MRI in men with negative biopsy and elevated PSA level—can it rule out clinically significant prostate cancer? *Urol Oncol* 2014;32:45.e17–22. <http://dx.doi.org/10.1016/j.urolonc.2013.06.007>.
  - [16] Park JJ, Kim CK, Park SY, Park BK, Lee HM, Cho SW. Prostate cancer: role of pretreatment multiparametric 3-T MRI in predicting biochemical recurrence after radical prostatectomy. *AJR Am J Roentgenol* 2014;202:W459–65. <http://dx.doi.org/10.2214/AJR.13.11381>.
  - [17] Le Bihan D, Poupon C, Amadon A, Lethimonnier F. Artifacts and pitfalls in diffusion MRI. *J Magn Reson Imaging* 2006;24:478–88. <http://dx.doi.org/10.1002/jmri.20683>.
  - [18] Donato F, Costa DN, Yuan Q, Rofsky NM, Lenkinski RE, Pedrosa I. Geometric distortion in diffusion-weighted MR imaging of the prostate-contributing factors and strategies for improvement. *Acad Radiol* 2014;21:817–23. <http://dx.doi.org/10.1016/j.acra.2014.02.001>.
  - [19] Pinto PA, Chung PH, Rastinehad AR, et al. Magnetic resonance imaging/ultrasound fusion guided prostate biopsy improves cancer detection following transrectal ultrasound biopsy and correlates with multiparametric magnetic resonance imaging. *J Urol* 2011;186:1281–5. <http://dx.doi.org/10.1016/j.juro.2011.05.078>.
  - [20] Napoli A, Anzidei M, De Nunzio C, Cartocci G, Panebianco V, De Dominicis C, et al. Real-time magnetic resonance-guided high-intensity focused ultrasound focal therapy for localised prostate cancer: preliminary experience. *Eur Urol* 2013;63: 395–8. <http://dx.doi.org/10.1016/j.eururo.2012.11.002>.
  - [21] Ahmed HU, Hindley RG, Dickinson L, Freeman A, Kirkham AP, Sahu M, et al. Focal therapy for localised unifocal and multifocal prostate cancer: a prospective development study. *Lancet Oncol* 2012;13:622–32. [http://dx.doi.org/10.1016/S1470-2045\(12\)70121-3](http://dx.doi.org/10.1016/S1470-2045(12)70121-3).
  - [22] Jezzard P, Balaban RS. Correction for geometric distortion in echo planar images from B0 field variations. *Magn Reson Med* 1995;34:65–73. <http://dx.doi.org/10.1002/mrm.1910340111>.
  - [23] Holland D, Kuperman JM, Dale AM. Efficient correction of inhomogeneous static magnetic field-induced distortion in echo planar imaging. *Neuroimage* 2010;50: 175–83. <http://dx.doi.org/10.1016/j.neuroimage.2009.11.044>.
  - [24] Andersson JLR, Skare S, Ashburner J. How to correct susceptibility distortions in spin-echo echo-planar images: application to diffusion tensor imaging. *Neuroimage* 2003;20:870–88. [http://dx.doi.org/10.1016/S1053-8119\(03\)00336-7](http://dx.doi.org/10.1016/S1053-8119(03)00336-7).
  - [25] White NS, Leergaard TB, D'Arceuil H, Bjaalie JG, Dale AM. Probing tissue microstructure with restriction spectrum imaging: histological and theoretical validation. *Hum Brain Mapp* 2013;34:327–46. <http://dx.doi.org/10.1002/hbm.21454>.
  - [26] White NS, McDonald CR, Farid N, Kuperman JM, Kesari S, Dale AM. Improved conspicuity and delineation of high-grade primary and metastatic brain tumors using "restriction spectrum imaging": quantitative comparison with high b-value DWI and ADC. *AJNR Am J Neuroradiol* 2012. <http://dx.doi.org/10.3174/ajnr.A3327>.
  - [27] White NS, Dale AM. Distinct effects of nuclear volume fraction and cell diameter on high b-value diffusion MRI contrast in tumors. *Magn Reson Med* 2013. <http://dx.doi.org/10.1002/mrm.25039> [n/a–n/a].
  - [28] Rakow-Penner R, White N, Parsons JK, Choi H, Liss M, Kuperman J, et al. Novel technique for characterizing prostate cancer utilizing MRI Restriction Spectrum Imaging: proof of principle and initial clinical experience with extra-prostatic extension. *Prostate Cancer Prostatic Dis* 2015;18:81–5. <http://dx.doi.org/10.1038/pcan.2014.50>.
  - [29] Thierfelder KM, Scherr MK, Notohamiprodjo M, Weib J, Dietrich O, Mueller-Lisse UG, et al. Diffusion-weighted MRI of the prostate: advantages of zoomed EPI with parallel-transmit-accelerated 2D-selective excitation imaging. *Eur Radiol* 2014;24:3233–41. <http://dx.doi.org/10.1007/s0030-014-3347-y>.
  - [30] Rosenkrantz AB, Chandarana H, Pfeuffer J, Triolo M, Shaikh MB, Mossa DJ, et al. Zoomed echo-planar imaging using parallel transmission: impact on image quality of diffusion-weighted imaging of the prostate at 3 T. *Abdom Imaging* 2015;40:120–6. <http://dx.doi.org/10.1007/s00261-014-0181-2>.



# MRI-derived restriction spectrum imaging cellularity index is associated with high grade prostate cancer on radical prostatectomy specimens

Michael A. Liss<sup>1\*</sup>, Nathan S. White<sup>2</sup>, J. Kellogg Parsons<sup>1</sup>, Natalie M. Schenker-Ahmed<sup>2</sup>, Rebecca Rakow-Penner<sup>2</sup>, Joshua M. Kuperman<sup>2</sup>, Hauke Bartsch<sup>2</sup>, Hyung W. Choi<sup>2</sup>, Robert F. Mattrey<sup>2</sup>, William G. Bradley<sup>2</sup>, Ahmed Shabaik<sup>3</sup>, Jiaoti Huang<sup>4</sup>, Daniel J. A. Margolis<sup>5</sup>, Steven S. Raman<sup>5</sup>, Leonard S. Marks<sup>6</sup>, Christopher J. Kane<sup>1</sup>, Robert E. Reiter<sup>6</sup>, Anders M. Dale<sup>2,7</sup> and David S. Karow<sup>2</sup>

<sup>1</sup> Department of Urology, University of California San Diego School of Medicine, San Diego, CA, USA

<sup>2</sup> Department of Radiology, University of California San Diego School of Medicine, San Diego, CA, USA

<sup>3</sup> Department of Pathology, University of California San Diego School of Medicine, San Diego, CA, USA

<sup>4</sup> Department of Pathology, University of California Los Angeles Geffen School of Medicine, Los Angeles, CA, USA

<sup>5</sup> Department of Radiology, University of California Los Angeles Geffen School of Medicine, Los Angeles, CA, USA

<sup>6</sup> Department of Urology, University of California Los Angeles Geffen School of Medicine, Los Angeles, CA, USA

<sup>7</sup> Department of Neurosciences, University of California San Diego, La Jolla, CA, USA

## Edited by:

Atreya Dash, University of Washington, USA

## Reviewed by:

Scott T. Tagawa, Weill Cornell Medical College, USA

Ari Adami, Santa Casa Hospital, Brazil

## \*Correspondence:

Michael A. Liss, UCSD Moores Cancer Center, 3855 Health Sciences Drive, MC 0987, La Jolla, CA 92093, USA  
e-mail: mliss008@gmail.com

**Purpose:** We evaluate a novel magnetic resonance imaging (MRI) technique to improve detection of aggressive prostate cancer (PCa).

**Materials and Methods:** We performed a retrospective analysis of pre-surgical prostate MRI scans using an advanced diffusion-weighted imaging technique called restriction spectrum imaging (RSI), which can be presented as a normalized z-score statistic. Scans were acquired prior to radical prostatectomy. Prostatectomy specimens were processed using whole-mount sectioning and regions of interest (ROIs) were drawn around individual PCa tumors. Corresponding ROIs were drawn on the MRI imaging and paired with ROIs in regions with no pathology. RSI z-score and conventional apparent diffusion coefficient (ADC) values were recorded for each ROI. Paired *t*-test, ANOVA, and logistic regression analyses were performed.

**Results:** We evaluated 28 patients with 64 ROIs (28 benign and 36 PCa). The mean difference in RSI z-score (PCa ROI–Benign ROI) was 2.17 (SE = 0.11;  $p < 0.001$ ) and in ADC was 551 mm<sup>2</sup>/s (SE = 80 mm<sup>2</sup>/s; paired *t*-test,  $p < 0.001$ ). The differences in the means among all groups (benign, primary Gleason 3, and primary Gleason 4) was significant for both RSI z-score ( $F_{3,64} = 97.7$ ,  $p < 0.001$ ) and ADC ( $F_{3,64} = 13.9$ ,  $p < 0.001$ ). A *t*-test was performed on only PCa tumor ROIs ( $n = 36$ ) to determine PCa aggressiveness (Gleason 3 vs. Gleason 4) revealing that RSI z-score was still significant ( $p = 0.03$ ), whereas, ADC values were no longer significant ( $p = 0.08$ ). In multivariable analysis adjusting for age and race, RSI z-score was associated with PCa aggressiveness (OR 10.3, 95% CI: 1.4–78.0,  $p = 0.02$ ) while ADC trended to significance ( $p = 0.07$ ).

**Conclusion:** The RSI-derived normalized cellularity index is associated with aggressive PCa as determined by pathologic Gleason scores. Further utilization of RSI techniques may serve to enhance standardized reporting systems for PCa in the future.

**Keywords:** prostate, MRI imaging, prostate cancer, cellularity, Gleason score

## INTRODUCTION

One current focus in prostate cancer (PCa) diagnosis is to distinguish indolent from more aggressive disease to reduce over-treatment (1, 2). Magnetic resonance imaging (MRI) may be a non-invasive imaging biomarker to incorporate into PCa detection and treatment strategies (3).

Recently, MRI has been increasingly investigated for use as a tool in the screening, staging, and monitoring of PCa (4–6). Imaging

techniques such as diffusion-weighted imaging (DWI) and the resultant quantitative apparent diffusion coefficient (ADC) have shown correlation with PCa; however, they have significant limitations regarding tumor conspicuity and localization (7, 8). A novel, advanced diffusion-based imaging technique, called restriction spectrum imaging (RSI), has been modified from previous studies in brain cancer detection to apply to patients with PCa (8, 9). Some benefits of the RSI technique include reduced spatial distortion,

enhanced tumor contrast-to-noise over conventional diffusion-weighted imaging (DWI), and a normalized *in vivo* measure of cellularity.

Within individual tumor regions of interest (ROIs), we investigate the association of final pathologic Gleason score from whole-mount prostatectomy specimens with the RSI cellularity index as compared to the current standard, ADC (10–16). Our primary outcome is the detection of primary pattern Gleason  $\geq 4$  PCa.

## MATERIALS AND METHODS

### PATIENTS

All patients were previously diagnosed with PCa via standard transrectal ultrasound guided prostate biopsy after prostate specific antigen (PSA) elevation or abnormal digital rectal examination (DRE). Pre-surgical pelvic MRI is routinely used at our institution to identify extraprostatic extension (EPE) in order to guide nerve-sparing surgery. Data were collected from chart review.

### MRI AND RSI

Patients underwent standard T2, perfusion (with Gadolinium) and diffusion protocols at 3 T (Siemens, Erlangen Germany) with an endorectal coil prior to radical prostatectomy. **Table 1** shows pulse sequence details. A modified Prostate Imaging-Reporting and Data System (PIRADS) score, termed “the UCLA assessment criteria,” was assigned to the scan based on the suspicion of cancer previously instituted at our institution (17). The ADC maps used to draw ROIs were generated from the low *b*-value, 800 s/mm<sup>2</sup>, derived from the same spectrum of *b*-values used in the RSI protocol. ADC maps were corrected for spatial distortion (18). The restriction spectrum diffusion tensor imaging protocol parameters include *b*-values of 0, 800, 1500, 4000 s/mm<sup>2</sup> in 30 unique diffusion directions for each non-zero *b*-value. RSI cellularity maps were reconstructed based on all *b*-values (8). The RSI cellularity maps were then standardized across the sample, using the mean and standard deviations of normal prostate signal from the raw

RSI maps in 20 patients to produce *z*-score maps. RSI maps were also corrected for spatial distortion (19).

### PATHOLOGY

After prostatectomy, whole-mount histopathology was routinely performed on 4  $\mu$ m thick sections of each specimen. A Gleason score was assigned to each representative tumor location. If two tumors were located, the Gleason score for each was assessed independently. The histopathology was evaluated and the boundaries of tumor vs. benign tissue were identified by an uropathologist.

### OUTCOMES

We defined our primary outcome as pathologic primary Gleason score of 4, which means that Gleason 4 is the dominant histologic architecture and includes 4 + 3, 4 + 4, and 4 + 5 Gleason patterns. The pathologic Gleason score is currently the standard of reference for PCa aggressiveness. Additionally, the ability of imaging to detect secondary Gleason patterns may be minimal; therefore, herein we focus on primary Gleason patterns. Our primary predictor variable was the normalized cellularity index called the “RSI *z*-score.” The most commonly utilized tool to identify and classify aggressive cancer on MRI currently is the ADC value from DWI; therefore, the RSI *z*-score was compared with ADC to assess the predictive value in differentiating cancer from normal ROI.

Each patient had at least one identified region of cancerous tissue. If two areas of cancer were detected, each region was evaluated and assigned a separate Gleason score, ADC, and *z*-score. Tumor ROIs were drawn based on the pathology in combination with ADC images that had been corrected for spatial distortion. A benign ROI was defined in a region of the prostate seen to be free of PCa on the whole-mount histology. ADC and RSI *z*-score values were recorded for all ROIs.

### STATISTICAL ANALYSIS

Each patient had at least one ROI of cancer and one ROI of benign tissue. Correlation between the RSI-derived *z*-score and ADC was determined by a Pearson correlation test assuming normal distribution. In order to investigate the association of RSI *z*-score and primary Gleason pattern 4 PCa vs. pattern 3 PCa, a *t*-test was performed. In order to compare the utility of MRI techniques (RSI *z*-score vs. ADC) for detecting aggressive cancer, we compared ROIs representing pathologically benign tissue with those representing increasing aggressive PCa (benign vs. Gleason 3 vs. Gleason 4 primary patterns) using ANOVA analysis (*F*-test). After removing the values for the benign ROIs, we also assessed variation in MRI values among different grades of cancerous tissue aggressiveness by performing a comparative *t*-test. Multivariable analysis included an ordinal logistic regression (benign vs. Gleason 3 vs. Gleason 4) and binary logistic regression (Gleason 3 vs. Gleason 4). *p*-values <0.05 were considered statistically significant using the statistical package SPSS v.21 (IBM, Chicago, IL, USA). Age and race were controlled for due to the risk of PCa associated with these variables and that they are inherent to each ROIs. However, other demographic variables associated with cancer (PSA, clinical stage, biopsy data, etc.) may not be associated with an individual ROI and may misrepresent the data as some patients have multiple ROIs. Therefore, the multivariable analysis only includes the

**Table 1 | MRI scan parameters for prostate MRI protocol at 3T.**

Pulse sequence	Parameters
T2	Axial 3D TSE T2 (Siemens SPACE), TR/TE 3800-5040/101, ETL 13, 14 cm FOV, 256 × 256 matrix, 1.5 mm contiguous slices
Diffusion-weighted (standard)	echoplanar, TR/TE 3900/60, 21 × 26 cm FOV, 130 × 160 matrix, 3.6 mm slices, 4 NEX, <i>b</i> -values 0, 100, 400, 800 s/mm <sup>2</sup>
T1 dynamic perfusion imaging	Siemens TWIST, TR/TE 3.9/1.4 ms, 12° flip angle, 26 × 26 cm FOV, 160 × 160 matrix, 3.6 mm slices, 4.75 s/acquisition over 6 minutes with 15 s injection delay, image analysis using iCAD Versavue
Restriction spectrum imaging	Spin echo EPI, TR/TE 5500/137, 26 cm × 26 cm FOV, 128 × 96 matrix, 3.6 mm slices, 30 directions at each <i>b</i> -value, <i>b</i> -values 0, 800, 1500, 4000 s/mm <sup>2</sup>

preselected variables of age and race without accounting for these other variables despite their significance in univariable analysis.

## RESULTS

After IRB approval (UCLA IRB#12-001301), we identified 28 patients who underwent preoperative MRI with RSI and subsequent whole-mount pathology after radical prostatectomy, with surgery taking place between May 2012 and May 2013. Demographics are displayed in **Table 2**. **Figure 1** shows representative examples of RSI across the Gleason spectrum and illustrates data collection methods. White arrows within the higher-grade RSI maps show areas of signal void that could be interpreted as false positives on the corresponding ADC maps. We identified 64 ROIs (28 benign and 36 PCa). Eight patients had two distinct tumor ROIs within one specimen. Seven of those patients had discordant tumors (two different Gleason scores) and only one patient had two concordant tumor ROIs (both Gleason 3 + 4). The RSI z-score data for all ROIs, grouped by Gleason score, is shown in **Figure 2**.

Apparent diffusion coefficient and RSI z-scores are normally distributed and did not need further transformation. There is

a significant correlation between ADC and RSI z-score (Pearson  $R = 0.69$ ;  $n = 64$ ,  $p < 0.001$ ) (see supplementary figure). ADC and RSI z-score are collinear (collinearity index 8.4); therefore, they cannot be placed within the same multivariate analytic model.

The mean cellularity index (RSI z-score) in PCa was 2.53 (SE = 0.10) and in benign tissue 0.39 (SE = 0.12;  $p < 0.001$ ). The mean ADC for PCa was 1169 mm<sup>2</sup>/s (SE = 67 mm<sup>2</sup>/s) and benign was 1679 mm<sup>2</sup>/s (SE = 81 mm<sup>2</sup>/s,  $p < 0.001$ ).

For the univariate and multivariate analyses, the data were grouped by primary Gleason pattern, either primary Gleason 3 (3 + 3 or 3 + 4) or Gleason 4 (4 + 3, 4 + 4, or 4 + 5). In univariable analysis, we investigate the association of RSI z-score and ADC with PCa on pathology (benign vs. Gleason 3 vs. Gleason 4) using ANOVA analysis. Both were able to distinguish benign from increasingly malignant PCa (both  $p < 0.001$ ) (**Table 3**). **Figure 3** displays a box plot developed from individual ROI RSI z-scores corresponding to benign tissue primary Gleason 3 pattern or primary Gleason 4 pattern PCa tumors. When removing the benign ROIs as to only compare low-grade (primary Gleason 3) to high-grade PCA (primary Gleason 4), RSI technique was able

**Table 2 | Demographics: perioperative demographics for 28 patients who underwent MRI with an endorectal coil and subsequently underwent radical prostatectomy.**

Age	Race	BMI	PSA	Clinical Stage	Biopsy Gleason	Positive cores	Maximum percent cancer %	Imaging criteria	Pathologic Gleason	Pathologic stage
63	White	20.1	7	T1c	3 + 4	3 of 15	30	4	3 + 3	T2
61	White	31.4	5.8	T1c	4 + 3	4 of 12	85	5	3 + 4	T3b
55	White	29.3	2.8	T1c	3 + 5	4 of 12	90	3	3 + 4	T3a
71	White	29.7	7.3	T2	3 + 3	9 of 19	60	3	3 + 4	T2
59	White	31.4	4.43	T2	3 + 3	4 of 12	33	3	3 + 4	T2c
61	White	21.4	9.2	T2	3 + 3	6 of 15	30	4	3 + 4	T2b
68	White	–	6.7	T1c	3 + 4	10 of 12	70	3	3 + 4	T2c
55	White	27.5	4.7	T1c	3 + 4	6 of 16	70	3	3 + 4	T2b
64	White	23.1	5.8	T1c	3 + 4	1 of 12	30	2	3 + 4	T2c
61	Other	26	3.4	T1c	3 + 4	6 of 13	95	3	3 + 4	T2c
60	Unknown	25.5	6	T1c	3 + 3	3 of 12	–	3	3 + 4	T2
61	White	29.8	6.6	T1c	–	–	–	4	3 + 4	T2
65	Unknown	29	5.4	T2	3 + 4	2 of 14	45	2	3 + 4	T2
50	White	31.2	8.9	T1c	3 + 4	2 of 12	20	4	3 + 4	T2
53	White	22.7	3.9	T1c	4 + 3	3 of 8	15	2	3 + 4	T3a
44	White	26.6	2.8	T1c	3 + 4	4 of 16	70	3	3 + 4	T2a
58	White	32.7	3.8	T1c	3 + 4	6 of 12	70	3	3 + 4	T2c
53	Asian	16.9	5.5	T1c	3 + 4	3 of 12	15	4	3 + 4	T2
62	African American	25.1	4.8	T1c	4 + 3	2 of 12	70	0	4 + 3	T2a
65	White	38.5	5.8	T2	4 + 3	5 of 12	88	5	4 + 3	T3a
64	White	26.9	4.2	T1c	3 + 5	12 of 12	94	5	4 + 3	T3a
56	Other	28	11.5	T1c	3 + 4	multiple	50	4	4 + 3	T3a
67	White	30.4	5.1	T1c	3 + 4	5 of 13	25	4	4 + 3	T3a
71	White	28.4	12.8	T1c	4 + 3	–	–	5	4 + 3	T3a
45	African American	23.5	6.5	T1c	4 + 3	9 of 16	80	1	4 + 4	T2c
65	White	30.1	8.2	T1c	5 + 4	–	55	4	4 + 5	T3b
62	White	25.8	4.6	T2	4 + 5	5 of 15	50	4	4 + 5	T2
70	Filipino	35.5	7.5	T2	4 + 3	9 of 12	90	3	4 + 5	T3a



to distinguish the two groups ( $p = 0.03$ ) and ADC trended to significance ( $p = 0.08$ ). We then investigated these same parameters in multivariable analysis and determined that both RSI z-score

and ADC were able to distinguish between the three groups in ordinal regression analysis adjusting for age and race (white vs. non-white); though the log odds of the parameter estimates suggest an improved distinction of the groups by RSI (RSI z-score and ADC,  $p < 0.001$ ). However, when determining the difference in the detection of low-grade and high-grade PCa, a higher RSI z-score was significantly associated with the higher-grade primary Gleason 4 pattern [Odds ratio 10.3 (1.4–78.0;  $p = 0.02$ )] and ADC showed a trend in distinguishing between the two Gleason patterns ( $p = 0.07$ ) (Table 4).

## DISCUSSION

Magnetic Resonance RSI normalized cellularity index (RSI z-score) is able to distinguish aggressive PCa (primary Gleason score of 4 compared to 3) in our population of men undergoing radical prostatectomy. Importantly, the RSI technique has displayed at least similar ability to distinguish Gleason grade to the current reference standard, ADC values.

Multiple studies have described the ability of ADC to detect PCa. However, the distinction between PCa aggressiveness has been less investigated. Donati et al. found that mean ADC could distinguish Gleason 6 from 7+ tumors in 131 men undergoing prostatectomy (AUC 0.706) and in another paper discussed the use of 10<sup>th</sup> percentile ADC correlation to aggressiveness (10, 16). The 10<sup>th</sup> percentile ADC was also used in combination with mean ADC, T2-weighted skewness, and  $K^{\text{trans}}$  to distinguish PCa using computer aided diagnosis (18). Moreover, a recent study has suggested that ADC entropy rather than mean ADC could better discriminate the proportion of Gleason 4 cancer among Gleason 3 + 4 and 4 + 3 tumors (20). The distinction in primary Gleason pattern may

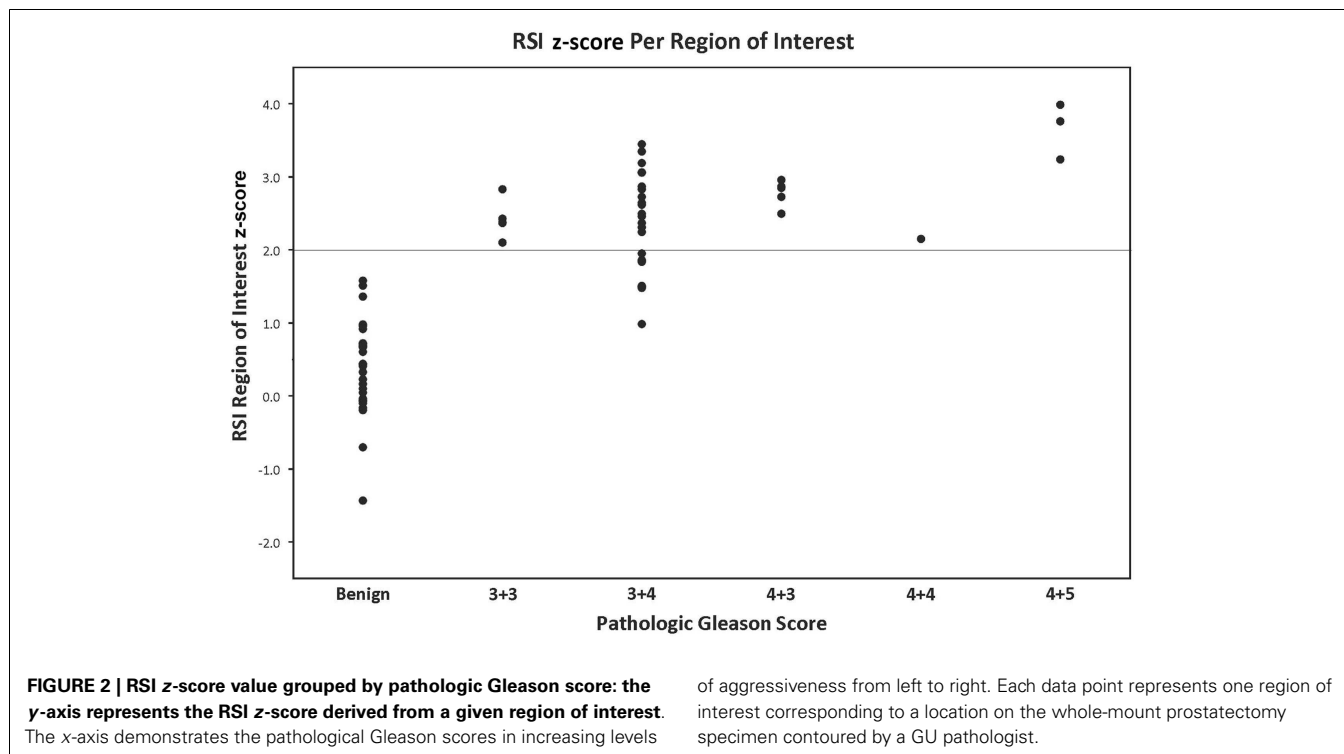
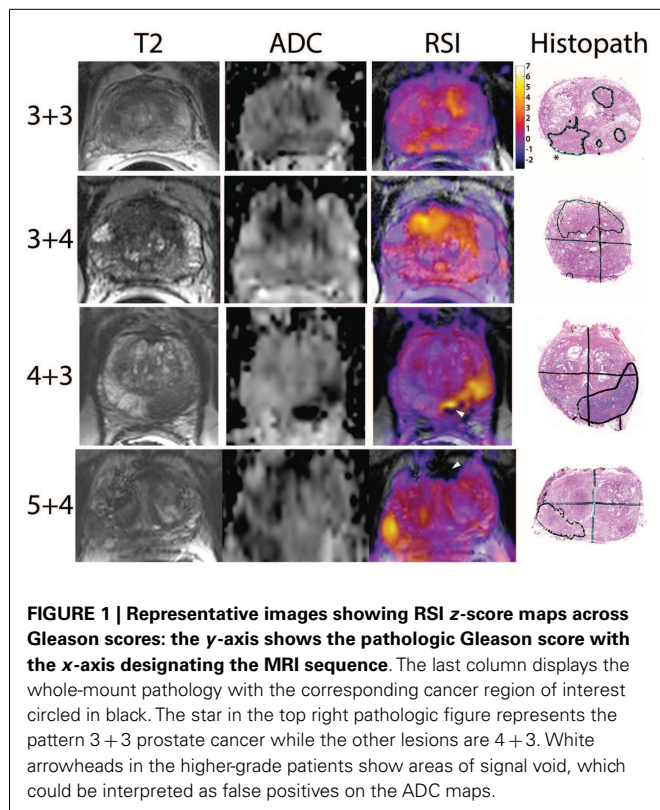




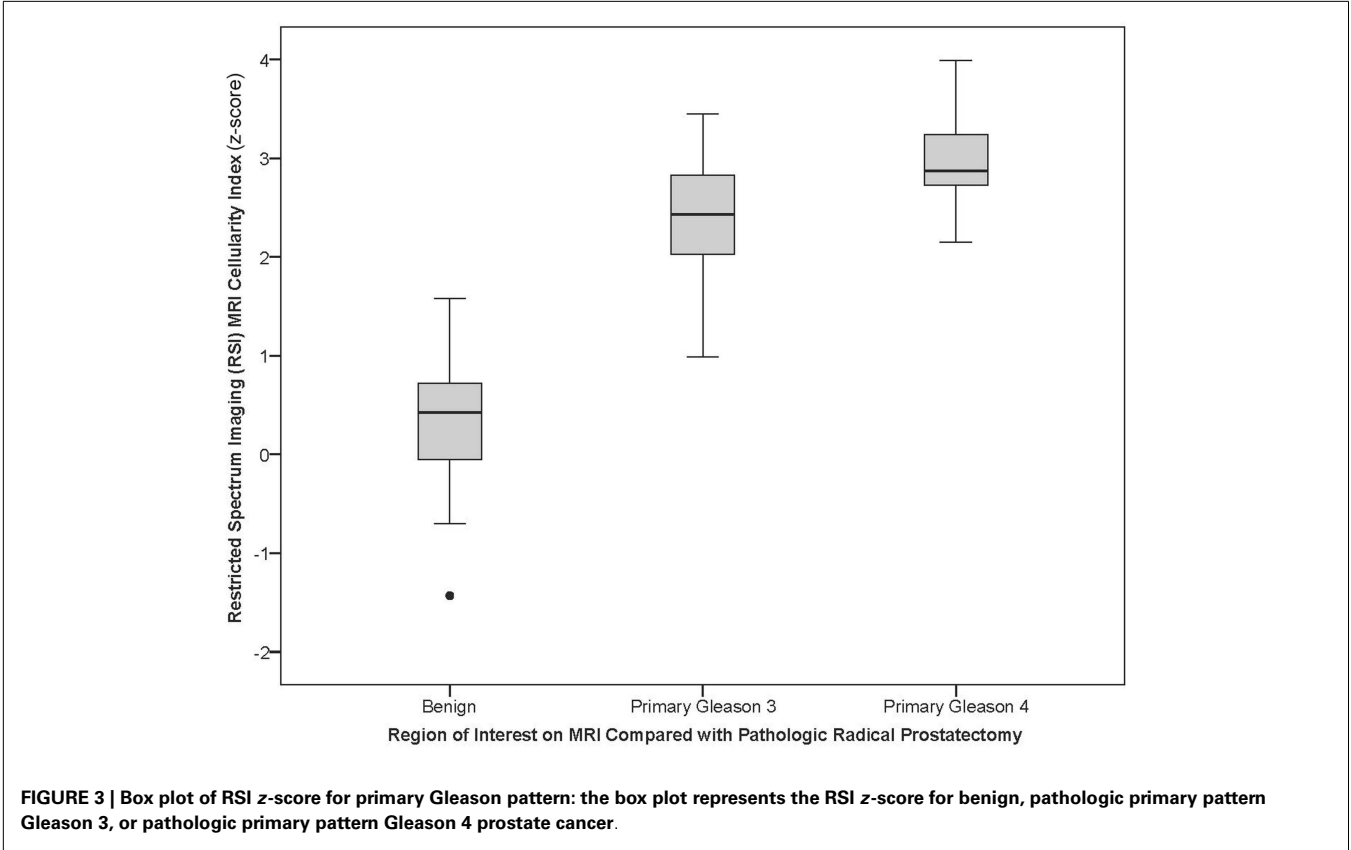
**Table 3 | Univariable analysis: restriction spectrum imaging (RSI) z-score and apparent diffusion coefficient (ADC) are independently investigated comparing individual regions of interest to their corresponding primary Gleason pattern.**

Sample size method			Means	Statistical test	<i>p</i> value
Detection of increasingly aggressive cancer <sup>a</sup>			Mean (standard error)	<i>F</i> -test	
64	Restricted spectrum imaging (RSI) z-score	Benign	0.65 (0.12)	97.7	<0.001
		Primary Gleason 3	2.4 (0.61)		
		Primary Gleason 4	2.9 (0.51)		
64	Apparent diffusion coefficient (ADC)	Benign	1680 (428)	13.9	<0.001
		Primary Gleason 3	1237 (425)		
		Primary Gleason 4	967 (221)		
Prostate cancer aggressiveness <sup>b</sup>			Mean difference	<i>t</i> -test	
36	Restricted spectrum imaging (RSI) z-score	34	0.5	2.22	0.033
36	Apparent diffusion coefficient (ADC)	34	269	1.81	0.079

The top half of the table uses ANVOA analysis to determine differences in detection comparing benign vs. primary Gleason 3 vs. Primary Gleason 4 prostate cancer. The bottom half of the table only compares Gleason 3 vs. 4 cancers with a t-test.

<sup>a</sup> Benign vs. Gleason 3 vs. Gleason 4.

<sup>b</sup> Gleason 3 vs. Gleason 4.



have significant clinical implications regarding PCa management decision-making.

Primary Gleason 4 pattern is a more aggressive cancer with patients experiencing higher rates of biochemical (PSA) failure after prostatectomy, systemic recurrence, and PCa mortality (21). Therefore, knowledge of high-grade cancer prior to making management decisions would be helpful in determining treatment strategy. For example, men without Gleason 4 pattern PCa are

**Table 4 | Multivariable analysis: restriction spectrum imaging (RSI) z-score and apparent diffusion coefficient (ADC) are independently investigated comparing individual regions of interest to their corresponding primary Gleason pattern.**

Sample size method			Parameter coefficient <sup>a</sup> (95% confidence interval)	<i>p</i> value	McFadden's <i>D</i>
Detection of increasingly aggressive prostate cancer <sup>b</sup>					
64	Restricted spectrum imaging (RSI) z-score	Benign	0	<0.001	0.613
		Primary Gleason 3	9.5 (−1.9 to 17.0)	0.014	
		Primary Gleason 4	15.8 (6.4–25.2)	0.001	
64	Apparent diffusion coefficient (ADC)	Benign	0	<0.001	0.202
		Primary Gleason 3	1.7 (−3.2 to 6.7)	0.483	
		Primary Gleason 4	4.5 (−0.5 to 9.6)	0.076	
Prostate cancer aggressiveness <sup>c</sup>		Wald test	Odds ratio (95% confidence interval)	<i>p</i> value	
36	Restricted spectrum imaging (RSI) z-score	5.1	10.3 (1.4–78.0)	0.024	
36	Apparent diffusion coefficient (ADC)	3.3	0.9 (0.9–1.00)	0.069	

The top half of the table uses ordinal logistic regression analysis to determine differences in detection comparing benign vs. primary Gleason 3 vs. Primary Gleason 4 prostate cancer (Log Odds). The bottom half of the table only compares Gleason 3 vs. 4 cancers to determine with binary logistic regression (Odds Ratio).

<sup>a</sup>Parameter coefficients are the log odds and can be converted to odds ratios by taking the exponent of the estimate. The numbers are too large therefore are kept as log odds for simplicity.

<sup>b</sup>Ordinal logistic regression (benign vs. Gleason 3 vs. Gleason 4) adjusting for age and race (White vs. Non-White).

<sup>c</sup>Binary logistic regression (Gleason 3 vs. Gleason 4) adjusting for age and race (White vs. Non-White).

more ideal candidates for active surveillance (22). Serial imaging may indicate progression of disease, assisting urologists in deciding when a biopsy-off of protocol is warranted. Additionally, PCa grade may influence the urologic surgeon to perform a pelvic lymph node dissection at the time of prostatectomy due to increased risk of nodal disease (23).

Currently, ADC serves as the most discriminatory parameter to assist radiologists for the detection of cancer. Moreover, recent examination of ADC and PCa has shown the association of ADC and PCa aggressiveness (10, 16). While we do show that ADC can differentiate the presence of cancer or not, our study shows that ADC is less able to determine the subtlety of primary pattern Gleason 3 vs. Gleason 4 PCa. Possible reasons include the proportion of pattern 3 vs. 4 disease in our population compared to prior populations, the *b*-values used in determining the ADC, how the ROI was chosen, the amount of stromal reaction, and technical factors such as degree of hemorrhage. However, the differences between ADC and RSI z-score in our study are small.

Restriction spectrum imaging techniques offer advantages when compared to conventional DWI and ADC maps. For example, one of the challenges of standard diffusion imaging is that the ADC values are not standardized across MRI scanners. The z-score is a standardized statistical method and inherently normalizes across the patient pool. Thus, the RSI z-score is a value that could potentially be compared across different scanners and institutions and provide a more robust value for relative comparison.

In addition, conventional DWI/ADC suffers from geometric distortion and can be difficult to interpret by clinicians

and untrained radiologists. Distortion correction techniques previously optimized in the brain for GBM, are incorporated into our RSI post-processing stream in order to derive spatially corrected cellularity maps. Distortion correction techniques are not routinely employed in conventional DWI and resultant ADC maps. Thus, the RSI maps can be co-registered with T2-weighted anatomic images with voxel accuracy. This has potential implications for more accurate detection of EPE and more accurate MRI-fused ultrasound targeted biopsy results (24).

Because of its greater sensitivity to restricted rather than hindered diffusion, RSI may be less subject to hemorrhage, inflammatory processes, and benign nodules in the transitional zone, all of which can exhibit lower ADC values leading to false positives. Theoretically, RSI-MRI reduces extracellular signal by focusing on the signal emanating from intracellular tumor cells (restricted diffusion) and less from the extracellular signal (hindered diffusion) (8, 9). This will need to be rigorously tested in future ROC performance studies.

Apparent diffusion coefficient maps will exhibit low signal in regions where there is overt chemical dephasing from gross calcium, hemorrhage, or other etiologies resulting in signal void. Unfortunately, these signal voids could be interpreted inaccurately, leading to a false positive result. White arrow heads in **Figure 1** show two such examples. For example, in the Gleason 5 + 4 case, the anterior region of signal void shows up as dark (low) on the ADC maps, potentially a false positive, while in the RSI maps, this is clearly interpreted as an area of signal void, not tumor. Thus,

RSI offers a number of potential advantages when compared to DWI/ADC.

Certain limitations of this study include small sample size and retrospective data collection. We have overcome the small sample size by using each patient as his own control to provide a paired analysis by using known benign tissue. However, because of the small sample size, we have fewer patients with extremely high-grade cancer (Gleason 5) and low-grade (Gleason 6 or less); therefore, we dichotomized based on the primary Gleason pattern. We justify this analysis by assuming that MRI imaging is unlikely to visualize smaller amounts (secondary patterns) of PCa architecture. The sample size was too small to evaluate upgrading or downgrading Gleason scores at prostatectomy from the initial biopsy results in order to determine if RSI could serve to differentiate these cases; however, this question will serve as a focus in future studies. We do have a selection bias regarding our patient population as all patients underwent radical prostatectomy. Therefore, our results may not necessarily apply to patients in the general PSA screening population undergoing prostate biopsy. The lack of patients in this study with pathologies at the extremes shows the need for a broader study.

## CONCLUSION

Restriction Spectrum Imaging cellularity index is associated with the detection of aggressive PCa as defined by Gleason score. Additionally, RSI-MRI includes correction of spatial distortion, a normalized measure of cellularity, and in general increased conspicuity when compared to conventional DWI/ADC. RSI technology warrants prospective evaluation in the PCa diagnostic arena.

## ACKNOWLEDGEMENTS

DoD, Prostate Cancer Research Program, Idea Development Award W81XWH-13-1-0391, #PC120532, ACS-IRG (American Cancer Society-Institutional Research Grant) #70-002, and UCSD Clinician Scientist Program.

## SUPPLEMENTARY MATERIAL

The Supplementary Material for this article can be found online at <http://www.frontiersin.org/Journal/10.3389/fonc.2015.00030/abstract>

## REFERENCES

- Johansson JE, Andrén O, Andersson SO, Dickman PW, Holmberg L, Magnusson A, et al. Natural history of early, localized prostate cancer. *JAMA* (2004) **291**:2713–9. doi:10.1001/jama.291.22.2713
- Loeb S, Bjurlin MA, Nicholson J, Tammela TL, Penson DF, Carter HB, et al. Overdiagnosis and overtreatment of prostate cancer. *Eur Urol* (2014) **65**:1046–55. doi:10.1016/j.eururo.2013.12.062
- van den Bergh RC, Ahmed HU, Bangma CH, Cooperberg MR, Villers A, Parker CC. Novel tools to improve patient selection and monitoring on active surveillance for low-risk prostate cancer: a systematic review. *Eur Urol* (2014) **65**:1023–31. doi:10.1016/j.eururo.2014.01.027
- Chamie K, Sonn GA, Finley DS, Tan N, Margolis DJ, Raman SS, et al. The role of magnetic resonance imaging in delineating clinically significant prostate cancer. *Urology* (2014) **83**:369–75. doi:10.1016/j.urol.2013.09.045
- Park BH, Jeon HG, Jeong BC, Seo SI, Lee HM, Choi HY, et al. Influence of magnetic resonance imaging in the decision to preserve or resect neurovascular bundles at robotic assisted laparoscopic radical prostatectomy. *J Urol* (2014) **192**(1):82–8. doi:10.1016/j.juro.2014.01.005
- Lee DJ, Ahmed HU, Moore CM, Emberton M, Ehdiaie B. Multiparametric magnetic resonance imaging in the management and diagnosis of prostate cancer: current applications and strategies. *Curr Urol Rep* (2014) **15**:390. doi:10.1007/s11934-013-0390-1
- Hambrock T, Somford DM, Huisman HJ, van Oort IM, Witjes JA, Hulsbergen-van de Kaa CA, et al. Relationship between apparent diffusion coefficients at 3.0-T MR imaging and Gleason grade in peripheral zone prostate cancer. *Radiology* (2011) **259**:453–61. doi:10.1148/radiol.11091409
- White NS, McDonald CR, Farid N, Kuperman JM, Kesari S, Dale AM. Improved conspicuity and delineation of high-grade primary and metastatic brain tumors using “restriction spectrum imaging”: quantitative comparison with high B-value DWI and ADC. *AJNR Am J Neuroradiol* (2013) **34**(958–64):S1. doi:10.3174/ajnr.A3327
- White NS, Leergaard TB, D’Arceuil H, Bjaalie JG, Dale AM. Probing tissue microstructure with restriction spectrum imaging: histological and theoretical validation. *Hum Brain Mapp* (2013) **34**:327–46. doi:10.1002/hbm.21454
- Donati OF, Afaq A, Vargas HA, Mazaheri Y, Zheng J, Moskowitz CS, et al. Prostate MRI: evaluating tumor volume and apparent diffusion coefficient as surrogate biomarkers for predicting tumor Gleason score. *Clin Cancer Res* (2014) **20**:3705–11. doi:10.1158/1078-0432.CCR-14-0044
- Kobus T, Vos PC, Hambrock T, et al. Prostate cancer aggressiveness: in vivo assessment of MR spectroscopy and diffusion-weighted imaging at 3 T. *Radiology* (2012) **265**:457–67. doi:10.1148/radiol.12111744
- Oto A, Yang C, Kayhan A, Tretiakova M, Antic T, Schmid-Tannwald C, et al. Diffusion-weighted and dynamic contrast-enhanced MRI of prostate cancer: correlation of quantitative MR parameters with Gleason score and tumor angiogenesis. *AJR Am J Roentgenol* (2011) **197**:1382–90. doi:10.2214/AJR.11.6861
- Turkbey B, Shah VP, Pang Y, Bernardo M, Xu S, Kruecker J, et al. Is apparent diffusion coefficient associated with clinical risk scores for prostate cancers that are visible on 3-T MR images? *Radiology* (2011) **258**:488–95. doi:10.1148/radiol.10100667
- Vargas HA, Akin O, Franiel T, Mazaheri Y, Zheng J, Moskowitz C, et al. Diffusion-weighted endorectal MR imaging at 3 T for prostate cancer: tumor detection and assessment of aggressiveness. *Radiology* (2011) **259**:775–84. doi:10.1148/radiol.11102066
- Vargas HA, Donati OF, Wibmer A, Goldman DA, Mulhall JP, Sala E, et al. Association between penile dynamic contrast-enhanced MRI-derived quantitative parameters and self-reported sexual function in patients with newly diagnosed prostate cancer. *J Sex Med* (2014) **11**(10):2581–8. doi:10.1111/jsm.12555
- Donati OF, Mazaheri Y, Afaq A, Vargas HA, Zheng J, Moskowitz CS, et al. Prostate cancer aggressiveness: assessment with whole-lesion histogram analysis of the apparent diffusion coefficient. *Radiology* (2014) **271**:143–52. doi:10.1148/radiol.13130973
- Sonn GA, Natarajan S, Margolis DJ, MacAiran M, Lieu P, Huang J, et al. Targeted biopsy in the detection of prostate cancer using an office based magnetic resonance ultrasound fusion device. *J Urol* (2013) **189**:86–91. doi:10.1016/j.juro.2012.08.095
- Peng Y, Jiang Y, Antic T, Giger ML, Eggen SE, Oto A. Validation of quantitative analysis of multiparametric prostate MR images for prostate cancer detection and aggressiveness assessment: a cross-imager study. *Radiology* (2014) **271**:461–71. doi:10.1148/radiol.14131320
- Holland D, Kuperman JM, Dale AM. Efficient correction of inhomogeneous static magnetic field-induced distortion in echo planar imaging. *Neuroimage* (2010) **50**:175–83. doi:10.1016/j.neuroimage.2009.11.044
- Rosenkrantz AB, Triolo MJ, Melamed J, Rusinek H, Taneja SS, Deng FM. Whole-lesion apparent diffusion coefficient metrics as a marker of percentage Gleason 4 component within Gleason 7 prostate cancer at radical prostatectomy. *J Magn Reson Imaging* (2014). doi:10.1002/jmri.24598
- Tollefson MK, Leibovich BC, Slezak JM, Zincke H, Blute ML. Long-term prognostic significance of primary Gleason pattern in patients with Gleason score 7 prostate cancer: impact on prostate cancer specific survival. *J Urol* (2006) **175**:547–51. doi:10.1016/S0022-5347(05)00152-7
- Klotz L, Zhang L, Lam A, Nam R, Mamedov A, Loblaw A. Clinical results of long-term follow-up of a large, active surveillance cohort with localized prostate cancer. *J Clin Oncol* (2010) **28**:126–31. doi:10.1200/JCO.2009.24.2180

23. Allaf ME, Partin AW, Carter HB. The importance of pelvic lymph node dissection in men with clinically localized prostate cancer. *Rev Urol* (2006) **8**: 112–9.
24. Rakow-Penner RA, White NS, Parsons JK, Choi HW, Liss MA, Kuperman JM, et al. Novel technique for characterizing prostate cancer utilizing MRI restriction spectrum imaging: proof of principle and initial clinical experience with extraprostatic extension. *Prostate Cancer Prostatic Dis* (2015). doi:10.1038/pcan.2014.50

**Conflict of Interest Statement:** The authors declare that the research was conducted in the absence of any commercial or financial relationships that could be construed as a potential conflict of interest.

Received: 05 November 2014; paper pending published: 18 December 2014; accepted: 29 January 2015; published online: 17 February 2015.

*Citation:* Liss MA, White NS, Parsons JK, Schenker-Ahmed NM, Rakow-Penner R, Kuperman JM, Bartsch H, Choi HW, Mattrey RF, Bradley WG, Shabaik A, Huang J, Margolis DJA, Raman SS, Marks LS, Kane CJ, Reiter RE, Dale AM and Karow DS (2015) MRI-derived restriction spectrum imaging cellularity index is associated with high grade prostate cancer on radical prostatectomy specimens. *Front. Oncol.* 5:30. doi: 10.3389/fonc.2015.00030

This article was submitted to Genitourinary Oncology, a section of the journal *Frontiers in Oncology*.

Copyright © 2015 Liss, White, Parsons, Schenker-Ahmed, Rakow-Penner, Kuperman, Bartsch, Choi, Mattrey, Bradley, Shabaik, Huang, Margolis, Raman, Marks, Kane, Reiter, Dale and Karow. This is an open-access article distributed under the terms of the Creative Commons Attribution License (CC BY). The use, distribution or reproduction in other forums is permitted, provided the original author(s) or licensor are credited and that the original publication in this journal is cited, in accordance with accepted academic practice. No use, distribution or reproduction is permitted which does not comply with these terms.

## ORIGINAL ARTICLE

# *In vivo* prostate cancer detection and grading using restriction spectrum imaging-MRI

KC McCammack<sup>1</sup>, CJ Kane<sup>2,7</sup>, JK Parsons<sup>2,7</sup>, NS White<sup>1</sup>, NM Schenker-Ahmed<sup>1</sup>, JM Kuperman<sup>1</sup>, H Bartsch<sup>1</sup>, RS Desikan<sup>1</sup>, RA Rakow-Penner<sup>1</sup>, D Adams<sup>3</sup>, MA Liss<sup>4</sup>, RF Mattrey<sup>1</sup>, WG Bradley<sup>1</sup>, DJA Margolis<sup>5</sup>, SS Raman<sup>5</sup>, A Shabaik<sup>3</sup>, AM Dale<sup>1,6</sup> and DS Karow<sup>1</sup>

**BACKGROUND:** Magnetic resonance imaging (MRI) is emerging as a robust, noninvasive method for detecting and characterizing prostate cancer (PCa), but limitations remain in its ability to distinguish cancerous from non-cancerous tissue. We evaluated the performance of a novel MRI technique, restriction spectrum imaging (RSI-MRI), to quantitatively detect and grade PCa compared with current standard-of-care MRI.

**METHODS:** In a retrospective evaluation of 33 patients with biopsy-proven PCa who underwent RSI-MRI and standard MRI before radical prostatectomy, receiver-operating characteristic (ROC) curves were performed for RSI-MRI and each quantitative MRI term, with area under the ROC curve (AUC) used to compare each term's ability to differentiate between PCa and normal prostate. Spearman rank-order correlations were performed to assess each term's ability to predict PCa grade in the radical prostatectomy specimens.

**RESULTS:** RSI-MRI demonstrated superior differentiation of PCa from normal tissue, with AUC of 0.94 and 0.85 for RSI-MRI and conventional diffusion MRI, respectively ( $P=0.04$ ). RSI-MRI also demonstrated superior performance in predicting PCa aggressiveness, with Spearman rank-order correlation coefficients of 0.53 ( $P=0.002$ ) and  $-0.42$  ( $P=0.01$ ) for RSI-MRI and conventional diffusion MRI, respectively, with tumor grade.

**CONCLUSIONS:** RSI-MRI significantly improves upon current noninvasive PCa imaging and may potentially enhance its diagnosis and characterization.

*Prostate Cancer and Prostatic Diseases* advance online publication, 12 January 2016; doi:10.1038/pcan.2015.61

## INTRODUCTION

Radiographic visualization of prostate tumors remains imperfect. Therefore, unlike other solid organ malignancies, definitive diagnosis still relies on systematic biopsy sampling of the entire gland, a procedure that carries risks of pain, bleeding and infection.<sup>1,2</sup> Improved imaging techniques that reliably detect prostate cancer (PCa) would allow for enhanced diagnosis, targeted prostate biopsies and improved clinical care.

Magnetic resonance imaging (MRI) demonstrates promise for PCa detection, staging and assessing disease aggressiveness. A multiparametric (MP) approach to MRI—consisting of diffusion-weighted imaging (DWI), dynamic contrast enhancement (DCE) and standard anatomic sequencing (T1/T2)—has produced the most reproducible results to date and serves as the standard of care for prostate imaging.<sup>3–6</sup> MP-MRI fused with ultrasound for targeting prostate biopsy preferentially detects high-grade PCa while minimizing the detection of low-risk disease.<sup>7,8</sup> These important data suggest targeted biopsy may represent the future standard of care for PCa diagnosis. However, data indicate that targeted biopsy relying on current standard of care prostate MRI fails to detect clinically significant PCa in a substantial number of cases.<sup>7,8</sup> Continued improvement of prostate MRI is necessary before the widespread acceptance of targeted techniques is achievable.

Restriction spectrum imaging-MRI (RSI-MRI) is a novel, advanced diffusion sequence designed to improve upon the strengths of conventional MRI while correcting its weaknesses. The goal of RSI-MRI is improved conspicuity of highly cellular tumors.<sup>9–12</sup> It is a multiple  $b$ -value, multidirectional diffusion technique, which—via modeling of water compartments in tissue made possible by obtaining an extended spectrum of diffusion images—theoretically focuses observed signals from intracellular, restricted water molecules of interest and attenuates signals from other water molecules that typically confound conventional DWI of the prostate.<sup>9,10</sup> By focusing on signal arising from intracellular water, the technique in effect images cellularity; highly cellular tumors are thus highlighted by this method. In addition, RSI-MRI corrects the often considerable distortion observed with conventional DWI methods, beneficial in the identification of tumor extension beyond the confines of the prostate.<sup>9,13</sup>

We hypothesized that RSI-MRI may be a more robust technique for detecting and assessing the aggressiveness of PCa than conventional MP-MRI. In a prior report, we suggested improved characterization of PCa aggressiveness by RSI-MRI.<sup>14</sup> In this study, our primary aim was rather to assess the ability of RSI-MRI compared with conventional MP-MRI to quantitatively differentiate between tumor and normal tissue. A secondary aim of the study was to again assess the ability of RSI-MRI to describe PCa

<sup>1</sup>Department of Radiology, University of California San Diego School of Medicine, San Diego, CA, USA; <sup>2</sup>Department of Urology, University of California San Diego School of Medicine, San Diego, CA, USA; <sup>3</sup>Department of Pathology, University of California San Diego School of Medicine, San Diego, CA, USA; <sup>4</sup>Department of Urology, University of Texas San Antonio School of Medicine, San Antonio, TX, USA; <sup>5</sup>Department of Radiology, University of California Los Angeles Geffen School of Medicine, Los Angeles, CA, USA and <sup>6</sup>Department of Neurosciences, University of California San Diego School of Medicine, San Diego, CA, USA. Correspondence: Dr DS Karow, Department of Radiology, University of California, San Diego, 200 W Arbor Dr, San Diego, CA 92103, USA. E-mail: dkarow@ucsd.edu

<sup>7</sup>These authors contributed equally to this work.

Received 18 July 2015; revised 19 November 2015; accepted 24 November 2015



**Table 1.** MRI sequence acquisition parameters

Sequence	Repetition time (ms)	Echo time (ms)	Field of view (mm)	Matrix	Section thickness (mm)	Flip angle (°)	No. of signals acquired
T2	2567–7367	80–90	200–260	384 × 192	3	90	1
DCE	4.484–4.648	2.1	200	256 × 168	3	30	1
DWI	3750	70.8–74.3	260	160 × 160	5	90	8
RSI <sup>a</sup>	9900	70–72	200–260	96 × 96	3	90	1

Abbreviations: DCE, dynamic contrast enhancement; DWI, diffusion-weighted imaging; MRI, magnetic resonance imaging; RSI, restriction spectrum imaging.

<sup>a</sup>RSI-MRI is performed at  $b$ -values of 0, 125, 375 and 1000 s mm<sup>-2</sup> with 6, 6 and 15 directions at each respective nonzero  $b$ -value.

aggressiveness, but in a completely non-overlapping cohort, without an endorectal coil and on a different imaging platform (GE rather than Siemens) to evaluate generalizability of the technique.

## MATERIALS AND METHODS

### Patients

The institutional review board approval was obtained for this retrospective study, with signed patient consent waived. Consent was not necessary as RSI-MRI has been integrated into the normal workflow and is performed on all patients undergoing prostate MRI at our institution. All patients who underwent MP-MRI with RSI-MRI performed within 6 months before radical prostatectomy with whole-mount pathology between September 2013 and December 2014 were screened. Required MP-MRI sequences included T1-weighted, T2-weighted, DCE and DWI (including ADC maps). In all, 34 patients fulfilled initial criteria, with one patient excluded from the study due to lack of an available conventional ADC map for the examination.

### MRI acquisition

All studies were performed on a 3.0-T GE Signa HDxt scanner (GE Medical Systems, Milwaukee, WI, USA) with a cardiac surface coil but without an endorectal coil. Glucagon was not administered to decrease rectal peristalsis and no bowel preparation was performed. The entire prostate was imaged, with axial slices oriented perpendicular to the rectal wall. The following conventional sequences were obtained: axial and coronal T2-weighted; axial T1-weighted; axial free-breathing DWI ( $b$ -values of 0 and 1000 s mm<sup>-2</sup>) and axial free-breathing DCE performed before, during and after single-dose injection of ~20 ml gadobenate dimeglumine (Bracco Imaging, Milan, Italy).

RSI-MRI was performed using spin echo, echo planar imaging at  $b$ -values of 0, 125, 375 and 1000 s mm<sup>-2</sup> with 6, 6 and 15 directions at each respective nonzero  $b$ -value. The  $b=0$  s mm<sup>-2</sup> images were performed with phase encoding in both the forward and reverse directions to correct for spatial distortion due to magnetic field inhomogeneity.<sup>15</sup> Additional specific sequence parameters are summarized in Table 1.

### Sample preparation

Whole-mount preparations are performed for all prostatectomies at our institution that have undergone preoperative MRI. After prostatectomy, each specimen was fixed in 10% neutral buffered formalin and then embedded in paraffin. Whole-mount histopathology was performed on 4-μm-thick sections stained with hematoxylin and eosin. A board-certified anatomic pathologist with over 24 years of experience evaluated the pathology, outlining the boundaries of each tumor and assigning a Gleason score (GS) to each identified tumor.

### Histologic–radiologic correlation

Dominant tumors at least 5 mm in diameter as outlined on transverse cut prostate sections by an expert anatomic pathologist (AS; greater than 10 years of specialty experience) were included. The highest GS tumor at least 5 mm in diameter was defined as the dominant tumor. Our pathologist was blinded to imaging results in all cases. For each defined tumor, a corresponding region of interest (ROI) was assigned by an experienced genitourinary radiologist (DK; greater than 3 years of subspecialty experience) on the axial T2-weighted image (Figure 1). In cases where the tumor was not clearly visible on the T2 images, locations were defined as best possible by using anatomic landmarks such as the urethra, ejaculatory ducts and surgical capsule. Each patient had one

tumor ROI included for analysis ( $n=33$ ). In addition to the tumor ROIs, the remaining normal peripheral zone (PZ) was also assigned as an ROI for each patient for comparison, also assigned by the experienced radiologist on the T2 images. These ROIs were then cross-referenced to the respective DCE images, ADC maps and RSI-MRI z-score maps (Figure 1). Two patients had PZ PCa involvement spanning the entirety of the gland, which accounts for the decreased number of control ROIs ( $n=31$ ). Total ROIs ( $n=64$ ) are summarized in Table 2.

### Quantitative image analyses

ADC maps were calculated from DWI images at  $b=0$  and 1000 s mm<sup>-2</sup> at the scanner console for each voxel of each slice of the prostate. Average voxel values were calculated for each defined ROI and included for analysis.

The Tofts two-compartment model was used in DCE image analysis to calculate the contrast agent transfer rate between blood and tissue ( $K^{trans}$ ), extravascular extracellular fractional volume ( $v_e$ ) and contrast backflux rate constant ( $k_{ep}$ ).<sup>16</sup> Respective maps were calculated using commercial software DynaCAD (Invivo, Gainesville, FL, USA) for each voxel of each slice of the prostate. Average voxel values were calculated for each defined ROI and included for analysis.

RSI-MRI cellularity maps (CMs) were reconstructed using data from all  $b$ -values, which were then standardized across all patients to obtain RSI-MRI z-score maps. RSI-MRI z-score maps were calculated by (1) measuring the mean and s.d. of normal prostate signal from the raw RSI-CM data of a representative normal population, (2) subtracting the measured mean value from each subject's CM and (3) dividing the result by the s.d. of measured normal prostate.

PIRADS, a reader-based qualitative standardized reporting system for MP-MRI, was not utilized in this study as this represented a quantitative analysis without reader assessment and scoring. No qualitative reports were used at any point during the study.

### Statistical analysis

The ability of each quantitative parameter to differentiate PCa from normal tissue was evaluated using receiver-operating characteristic (ROC) curves, formulated using maximum likelihood estimation. Area under the ROC curve (AUC) analysis was used as a general indicator of quality and was compared statistically between terms using DeLong's test and bootstrapping. RSI-MRI was compared with each individual MP-MRI term even though MP-MRI as a whole serves as the current standard of care, because MP-MRI interpretation of all components is a reader-based qualitative process, whereas this served by design as a quantitative study comparing RSI-MRI with each MP-MRI term objectively. The Spearman rank-order correlation coefficient ( $\rho$ ) was calculated for each quantitative term to evaluate its strength of association with post-prostatectomy GS. All tests were two-sided, with  $P < 0.05$  deemed to reflect statistical significance. All analyses were performed using R version 3.1.2 (The R Foundation for Statistical Computing, Vienna, Austria).

### Qualitative analysis

In a subset of the 33 patients in this study, initial tumor was discovered by MR-fused ultrasound-targeted biopsy rather than conventional biopsy. For purposes of showing the qualitative conspicuity of RSI-MRI over conventional DWI and perfusion imaging, tumor ROIs in the biopsy planning software DynaCad, UroNav (Invivo) are shown (Figure 2).

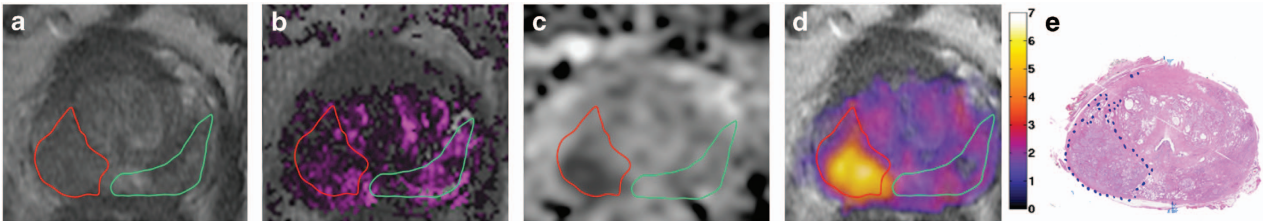


**Figure 1.** Example tumor (red) and normal peripheral zone (green) region of interest (ROI) assignment to the patient’s T2 image (a), subsequently coregistered to the  $K^{trans}$  map overlaid on T2 (b), conventional ADC map (c) and restriction spectrum imaging-magnetic resonance imaging (RSI-MRI) map overlaid on T2. The provided RSI-MRI color bar scale demonstrates corresponding z-score (d). ROI definitions were made on T2 images by an experienced radiologist based on the whole-mount hematoxylin and eosin section (e) tumor outlines provided by genitourinary pathology. Final pathology in this case demonstrated Gleason score 4+5 = 9.

Table 2. Characteristics of tumor and normal PZ ROIs							
Characteristic	GS 6	GS 7	GS 8	GS 9	GS 10	All PCa	Normal PZ
No. of ROIs	3	23	3	3	1	33	31
ROI size (mm <sup>2</sup> ) <sup>a</sup>	72 (83–124)	136 (43–846)	156 (82–260)	532 (88–749)	676	168 (43–846)	224 (46–610)

Abbreviations: GS, Gleason score; PCa, prostate cancer; PZ, peripheral zone; ROI, region of interest. <sup>a</sup>ROI size reported as mean values with respective ranges.

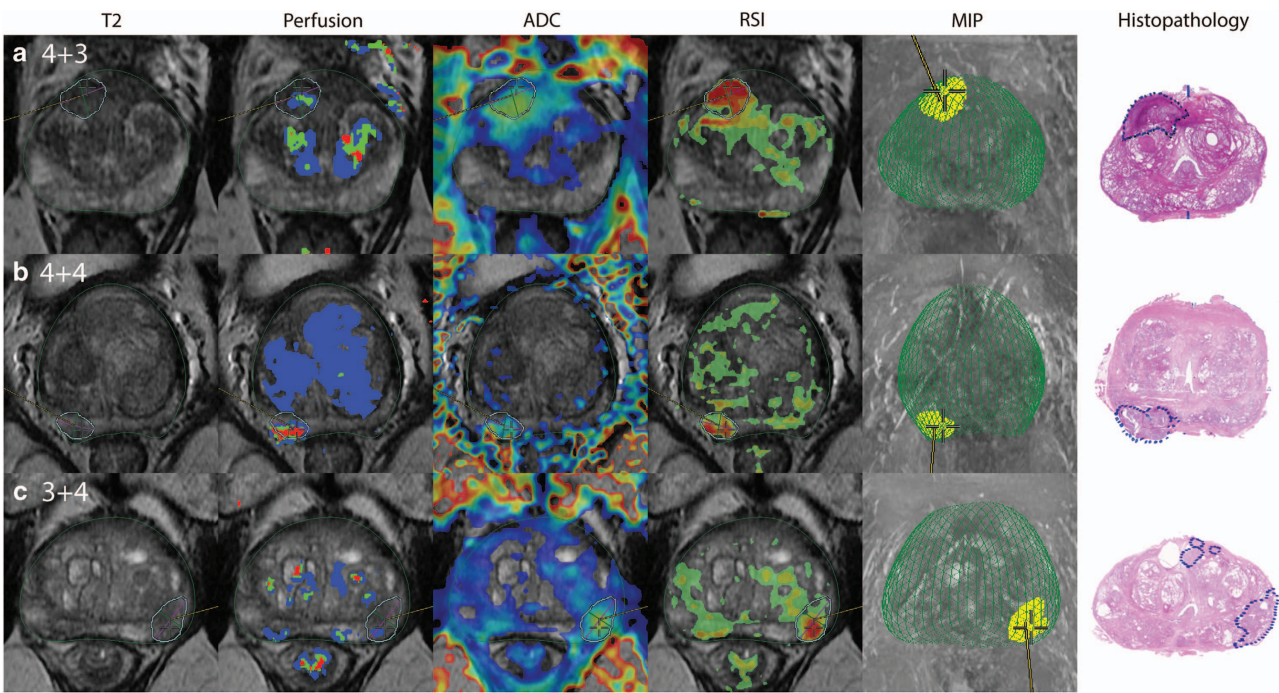


**Figure 2.** Conventional multiparametric-magnetic resonance imaging components and restriction spectrum imaging-magnetic resonance imaging (RSI-MRI) as used for targeting biopsy. (a) 4+3 Gleason score (GS) prostate cancer (PCa) in the right anterior mid central gland, (b) 4+4 GS PCa in the right posterior base peripheral zone, (c) 3+4 GS PCa in the left posterior mid peripheral zone. In these cases, RSI-MRI more conspicuously demarcates PCa for targeted biopsy than T2, dynamic contrast enhancement or conventional diffusion-weighted imaging techniques as confirmed by post-prostatectomy whole-mount pathology.

RESULTS

**Patient characteristics**

A total of 33 patients satisfied the inclusion criteria for this study. Mean patient age was 62.5 (range 48–75) years. Mean preoperative PSA concentration was 8.8 (range 1.1–28.0) ng ml<sup>−1</sup>. Mean time interval between MRI and prostatectomy was 48.9 (range 5–117) days. Pathological disease stage was most commonly pT2c

(N = 17), ranging from PT2a to PT3b. Additional patient characteristics are summarized in Table 3.

**Discrimination between PCa and normal prostate**

We assessed the ability of RSI-MRI to detect PCa tumors relative to conventional DWI and DCE methods. Figure 1 shows a representative case. The tumor ROI (red) and normal ROI (green) were

drawn on the T2-weighted imaging based on histopathology, and transposed to perfusion, ADC and RSI-MRI maps. RSI-MRI z-scores demonstrated the greatest single-term AUC of 0.94. Conventional ADC values demonstrated an AUC of 0.85, statistically inferior performance compared with RSI z-scores ( $P=0.04$ ). RSI-MRI z-scores also outperformed the DCE parameters of  $K^{\text{trans}}$  ( $P=0.03$ ),  $k_{\text{ep}}$  ( $P=0.007$ ) and  $v_e$  ( $P=0.02$ ). Maximum accuracy for RSI-MRI, ADC and  $K^{\text{trans}}$  was 87.5%, 79.7% and 78.1%, respectively. The ability of each quantitative term to discriminate between PCa and normal PZ tissue as evaluated by ROC curves is shown in Table 4 and Figure 3.

#### Correlation with GS

We observed a strong correlation with dominant tumor GS in the radical prostatectomy specimens for RSI-MRI ( $\rho=0.53$ ,  $P=0.002$ ), higher than that seen with conventional diffusion MRI ( $\rho=-0.42$ ,  $P=0.01$ ) and PSA ( $\rho=0.36$ ,  $P=0.04$ ) (Table 5). We found no significant correlation for  $K^{\text{trans}}$  ( $\rho=0.18$ ,  $P=0.30$ ),  $k_{\text{ep}}$  ( $\rho=0.18$ ,  $P=0.32$ ) or  $v_e$  ( $\rho=0.19$ ,  $P=0.30$ ; Table 5).

## DISCUSSION

Compared with conventional MRI, RSI-MRI demonstrated superior accuracy for discriminating between PCa and normal prostate tissue and better correlated with prostatectomy GS. We conclude that RSI-MRI significantly improves upon the clinical performance of conventional MRI for PCa detection, and offers promise as an

improved noninvasive biomarker for PCa grading. Another advantage is that RSI-MRI does not require an endorectal coil.

MRI fused with ultrasound for purposes of PCa-targeted biopsy is currently under investigation. It detects PCa missed by systematic biopsy, provides a greater PCa yield per core and preferentially identifies high-grade PCa.<sup>7,8,17,18</sup> In addition, it decreases the detection of clinically insignificant PCa.<sup>7,8</sup> Given these recent data, it appears targeted techniques likely represent the future standard of care. However, a limitation to this transition remains that, as currently practiced, targeted biopsy misses some high-grade, clinically significant PCa, which would be detected by traditional non-targeted systematic biopsy.<sup>7,8</sup> This is presumably a reflection of the known limitations in the current standard-of-care prostate MRI methodology. Advances in MRI performance likely offer the greatest opportunity to improve targeted biopsy, and RSI-MRI may represent an important step in this effort.

We qualitatively observe greater PCa conspicuity on RSI-MRI compared with standard-of-care MRI regularly and use these data to guide our biopsy targeting efforts more frequently than DCE or conventional DWI (Figure 2). A quantitative validation of this approach is now provided in this study. Specifically, in a group of patients with known PCa, ROC analyses demonstrate that RSI-MRI exhibits greater discrimination accuracy than other parameters included in standard-of-care MRI, with an AUC of 0.94. This figure is admittedly quite high in large part due to study design, which involved placing ROIs for analysis in areas of known PCa as guided by subsequent whole-mount pathology, even when prospective qualitative analysis by a radiologist may not identify disease. However, this is a design with precedent in the literature, which allows direct comparison of quantitative terms in a format impervious to reader error and potential bias, and our results with RSI-MRI are among the most impressive of those studies.<sup>3,4,19,20</sup> Although not performed at precisely the same  $b$ -values as RSI-MRI, conventional ADC values demonstrated reasonable discrimination, with an AUC similar to or better than other published data at 0.85, however this performance is statistically inferior to RSI-MRI.<sup>3,19,20</sup> Peritumoral edema and necrosis may negatively affect the ability of conventional DWI to localize PCa, as well as signal heterogeneity within normal prostatic tissue itself, leading to the inferior ROC performance, factors that should not as significantly affect RSI-MRI by design.<sup>10–12</sup> DCE parameters were also outperformed by RSI-MRI, with AUC figures in agreement with published data.<sup>3,4</sup> With the superior imaging performance of RSI-MRI, we expect improved targeted biopsy performance relative to prior studies and are currently evaluating our results relative to traditional non-targeted systematic biopsy in both screening and active surveillance populations.

ADC values are predictive of PCa aggressiveness on biopsy or prostatectomy GS.<sup>21–23</sup> A noninvasive imaging biomarker for disease aggressiveness would be valuable for prognostication. Our data support RSI-MRI as a superior imaging biomarker for PCa grading, outperforming DWI in this patient cohort at identical

**Table 3.** Comprehensive clinical patient characteristics

Characteristic	Average (range)
Age (years)	62.5 (48–75)
Preoperative PSA (ng ml <sup>-1</sup> )	8.8 (1.1–28.0)
Tumor volume (ml)	6.5 (0.3–41.8)
Prostate volume (ml)	45.6 (18.0–153.8)
BMI (kg/m <sup>2</sup> )	26.8 (20.7–32.6)
Clinical T stage	Number
T1c	21
T2a	9
T2b	2
T2c	1
Pathological T stage	Number
pT2a	2
pT2c	17
pT3a	12
pT3b	2

Abbreviation: BMI, body mass index.

**Table 4.** Effectiveness of quantitative imaging features in the differentiation of prostate cancer from normal gland

Test	AUC (%)	$p^a$	Maximum accuracy (%)	Cutoff value
RSI z-score	93.6 (87.6–99.7)	1	87.5	0.47
ADC values	84.8 (75.4–94.3)	0.04	79.7	1253 mm <sup>2</sup> s <sup>-1</sup>
$K^{\text{trans}}$	79.2 (67.7–90.6)	0.03	78.1	0.85 ml g <sup>-1</sup> min <sup>-1</sup>
$k_{\text{ep}}$	74.0 (61.6–86.4)	0.007	70.3	3.66 min <sup>-1</sup>
$v_e$	77.9 (66.8–89.1)	0.02	71.9	0.29 ml g <sup>-1</sup>

Abbreviation: AUC, area under the receiver-operating characteristic curve; MRI, magnetic resonance imaging; RSI, restriction spectrum imaging. <sup>a</sup>Each  $P$ -value compares the individual term AUC to RSI-MRI AUC.



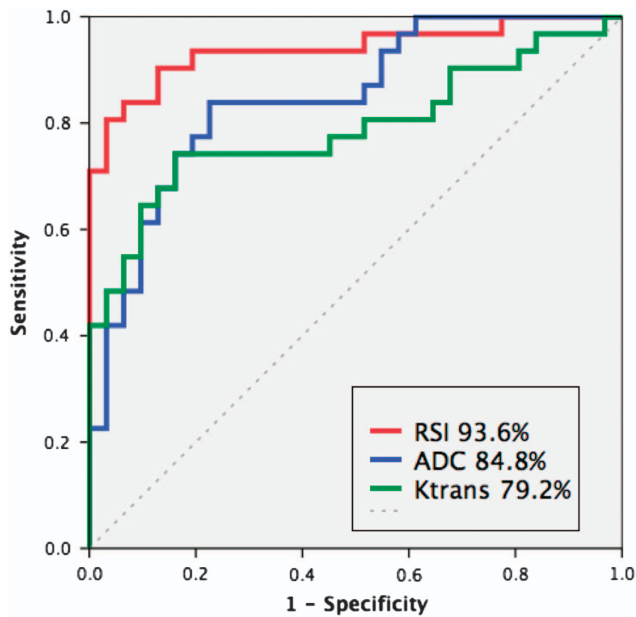


**Figure 3.** Receiver-operating characteristic (ROC) curves demonstrating performance of restriction spectrum imaging (RSI)-magnetic resonance imaging z-score, conventional ADC values and  $k_{\text{trans}}$  for the quantitative discrimination of prostate cancer from normal peripheral zone. Respective areas under the ROC curve are listed in the legend.

maximum  $b$ -value (Table 3). We have suggested this improved capacity of RSI-MRI over DWI previously, and the current data support that preliminary conclusion using data acquired on a different imaging platform (GE rather than Siemens), as well as without an endorectal coil.<sup>14</sup> These data support the performance of RSI-MRI as generalizable across different platforms and additionally addresses quantitative PCa discrimination by RSI-MRI, which we have not previously investigated in any population.

Equally important as improved PCa conspicuity is accuracy of tumor localization, with image distortion a particularly problematic challenge encountered with conventional DWI.<sup>15</sup> RSI-MRI employs spatial distortion correction using opposed phase-encoding polarities, allowing for efficient anatomic localization, an advance that has demonstrated promise for improved preoperative determination of extraprostatic extension of disease.<sup>9,13,15,24</sup> Although not specifically examined in this work, this spatial distortion correction may allow the use of the superior tumor conspicuity available with RSI-MRI for accurate targeted biopsy and/or treatment strategies, and these are currently under investigation by our group.

Finally, given the success of RSI-MRI for noninvasive tumor detection in the brain and now prostate, we are optimistic that this technique will be generalizable for the detection of other solid organ tumors. Recent work shows that two-thirds of cancers have no genetic or environmental predisposition.<sup>25</sup> This highlights the importance of noninvasive screening measures that can be performed rapidly and inexpensively. RSI-MRI can be performed in 5 min, does not require intravenous contrast and is non-radiation-based. A noninvasive imaging technique that can accurately detect, localize and grade tumors will serve an important diagnostic role but also may serve to guide biopsies and interventions. Further work will assess whether RSI-MRI is a useful biomarker for additional solid organ tumors.

One potential limitation of this study is the relatively small sample size. However, every patient had a prostatectomy sample available for comparison, and utilizing prostatectomy as the gold standard avoided the inaccuracies associated with systematic

**Table 5.** Spearman rank-order correlation with post-prostatectomy GS results

Test	$\rho$	P
RSI z-score	0.53	0.002
ADC values	-0.42	0.01
PSA	0.36	0.04
$k_{\text{trans}}$	0.18	0.30
$k_{\text{ep}}$	0.18	0.32
$v_e$	0.19	0.30

Abbreviations: GS, Gleason score; RSI, restriction spectrum imaging.

biopsy results.<sup>26–28</sup> A second potential limitation is that we compared PCa tumor ROIs only with normal PZ ROIs in this study. Central gland imaging is a known challenge with regards to PCa however, due to the known predominance of PCa in the PZ, we opted to focus on this location for the quantitative evaluation of RSI-MRI performance in the prostate.<sup>29–31</sup> In addition, most previously published quantitative studies focus on comparison with the normal PZ as well.<sup>3,6,19,20</sup> With increased sample size, dedicated central gland performance evaluation will be appropriate and we suspect RSI-MRI will lend itself particularly well in this effort due to its decreased vulnerability to background tissue heterogeneity resulting from the focus on signal arising from within individual cells. Third, the retrospective study design serves as a potential limitation. As a result of this design, some variation in time interval between imaging and prostatectomy is to be expected, which could conceivably be minimized in a prospective study design. Given the indolent progression of PCa, this is likely of minimal impact, if any. In addition, utilizing retrospective assignment of ROIs based on whole-mount pathology does not fully support the improved clinical utility of RSI-MRI over MP-MRI, and prospective reader-based blinded data evaluating this will be needed to evaluate for true clinical utility.

In summary, RSI-MRI shows promise as a noninvasive imaging PCa biomarker, with improved PCa discrimination relative to current standard-of-care conventional MRI terms, as well as more accurate assessment of disease aggressiveness. Our work additionally suggests that RSI-MRI, with its increased accuracy and characterization capabilities, may enable further optimization of image-guided biopsies.

## CONFLICT OF INTEREST

The authors declare no conflict of interest.

## ACKNOWLEDGEMENTS

This study was funded by grant R01EB000790; American Cancer Society, Institutional Research Grant Number 70-002; DoD, Prostate Cancer Research Program, Idea Development Award W81XWH-13-1-0391, #PC120532; National Science Foundation, Grant Number 1430082; UCSD Clinician Scientist Program; and General Electric, Investigator-Initiated Research Award BOK92325.

## REFERENCES

- 1 Chou R, Crosswell JM, Dana T, Bougatsos C, Blazina I, Fu R *et al*. Screening for prostate cancer: a review of the evidence for the U.S. Preventive Services Task Force. *Ann Intern Med* 2011; **155**: 762–771.
- 2 Moyer VA. Screening for prostate cancer: US Preventive Services Task Force recommendation statement. *Ann Intern Med* 2014; **157**: 120–134.
- 3 Langer DL, van der Kwast TH, Evans AJ, Trachtenberg J, Wilson BC, Haider MA. Prostate cancer detection with multi-parametric MRI: logistic regression analysis of quantitative T2, diffusion-weighted imaging, and dynamic contrast-enhanced MRI. *J Magn Reson Imaging* 2009; **30**: 327–334.
- 4 Engelbrecht M, Huisman H, Laheij R, Jager G, van Leenders G, Hulsbergen-Van De Kaa C *et al*. Discrimination of prostate cancer from normal

- peripheral zone and central gland tissue by using dynamic contrast-enhanced MR imaging. *Radiology* 2003; **229**: 248–254.
- 5 Kozlowski P, Chang SD, Jones EC, Berean KW, Chen H, Goldenberg SL. Combined diffusion-weighted and dynamic contrast-enhanced MRI for prostate cancer diagnosis—correlation with biopsy and histopathology. *J Magn Reson Imaging* 2006; **24**: 108–113.
  - 6 Turkbey B, Pinto PA, Mani H, Bernardo M, Pang Y, McKinney YL *et al*. Prostate cancer: value of multiparametric MR imaging at 3T for detection—histopathologic correlation. *Radiology* 2010; **255**: 89–99.
  - 7 Siddiqui MM, Rais-Bahrami S, Truong H, Stamatakis L, Vourganti S, Nix J *et al*. Magnetic resonance imaging/ultrasound-fusion biopsy significantly upgrades prostate cancer versus systematic 12-core transrectal ultrasound biopsy. *Eur Urol* 2013; **64**: 713–719.
  - 8 Siddiqui MM, Rais-Bahrami S, Turkbey B, George AK, Rothwax J, Shakir N *et al*. Comparison of MR/ultrasound fusion-guided biopsy with ultrasound-guided biopsy for the diagnosis of prostate cancer. *JAMA* 2015; **313**: 390–397.
  - 9 White NS, McDonald CR, Farid N, Kuperman J, Karow D, Schenker-Ahmed NM *et al*. Diffusion-weighted imaging in cancer: physical foundations and applications of restriction spectrum imaging. *Cancer Res* 2014; **74**: 4638–4652.
  - 10 White NS, Leergaard TB, D'Arceuil H, Bjaalie JG, Dale AM. Probing tissue microstructure with restriction spectrum imaging: Histological and theoretical validation. *Hum Brain Mapp* 2013; **34**: 327–346.
  - 11 Kothari P, White N, Farid N, Chung R, Kuperman J, Girard H *et al*. Longitudinal restriction spectrum imaging is resistant to pseudoresponse in patients with high-grade gliomas treated with bevacizumab. *AJNR Am J Neuroradiol* 2013; **34**: 1752–1757.
  - 12 White N, McDonald C, Farid N, Kuperman J, Kesari S, Dale A. Improved conspicuity and delineation of high-grade primary and metastatic brain tumors using “restriction spectrum imaging”: quantitative comparison with high B-value DWI and ADC. *AJNR Am J Neuroradiol* 2013; **34**: 958–964.
  - 13 Rakow-Penner R, White N, Parsons J, Choi H, Liss M, Kuperman J *et al*. Novel technique for characterizing prostate cancer utilizing MRI restriction spectrum imaging: proof of principle and initial clinical experience with extraprostatic extension. *Prostate Cancer Prostatic Dis* 2015; **18**: 81–85.
  - 14 Liss MA, White NS, Parsons JK, Schenker-Ahmed NM, Rakow-Penner R, Kuperman JM *et al*. MRI-derived restriction spectrum imaging cellularity index is associated with high grade prostate cancer on radical prostatectomy specimens. *Front Oncol* 2015; **5**: 1–8.
  - 15 Holland D, Kuperman JM, Dale AM. Efficient correction of inhomogeneous static magnetic field-induced distortion in Echo Planar Imaging. *Neuroimage* 2010; **50**: 175–183.
  - 16 Tofts P, Brix G, Buckley DL, Evelhoch JL, Henderson E, Knopp MV *et al*. Estimating kinetic parameters from dynamic contrast-enhanced T1-weighted MRI of a diffusible tracer: standardized quantities and symbols. *J Magn Reson Imaging* 1999; **10**: 223–232.
  - 17 Vourganti S, Rastinehad A, Yerram NK, Nix J, Volkin D, Hoang A *et al*. Multiparametric magnetic resonance imaging and ultrasound fusion biopsy detect prostate cancer in patients with prior negative transrectal ultrasound biopsies. *J Urol* 2012; **188**: 2152–2157.
  - 18 Sonn G a, Chang E, Natarajan S, Margolis DJ, Macairan M, Lieu P *et al*. Value of targeted prostate biopsy using magnetic resonance-ultrasound fusion in men with prior negative biopsy and elevated prostate-specific antigen. *Eur Urol* 2014; **65**: 809–815.
  - 19 Peng Y, Jiang Y, Yang C, Brown J, Antic T, Sethi I *et al*. Quantitative analysis of multiparametric prostate MR images: differentiation between prostate cancer and normal tissue and correlation with Gleason score—a computer-aided diagnosis development study. *Radiology* 2013; **267**: 787–796.
  - 20 Peng Y, Jiang Y, Antic T, Giger M, Eggener S, Oto A. Validation of quantitative analysis of multiparametric prostate MR images for prostate cancer detection and aggressiveness assessment: a cross-imager study. *Radiology* 2014; **271**: 461–471.
  - 21 Oto A, Yang C, Kayhan A, Tretiakova M, Antic T, Schmid-Tannwald C *et al*. Diffusion-weighted and dynamic contrast-enhanced MRI of prostate cancer: correlation of quantitative MR parameters with Gleason score and tumor angiogenesis. *AJR Am J Roentgenol* 2011; **197**: 1382–1390.
  - 22 Nagarajan R, Margolis D, Raman S, Sheng K, King C, Reiter R *et al*. Correlation of Gleason scores with diffusion-weighted imaging findings of prostate cancer. *Adv Urol* 2012; **2012**: 1–5.
  - 23 Bittencourt LK, Barentsz JO, de Miranda LC, Gasparetto EL. Prostate MRI: diffusion-weighted imaging at 1.5T correlates better with prostatectomy Gleason Grades than TRUS-guided biopsies in peripheral zone tumours. *Eur Radiol* 2012; **22**: 468–475.
  - 24 Rakow-Penner RA, White NS, Margolis DJ, Parsons JK, Schenker-Ahmed N, Kuperman JM *et al*. Prostate diffusion imaging with distortion correction. *Magn Reson Imaging* 2015; **33**: 1178–1181.
  - 25 Tomasetti C, Vogelstein B. Variation in cancer risk among tissues can be explained by the number of stem cell divisions. *Science* 2014; **347**: 78–81.
  - 26 Cohen MS, Hanley RS, Kurteva T, Ruthazer R, Silverman ML, Sorcini A *et al*. Comparing the Gleason prostate biopsy and Gleason prostatectomy grading system: the Lahey Clinic Medical Center experience and an international meta-analysis. *Eur Urol* 2008; **54**: 371–381.
  - 27 Kvåle R, Møller B, Wahlqvist R, Fosså SD, Berner A, Busch C *et al*. Concordance between Gleason scores of needle biopsies and radical prostatectomy specimens: a population-based study. *BJU Int* 2009; **103**: 1647–1654.
  - 28 Rajinikanth A, Manoharan M, Soloway CT, Civantos FJ, Soloway MS. Trends in Gleason score: concordance between biopsy and prostatectomy over 15 years. *Urology* 2008; **72**: 177–182.
  - 29 Oto A, Kayhan A, Jiang Y, Tretiakova M, Yang C, Antic T *et al*. Prostate cancer: differentiation of central gland cancer from benign prostatic hyperplasia by using diffusion-weighted and dynamic contrast-enhanced MR imaging. *Radiology* 2010; **257**: 715–723.
  - 30 Akin O, Sala E, Moskowitz CS, Kuroiwa K, Ishill NM, Pucar D *et al*. Transition zone prostate cancers: features, detection, localization, and staging at endorectal MR imaging. *Radiology* 2006; **239**: 784–792.
  - 31 Li H, Sugimura K, Kaji Y, Kitamura Y, Fujii M, Hara I *et al*. Conventional MRI capabilities in the diagnosis of prostate cancer in the transition zone. *AJR Am J Roentgenol* 2006; **186**: 729–742.



# Restriction spectrum imaging improves MRI-based prostate cancer detection

Kevin C. McCammack,<sup>1</sup> Natalie M. Schenker-Ahmed,<sup>1</sup> Nathan S. White,<sup>1</sup> Shaun R. Best,<sup>1</sup> Robert M. Marks,<sup>2</sup> Jared Heimbigner,<sup>2</sup> Christopher J. Kane,<sup>3</sup> J. Kellogg Parsons,<sup>3</sup> Joshua M. Kuperman,<sup>1</sup> Hauke Bartsch,<sup>1</sup> Rahul S. Desikan,<sup>1</sup> Rebecca A. Rakow-Penner,<sup>1</sup> Michael A. Liss,<sup>4</sup> Daniel J. A. Margolis,<sup>5</sup> Steven S. Raman,<sup>5</sup> Ahmed Shabaik,<sup>6</sup> Anders M. Dale,<sup>1,7</sup> David S. Karow<sup>1</sup>

<sup>1</sup>Department of Radiology, University of California San Diego School of Medicine, 200 W Arbor Dr, San Diego, CA 92103, USA

<sup>2</sup>Department of Radiology, Naval Medical Center San Diego, San Diego, USA

<sup>3</sup>Department of Urology, University of California San Diego School of Medicine, San Diego, USA

<sup>4</sup>Department of Urology, University of Texas San Antonio School of Medicine, San Antonio, USA

<sup>5</sup>Department of Radiology, University of California Los Angeles Geffen School of Medicine, Los Angeles, USA

<sup>6</sup>Department of Pathology, University of California San Diego School of Medicine, San Diego, USA

<sup>7</sup>Department of Neurosciences, University of California San Diego School of Medicine, San Diego, USA

## Abstract

**Purpose:** To compare the diagnostic performance of restriction spectrum imaging (RSI), with that of conventional multi-parametric (MP) magnetic resonance imaging (MRI) for prostate cancer (PCa) detection in a blinded reader-based format.

**Methods:** Three readers independently evaluated 100 patients (67 with proven PCa) who underwent MP-MRI and RSI within 6 months of systematic biopsy ( $N = 67$ ; 23 with targeting performed) or prostatectomy ( $N = 33$ ). Imaging was performed at 3 Tesla using a phased-array coil. Readers used a five-point scale estimating the likelihood of PCa present in each prostate sextant. Evaluation was performed in two separate sessions, first using conventional MP-MRI alone then immediately with MP-MRI and RSI in the same session. Four weeks later, another scoring session used RSI and T2-weighted imaging (T2WI) without conventional diffusion-weighted or dynamic contrast-enhanced imaging. Reader interpretations were then compared to prostatectomy data or biopsy results. Receiver operating characteristic curves were performed, with area under the curve (AUC) used to compare across groups.

**Results:** MP-MRI with RSI achieved higher AUCs compared to MP-MRI alone for identifying high-grade (Gleason score greater than or equal to  $4 + 3 = 7$ ) PCa (0.78 vs. 0.70 at the sextant level;  $P < 0.001$  and 0.85 vs. 0.79 at the hemigland level;  $P = 0.04$ ). RSI and T2WI alone achieved AUCs similar to MP-MRI for high-grade PCa (0.71 vs. 0.70 at the sextant level). With hemigland analysis, high-grade disease results were similar when comparing RSI + T2WI with MP-MRI, although with greater AUCs compared to the sextant analysis (0.80 vs. 0.79).

**Conclusion:** Including RSI with MP-MRI improves PCa detection compared to MP-MRI alone, and RSI with T2WI achieves similar PCa detection as MP-MRI.

**Key words:** Prostate MRI—Prostate cancer—Diffuse weighted imaging—Restriction spectrum imaging—Prostate diffusion imaging

**Electronic supplementary material** The online version of this article (doi:10.1007/s00261-016-0659-1) contains supplementary material, which is available to authorized users.

Correspondence to: David S. Karow; email: dkarow@ucsd.edu

Prostate cancer (PCa) is the most commonly diagnosed noncutaneous malignancy and second leading cause of cancer death for men in the United States [1]. Magnetic resonance imaging (MRI) has proven useful for PCa detection, localization, and staging, and most recently has demonstrated value for guiding prostate biopsy when fused with ultrasound [2–5]. Conventional multi-parametric (MP) MRI, including diffusion-weighted imaging

(DWI), dynamic contrast enhancement (DCE), and standard anatomic imaging consisting of T1- (T1WI) and T2-weighted imaging (T2WI) has produced the most consistent results to date and serves as the standard-of-care for in situ PCa imaging [2, 3, 6, 7]. However, improved PCa detection by MRI is the goal of considerable ongoing effort.

Conventional DWI is arguably the most important contributor of the individual MP-MRI components for PCa detection, outperforming standard anatomic imaging, and DCE methodologies [3, 7–12]. Diffusion techniques are particularly attractive because they are rapid and utilize inherent tissue contrast properties, not requiring intravenous gadolinium agents with their associated risk, cost, and inconvenience. However, conventional DWI is limited in many contexts commonly encountered in the prostate, including hemorrhage, infection, and inflammation. An additional significant limitation of conventional DWI is its frequent degradation by marked spatial distortion [13]. Improvements in DWI technique may substantially improve the clinical utility of PCa imaging.

Restriction spectrum imaging (RSI) [14] is an innovative, advanced diffusion sequence that aims to improve upon the strengths and address the shortcomings of conventional DWI in oncologic imaging [15, 16]. It uses the data obtained from an extended range of multiple  $b$  value, multidirectional diffusion images to model a distribution, or spectrum of isotropic and anisotropic water compartments in tissue. The spectrum parameters can then be used to isolate the signal contribution from intracellular restricted water molecules, while attenuating the signal contribution from the extracellular hindered and free water pools which typically confound conventional DWI [14–17]. The goal is improved conspicuity of highly cellular tumors, which has proven effective in the brain [16–19] and more recently the prostate, though these prior studies were limited by design which involved placement of regions of interest based on knowledge of tumor location [20, 21]. RSI additionally corrects for spatial distortion through acquiring  $b = 0$  images with both forward and reverse phase encoding polarities, and corrects for Eddy currents, allowing for more precise tumor localization and useful in the identification of extraprostatic extension of PCa [20, 22, 23].

In this study, we investigated the clinical efficacy of RSI for PCa detection, comparing it directly to current standard-of-care MP-MRI in a blinded reader-based format, which most accurately reflects the current practice model in most centers, to evaluate for true clinical utility of the technique.

## Methods

### Patients

Institutional review board approval was obtained for this retrospective study, with signed patient consent waived as

RSI has been integrated into the standard prostate MRI workflow at our institution as a diffusion tensor imaging product sequence-based technique with multiple  $b$  values, anteroposterior/posteroanterior distortion correction, and unique post-processing. We evaluated 111 patients with imaging consisting of MP-MRI with RSI performed within 6 months of either radical prostatectomy with whole mount pathology or systematic biopsy. The indications for MP-MRI in this patient population are summarized in Table 1. Forty-five patients had already had prior biopsy performed, with 40 returning results positive for PCa. Required pulse sequences included T1WI, T2WI, DCE, DWI (including ADC maps), and RSI. Eleven patients were excluded from the study due to lack of an available ADC map for the evaluation (Fig. 1).

### MRI acquisition

All studies were performed on a 3.0-T GE Signa HDxt scanner (GE Medical Systems, Milwaukee, WI) using a

**Table 1.** Imaging indications

Indication	Number
Surgical planning	34
Elevated PSA	33
Active surveillance	25
Targeted biopsy planning	11
Abnormal DRE	5
Other <sup>Ψ</sup>	3

<sup>Ψ</sup> Other causes include perineal pain after biopsy, recurrent prostatitis, and BPH

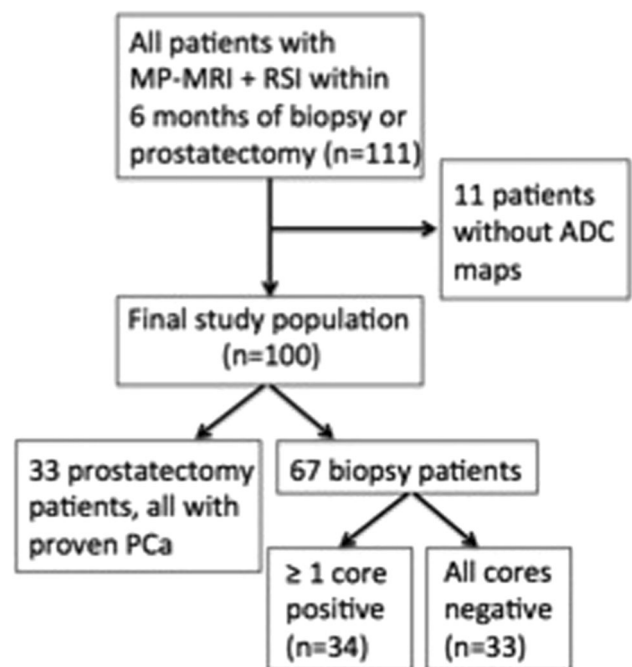


**Fig. 1.** Flowchart summarizes patient selection and tissue standard.

cardiac surface coil but without an endorectal coil. Glucagon is not administered at our center to decrease rectal peristalsis and no bowel preparation is performed. The entire prostate is imaged, with axial slices oriented perpendicular to the rectal wall. The following conventional sequences were obtained: axial and coronal T2WI, axial T1WI, axial free-breathing DWI ( $b$  values of 0 and 1000 s/mm<sup>2</sup>), and axial free-breathing DCE performed before, during, and after single-dose injection of approximately 20 mL gadobenate dimeglumine (Multihance, Bracco Imaging, Milan, Italy). DCE is performed with 32 output temporal phases at approximately 8 s per phase for a total scan time of approximately 4 min with no injection delay.

RSI was performed using spin echo, echo planar imaging at  $b$  values of 0, 125, 375, and 1000 s/mm<sup>2</sup> with 6, 6, and 15 directions at each respective nonzero  $b$  value. The  $b = 0$  s/mm<sup>2</sup> images were performed with phase encoding in both the forward and reverse directions to correct for spatial distortion due to magnetic field inhomogeneity. The sequence takes approximately 5 min to perform on the HDxt system. RSI cellularity maps (CMs) were derived using the signal fraction of the restricted isotropic component of the diffusion spectrum [16] and coregistered to axial T2WI images (Fig. 2). RSI-CMs were reconstructed using data from all  $b$  values, which were then standardized across all patients to obtain RSI-MRI  $z$  score maps. RSI  $z$  score maps were

calculated by (1) measuring the mean and standard deviation of normal prostate signal from the raw RSI-CM data of a representative normal population (three normal subjects, as determined by radiologist interpretation (DSK), which were separate from the current study population), (2) subtracting the measured mean value from each subject's CM, and (3) dividing the result by the standard deviation of measured normal prostate. Additional specific sequence parameters are summarized in Table 2.

### Image interpretation

Three radiologists (SRB, a body imaging fellow with dedicated interest in prostate imaging and over 1 year of experience interpreting prostate MRI; JH, a body imaging fellowship-trained attending radiologist with over 2 years of experience interpreting prostate MRI; RMM, a body imaging fellowship-trained attending radiologist with over 3 years of experience interpreting prostate MRI) who were each blinded to clinical and laboratory data evaluated MRI cases independently. Overall, three different sets of imaging data were evaluated in two sessions. During the initial session, cases were first scored using just MP-MRI (consisting of T1WI and T2WI, DWI with ADC, and DCE), then immediately thereafter scored again using RSI in addition to MP-

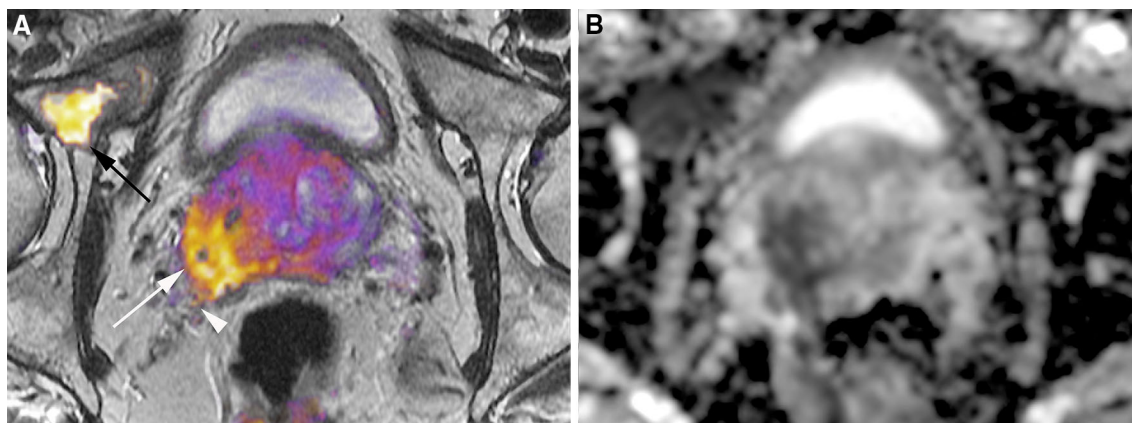


**Fig. 2.** **A** RSI overlaid on T2WI and **B** conventional ADC map in a 64-year-old male with a prostate-specific antigen level of 25.3 ng/mL demonstrates biopsy proven Gleason 4 + 5 involving the right base peripheral zone (*white arrow*) with right-sided extraprostatic extension (*white arrowhead*)

and osseous metastatic disease to the right anterior acetabular column (*black arrow*). The ADC map demonstrates marked distortion in the anteroposterior direction, making detection of extraprostatic disease difficult, and demonstrates relatively poor conspicuity of the right acetabular metastasis.

**Table 2.** Imaging parameters

Sequence	Repetition time (ms)	Echo time (ms)	Field of view (mm)	Matrix	Section thickness (mm)	Flip angle (°)	No. of signals acquired
T2WI	4517	90	200–260	384 × 192	3	90	1
DCE	4.5	2.1	200–240	256 × 168	3	30	1
DWI	3750	74	260–360	160 × 160	5	90	8
RSI*	9900	72	200–260	96 × 96	3	90	1

\* RSI is performed at  $b$ -values of 0, 125, 375, and 1000 s/mm<sup>2</sup> with 6, 6, and 15 directions at each respective non-zero  $b$ -value

MRI. After a 4 week wash-out period, the cases were then scored using just RSI and T2WI. Readers were instructed to interpret RSI-CMs as suspicious for PCa when focal/asymmetrically increased signal was identified in the PZ, or within the TZ in areas not clearly corresponding to benign prostatic hyperplasia nodules as suggested by the presence of a hypointense capsule on T2WI. The sextant model was utilized (right and left base, midgland, and apex), with a 5-point Likert scale assigned for each sextant (1, definitely absent; 2, probably absent; 3, indeterminate; 4, probably present; and 5, definitely present). For the purposes of subsequent statistical analyses, reader scores of 4 and 5 were considered positive for PCa by imaging as per precedent established by prior similarly structured studies [7, 24]. Prostate Imaging and Data Reporting System version 2 (PIRADSv2) was not employed.

### *Reference standard*

Thirty-three patients underwent prostatectomy. After prostatectomy, each specimen was fixed in 10% neutral-buffered formalin and then embedded in paraffin. Whole mount histopathology was performed on 4- $\mu$ m-thick sections stained with hematoxylin and eosin (H&E). A board-certified anatomic pathologist with over 24 years of prostate expertise evaluated the pathology, outlining the boundaries of each tumor and assigning a Gleason score (GS) to each identified tumor.

Biopsy results were used as the reference standard in 67 patients. Twelve cores are routinely performed at our institution via the extended sextant model, and are then interpreted by experienced genitourinary pathologists, assigning GS to each core as well as a percentage core involvement with PCa, when present. While biopsy targeting planning served as the study indication for 11 of our patients, overall biopsy targeting was performed in 23 patients for whom biopsy served as the reference standard. Otherwise, systematic biopsy core locations were defined by the urologist at the time of sampling, and were unable to be definitively correlated with MRI imaging.

For this evaluation, distinction was made between high and low/intermediate grade cancer, as per precedent established by prior Standards of Reporting for MRI-targeted Biopsy Studies working group recommendations [4, 5, 25]. Specifically, GS greater than or equal to  $4 + 3 = 7$  was considered as high grade.

### *Statistical analysis*

Receiver operating characteristic (ROC) curves were created using maximum-likelihood estimation for each reader and each of the three imaging sets. Analysis was first performed on the sextant level overall, and then using the prostatectomy cases alone. Additionally, be-

cause one-to-one matching was not performed for the whole mount pathology, and because prostate midgland definition can vary from practitioner to practitioner, a sidedness evaluation was undertaken to maximize the PCa detection rate. Area under the ROC curve (AUC) was used as a general indicator of quality and compared across data sets using the nonparametric method proposed by Obuchowski [26]. Comprehensive comparisons were made by covarying for reader. Sensitivity, specificity, positive predictive value, and negative predictive value on the sextant level were calculated. For all tests,  $P$  values of  $<0.05$  were denoted as statistical significance.

Inter-reader agreement analysis was performed using kappa statistics with quadratic weights. Cohen's Kappa was performed to evaluate agreement between any two readers, while the adapted Fleiss Kappa was used to assess agreement between all three readers simultaneously. Kappa values of 0–0.20 denoted slight agreement, 0.21–0.40 fair agreement, 0.41–0.60 moderate agreement, 0.61–0.80 substantial agreement, and 0.81–1 almost perfect agreement [27].

All statistical analyses were performed using R version 3.1.2 software (The R Foundation for Statistical Computing, Vienna, Austria).

## **Results**

### *Histopathology*

PCa was present in 67 of 100 patients (67%) and 176 of 600 sextants (29%). High-grade PCa specifically was identified in 30 of 100 patients (30%) and 88 of 600 sextants (15%). Additional GS information as well as clinical data are summarized in Table 3. Representative cases of imaging with subsequent histopathology are demonstrated in Fig. 3.

### *Diagnostic performance*

For the identification of all PCa as well as specifically high-grade PCa, MP-MRI in combination with RSI produced superior performance (Table 4). On the sextant level, MP-MRI with RSI produced a combined AUC of 0.66 for all PCa and 0.78 for specifically high-grade PCa. This improved capability of MP-MRI plus RSI over MP-MRI alone was statistically significant for all three readers for all PCa ( $P < 0.001$ ) and specifically high-grade PCa ( $P < 0.001$ ). Hemigland analysis produced similar results, with superior performance of MP-MRI plus RSI relative to MP-MRI alone for all PCa ( $P = 0.001$ ) and specifically high-grade PCa (AUC of 0.85 vs. 0.79;  $P = 0.04$ ).

RSI and T2WI alone on the sextant level produced statistically equivalent performance to MP-MRI for readers 1 and 3 for both all PCa and high-grade PCa. For reader 2, RSI and T2WI outperformed MP-MRI on the sextant level ( $P < 0.001$  for all PCa and  $P = 0.03$



**Table 3.** Patient characteristics

Characteristic	Mean (range)
Age (years)	63.5 (45–80)
PSA (ng/mL)	7.2 (1.1–29.2)
Prostate Volume (mL)	47.3 (16.2–153.8)
Time between MRI and biopsy or prostatectomy (days)	53.4 (5–135)
Biopsy Gleason score	Number
Benign	33
3 + 3	15
3 + 4	10
4 + 3	2
≥4 + 3	7
Prostatectomy Gleason score	
3 + 3	3
3 + 4	9
4 + 3	14
≥4 + 3	7
Prostatectomy pathologic T stage	
pT2a	2
pT2c	17
pT3a	12
pT3b	2

for high-grade PCa) (Table 4). Hemigland analysis demonstrates similar AUCs when comparing RSI and T2WI with MP-MRI (e.g., AUCs of 0.80 vs. 0.79;  $P = 0.77$  for high-grade disease), with reader 2 trending toward superior performance using RSI + T2WI (Table 4).

Sensitivity, specificity, positive and negative predictive value figures on the sextant basis are listed in the supplementary Table.

*Inter-reader agreement*

By accepted criteria, there was moderate agreement for all imaging protocols for all comparisons between any two readers as well as between all three simultaneously [27]. There was a trend toward increased inter-reader agreement with incorporation of RSI, with the greatest agreement utilizing RSI and T2WI alone. Between readers 1 and 2, actually there was substantial agreement with RSI and T2WI alone, the only comparison to reach that level within this data set (Table 5).

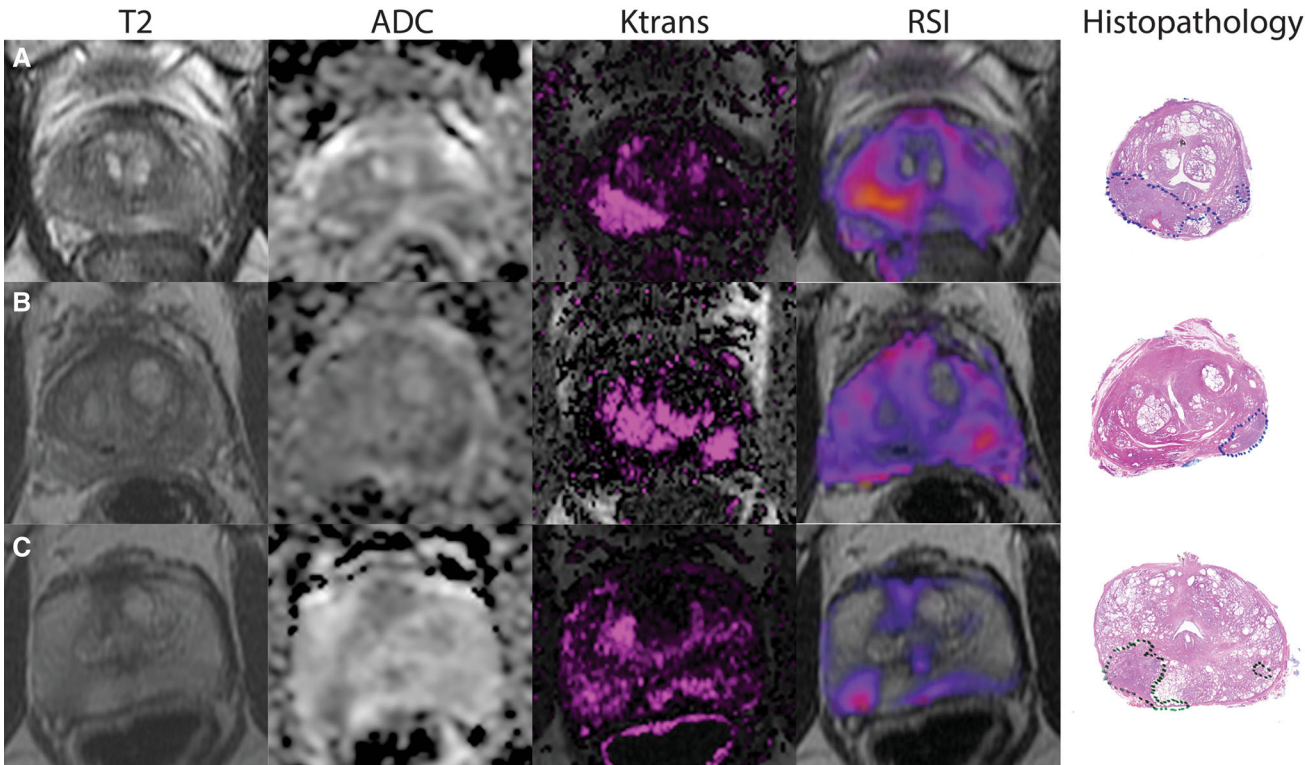


**Fig. 3.** Axial T2WI, ADC map,  $K^{trans}$  maps, and RSI color maps, with subsequent whole mount histopathology in **A** a 58-year-old male with prostate-specific antigen level of 8.2 ng/mL with Gleason Score 4 + 3 disease in the right apex peripheral zone, **B** a 69-year-old male with prostate-specific antigen level of 4.9 ng/mL with Gleason Score 4 + 3 disease in the left base

peripheral zone, and **C** a 71-year-old male with prostate-specific antigen level of 6.2 ng/mL with Gleason Score 4 + 3 disease in the right mid peripheral zone. Each case demonstrates increased qualitative conspicuity of prostate cancer on RSI relative to MP-MRI.



**Table 4.** ROC analysis

Reader	MP-MRI	MP-MRI + RSI	$P^*$	RSI	$P^\Phi$
Sextant-based analysis					
All PCa					
1	0.63 (0.65)	0.68 (0.70)	<0.001	0.61 (0.60)	0.39
2	0.58 (0.60)	0.64 (0.68)	<0.001	0.63 (0.64)	<0.001
3	0.61 (0.63)	0.66 (0.68)	0.001	0.58 (0.58)	0.08
Combined	0.61 (0.63)	0.66 (0.69)	<0.001	0.61 (0.61)	0.85
High-grade PCa					
1	0.71 (0.69)	0.80 (0.79)	0.01	0.73 (0.69)	0.62
2	0.66 (0.66)	0.75 (0.77)	0.01	0.74 (0.72)	0.03
3	0.72 (0.72)	0.79 (0.78)	0.04	0.66 (0.62)	0.08
Combined	0.70 (0.69)	0.78 (0.78)	<0.001	0.71 (0.68)	0.62
Hemigland-based analysis					
All PCa					
1	0.70 (0.71)	0.71 (0.72)	0.47	0.65 (0.67)	0.13
2	0.63 (0.65)	0.69 (0.71)	<0.001	0.67 (0.69)	0.10
3	0.64 (0.66)	0.69 (0.69)	0.09	0.62 (0.63)	0.48
Combined	0.66 (0.68)	0.70 (0.71)	0.001	0.65 (0.66)	0.64
High-grade PCa					
1	0.82 (0.81)	0.85 (0.84)	0.4	0.82 (0.80)	0.97
2	0.75 (0.75)	0.83 (0.85)	0.1	0.82 (0.79)	0.14
3	0.80 (0.79)	0.85 (0.85)	0.22	0.76 (0.77)	0.45
Combined	0.79 (0.78)	0.85 (0.85)	0.04	0.80 (0.79)	0.77

Data presented are area under the ROC curves (AUC). Data in parentheses represent calculations based on prostatectomy cases alone

\* Represents comparison between MP-MRI and MP-MRI plus RSI AUC

$^\Phi$  Represents comparison between MP-MRI and RSI AUC

**Table 5.** Inter-reader agreement kappa scores for all possible reader combinations

Reader combination	1,2	2,3	1,3	1,2,3
Protocol				
MP-MRI	0.54	0.52	0.51	0.51
MP-MRI + RSI	0.57	0.53	0.52	0.52
RSI	0.62	0.55	0.55	0.57

## Discussion

Our data indicate that RSI combined with MP-MRI improves PCa detection, and that RSI + T2WI may perform similarly to or better than MP-MRI. Additionally, our study suggests that RSI may promote greater consensus in reader interpretation, with inter-reader agreement increasing when RSI is combined with MP-MRI and most uniform when readers use RSI alone, though admittedly the effect was modest in this study.

Prior studies have supported the importance of diffusion techniques, particularly conventional DWI, in MP-MRI for PCa detection, and localization [3, 7–12]. With more robust gradient performance made possible by improved scanner technologies, advanced diffusion techniques have been devised and methodologies such as diffusion kurtosis imaging have been evaluated for PCa identification with mixed results to date [28–30]. RSI is an advanced diffusion technique that employs multiple  $b$  values and multiple directions to focus recorded signal from the isotropic, truly restricted pool of water molecules in tissue. RSI can be acquired on any 3 Tesla

imaging platform and the post-processing performed on any independent workstation via readily available post-processing software. The goal is improved conspicuity of cellular lesions, originally devised for the evaluation of brain tumors [16–19], and applied more recently with promise in the prostate [20, 21]. This study is the first reader-based evaluation of RSI for PCa detection and localization.

RSI may provide a viable diagnostic MRI option to those patients for whom MP-MRI is not possible, most notably those with contraindications to intravenous contrast material due to renal insufficiency or allergy, or those unable to tolerate prolonged scan times. The sequence is achieved without the need for any intravenous gadolinium administration and requires only up to 5 min depending on scanner type and gradient performance. These data also raise the possibility of evaluating RSI + T2WI in isolation as a short, targeted screening exam in at risk individuals. Our data suggest these patients will have the benefit of comparable reader interpretation performance using RSI as those with the more exhaustive MP-MRI.

Reader interpretations also demonstrated less variability when RSI was incorporated with MP-MRI, and inter-reader agreement was in fact the highest when RSI was evaluated in isolation. This suggests that in addition to the improved PCa detection allowed by RSI, it also provides greater consistency between readers perhaps through relative ease of interpretation. MP-MRI involves numerous sequences and its interpretation is relatively labor intensive; it is possible that through processing these data involved, readers become more

prone to variability in their analyses. RSI color maps are simply overlaid on T2WI and require much less reader effort due to the clarity and relative paucity of images compared to MP-MRI, at a comparable rate of performance.

Prior reader-based evaluations of current standard-of-care MP-MRI for PCa detection demonstrate AUC figures ranging from as low as 0.67 to as high as 0.90 [6, 7, 31]. Our results fall within this range, albeit toward the lower end. This may be due to the fact that our cases represent predominantly low-grade PCa, which is known to be detected less accurately than high-grade PCa by MRI [24]. Additionally, approximately two-thirds of our cases utilized biopsy results as the tissue standard which would be expected to adversely impact our calculations due to known inaccuracies associated with biopsy compared to prostatectomy [32–34]. Further, one-to-one matching between imaging, biopsy, and prostatectomy was not performed, which may allow variations in anatomic definition between practitioners to adversely affect our figures. Specifically, while definitions of apex, midgland, and base may differ between imaging interpretation, biopsy location definition based on ultrasound, and pathologic evaluation of prostatectomy specimens, sidedness would be expected to remain constant. Hemigland analysis performed to address this possibility did in fact increase our AUC calculations more toward published numbers [6, 7, 31]. Lastly, our readers are at the early stages of their careers, with a maximum of 3 years of dedicated experience, whereas prior studies utilized more senior readers [6, 7, 31]. While this may adversely impact our AUC calculations, the demonstrated efficacy of RSI in relatively naïve readers may actually serve as a study strength, supporting the generalizability of this technique to a wide audience. It is important to note, however, that this study was not designed to compare with prior published AUC data, but rather to directly compare the performance of RSI to MP-MRI. We contend the above factors are effectively controlled for across the different imaging protocols in this study, as the same tissue standard and readers were used throughout. Further, the same trends hold with the data stratified between patients with biopsy results vs. those with whole mount pathology.

Our study has possible limitations in addition to those already discussed above. First, we did not differentiate between PZ and TZ PCa in this study as systematic biopsies at our institution do not routinely differentiate between these regions. Given that two-thirds of our cases relied upon biopsy tissue for analysis, we were limited in our ability to distinguish between PZ and TZ PCa in this population. It would be useful to evaluate the performance characteristics of RSI relative to MP-MRI in both the PZ and TZ in the future. TZ PCa imaging is a known challenge confronting MP-MRI, and we would expect RSI to perform well in comparison due to its decreased

vulnerability to background tissue heterogeneity by theoretically focusing on signal arising from within cells themselves. Second, due to the retrospective study design, there was some inevitable variation between MRI and the acquisition of the tissue standard for comparison that could likely be minimized in a prospective design. Given the indolent progression of PCa, this is likely of minimal impact. Finally, no cost analysis was performed to evaluate the impact of implementation of this technology.

In summary, RSI shows promise for PCa detection and localization, statistically improving the ability of readers to localize disease when used in combination with MP-MRI. Further, RSI and T2WI in isolation allows performance comparable to MP-MRI, which may allow adequate imaging in patients unable to receive intravenous contrast material, those unable to tolerate long imaging times, or as a potential surrogate for MP-MRI in specific clinical situations.

**Acknowledgments.** This study was supported by NIH Grant R01EB000790, American Cancer Society, Institutional Research Grant Number 70-002, Department of Defense Prostate Cancer Research Program, Idea Development Award W81XWH-13-1-0391#PC120532, National Science Foundation Grant Number 1430082, and General Electric Investigator Initiated Research Award BOK92325.

#### *Compliance with ethical standards*

**Conflict of Interest** All authors declared that they have no conflict of interest.

**Disclaimer** The views expressed in this presentation are those of the authors and do not necessarily reflect the official policy or position of the Department of the Navy, Department of Defense, or the United States Government. The authors are military service members. This work was prepared as part of official duties. Title 17 U.S.C. 105 provides that ‘Copyright protection under this title is not available for any work of the United States Government.’

**Ethical Approval** All procedures performed in studies involving human participants were in accordance with the ethical standards of the institutional and/or national research committee and with the 1964 Helsinki declaration and its later amendments or comparable ethical standards.

**Funding** The authors were funded by R01EB000790, American Cancer Society, Institutional Research Grant Number 70-002; DoD, Prostate Cancer Research Program; Idea Development Award W81XWH-13-1-0391, #PC120532; National Science Foundation, Grant Number 1430082; UCSD Clinician Scientist Program; and General Electric, Investigator Initiated Research Award BOK92325.

**Informed Consent** Signed informed consent was waived by our Institutional Review Board as RSI has been integrated into the standard prostate MRI workflow at our institution as a diffusion tensor imaging product sequence-based technique with multiple *b* values, anteroposterior/posteroanterior distortion correction, and unique post-processing.

#### **References**

1. American Cancer Society (2013) *Cancer facts and figures*. Atlanta: American Cancer Society

2. Turkbey B, Pinto PA, Mani H, et al. (2010) Prostate cancer: value of multiparametric MR imaging at 3T for detection—histopathologic correlation. *Radiology* 255:89–99
3. Isebaert S, Van den Bergh L, Haustermans K, et al. (2013) Multiparametric MRI for prostate cancer localization in correlation to whole-mount histopathology. *J Magn Reson Imaging* 37:1392–1401. doi:[10.1002/jmri.23938](https://doi.org/10.1002/jmri.23938)
4. Siddiqui MM, Rais-Bahrami S, Turkbey B, et al. (2015) Comparison of MR/ultrasound fusion-guided biopsy with ultrasound-guided biopsy for the diagnosis of prostate cancer. *JAMA* 313:390–397. doi:[10.1001/jama.2014.17942](https://doi.org/10.1001/jama.2014.17942)
5. Siddiqui MM, Rais-Bahrami S, Truong H, et al. (2013) Magnetic resonance imaging/ultrasound-fusion biopsy significantly upgrades prostate cancer versus systematic 12-core transrectal ultrasound biopsy. *Eur Urol* 64:713–719. doi:[10.1016/j.eururo.2013.05.059](https://doi.org/10.1016/j.eururo.2013.05.059)
6. Kitajima K, Kaji Y, Fukabori Y, et al. (2010) Prostate cancer detection with 3 T MRI: comparison of diffusion-weighted imaging and dynamic contrast-enhanced MRI in combination with T2-weighted imaging. *J Magn Reson Imaging* 31:625–631. doi:[10.1002/jmri.22075](https://doi.org/10.1002/jmri.22075)
7. Donati OF, Jung SI, Vargas HA, et al. (2013) Multiparametric prostate MR imaging with T2-weighted, diffusion-weighted, and dynamic contrast-enhanced sequences: are all pulse sequences necessary to detect locally recurrent prostate cancer after radiation therapy? *Radiology* 268:440–450. doi:[10.1148/radiol.13122149/-/DC1](https://doi.org/10.1148/radiol.13122149/-/DC1)
8. Tan CH, Wei W, Johnson V, Kundra V (2012) Diffusion-weighted MRI in the detection of prostate cancer: meta-analysis. *AJR Am J Roentgenol* 199:822–829. doi:[10.2214/AJR.11.7805](https://doi.org/10.2214/AJR.11.7805)
9. Soylu FN, Peng Y, Jiang Y, et al. (2013) Seminal vesicle invasion in prostate cancer: evaluation by using multiparametric endorectal MR imaging. *Radiology* 267:797–806. doi:[10.1148/radiol.13121319/-/DC1](https://doi.org/10.1148/radiol.13121319/-/DC1)
10. Langer DL, van der Kwast TH, Evans AJ, et al. (2009) Prostate cancer detection with multi-parametric MRI: logistic regression analysis of quantitative T2, diffusion-weighted imaging, and dynamic contrast-enhanced MRI. *J Magn Reson Imaging* 30:327–334. doi:[10.1002/jmri.21824](https://doi.org/10.1002/jmri.21824)
11. Peng Y, Jiang Y, Yang C, et al. (2013) Quantitative analysis of multiparametric prostate MR images: differentiation between prostate cancer and normal tissue and correlation with Gleason score—a computer-aided diagnosis development study. *Radiology* 267:787–796
12. Peng Y, Jiang Y, Antic T, et al. (2014) Validation of quantitative analysis of multiparametric prostate MR images for prostate cancer detection and aggressiveness assessment: a cross-imager study. *Radiology* 271:461–471
13. Donato F, Costa DN, Yuan Q, et al. (2014) Geometric distortion in diffusion-weighted MR imaging of the prostate-contributing factors and strategies for improvement. *Acad Radiol* 21:817–823. doi:[10.1016/j.acra.2014.02.001](https://doi.org/10.1016/j.acra.2014.02.001)
14. White NS, Leergaard TB, D'Arceuil H, Bjaalie JG, Dale AM (2013) Probing tissue microstructure with restriction spectrum imaging: histological and theoretical validation. *Hum Brain Mapp* 34:327–346. doi:[10.1002/hbm.21454](https://doi.org/10.1002/hbm.21454)
15. White NS, McDonald CR, Farid N, et al. (2014) Diffusion-weighted imaging in cancer: physical foundations and applications of restriction spectrum imaging. *Cancer Res* 74:4638–4652. doi:[10.1158/0008-5472.CAN-13-3534](https://doi.org/10.1158/0008-5472.CAN-13-3534)
16. White N, McDonald C, Farid N, et al. (2013) Improved conspicuity and delineation of high-grade primary and metastatic brain tumors using “restriction spectrum imaging”: quantitative comparison with high B-value DWI and ADC. *AJNR Am J Neuroradiol* 34:958–964
17. McDonald C, White N, Farid N, et al. (2013) Recovery of white matter tracts in regions of peritumoral FLAIR hyperintensity with use of restriction spectrum imaging. *AJNR Am J Neuroradiol* 34:1157–1163. doi:[10.3174/ajnr.A3372](https://doi.org/10.3174/ajnr.A3372)
18. Kothari P, White N, Farid N, et al. (2013) Longitudinal restriction spectrum imaging is resistant to pseudoresponse in patients with high-grade gliomas treated with bevacizumab. *AJNR Am J Neuroradiol* 34:1752–1757
19. Farid N, Almeida-Freitas DB, White NS, et al. (2013) Restriction-spectrum imaging of bevacizumab-related necrosis in a patient with GBM. *Front Oncol* 30:1–5. doi:[10.3389/fonc.2013.00258](https://doi.org/10.3389/fonc.2013.00258)
20. Rakow-Penner R, White N, Parsons J, et al. (2015) Novel technique for characterizing prostate cancer utilizing MRI restriction spectrum imaging: proof of principle and initial clinical experience with extraprostatic extension. *Prostate Cancer Prostatic Dis* 18:1–5. doi:[10.1038/pcan.2014.50](https://doi.org/10.1038/pcan.2014.50)
21. Liss MA, White NS, Parsons JK, et al. (2015) MRI-derived restriction spectrum imaging cellularity index is associated with high grade prostate cancer on radical prostatectomy specimens. *Front Oncol* 5:1–8. doi:[10.3389/fonc.2015.00030](https://doi.org/10.3389/fonc.2015.00030)
22. Rakow-Penner RA, White NS, Margolis DJ, et al. (2015) Prostate diffusion imaging with distortion correction. *Magn Reson Imaging* 33:1178–1181. doi:[10.1016/j.mri.2015.07.006](https://doi.org/10.1016/j.mri.2015.07.006)
23. Holland D, Kuperman JM, Dale AM (2010) Efficient correction of inhomogeneous static magnetic field-induced distortion in echo planar imaging. *Neuroimage* 50:175–183. doi:[10.1016/j.neuroimage.2009.11.044](https://doi.org/10.1016/j.neuroimage.2009.11.044)
24. Vargas HA, Akin O, Shukla-Dave A, et al. (2012) Performance characteristics of MR imaging in the evaluation of clinically low-risk prostate cancer: a prospective study. *Radiology* 265:478–487
25. Moore CM, Kasivisvanathan V, Eggener S, et al. (2013) Standards of reporting for MRI-targeted biopsy studies (START) of the prostate: recommendations from an International Working Group. *Eur Urol* 64:544–552. doi:[10.1016/j.eururo.2013.03.030](https://doi.org/10.1016/j.eururo.2013.03.030)
26. Obuchowski N (1997) Nonparametric analysis of clustered ROC curve data. *Biometrics* 53:567–578
27. Landis J, Koch G (1977) The measurement of observer agreement for categorical data. *Biometrics* 33:159–174
28. Tamura C, Shinmoto H, Soga S, et al. (2014) Diffusion kurtosis imaging study of prostate cancer: preliminary findings. *J Magn Reson Imaging* 40:723–729. doi:[10.1002/jmri.24379](https://doi.org/10.1002/jmri.24379)
29. Roethke MC, Kuder TA, Kuru TH, et al. (2015) Evaluation of diffusion kurtosis imaging versus standard diffusion imaging for detection and grading of peripheral zone prostate cancer. *Investig Radiol* 50:483–489
30. Suo S, Chen X, Wu L, et al. (2014) Non-Gaussian water diffusion kurtosis imaging of prostate cancer. *Magn Reson Imaging* 32:421–427. doi:[10.1016/j.mri.2014.01.015](https://doi.org/10.1016/j.mri.2014.01.015)
31. Vargas HA, Akin O, Franiel T, et al. (2011) Diffusion-weighted endorectal MR imaging at 3 T for prostate cancer: tumor detection and assessment of aggressiveness. *Radiology* 259:775–784
32. Cohen MS, Hanley RS, Kurteva T, et al. (2008) Comparing the Gleason prostate biopsy and Gleason prostatectomy grading system: the Lahey Clinic Medical Center experience and an international meta-analysis. *Eur Urol* 54:371–381. doi:[10.1016/j.eururo.2008.03.049](https://doi.org/10.1016/j.eururo.2008.03.049)
33. Kvåle R, Møller B, Wahlqvist R, et al. (2009) Concordance between Gleason scores of needle biopsies and radical prostatectomy specimens: a population-based study. *BJU Int* 103:1647–1654. doi:[10.1111/j.1464-410X.2008.08255.x](https://doi.org/10.1111/j.1464-410X.2008.08255.x)
34. Rajinikanth A, Manoharan M, Soloway CT, Civantos FJ, Soloway MS (2008) Trends in Gleason score: concordance between biopsy and prostatectomy over 15 years. *Urology* 72:177–182. doi:[10.1016/j.urolgy.2007.10.022](https://doi.org/10.1016/j.urolgy.2007.10.022)

# Voxel Level Radiologic–Pathologic Validation of Restriction Spectrum Imaging Cellularity Index with Gleason Grade in Prostate Cancer

Ghiam Yamin<sup>1</sup>, Natalie M. Schenker-Ahmed<sup>1</sup>, Ahmed Shabaik<sup>2</sup>, Dennis Adams<sup>2</sup>, Hauke Bartsch<sup>1</sup>, Joshua Kuperman<sup>1</sup>, Nathan S. White<sup>1</sup>, Rebecca A. Rakow-Penner<sup>1</sup>, Kevin McCammack<sup>1</sup>, J. Kellogg Parsons<sup>3</sup>, Christopher J. Kane<sup>3</sup>, Anders M. Dale<sup>1,4</sup>, and David S. Karow<sup>1</sup>

## Abstract

**Purpose:** Restriction spectrum imaging (RSI-MRI), an advanced diffusion imaging technique, can potentially circumvent current limitations in tumor conspicuity, *in vivo* characterization, and location demonstrated by multiparametric magnetic resonance imaging (MP-MRI) techniques in prostate cancer detection. Prior reports show that the quantitative signal derived from RSI-MRI, the cellularity index, is associated with aggressive prostate cancer as measured by Gleason grade (GG). We evaluated the reliability of RSI-MRI to predict variance with GG at the voxel-level within clinically demarcated prostate cancer regions.

**Experimental Design:** Ten cases were processed using whole mount sectioning after radical prostatectomy. Regions of tumor were identified by an uropathologist. Stained prostate sections were scanned at high resolution (75  $\mu\text{m}/\text{pixel}$ ). A grid of tiles corresponding to voxel dimensions was graded using the GG system. RSI-MRI cellularity index was calculated from presurgical prostate MR scans and presented as normalized z-score

maps. In total, 2,795 tiles were analyzed and compared with RSI-MRI cellularity.

**Results:** RSI-MRI cellularity index was found to distinguish between prostate cancer and benign tumor ( $t = 25.48$ ,  $P < 0.00001$ ). Significant differences were also found between benign tissue and prostate cancer classified as low-grade ( $\text{GG} = 3$ ;  $t = 11.56$ ,  $P < 0.001$ ) or high-grade ( $\text{GG} \geq 4$ ;  $t = 24.03$ ,  $P < 0.001$ ). Furthermore, RSI-MRI differentiated between low and high-grade prostate cancer ( $t = 3.23$ ;  $P = 0.003$ ).

**Conclusions:** Building on our previous findings of correlation between GG and the RSI-MRI among whole tumors, our current study reveals a similar correlation at voxel resolution within tumors. Because it can detect variations in tumor grade with voxel-level precision, RSI-MRI may become an option for planning targeted procedures where identifying the area with the most aggressive disease is important. *Clin Cancer Res*; 22(11): 2668–74. ©2016 AACR.

## Introduction

Prostate cancer is the most common noncutaneous cancer and the second leading cause of cancer-related death in U.S. men (1). Most prostate cancers are adenocarcinomas (95%) that develop from prostatic gland secretory luminal cells; approximately 70% arise in the peripheral zone (2, 3), approximately 20%–25% arise in the transition zone (3, 4), and approximately 8% arise in the central zone (3). Randomized trials have confirmed the efficacy of prostate-specific antigen

(PSA) population screening to diminish prostate cancer mortality (5). However, aggressive population screening with PSA increases the detection of both lethal and nonlethal cancers, which can promote overdiagnosis and overtreatment of nonlethal cancers. Decreasing prostate cancer mortality, while minimizing the potential morbidities of overdiagnosis and overtreatment, requires refined approaches to screening and diagnosis using novel, noninvasive biomarkers to differentiate indolent from clinically significant disease.

Multiparametric magnetic resonance imaging (MP-MRI) is a rapidly evolving noninvasive diagnostic tool that has been used to complement other emerging biomarkers in the screening, staging, monitoring, and treatment of prostate cancer (6). However, prostate MRI is confounded by variable sensitivity (36%–100%) and specificity (64%–95%), which curtails its clinical utility (7, 8). Diffusion weighted imaging (DWI), an advanced MRI modality, detects the impeded diffusivity of water in the intra- and extracellular compartments and has shown correlation with prostate cancer. However, DWI is limited by magnetic field inhomogeneity and high false-positive rates from inflammation, hemorrhage, or benign nodules in the transitional zone, which limit tumor conspicuity and location (9).

Restriction spectrum imaging (RSI-MRI) is an advanced imaging technique that shows improved conspicuity and differentiation of solid tumors compared with traditional

<sup>1</sup>Department of Radiology, University of California San Diego School of Medicine, San Diego, California. <sup>2</sup>Department of Pathology, University of California San Diego School of Medicine, San Diego, California. <sup>3</sup>Department of Surgery, University of California San Diego School of Medicine, San Diego, California. <sup>4</sup>Department of Neurosciences, University of California, San Diego, La Jolla, California.

**Note:** Supplementary data for this article are available at Clinical Cancer Research Online (<http://clincancerres.aacrjournals.org/>).

G. Yamin and N.M. Schenker-Ahmed contributed equally to this article.

**Corresponding Author:** David S. Karow, University of California, San Diego, 200 W Arbor Dr, #8756, San Diego, CA 92103. Phone: 619-543-3534; Fax: 619-543-3746; E-mail: [dkarow@ucsd.edu](mailto:dkarow@ucsd.edu)

doi: 10.1158/1078-0432.CCR-15-2429

©2016 American Association for Cancer Research.



### Translational Relevance

Current multiparametric magnetic resonance imaging (MP-MRI) techniques for detecting prostate cancer are limited with respect to tumor conspicuity assessment, *in vivo* characterization, and localization. We have demonstrated that a novel diffusion-based MRI technique, restriction spectrum imaging (RSI-MRI), differentiates among benign, low-grade, and high-grade prostate cancer at a voxel-level resolution. Use of an RSI-MRI index to differentiate between clinically relevant low- and high-grade categories of tumor prostate cancer aggressiveness may help improve and refine diagnosis and staging of prostate cancer. In addition, because it can detect intratumor variation, RSI-MRI may have particular relevance for the planning targeted therapies such as radiation seed therapy placement, magnetic resonance (MR)-guided focused ultrasound surgery, and MR-guided targeted biopsy.

DWI methods (10, 11). The RSI-MRI method can differentiate hindered versus restricted diffusion, thought to correspond to the extracellular and intracellular water compartments, respectively (12). RSI-MRI demonstrates improved signal-to-noise in tumor detection and exhibits reduced spatial distortion. We previously reported that the RSI-MRI cellularity index is associated with the detection of aggressive prostate cancer as defined by GG (13), and RSI-MRI provides improved sensitivity in the detection of extraprostatic extension of prostate cancer compared with standard MRI (14). To account for tumor grade heterogeneity within and between tumors, we sought to analyze histopathologic whole mount (WM) prostate cancer section at the voxel level. We hypothesized that pathology grading at this level of resolution would provide a more accurate representation of the intratumor variability that may be masked within an overall grade assigned to large tumor regions of interest (ROI). Here, we report the correlation of voxel-level Gleason graded prostate cancer specimens with RSI-MRI and discuss possible diagnostic and prognostic information gained from such analyses.

## Materials and Methods

### RSI

All patients in this Institutional review board–approved study were previously diagnosed with prostate cancer status after ultrasound-guided transrectal biopsy. Prior to radical prostatectomy, a pelvic MRI was performed to aid in surgical planning. Patients were scanned using a 3.0-T SignaHDxt MRI Scanner (General Electric) and a cardiac coil; no endorectal coil was used. The entire prostate was imaged, with axial slices oriented perpendicular to the rectal wall. T2-weighted images were acquired using a fast spin echo protocol with 3.0 mm contiguous slices. The RSI-MRI protocol parameters included *b*-values of 0, 125 (6 unique directions), 375 (6 unique directions), and 1,000 (15 unique directions) s/mm<sup>2</sup>. The RSI-MRI protocol increased the total duration of the MRI scan time by 5 minutes. Additional details of the pulse sequence parameters can be found in Supplementary Table S1. RSI-MRI maps were reconstructed on the basis of all *b*-values and standardized across the sample to produce the *z*-score cellularity map. Specifically, *z*-score cellularity maps were produced using

mean and SDs of normal prostate signal from the raw RSI-MRI maps in the benign tissue in the patient population, subtracting the mean value from an individual subjects' RSI-MRI cellularity map, and dividing by the benign prostate SD. Corrections for spatial distortion due magnetic field inhomogeneity in echo planar imaging were accomplished with an alternating phase-encode technique (15). After correction for spatial distortion, RSI-MRI maps were coregistered to the T2 images.

### Digital histopathology and scoring

In general, the radical prostatectomy cases were consecutive surgeries; however, some cases were excluded because of significant artifacts in the histology, which would have made coregistration nearly impossible. Status post–radical prostatectomy, WM histopathology was performed on 5- $\mu$ m thick sections. Each hematoxylin and eosin (H&E)-stained histopathologic section was reviewed by a board-certified surgical pathologist (A. Sha-baik), who demarcated ROIs corresponding to tumor. The H&E digital images were acquired with a Keyence BZ-X710 All-in-one fluorescence microscope (Osaka) using transmitted light with a CFI Plan Apo  $\lambda$  10 $\times$  objective lens. To image the entire tissue section, the perimeter of the stained tissue was marked using low magnification (2 $\times$ ), and then automatically acquired with the 10 $\times$  objective. The microscope automatically focused each image tile of the mosaic. Exposure time and white balance were calculated automatically by the system. All scans were acquired at high resolution (0.75488  $\mu$ m/pixel). Tiles representing the entire image were then reconstructed into a "digital prostate map" interface and tumor ROIs overlaid with an alphanumeric grid containing tiles corresponding to voxel dimensions as shown in Fig. 1 and 2.

GG is the gold standard for grading prostate cancer aggressiveness (16–18), and is used to categorize prostate tissue based on histologic patterns. Tissue is given a grade from 1–5, with larger numbers typically indicating more aggressive cancer, characterized by poorly differentiated tissue, and, generally, a worse prognosis. Each tile in the overlaid alphanumeric grid was assessed for primary GG. Scoring for the current study focused on the primary grade that covered greater than 51% of the tile area, despite presence of other secondary grades that were higher or lower. For example, if 60% of the tile represented GG 4 but the rest was GG 5 (traditionally assigned a 4 + 5 Gleason score pattern), the final GG used for that tile in this study would be GG 4. Following current practice, only tiles with tissue of grades 3–5 were assigned a score; other tiles were scored as benign. A score of 0 was used to represent a benign area. Scored digital tiles were reviewed for accuracy by the same uropathologist who reviewed the H&E-stained histopathologic slide. A recent similarly conceptualized scoring framework, based on a five-grade group system founded on Gleason score, has shown improved risk stratification compared with the modern Gleason scoring system (17).

### Registration of RSI-MRI with histopathology

A radiologist with experience in prostate cancer MR imaging (D.S. Karow) selected the slice from the T2 MRI series that corresponded most closely to the plane of the histopathology section. To correct for deformation of the 2D slice that may have occurred during histologic processing, the Control Point Selection Tool in MATLAB (Release 2010b, The MathWorks,



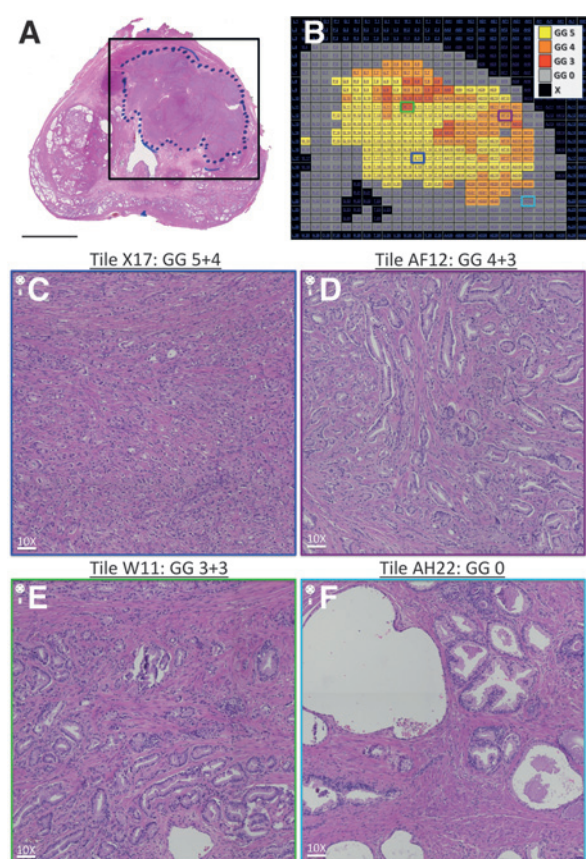


**Figure 1.**

"Digital prostate map" histopathologic section and example grid overlay. A, H&E-stained WM histopathologic prostate with a black box surrounding tumor ROI that represents the boundaries of a grid for sectioning the tumor area into voxel-sized tiles for grading purposes. Scale bar, 1 cm. B, H&E-stained WM histopathologic prostate section reconstructed into a "digital prostate map" interface online. Alphanumeric grid represents the outlined box in A surrounding the tumor ROI. Gleason grade is coded by color as defined by the key. C, representative tile (X17), showing Gleason grade 5+4 = 9 tumor architecture at 10 $\times$  magnification. Scale bar, 75.5  $\mu$ m. D, representative tile (AF12) showing Gleason grade 4+3 = 7 tumor architecture at 10 $\times$  magnification. Scale bar, 75.5  $\mu$ m. E, representative tile (W11), showing Gleason grade 3+3 = 6 tumor architecture at 10 $\times$  magnification. Scale bar, 75.5  $\mu$ m. F, representative tile (AH22), showing benign architecture at 10 $\times$  magnification. Scale bar, 75.5  $\mu$ m.

Inc.) was used to affine transform the selected T2 MRI slice to the shape and dimension of the histopathology section. The same transformation was applied to the registered RSI-MRI cellularity maps (Fig. 2). Anatomical landmarks, including the prostate shape, position of the urethra, and prominent benign prostatic hyperplasia nodules, were used to align the T2 MRI image as much as possible to the whole-mount sections. The Euclidean distance between transformed points and target points was calculated. The average registration error across all 10 subjects was 1.84  $\mu$ m.

#### Statistical analysis

Linear mixed-effect with a random effect (19) of subject was used to determine the effectiveness of RSI-MRI in detecting tumor aggressiveness, by comparing benign tissue to increasingly aggres-

sive tissue [benign vs. low-grade prostate cancer (Gleason 3) vs. high-grade prostate cancer (Gleason 4 and Gleason 5)]. *Post hoc* multiple comparison *t* tests (20) were used to assess RSI-MRI's ability to differentiate between normal prostate tissue and different levels of tumor aggressiveness (benign vs. low-grade prostate cancer and benign vs. high-grade prostate cancer) and between tumor grades (low-grade prostate cancer vs. high-grade prostate cancer). Statistical significance,  $P < 0.05$ , was determined using the software program R (21). The data were then plotted using SigmaPlot 12.5 (Systat Software Inc.).

## Results

Ten patients, representing a range of tumor aggressiveness, who were evaluated with a preoperative MRI and RSI-MRI underwent radical prostatectomy and underwent surgery between March 2014 to December 2014 with WM specimens (Table 1). T2-weighted MRI images and RSI-MRI cellularity maps were coregistered with the WM prostate histopathologic section as depicted in four cases (Fig. 2). The 10 WM prostate cancer cases encompassed 17 tumor ROIs. Two patients had two distinct tumor ROIs, one patient had three distinct tumors ROIs, and another patient had four distinct tumor ROIs within one specimen. All patients with  $\leq 2$  ROIs had concordant tumors. Tumor ROIs were overlaid with an alphanumeric grid (Fig. 1), with the size of each square of the grid corresponding to the voxel dimensions used for acquisition of the RSI-MRI. We analyzed 2,795 total squares of WM prostate H&E-stained sections, of which 1,573 and 1,222 (Gleason 3: 267; Gleason 4: 392; Gleason 5: 563) comprised benign and tumor tissue, respectively.

RSI-MRI data for both normal and tumor regions were normally distributed. The mean cellularity index in prostate cancer was 1.81 (SEM = 0.05) and in benign tissue was  $-0.32$  (SEM = 0.03). A linear mixed-effect with a random effect (19) of subject was employed to determine the association of RSI-MRI cellularity index with prostate cancer (benign vs. low-grade prostate cancer vs. high-grade prostate cancer; Table 2). RSI-MRI cellularity index distinguished benign from increasingly malignant prostate cancer ( $P < 1 \times 10^{-5}$ ; Table 2). Both low- and high-grade prostate cancer showed significant differences in RSI-MRI signal compared with benign tissue (both  $P < 0.001$ ; Table 3). Furthermore, significant difference in the RSI-MRI signal between pathologic categories, namely between low- and high-grade prostate cancer, was observed ( $P = 0.003$ ; Table 3). Of note, we observed a trend of higher mean RSI-MRI cellularity with increasing grade (Gleason 3–5) versus benign tissue (Fig. 3). By leaving out either individual voxels or individual subjects, we conducted leave-one-out analyses, and in each case recalculated the model and predicted the left out RSI-MRI values using the new model. The resulting root mean squared errors from this analysis were 1.425 and 1.618 for leaving out voxels and subjects, respectively.

## Discussion

We analyzed voxel-level Gleason-graded histopathologic samples in comparison with RSI-MRI cellularity indices obtained from presurgical *in vivo* MR scans. The data from the current study build on our previous findings of correlation between GG and the RSI-MRI cellularity index at the tumor

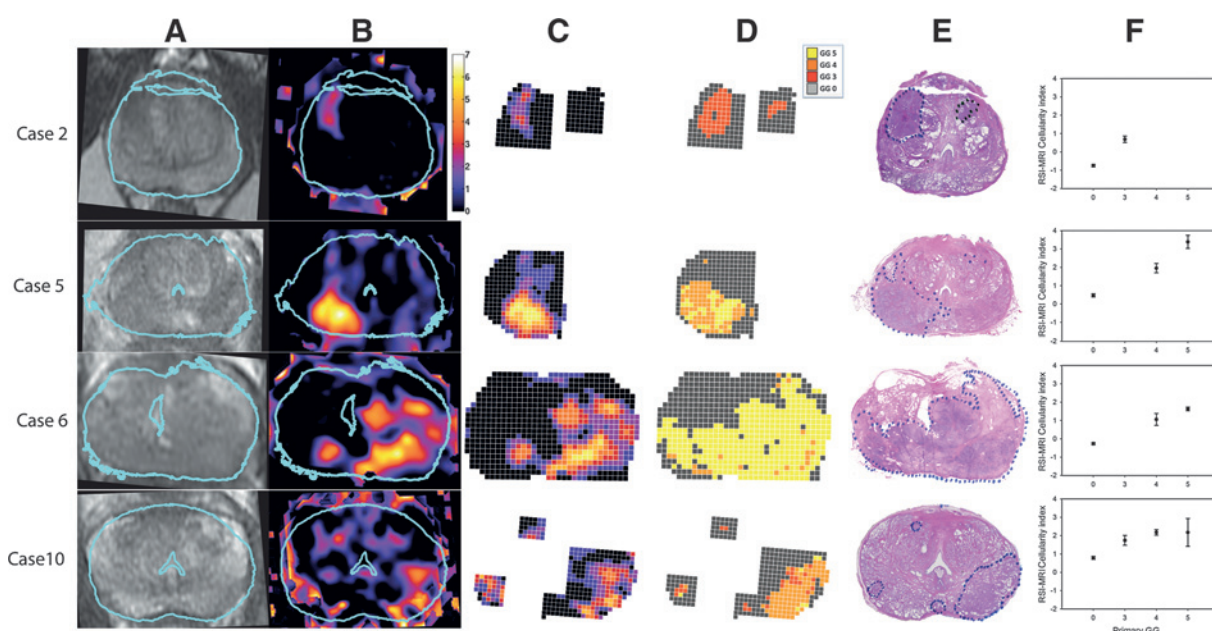


**Figure 2.**

T2, RSI-MRI, GG, and H&E: Cases 2, 5, 6, and 10. A, T2-weighted MR images, after in-plane affine transformation to correspond to the histopathology slides, RSI-MRI color coded cellularity maps (B), "Digital prostate map" grid overlay color-coded for RSI-MRI cellularity index (C), "Digital prostate map" grid overlay color-coded for Gleason grade (D), H&E-stained WM histopathologic prostate section with tumor area(s) outlined (E), plots for each case of the mean RSI-MRI signal corresponding to each histologic GG based on voxel-level analysis (F). Error bars, SEM. Blue outline in A and B indicates the correspondence of the histopathology slide to the MR image.

level in a sample that included the 10 patients in the current study (22) and reveal a correlation between the same parameters at the voxel level, demonstrating the ability of the RSI-MRI cellularity index to detect variation of GG within a single tumor.

MP-MRI is currently regarded as the standard-of-care noninvasive imaging biomarker for diagnosing and staging prostate cancer, despite its variable reliability in providing accurate diagnosis. The RSI-MRI method overcomes the limitations of DWI in MP-MRI by minimizing the extracellular diffusivity (or hindered component) seen in conventional DWI and capitalizing on the intracellular signal diffusivity (or restricted component) to detect regions of high cellularity, which can be associated with increased tumor burden (13, 14). RSI-MRI presents several advancements to currently implemented MP-MRI tumor imaging, including improved signal-to-noise in tumor detection and reduced spatial distortion.

RSI-MRI is designed to optimize the signal from the restricted intracellular water compartment, which is increased in tumor cells (12). Although GG is not a direct measure of cellularity, it is qualitatively based on architectural features that may indirectly relate to cellularity. Therefore, we expect the RSI-MRI cellularity index to correlate with tumor aggressiveness as measured by pathologic grade or GG. Novel to the traditional method of Gleason reporting and its application to radiologic-pathologic correlation with RSI-MRI, is our use of WM histopathologic sections scored at the voxel level. Traditionally, the pathologist highlights a tumor ROI and reports a general score for that area. In fact, this methodological approach was used recently to demonstrate that RSI-MRI detects increasingly aggressive prostate cancer, as defined by Gleason scores (13). We performed voxel-level pathologic grading with the rationale

that pathologic assessment at this level of resolution is a more accurate representation of tumor variability. It is possible that the heterogeneity of different tumor grades may be masked within an overall grade assigned to large tumor ROIs.

Our previous studies (13, 22) have demonstrated the ability of RSI-MRI to discriminate among different grades of prostate cancer on a tumor-by-tumor basis. This study takes those findings to a resolution that is at least two orders of magnitude higher. Instead of analyzing each tumor as a whole, we analyzed each tumor at the level of the RSI-MRI voxel resulting in hundreds of samples per subject. This enabled us to investigate the ability of RSI-MRI to detect pathologic variation within tumors. In concordance with our prior radiologic-pathologic correlation performed on ROIs (13), the data in the current study demonstrate that the RSI-MRI cellularity index distinguishes between prostate cancer aggressiveness within tumors' GG at the voxel level.

The ability of RSI-MRI to differentiate tumor aggressiveness (low-grade vs. high grade) could have clinical implications in regards to prostate cancer management and treatment. Patients with low-grade disease are candidates for active surveillance. In contrast, patients with high-grade disease are subject to more aggressive treatment (radiation, surgery, and/or hormonal therapy; ref. 6). The goal of active surveillance is to detect aggressive forms of prostate cancer that have metastatic potential while actively monitoring indolent tumors. Knowledge of pathologic progression during monitoring, aided by a noninvasive method, could improve our management decisions in determining treatment. In this regard, serial imaging with RSI-MRI may afford the clinician an opportunity to monitor disease progression and assist in determining when biopsy is necessary. Furthermore, the ability of RSI-MRI to detect within tumor variability has implications for

**Table 1.** Demographics of 10 patients who had a preoperative MRI with subsequent radical prostatectomy

Case	Race	Age	PSA	Clinical stage	Location of positive biopsy <sup>a</sup>	Biopsy grade	Days between biopsy and MRI	Positive cores	Tumor volume (%)	WM Grade	Pathologic stage
1	White	61	9.8	T1c	L. Lateral Base	3+4	553	2 of 12	1.3	3+4 <sup>b</sup>	pT2cNX
2	White	58	5.7	T2a	L. Medial Base	3+3	314	3 of 12	9	3+3 <sup>b</sup>	pT2cN0
					R. Mid	3+4					
					L. Lateral Base	3+4					
					L. Apex	3+4					
3	White	68	4.7	T1c	L. Lateral Base	3+4	65	2 of 12	2.9	4+3	pT2aNO
					L. Lateral Mid	3+4					
4	White	73	6.2	T1c	L. Apex	3+4	97	3 of 19	12.6	5+3	pT2cN0
					L. Lateral Mid	3+3					
					R. Lateral Mid	3+3					
5	White	69	7.4	T2c	R. Lateral Apex <sup>c</sup>		33	7 of 12	18	4+5 <sup>d</sup>	pT3aNO
					R. Lateral Mid <sup>c</sup>	5+4			0.8	4+5 <sup>e</sup>	
					R. Lateral Base <sup>c</sup>	3+5			0.28	3+3 <sup>e</sup>	
					R. Medial Base <sup>c</sup>						
					L. Lateral Mid <sup>f</sup>	5+4					
					L. Lateral Base	5+5					
					L. Medial Mid <sup>f</sup>						
6	White	54	16.7	T2c	R. Lateral Base	4+5	26	9 of 14	60-70	5+4	pT3bN1
					R. Medial Base	5+5					
					R. Medial Mid	5+5					
					L. Lateral Apex	5+4					
					L. Lateral Mid	5+4					
					L. Lateral Base	5+4					
					L. Medial Base	5+5					
					L. Medial Mid	5+5					
					L. Transi. Zone	5+5					
7	White	68	21.5	T1c	R. Medial Apex <sup>g</sup>	4+3	33	5 of 17	26	4+4	pT3aNO
8	White	66	1.05	T2a	R. Lateral Mid	3+3	61	1 of 12	5.3	3+4	pT2cNX
									1	3+3 <sup>h</sup>	
9	White	63	9.4	T1c	Not specified	3+3	127	2 of 7	<2	4+3 <sup>i</sup>	pT2cNX
10	African American	51	9.3	T1c	L. Lateral Mid	3+4	85	2 of 14	4.4	4+3 <sup>j</sup>	pT2cN0
					L. Lateral Apex	3+4			<1	3+3 <sup>k</sup>	

Abbreviations: L., Left; Med., Medial; MRI, magnetic resonance imaging; PSA, prostate serum antigen; R., Right; WM, whole mount.

<sup>a</sup>Standard 12-core biopsies.<sup>b</sup>Additional outlined tumors of concurrent grade marked by pathologist.<sup>c</sup>Intraductal carcinoma.<sup>d</sup>Dominant tumor in R. apex to base.<sup>e</sup>Additional tumors in L. Base and L. Apex.<sup>f</sup>High-grade prostatic intraepithelial neoplasia.<sup>g</sup>Five of six cores for the R. Medial Apex were contained adenocarcinoma.<sup>h</sup>Scattered microscopic foci.<sup>i</sup>Two additional microscopic foci present.<sup>j</sup>Dominant tumor in L. mid lateral with additional outlined tumors of concurrent grade in the R. mid prostate, R. apex, and L. base.<sup>k</sup>Multiple microscopic foci.

targeted treatments or procedures, such as MRI-guided fusion biopsies. With this novel technology, such biopsies would be better able to target the foci that contain the highest grade of disease. Similarly, evolving image-guided focal therapies could

conceivably target the area of the highest grade disease with voxel-level precision.

Limitations of our study include a restricted patient sample pool (10 patients). However, this is mitigated by the large sample

**Table 2.** Voxel level statistical analysis of RSI-MRI cellularity index versus benign or malignant tissue in histopathological section (GGs 3–5). A linear mixed-effects model with a random effect of subject was implemented to compare difference in detection among benign tissue versus low-grade prostate cancer (primary Gleason 3) versus high-grade prostate cancer (primary Gleason  $\geq 4$ )

b) Versus high-grade prostate cancer (primary Gleason $\geq 7$ )					
Random effects: Subject					
	Intercept	Residual			
SD	0.7444	1.423			
Fixed effects: RSI-MRI cellularity index vs. prostate cancer tumor grade					
	Value	SE	DF	t value	P
(Intercept)	0.1589	0.2386	2783	0.6660	0.5055
Low-grade	1.153	0.0998	2783	11.56	$<1 \times 10^{-5}$
High-grade	1.516	0.0631	2783	24.03	$<1 \times 10^{-5}$

Abbreviation: DF, degrees of freedom.



**Table 3.** Voxel level statistical comparing RSI-MRI cellularity index between prostate cancer Gleason categories versus normal tissues and between pathologic grades. *Post hoc* multiple comparison *t* tests were implemented in comparing difference in detection of prostate cancer aggressiveness [low-grade prostate cancer (primary Gleason 3) and high-grade prostate cancer (primary Gleason  $\geq 4$ )] versus benign tissue and between tumor grades (low-grade prostate cancer versus high-grade prostate cancer)

Group		Mean difference (SE)	P
Pathology vs. normal	Low grade vs. normal	1.153 (0.100)	<0.001
	High grade vs. normal	1.516 (0.063)	<0.001
Between pathologic grades	High grade vs. low grade	0.364 (0.113)	0.003

size (>2,700) of our voxel-based analysis, which is a novel approach that is not previously reported elsewhere. Other possible limitations include potential signal coregistration artifacts by tumor burden adjacent to the prostate boundary. Further limitations include lack of secondary pathologic characteristic by not accounting for areas of primary score versus secondary score. Truly heterogeneous tumors that exhibit intermixing of different GGs can confound simple grading criteria, especially if tumor characteristics represent a hybrid of  $\geq 2$  different grades. We contend that secondary pathologic characteristics are less likely when examining the histopathology at voxel-level accuracy versus whole tumors.

Moreover, because GG does not directly represent cellularity, it may not be the most effective measure for understanding how RSI-MRI reflects tissue components. For instance, we expect that RSI-MRI will have lesser ability to detect low-grade disease ( $GG \leq 3$ ); however, in certain cases (e.g. Fig. 2, Case 2), we find that the RSI-MRI signal is greater within the tumor than we would expect. In such cases, quantitative analysis of tissue compartments, such as the glandular structure and cell number and density, may yield a greater understanding of the nature of the RSI-MRI signal. Future studies are planned to determine the relationship of RSI-MRI to quantitative tumor cellular characteristics, including extracellular, intracellular, and intranuclear compartments.

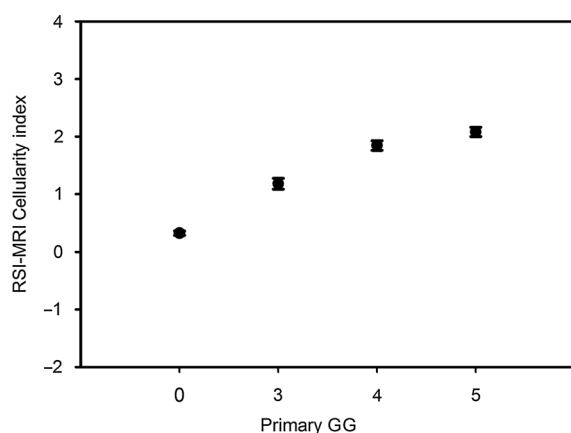


**Figure 3.** RSI-MRI mean cellularity index grouped by pathologic Gleason grade. Mean RSI-MRI cellularity index represented as a z-score corresponding to histologic Gleason grade using data from all voxels graded in all cases. Error bars, SEM.

Another interesting question not addressed in this study is the issue of variation between different zones within the prostate that is apparent in both MRI and in histology. (23, 24) We have not yet investigated the variability of RSI-MRI signal among tumors in different regions. Future studies investigating this issue will require more cases with tumor burden in a wide variety of locations to answer this question.

## Conclusions

Building on our previous findings of correlation between GG and the RSI-MRI among whole tumors, our current study reveals a similar correlation at voxel resolution within tumors. The relationship between GG and RSI-MRI suggests that RSI-MRI may be used as a component of active surveillance to noninvasively detect high-grade cancer and affect staging and treatment. Furthermore, because it can detect variations in tumor grade with voxel-level precision, RSI-MRI may be a promising option for planning of focal procedures, such as MRI-guided targeted biopsies and targeted radiotherapy, where identifying the area with the most aggressive disease is particularly important.

## Disclosure of Potential Conflicts of Interest

A. Dale has ownership interest (including patents) in and is a consultant/advisory board member for Human Longevity, Inc. and CorTechs Labs, Inc., and reports receiving commercial research grants from General Electric Healthcare. No potential conflicts of interest were disclosed by the other authors.

## Authors' Contributions

**Conception and design:** G. Yamin, N.M. Schenker-Ahmed, J. Kuperman, N.S. White, R. Rakow-Penner, K.C. McCammack, J.K. Parsons, A. Dale, D.S. Karow

**Development of methodology:** G. Yamin, N.M. Schenker-Ahmed, H. Bartsch, J. Kuperman, K.C. McCammack, A. Dale, D.S. Karow

**Acquisition of data (provided animals, acquired and managed patients, provided facilities, etc.):** G. Yamin, N.M. Schenker-Ahmed, D. Adams, J. Kuperman, C.J. Kane, A. Dale, D.S. Karow

**Analysis and interpretation of data (e.g., statistical analysis, biostatistics, computational analysis):** G. Yamin, N.M. Schenker-Ahmed, A. Shabaik, D. Adams, J. Kuperman, N.S. White, A. Dale, D.S. Karow

**Writing, review, and/or revision of the manuscript:** G. Yamin, N.M. Schenker-Ahmed, A. Shabaik, D. Adams, J. Kuperman, R. Rakow-Penner, K.C. McCammack, J.K. Parsons, C.J. Kane, A. Dale, D.S. Karow

**Administrative, technical, or material support (i.e., reporting or organizing data, constructing databases):** G. Yamin, N.M. Schenker-Ahmed, D. Adams, H. Bartsch, J. Kuperman, A. Dale, D.S. Karow

**Study supervision:** G. Yamin, A. Shabaik, A. Dale, D.S. Karow

## Grant Support

This work was supported by the Department of Defense (DoD) grant, Prostate Cancer Research Program (#W81XWH-13-1-0391), the American Cancer Society Institutional Research grant (#70-002), UCSD Clinician Scientist Program (#5T32EB005970-07), UCSD School of Medicine Microscopy Core and NINDS P30 core grant (#NS047101), and General Electric, Investigator Initiated Research Award BOK92325. This material is based upon work supported by the National Science Foundation under grant no. 1430082.

The costs of publication of this article were defrayed in part by the payment of page charges. This article must therefore be hereby marked *advertisement* in accordance with 18 U.S.C. Section 1734 solely to indicate this fact.

Received October 7, 2015; revised December 22, 2015; accepted January 5, 2016; published online June 1, 2016.

## References

1. American Cancer Society. Cancer Facts & Figures 2015. Atlanta, GA: American Cancer Society; 2015.
2. Epstein JI. The lower urinary tract and male genital system. In: Jumar V, Abbas AK, Fausto N, editors. Robbins and Cotran Pathologic Basis of Disease. 7th ed., Philadelphia, PA: Saunders; 2004, p. 1050–8.
3. McNeal JE, Redwine EA, Freiha FS, Stamey TA. Zonal distribution of prostatic adenocarcinoma: correlation with histologic pattern and direction of spread. *Am J Surg Pathol* 1988;12:897–906.
4. Augustin H, Erbersdobler A, Graefen M, Fernandez S, Palisaar J, Hülndt H, et al. Biochemical recurrence following radical prostatectomy: A comparison between prostate cancers located in different anatomical zones. *Prostate* 2003;55:48–54.
5. Carroll PR, Parsons JK, Andriole G, Bahnson RR, Barocas DA, Catalona WJ, et al. Prostate Cancer Early Detection, Version 1.2014: featured updates to the NCCN guidelines. *J Natl Compr Cancer Netw* 2014;12:1211–9.
6. Johnson LM, Turkbey B, Figg WD, Choyke PL. Multiparametric MRI in prostate cancer management. *Nat Rev Clin Oncol* 2014;11:346–53.
7. Wu LM, Xu JR, Ye YQ, Lu Q, Hu JN. The clinical value of diffusion-weighted imaging in combination with T2-weighted imaging in diagnosing prostate carcinoma: A systematic review and meta-analysis. *Am J Roentgenol* 2012;199:103–10.
8. Isebaert S, Van Den Bergh L, Haustermans K, Joniau S, Lerut E, De Wever L, et al. Multiparametric MRI for prostate cancer localization in correlation to whole-mount histopathology. *J Magn Reson Imaging* 2013;37:1392–401.
9. Rosenkrantz AB, Taneja SS. Radiologist, be aware: Ten pitfalls that confound the interpretation of multiparametric prostate MRI. *Am J Roentgenol* 2014;202:109–20.
10. White NS, Leergaard TB, D'Arceuil H, Bjaalie JG, Dale AM. Probing tissue microstructure with restriction spectrum imaging: Histological and theoretical validation. *Hum Brain Mapp* 2013;34:327–46.
11. Farid N, Almeida-Freitas DB, White NS, McDonald CR, Kuperman JM, Almutairi A, et al. Combining diffusion and perfusion differentiates tumor from bevacizumab-related imaging abnormality (bria). *J Neurooncol* 2014;120:539–46.
12. White NS, McDonald CR, Farid N, Kuperman J, Karow D, Schenker-Ahmed NM, et al. Diffusion-weighted imaging in cancer: physical foundations and applications of restriction Spectrum imaging. *Cancer Res* 2014;74:4638–52.
13. Liss MA, White NS, Parsons JK, Schenker-Ahmed NM, Rakow-Penner R, Kuperman JM, et al. MRI-derived restriction spectrum imaging cellularity index is associated with high grade prostate cancer on radical prostatectomy specimens. *Front Oncol* 2015;5:1–8.
14. Rakow-Penner RA, White NS, Parsons JK, Choi HW, Liss M a, Kuperman JM, et al. Novel technique for characterizing prostate cancer utilizing MRI restriction spectrum imaging: proof of principle and initial clinical experience with extraprostatic extension. *Prostate Cancer Prostatic Dis* 2015;18:81–5.
15. Holland D, Kuperman JM, Dale AM. Efficient correction of inhomogeneous static magnetic field-induced distortion in Echo Planar Imaging. *Neuroimage* 2010;50:175–83.
16. Epstein JI, Allsbrook WCJ, Amin MB, Egevad LL. The 2005 International society of urological pathology (ISUP) consensus conference on Gleason grading of prostatic carcinoma. *Am J Surg Pathol* 2005;29:1228–42.
17. Epstein JI, Zelefsky MJ, Sjoberg DD, Nelson JB, Egevad L, Magi-Galluzzi C, et al. A contemporary prostate cancer grading system: a validated alternative to the gleason score. *Eur Urol* 2015;1–8.
18. Gleason DF. Classification of prostatic carcinomas. *Cancer Chemother Rep* 1966;50:125–8.
19. Bates D, Mächler M, Bolker BM, Walker SC. Fitting linear mixed-effects models using lme4. *J Stat Softw* 2015;67:1–48.
20. Hothorn T, Bretz F, Westfall P. Simultaneous inference in general parametric models. *Biometrical J* 2008;50:346–63.
21. R Core Team. R: A language and environment for statistical computing. Vienna, Austria: R Foundation for Statistical Computing; 2015.
22. McCammack KC, Kane CJ, Parsons JK, White NS, Schenker-Ahmed NM, Kuperman JM, et al. *In vivo* prostate cancer detection and grading using Restriction Spectrum Imaging-MRI. *Prostate Cancer Prostatic Dis* 2016 Jan 12. [Epub ahead of print].
23. Hricak H, Dooks GC, McNeal JE, Mark AS, Marotti M, Avallone A, et al. MR imaging of the prostate gland: normal anatomy. *AJR Am J Roentgenol* 1987;148:51–8.
24. Myers RP. Structure of the adult prostate from a Clinician's Standpoint. *Clin Anat* 2000;215:214–5.



# Restriction Spectrum Imaging: An Evolving Imaging Biomarker in Prostate MRI

Ryan L. Brunsing, MD, PhD,<sup>1</sup> Natalie M. Schenker-Ahmed, PhD,<sup>1</sup>  
 Nathan S. White, PhD,<sup>1</sup> J. Kellogg Parsons, MD, MHS,<sup>2</sup> Christopher Kane, MD,<sup>2</sup>  
 Joshua Kuperman, PhD,<sup>1</sup> Hauke Bartsch, PhD,<sup>1</sup> Andrew Karim Kader, MD, PhD,<sup>2</sup>  
 Rebecca Rakow-Penner, MD, PhD,<sup>1</sup> Tyler M. Seibert, MD, PhD,<sup>3</sup>  
 Daniel Margolis, MD,<sup>4</sup> Steven S. Raman, MD,<sup>4</sup> Carrie R. McDonald, PhD,<sup>5</sup>  
 Nikdokht Farid, MD,<sup>1</sup> Santosh Kesari, MD, PhD,<sup>6</sup> Donna Hansel, MD, PhD,<sup>7</sup>  
 Ahmed Shabaik, MD,<sup>7</sup> Anders M. Dale, PhD,<sup>1,8</sup> and David S. Karow, MD, PhD<sup>1\*</sup>

Restriction spectrum imaging (RSI) is a novel diffusion-weighted MRI technique that uses the mathematically distinct behavior of water diffusion in separable microscopic tissue compartments to highlight key aspects of the tissue micro-architecture with high conspicuity. RSI can be acquired in less than 5 min on modern scanners using a surface coil. Multiple field gradients and high b-values in combination with postprocessing techniques allow the simultaneous resolution of length-scale and geometric information, as well as compartmental and nuclear volume fraction filtering. RSI also uses a distortion correction technique and can thus be fused to high resolution T2-weighted images for detailed localization, which improves delineation of disease extension into critical anatomic structures. In this review, we discuss the acquisition, postprocessing, and interpretation of RSI for prostate MRI. We also summarize existing data demonstrating the applicability of RSI for prostate cancer detection, in vivo characterization, localization, and targeting.

J. MAGN. RESON. IMAGING 2016;00:000–000.

Prostate cancer (PCa) is the most common noncutaneous malignancy in males and the second leading cause of cancer-related death among men in the United States,<sup>1</sup> with an estimated one in six American men diagnosed with PCa in their lifetime.<sup>2</sup> MRI has demonstrated potential value for PCa staging, treatment planning, and follow-up.<sup>3–8</sup> However, suboptimal sensitivity and specificity and inconsistency in identifying foci of high-grade disease highlight that current MRI protocols remain suboptimal for cancer detection, staging, and in vivo characterization.<sup>9–12</sup> Thus, more robust diagnostic tools are needed to maximize the potential of this promising imaging modality.

Advances in MR scanner technology have allowed the development of powerful MRI sequence protocols that highlight specific biophysical properties of tissue. One such technique is diffusion-weighted MRI (DWI), which detects limitations in the microscopic movement of water molecules due to tissue architecture. DWI has a high conspicuity for PCa relative to normal tissue,<sup>8–21</sup> and when combined with T2-weighted imaging offers higher sensitivity and specificity in cancer detection (0.76 and 0.94, respectively) as compared to T2-weighted images alone (0.61 and 0.91, respectively).<sup>10</sup> Based on an abundance of supporting data, the recently released American College of Radiology guidelines

View this article online at [wileyonlinelibrary.com](http://wileyonlinelibrary.com). DOI: 10.1002/jmri.25419

Received May 24, 2016, Accepted for publication Jul 25, 2016.

\*Address reprint requests to: D.S.K., Multimodal Imaging Laboratory (MMIL), 8950 Villa La Jolla Dr., Suite C101, La Jolla, CA 92037. E-mail: [dkarow@ucsd.edu](mailto:dkarow@ucsd.edu)

From the <sup>1</sup>Department of Radiology, University of California San Diego, San Diego, California, USA; <sup>2</sup>Department of Surgery, University of California San Diego, San Diego, California, USA; <sup>3</sup>Department of Radiation Medicine, University of California San Diego, San Diego, California, USA; <sup>4</sup>Department of Radiology, University of California Los Angeles, Los Angeles, California, USA; <sup>5</sup>Department of Psychiatry, University of California San Diego, La Jolla, California, USA; <sup>6</sup>Department of Translational Neuro-Oncology and Neurotherapeutics, Pacific Neuroscience Institute and John Wayne Cancer Institute at Providence Saint John's Health Center, Los Angeles, California, USA; <sup>7</sup>Department of Pathology, University of California San Diego, San Diego, California, USA; and <sup>8</sup>Department of Neurosciences, University of California San Diego, La Jolla, California, USA

Drs. Brunsing and Schenker-Ahmed contributed equally to this work.

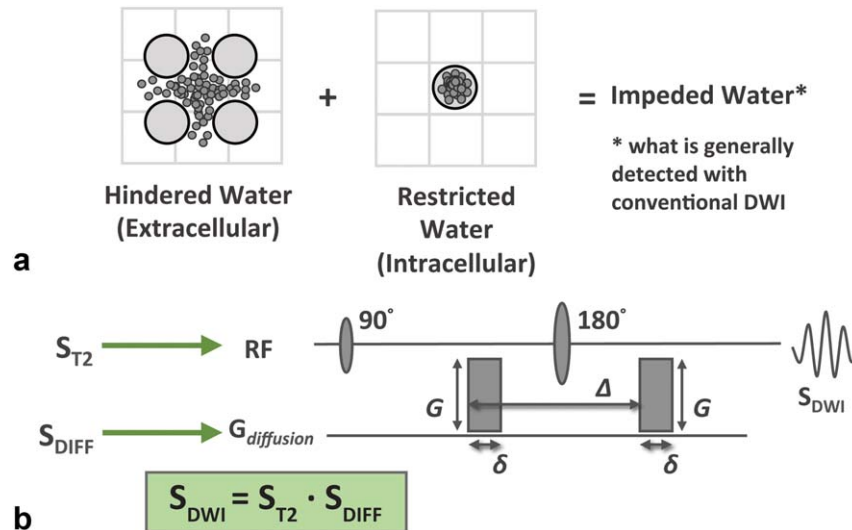


**FIGURE 1: Foundations of DWI. A:** Water within tissue can be confined to the intracellular or extracellular compartment, the intracellular water having a limited range determined by the configuration of the plasma membrane. The combined signal from both is measured in conventional DWI and referred to as impeded water. **B:** Standard spin-echo echo-planar pulse sequence used in conventional diffusion weighted imaging. It is important to note that signal from diffusion imaging represents the sum effect of both the diffusion and T2 properties of the tissue being probed.

for PCa MRI interpretation, PI-RADS version 2 (PIRADSv2), uses DWI as the core sequence for assessing peripheral zone lesions.<sup>22,23</sup> Current standard-of-care PCa MRI also includes a dynamic contrast enhanced imaging (DCE) and anatomic T1 and T2-weighted (T1w and T2w) sequences in addition to DWI. Despite its clinical utility, there are some notable limitations of conventional DWI. Information from the T2 component of the signal is not used; information about the underlying geometry is not obtained; signal from intracellular and extracellular water is mixed; and inherent spatial distortion issues caused by field inhomogeneities are not addressed.

A recently developed advanced diffusion-based technique termed restriction spectrum imaging (RSI) attempts to address many of these limitations.<sup>24</sup> In this review, we discuss the acquisition, postprocessing, and interpretation of RSI in the setting of prostate cancer. We also summarize existing data demonstrating the applicability of RSI for prostate cancer detection, in vivo characterization, localization, and targeting

## Principles of Diffusion Weighted Imaging

Signal in DWI is inversely related to the net movement of water within the tissue being probed. Water molecules spread apart due to random motion driven by thermal energy. In pure solution they will disperse in a predictable way following a Gaussian distribution in a process called “free diffusion.” However, in biological tissues the process is more complex. Water diffusion can be impeded by one of two general mechanisms: hindrance by the physical boundaries of the extracellular space (predominantly determined by the geometric tortuosity associated with the cell packing density – see Fig. 1A) or restriction of water within the intracellular compartment (Fig. 1A). For

discussion purposes in this paper, restricted diffusion refers specifically to water trapped within the intracellular space, as defined classically,<sup>25,26</sup> and “impeded diffusion” refers to the collective signal from restricted and hindered compartments. By this definition, conventional DWI generally reflects signal attenuation due to impeded diffusion, noting that increased sensitivity to restricted diffusion can be achieved with increasing diffusion-weighting (b-value, see below).

There are two discrete properties of diffusion that can be measured using diffusion-based techniques. The first is the length-scale distribution, reflecting the scalar distance that water is able to travel over a given time (e.g., the diffusion time). The second is orientation or geometric information, reflecting preferential diffusion vectors in three-dimensional (3D) space resulting from regional tissue architecture (for example water will tend to travel along an axon rather than through its membrane). In general, the mathematical frameworks used for current clinical diffusion-based MRI protocols calculate one of these two diffusion properties at the expense of the other. MR tractography, such as diffusion tensor imaging (DTI), is an example of a clinical diffusion-based technique that collects geometric information.<sup>27</sup>

Most conventional DWI protocols are based on the classic Stejskal-Tanner single-shot pulsed-gradient spin-echo (PGSE) technique<sup>28</sup> which measures length-scale distribution properties. In this sequence, signal is generated from a “root” spin-echo sequence where the inversion pulse is flanked by diffusion gradients of strength  $G$  for a duration  $\delta$  separated by a time  $\Delta$  (Fig. 1B). The first gradient serves to encode the initial physical position of the water molecule relative to the gradient field and the second gradient serves as a refocusing pulse. Increased movement of water (by

means of diffusion) along the diffusion gradient axis in the time  $\Delta$  results in decreased signal due to increasingly ineffective refocusing. Thus impeded water movement results in a less attenuated (or relatively increased) diffusion signal compared with free water.

An important aspect of the PGSE sequence, which is often overlooked, is that it is a T2-weighted sequence. This means that the strength of the DWI signal within a given voxel is determined by both the degree of diffusion and the inherent T2 of the tissues therein. Mathematically, the signal from DWI ( $S_{DWI}$ ) is equal to the intrinsic T2-weighted signal of the tissue ( $S_{T2}$ ) multiplied by the diffusion gradient effects ( $S_{DIFF}$ ) described in the preceding paragraph.

$$S_{DWI} = S_{T2} \cdot S_{DIFF}$$

(see Fig. 1B)

To distinguish between the two sources of DWI signal, images are compared with apparent diffusion coefficient (ADC) maps, calculated from a mathematical framework proposed by Stejskal and Tanner in 1965.<sup>28</sup> Lower ADC values represent true impeded diffusion, while high signal on both DWI and ADC represent T2 shine-through. In the Stejskal and Tanner model, signal from the diffusion component ( $S_{DIFF}$ ) decays exponentially according to the ADC value, encompassing the length-based diffusion properties of the system, and the b-value, encompassing effects of the machine-controlled parameters:

$$S_{DIFF} = S_0 \cdot e^{-(b \cdot ADC)}$$

$$b = (G^2 \cdot \gamma^2 \cdot \delta^2) \cdot (\Delta - \delta/3)$$

where  $S_0$  is the signal at  $b = 0$  and  $\gamma$  = the Lamor frequency of protons remaining parameters defined in Figure 1B.

Decay of the diffusion component of the signal ( $S_{DIFF}$ ) can be enhanced by increasing the b value, which may be achieved by increasing the diffusion time  $\Delta$ , gradient strength  $G$ , or both. In this setting, only tissues that have high levels of impeded water will retain signal. These properties explain why DWI has been so widely investigated as a tool for oncologic imaging: highly cellular tumors have increased volumes of restricted intracellular water and should theoretically exhibit high signal on conventional DWI and low values on the quantifiable ADC maps.

While powerful, this framework has several limitations: As a composite measure, the standard DWI measurement of the apparent diffusion coefficient (ADC) reflects the average molecule displacements of water molecules within the imaging voxel and does not differentiate diffusion signals stemming from separable tissue sub-compartments (e.g. intracellular and extracellular spaces). This limitation in the ability to distinguish signals from different sub-compartments likely contributes to the suboptimal sensitivity and specificity of ADC in discriminating cancer from healthy tissue.<sup>9-12</sup> This issue is

further compounded in the setting of iatrogenic changes to the tumor microenvironment such as postbiopsy hemorrhage.<sup>29</sup> Additionally, DWI does not take advantage of information from the T2 component of the signal nor the geometric information embedded in the mechanism of signal acquisition. Finally, conventional DWI images are subject to significant distortion from  $B_0$  magnetic field inhomogeneities created by material interfaces, patient geometry, and eddy currents,<sup>30</sup> limiting DWI's role in discerning anatomic localization for biopsy, cancer staging, and treatment planning.

## Restriction Spectrum Imaging Theory and Acquisition

The major advantage of RSI over most other diffusion techniques is that it uses diffusion data collected with multiple gradient directions and b-values (termed a "multi-shell" acquisition), together with an advanced linear mixture model to resolve a spectrum of length scales (hence, "restriction spectrum imaging")<sup>25</sup> while simultaneously acquiring geometric information.<sup>24</sup> This is accomplished using a linear mathematical framework allowing reasonable computation times. In addition, because the multi-shell sequence acquisition used for RSI captures information across a broader set of variables than conventional DWI, RSI has the potential to be normalized across institutions, unlike ADC, which remains machine and technique dependent. In the future, this may eliminate one of the major roadblocks that have undermined clinical application of ADC maps.

For prostate MRI, RSI is used to separate restricted diffusion within small spherical cells from extra-cellular hindered and free water compartments. RSI cellularity index (RSI CI), derived from the spherically restricted diffusion signal, has demonstrated correlation to the nuclear-cytoplasmic ratio in a simulated cancer cell model<sup>28</sup> and shows great promise as a quantitative imaging biomarker. Finally, RSI incorporates an advanced postprocessing technique for distortion correction based on the reverse phase encode method<sup>29</sup> that allows for accurate colocalization with fast spin-echo T2-weighted sequences for discrete anatomic precision.<sup>30-32</sup> Importantly, RSI maintains the many strengths of conventional DWI, including high signal-to-noise ratio (SNR) and does not require a separate pulse-sequence or additional scan time. The mathematical foundations of RSI have previously been described in detail by White et al.<sup>24</sup> That manuscript also includes a discussion of other advanced diffusion-based techniques.

## Protocol

The current institutional prostate RSI protocol uses non-zero b-values of 125, 375, and 1000 s/mm<sup>2</sup> with 6, 6, and 15 diffusion gradients, respectively (Table 1 and Fig. 2A) using a cardiac coil on a 3.0 Tesla (T) GE (Milwaukee, WI) platform. Following postprocessing (described below), RSI Cellularity Maps, acquired using the parameters outlined in Table 1, are

**TABLE 1. Prostate RSI Protocol**

Coil: cardiac, no endorectal coil is required
Repetition time: 9900 ms
Echo time: 69-72 ms
Field of View: 200-260 mm
Matrix: 96×96
Slice thickness: 3.0 mm
<i>b</i> values (s/mm <sup>2</sup> ):
0: alternate phase encoding direction for distortion correction
125: 6 diffusion gradient directions
375: 6 diffusion gradient directions
1000: 15 diffusion gradient directions

fused to axial T2w images. Currently, all patients who undergo prostate MRI at our institution receive RSI as part of their exam in addition to current standard-of-care sequences; axial T2w images, axial dynamic contrast enhanced images (DCE), and axial DWI images ( $b = 0$  and 1000) with ADC map reconstruction. For purposes of discussion, this collective protocol will be referred to as mpMRI+RSI. Furthermore, any patients referred to our institution for prostate MRI receive RSI as part of their exam. To date, RSI has been acquired on both GE and Siemens (Erlangen, Germany) 3T scanners.

## RSI Postprocessing in PCA

### Compartmental Filtering

As discussed above conventional DWI does not reliably and predictably differentiate between the intracellular and

extracellular water compartments, which demonstrate distinct diffusion properties ( $S_{\text{DIFF}}$ ) and T2 signal characteristics ( $S_{\text{T2}}$ ), and likely have distinct implications in tumor detection, characterization, localization, and treatment. Signal diffusion-based techniques, including RSI ( $S_{\text{RSI}}$ ), is the sum of unique signals from the hindered ( $S_{\text{H}}$ ) and restricted compartments ( $S_{\text{R}}$ ) as well as signal from free water ( $S_{\text{F}}$ ):

$$S_{\text{DWI/RSI}} = S_{\text{H}}(\text{Hindered}) + S_{\text{R}}(\text{Restricted}) + S_{\text{F}}(\text{Free}).$$

Upon closer investigation into the diffusion characteristics of the two compartments (Fig. 2A), it is clear that water in the extracellular compartment has essentially unlimited range to travel, while intracellular water is confined by the walls of the cell. (Note: in reality there is exchange of water between the intra- and extracellular compartments, however, on the time scales used in RSI exchange effects are small.<sup>31</sup>) Therefore, as one increases the diffusion weighting, e.g., by increasing the diffusion time  $\Delta$ , signal drops out more quickly in the extracellular compartment. At high  $b$  values, signal from intracellular water can be isolated (Fig. 2A). In this setting, increasing signal correlates with increasing intracellular water and thus tissue cellularity (Fig. 2B). RSI uses multiple  $b$ -values to separate a spectrum of length-scales, which correlate with distinct compartments within a tissue. In the setting of PCa, signal from this highly restricted intracellular compartment is highlighted. This concept forms one of the two foundations of PCa RSI cellularity maps.

### Geometric Filtering

The second foundation for RSI cellularity maps comes from the ability to simultaneously separate water fractions based on geometric information. Using advanced postprocessing

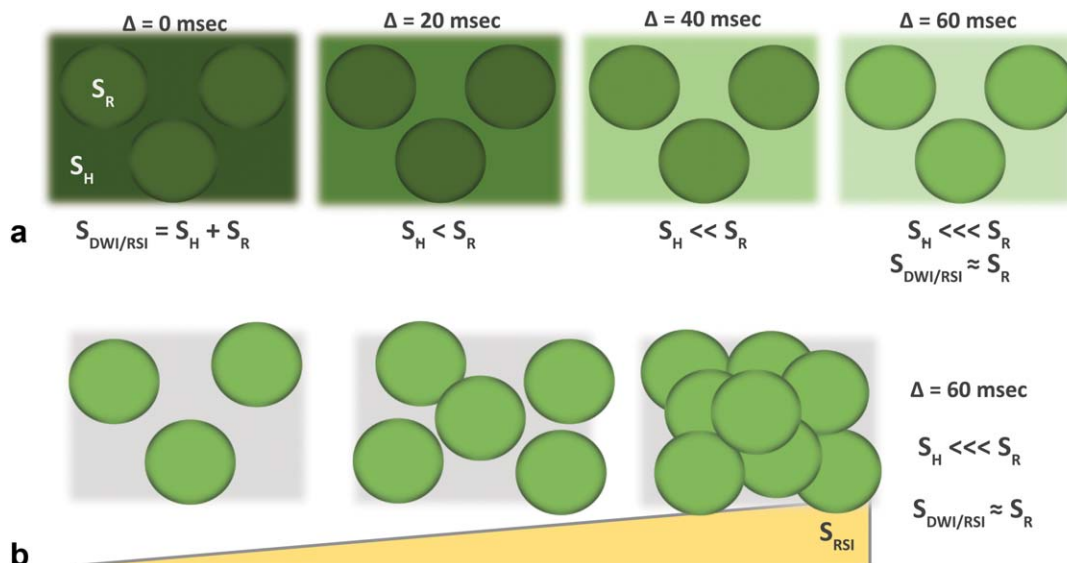


**FIGURE 2: Foundations of RSI, compartmental filtering. A:** With time, the signal from hindered water dissipates more quickly than that from restricted water (darker green indicates greater signal). **B:** Signal from RSI increases with greater cell density.



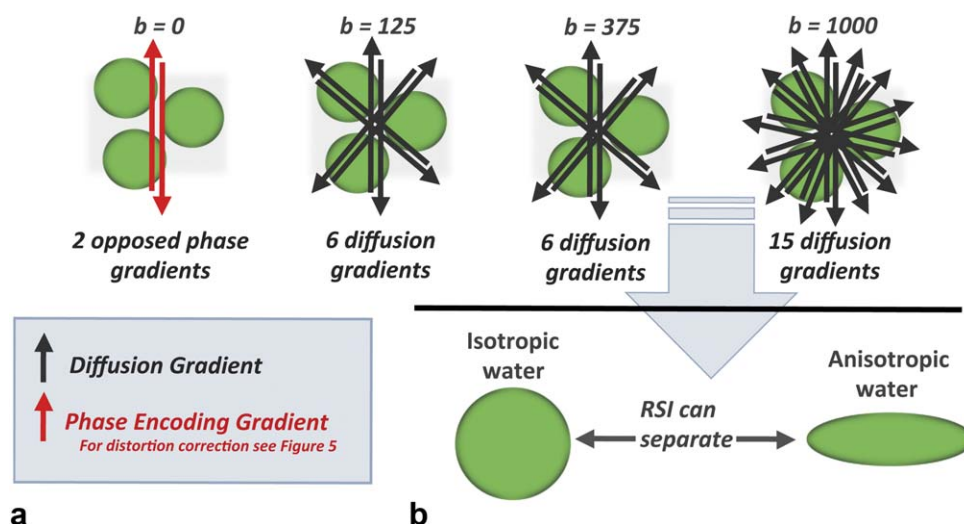


**FIGURE 3: Foundations of RSI, geometric filtering. A:** Schematic outlining the basic parameters of the RSI multishell acquisition, with opposed phase encoding gradients in the  $b = 0$  acquisition used for distortion correction and 6, 6, and 15 nonparallel gradients for the non-zero  $b$  values. **B:** Using this data, RSI can simultaneously acquire length-scale distribution data and geometric information, allowing isolation of isotropic and anisotropic orientation data. In prostate cancer, RSI is used to isolate signal from highly restricted and isotropic water.

techniques discussed,<sup>24,32,33</sup> the high number of distinct gradient directions (Fig. 3A) allows for water exhibiting isotropic (spherical) diffusion (as would be seen within tumor cell that is small and round, for example) to be distinguished from water exhibiting anisotropic (cylindrical) diffusion (as would be seen in axons, for example), similar to the diffusion tensor based techniques used in tractography<sup>27</sup> (Fig. 3B). For PCa, RSI cellularity maps represent isotropic diffusion signal.

In summary, RSI uses a range of high  $b$ -values and multiple diffusion gradients to simultaneously separate multiple length-scales / compartments and geometric information, respectively. In the setting of PCa, RSI cellularity maps are tuned to highlight signal from highly restricted spherical compartments of water, such as those expected in small round tumor cells.

### Nuclear Volume Fraction filtering

The concept of an imaging biomarker centers on the usage of quantitative information derived from medical imaging to guide preclinical development and clinical decision making.<sup>34</sup> Imaging biomarkers hold great promise in personalized cancer care,<sup>35</sup> where matching the patient to the appropriate therapeutic regimen will become increasingly complex and important. Despite a great deal of focus on the use of ADC as an imaging biomarker in oncology,<sup>36</sup> overlap between theoretical reference ranges<sup>37</sup> and confounding results<sup>38</sup> continue to make clinical guidance using ADC values untenable. New techniques are needed to build upon the promising, but thus far unrealized, quantitative potential of diffusion-based imaging.

In PCa, one area where imaging biomarkers could provide valuable clinical guidance would be in predicting Gleason grade. RSI approaches this by using the T2 properties of

the intracellular space. The inherent T2 values of the nucleus and cytoplasm differ substantially measuring approximately 65 ms and 25 ms, respectively<sup>31</sup> (Fig. 4A). As the ratio of nuclear to cytoplasmic space increases, the percentage of intracellular water contained within the nucleus correspondingly increases. This percentage has previously been termed the nuclear volume fraction (NVF),<sup>33</sup> and correlates with the histopathologic concept nuclear-to-cytoplasmic ratio.

As NVF increases, the effective T2 of the intracellular space and thus the signal  $S_{T2}$  also increase (Fig. 4B). Note that the diffusion characteristics ( $S_{DIFF}$ ) of the nucleus and cytoplasm are the same. Therefore, when the underlying cellularity remains unchanged, increased signal within a voxel on the RSI cellularity map represents a proportional increase in NVF within that voxel (Fig. 4B) due to increasing  $S_{T2}$ . An example is provided in Figure 4c. The glioblastoma in the left panel (WHO grade 4) demonstrates high signal on the RSI Cellularity map, correlating with the small isotropic cells seen on the histopathological section and with a high NVF.

Conversely, there is minimal RSI signal on the WHO grade 2 glioma in the right panel, correlating with the lower NVF seen on the histopathological section. By normalizing to remove effects from the diffusion component, NVF can be mathematically estimated from RSI cellularity map (RSI-CM) data acquired at multiple echo times. Within this framework, one would theoretically expect the RSI Z-scores (referred to as “cellularity index,”<sup>39</sup> calculated below) to correlate with NVF. Preliminary data obtained from the application of prostate MRI suggests that this is true<sup>40,41</sup> as discussed below. This represents a major advancement beyond current DWI, which is indifferent to intracellular changes in histopathologic architecture.

In practice, the approach has been to calculate the mean value ( $MV_N$ ) and standard deviation ( $SD_N$ ) of RSI

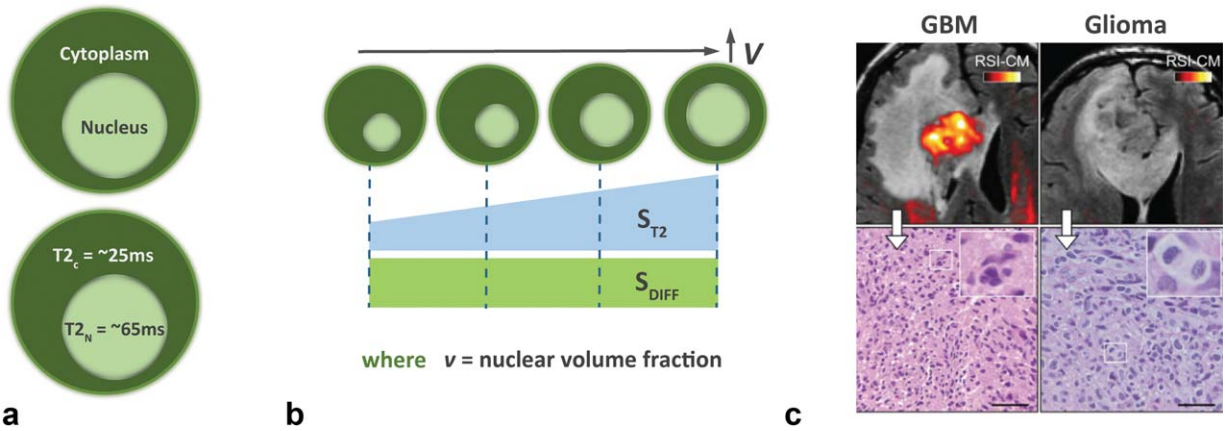


**FIGURE 4: Foundations of RSI, nuclear volume fraction.** **A:** The inherent T2 signal of the cytoplasm and nucleus differ substantially. **B:** Increasing nuclear volume fraction (NVF) results in a corresponding increase in effective T2. As the nucleus and cytoplasm exhibit similar diffusion properties, this change in effective T2 can be measured and used to calculate NVF.

signal per voxel from a normal region of the tissue in question. This can be done from individual or pooled patient data. The RSI cellularity index (CI) (representing the Z-score) can then be calculated as:

$$\text{RSI CI} = (\text{RSI-CM VOXEL SIGNAL} - \text{MV}_N) / \text{SD}_N$$

#### Distortion Correction

DWI is prone to image distortion due to  $B_0$  magnetic field inhomogeneities.<sup>30,33</sup> Distortion can lead to misregistration

of signal by up to  $13\text{ mm}^{32}$  and is of particular importance in the phase-encoding direction because of the time between sample points. This carries large implications for cancer staging.<sup>42</sup> Dilemmas at critical treatment decision points can arise when tumor margins approach important anatomic landmarks or when suspicious lesions detected outside the primary mass do not declare themselves as benign or malignant. To address this, RSI uses a distortion correction technique based on the acquisition of  $b=0$  images with opposite phase encoding polarizations<sup>43</sup> (Fig. 5A). This technique has been applied to the PCa RSI protocol<sup>32</sup> and

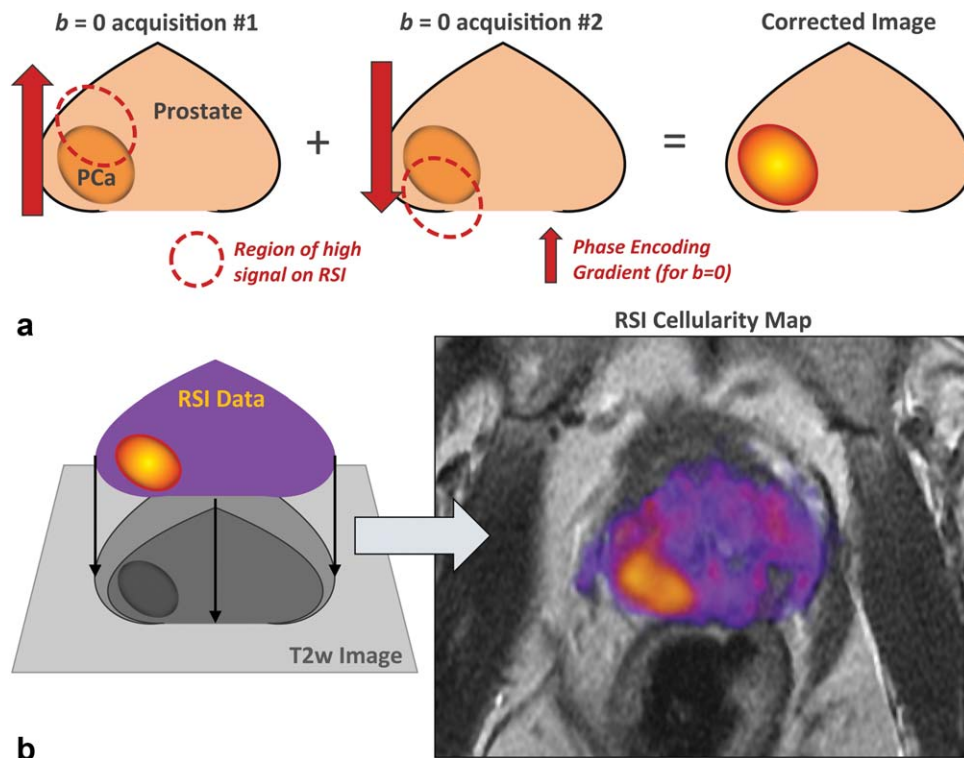


**FIGURE 5: Foundations of RSI, distortion correction.** Opposed phase encode gradients are used to cancel out distortion caused by magnetic field inhomogeneities (A), allowing for the fusion of RSI cellularity maps with high resolution anatomic images (B). These fused images are the foundation of clinical RSI interpretation.

**TABLE 2. Advantages of RSI**

	<b>Compartmental filtering</b>	<b>Geometric filtering</b>	<b>Nuclear fraction</b>	<b>Distortion correction</b>
DWI/ADC	Possible	No	No	Possible
RSI	Yes	Yes	Yes	Yes

DWI = diffusion-weighted imaging; ADC = apparent diffusion coefficient; RSI = restriction spectrum imaging.

others, allowing RSI cellularity maps to be fused to high resolution T2-weighted sequences for detailed anatomic localization (Fig. 5B) on a voxel-by-voxel level.

In PCa, distortion correction is particularly valuable for identifying extra-prostatic extension (EPE) beyond the capsule, which has important staging and surgical implications.<sup>5,42</sup> In a proof of concept study by Rakow-Penner et al, fused T2-RSI images with distortion correction demonstrated improved sensitivity for EPE in prostate cancer patients (8/9, 89%) versus standard of care mpMRI alone (2/9, 22%).<sup>44</sup> Notably, this was a nonblinded pilot study with small patient numbers. While theoretically possible to apply to conventional DWI, most current clinical protocols do not use distortion correction.

### Summary of Filtering Techniques

For prostate MRI, RSI provides a direct estimate of tissue cellularity by isolating signal from isotropic intracellular water, uses T2 signal characteristics to provide quantitative information about nuclear volume fraction, and incorporates distortion correction techniques allowing fusion of RSI cellularity maps with high spatial resolution imaging. While the first and last of these are theoretically possible with conventional DWI, they are not widely used. The other two, which represent advancements for quantitative imaging, are unique to RSI. A comparison of the two approaches can be found in Table 2.

### Interpretation of Prostate MRI with RSI: Existing Data

Next follows a summary of publications to date demonstrating the utility of RSI as an imaging biomarker for prostate cancer detection, in vivo characterization, and localization/targeting.

#### Cancer Detection

Cancer treatment begins with cancer detection. Diffusion-based techniques are attractive as a tool in cancer detection given their high conspicuity and fast acquisition and have already proven clinical utility in prostate cancer.<sup>3-6,8-16</sup> However, as noted earlier, these techniques remain marred by several limitations including suboptimal sensitivity and specificity.<sup>9-12</sup>

The power of RSI as a tool for cancer detection was initially demonstrated by work with intracranial neoplasms.

In a study evaluating 10 patients with CNS malignancy, RSI demonstrated (i) increased tumor conspicuity and (ii) greater sensitivity/specificity (based on receiver-operating characteristic curve data) in delineating malignant tissue from normal white matter tracts (which can also exhibit some degree of impeded diffusion) as compared to DWI images and ADC maps derived from b-values of 500, 1500, and 4000.<sup>49</sup> Additionally, bevacizumab treatment of intracranial neoplasms can be associated with regions of persistent DWI signal despite elimination of the underlying tumor, so called bevacizumab-related imaging abnormalities (BRIA).<sup>50</sup> In fact, the presence of impeded diffusion following bevacizumab treatment of malignant gliomas correlated with improved overall survival,<sup>51</sup> suggesting prognostic value. RSI demonstrated increased sensitivity in detecting areas of persistent restricted diffusion relative to conventional DWI, and when combined with relative cerebral blood volume measurements may be able to differentiate BRIA from residual tumor.<sup>45,46</sup> Prior manuscripts have presented and discussed the promising results using RSI in intracranial neoplasms.<sup>33,45-48</sup>

In PCa, McCammack et al directly compared the detection capacity of RSI cellularity maps to that of quantitative maps from current mpMRI sequences,<sup>40</sup> namely DWI (ADC) and DCE ( $K^{\text{trans}}$ ,  $K_{\text{ep}}$ , and  $V_e$ ). Tumors were defined and graded by an experienced uropathologist using thin whole-mount sections from 33 patients who underwent pre-operative mpMRI+RSI before radical prostatectomy. Corresponding regions of interest (ROIs) were drawn on T2w images by an experienced radiologist, and subsequently cross referenced to the above quantitative maps for direct comparison of histopathological results and imaging data. RSI CI significantly outperformed ADC values in differentiating tumor from normal tissue. Both RSI and ADC significantly outperformed DCE-based measures<sup>40</sup> (Fig. 6). The MRIs in this study were acquired using a current clinical-grade protocol with a cardiac surface coil on a GE platform. No bowel prep or endorectal coil was required. These results demonstrate that RSI can outperform current mpMRI tools in detecting PCa as assessed by direct comparison to histopathological data.

To evaluate the clinical performance of RSI in PCa detection, McCammack et al conducted a retrospective

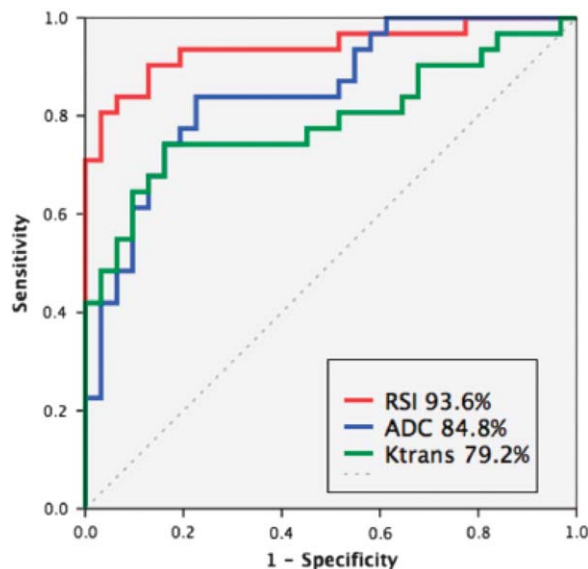


**FIGURE 6:** Receiver-operating characteristic curves for the quantitative discrimination of prostate cancer from normal peripheral zone. Areas under the curve are listed in the legend. Used with permission from McCammack et al. *PCAN*, 2016.<sup>40</sup>

study of 100 patients (67 with pathologically proven prostate cancer, 30 of which were high-grade) who underwent mpMRI+RSI within 6 months of systematic biopsy or prostatectomy.<sup>41</sup> Studies were reviewed by three independent radiologists.<sup>41</sup> Analysis at both the sextant and hemigland level demonstrated that mpMRI with RSI (area under the receiver operating characteristics curve [AUC] 0.69 and 0.71, respectively) outperformed mpMRI alone (AUC 0.63 and 0.68). At the sextant level, the independent performance of all three readers was significantly improved with the incorporation of RSI. Moreover, inter-reader agreement was higher when RSI was added to mpMRI. These results demonstrate that RSI-MRI can outperform current standard of care mpMRI in the clinical setting as well.

Additional data from this same study may have implications for PCa screening programs. Population screening with serum prostate specific antigen (PSA) testing reduces prostate cancer mortality, but is limited by PSA's relatively low specificity, which can lead to PCa over-detection and over-treatment.<sup>52</sup> In an abbreviated MR protocol using RSI and T2 (RSI+T2) in the same cohort of 100 patients, RSI+T2 was found to be at least as effective as conventional mpMRI in detecting high-grade PCa (primary Gleason grade  $\geq 4$ ). Moreover, variability in reader interpretations was the lowest when RSI was evaluated in isolation, possibly due to the increased conspicuity that makes RSI images easier to read. Notably, this RSI+T2 protocol does not require administration of contrast and can be acquired in less than 10 min on a GE Signa HDxt 3.0T machine using a cardiac surface coil. Use of a more modern scanner would reduce the time required even further. The combination of robust delineation of disease, reproducibility of interpretation, and

ease of acquisition make this limited protocol an interesting prototype for MRI-based PCa screening. It may also prove valuable as a follow-up tool in patients who cannot tolerate prolonged positioning in the MR scanner.

### **In Vivo Characterization**

One of the primary goals of an imaging biomarker is to inform clinical decisions. In cancer, pathological grading is central to predicting tumor behavior. Due to the relatively high prevalence of clinically indolent tumors, distinguishing aggressive high grade tumors from lower grade lesions is particularly important for the appropriate management of PCa, as patients with lower grade disease may benefit from active surveillance rather than curative treatment.<sup>52</sup> Thus tools that can reliably distinguish low grade from high grade PCa are needed. RSI is well suited for evaluating tumor histopathology based on the fact that: cellularity maps can highlight intracellular water, reflecting tissue cellularity (Fig. 2) and the RSI CI signal should increase with increasing nuclear volume fraction (Fig. 4B). Both of these tissue characteristics play a role in histopathological grading.

In a retrospective analysis of 36 tumors from 28 patients,<sup>39</sup> Liss et al demonstrated that the RSI CI in aggressive PCa (primary Gleason score of  $\geq 4$ ) was statistically different from lower grade lesions (primary Gleason 3 or less), while ADC values trended toward, but did not achieve, statistical significance in this sample. This later result is likely attributable to the small number of patients in the study, as several prior studies have demonstrated a statistically significant correlation between primary Gleason grade and ADC value.<sup>53,54</sup> For example, in a study of 131 men who underwent 1.5T MRI with an endorectal coil before prostatectomy, Donati et al<sup>53</sup> demonstrated a Spearman coefficient of -0.36 when ADC value ( $b = 0,1000$ ) was compared with Gleason grade. They also showed that 10th percentile ADC value can distinguish Gleason 6 from Gleason 7 lesions with an AUC of 0.76.<sup>53</sup>

Building upon the results of Liss et al,<sup>39</sup> McCammack et al<sup>40</sup> (described above) compared Gleason grade from 33 tumors as determined on whole-mount section to RSI cellularity, ADC, and  $K^{trans}$  map values derived from preoperative MRIs. Gleason grade was also compared with preoperative PSA levels. RSI CI had the closest correlation to Gleason grade (Spearman rank-order correlation coefficient ( $\rho$ ) = 0.53), outperforming ADC maps ( $\rho$  = -0.42, negative value due to inverse relationship) and PSA levels ( $\rho$  = 0.36). An example case in which ADC was relatively equivocal while RSI was positive can be seen in Figure 7A.  $K^{trans}$  values did not significantly correlate with Gleason grade.<sup>40</sup> Further analysis of these data demonstrated a strong association between the upper quartile of the RSI CI for each ROI and primary Gleason grade (Fig. 8A). Thus RSI



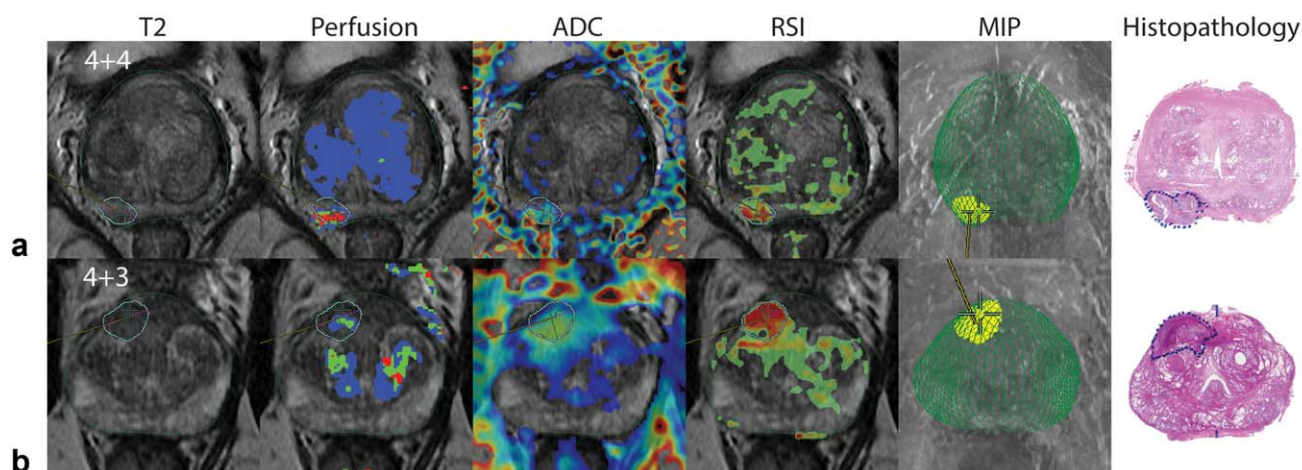


**FIGURE 7: A: RSI guided biopsy where ADC is equivocal, but RSI clearly identifies the lesion. B: RSI guided biopsy finds high grade disease after repeated negative systematic biopsies. Modified with permission from McCammack et al. PCAN 2016.<sup>40</sup>**

CI reliably and predictably correlates with underlying histopathology (Fig. 8B–D) (unpublished data).

Yamin et al further validated these findings at the voxel level. Regions of tumor were identified by a uropathologist on thin whole-mount sections from 10 patients with PCa with presurgical MR imaging. The sections were stained, scanned at high resolution (75  $\mu\text{m}/\text{pixel}$ ), and then divided into voxel size tiles. Each tile was graded on the Gleason scale and then compared with the RSI CI from preoperative MRI. In total 2795 individual tiles were reviewed and analyzed. On a voxel-by-voxel basis, RSI CI was significantly different among benign (mean RSI cellularity index = 0.16), low grade (mean score = 1.15) and high grade disease (mean score = 1.52) with increasing cellularity index correlating to increasing Gleason grade. Thus RSI CI correlates with Gleason grade at the voxel level, reflecting variation within individual tumors.<sup>55</sup>

### Localization and Targeting

Once cancer has been detected by screening PSA or imaging, it must be confirmed by biopsy. Ultrasound-guided biopsy with a minimum of 10–12 cores systematically sampled from various regions of the prostate using a standard template remains the gold standard for PCa diagnosis.<sup>52</sup>

However, the diagnostic yield of random systematic prostate biopsy remains limited, and variations between biopsy Gleason sum and surgery Gleason sum are relatively common. For example, in one study of 1113 men with prostate cancer diagnosed with systematic biopsy, 27% of cases were upgraded and 11% downgraded based on the radical prostatectomy specimen.<sup>56</sup>

Promising results have demonstrated that targeted biopsy using MRI, fused to ultrasound or using direct MRI guidance, may improve the detection of clinically significant disease while decreasing the diagnosis of clinically indolent disease.<sup>57–59</sup> One challenge with this approach is that targeted biopsies alone may miss clinically significant lesions found using current systematic biopsy methods.<sup>58,59</sup> This is thought to relate to imperfections in the diagnostic accuracy of current mpMRI protocols, both in distinguishing PCa from normal tissue and in identifying areas of high grade disease within the tumor. Areas of clinically relevant disease missed on imaging would naturally not be targeted for biopsy, while these sites may be found by chance using the systematic biopsy approach. In the prior sections “Cancer detection” and “In vivo characterization,” we outlined data demonstrating the superior detection accuracy of RSI over current mpMRI, and showed that RSI CI strongly correlates

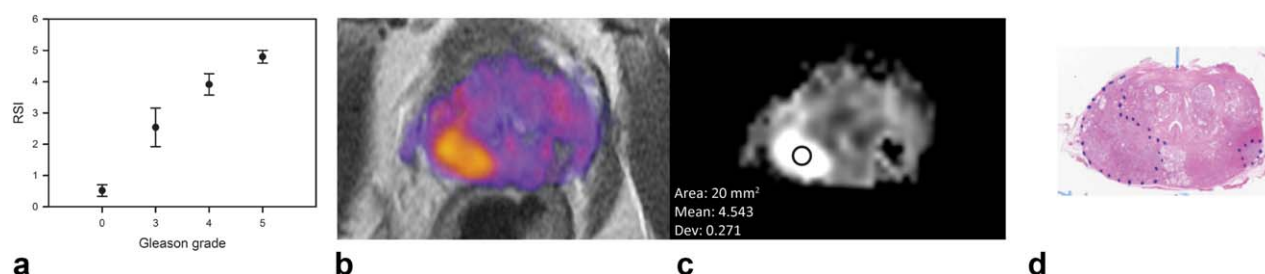


**FIGURE 8: A: Correlation between primary Gleason score and RSI cellularity index, using the same data presented in McCammack et al. PCAN, 2016,<sup>40</sup> reanalyzed to show the top quartile for each ROI. Benign, 0–1.5; Primary 3, 1.5–3; Primary 4, 3–4.5; Primary 5, >4.5. B: RSI cellularity map in color. C: RSI cellularity map in gray-scale, showing the RSI cellularity index for the indicated ROI. D: corresponding whole-mount histopathology slide with the tumor outline in blue.**

with Gleason grade. This combination of assets suggests that areas of high-grade disease can be identified and directly targeted under RSI guidance, potentially increasing sampling yield and diagnostic accuracy while reducing the need for repeat procedures.

Distortion correction techniques also carry implications for targeted biopsies. Rakow-Penner et al developed distortion maps derived from direct comparison of pre- and postdistortion corrected images from preoperative MRIs of 27 PCa patients. Their findings demonstrate that uncorrected diffusion weighted images can have spatial registration errors of up to 13 mm (SD 3.1)<sup>32</sup> or up to one third of the prostate gland itself. Misregistration on that scale could have significant deleterious effects on targeted biopsy, as well as staging and treatment planning. Correction for spatial distortion opens the door to image-guided targeting of small volume lesions suspected to be high-grade disease. This would overcome one of the major limitations of systematic biopsy, which can miss smaller lesions.<sup>60,61</sup>

A previously published example demonstrates the power of this approach, with RSI guided-biopsy revealing Gleason 4 + 3 disease in a patient who had three previous negative systematic biopsies (Fig. 7B).<sup>40</sup> While systematic biopsy currently remains the gold standard for diagnosis in patients undergoing initial prostate biopsy, RSI can serve a role in identification of biopsy targets, particularly in patients who have undergone at least one prior negative prostate biopsy.<sup>62</sup>

### Interpretation of Prostate MRI with RSI: Clinical Practice

The studies presented above demonstrate that the addition of RSI (mpMRI + RSI) provides superior diagnostic accuracy in both computer-based and clinical radiologist-based detection of prostate cancer as compared to current standard-of-care multiparametric MRI. Given these findings, we now incorporate the RSI sequence into all prostate MRIs at our institution, with the fused axial T2 + RSI cellularity maps forming the foundation for RSI interpretation (Fig. 5B). In practice, the same principle outlined for interpretation of ADC in the PIRADS version 2 (v2) guidelines are applied to the RSI cellularity map (RSI-CM). Information from the ADC map and RSI-CM are interpreted in conjunction for initial scoring of peripheral zone lesions; in keeping with PIRADS v2 principles (Fig. 9A). Conversely, transitional zone lesions are primarily scored using findings from T2w images with RSI-CM used in conjunction with ADC maps to further characterize T2w grade 3 lesions; also in line with PIRADS v2 guidelines (Fig. 9B). Moreover, the data outlined above also underscore that the RSI CI, derived from the RSI cellularity maps, strongly correlates with histopathological Gleason grade down to the voxel level. In light of these results we sometimes include a predicted Gleason

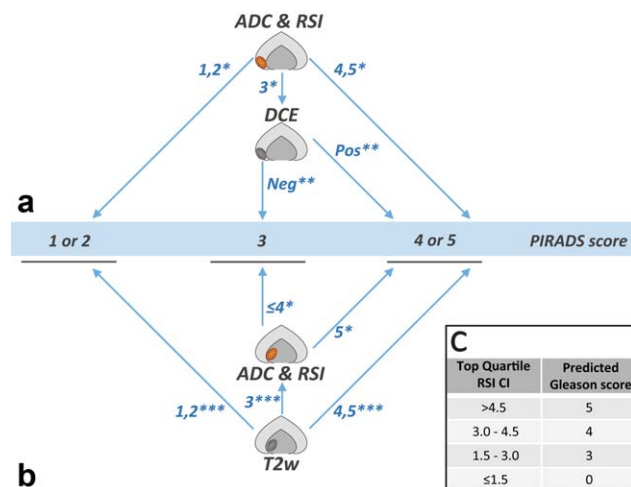


**FIGURE 9: Proposed follow-up guidelines based on PIRADSv2 incorporating RSI-MRI. A: Peripheral zone. B: Transitional zone. C: Predicted Gleason score based on RSI Cellularity index (CI). \*using PIRADSv2 guidelines for conventional DWI; \*\*using PIRADSv2 guidelines for dynamic contrast enhancement; \*\*\*using PIRADSv2 guidelines for T2-weighted images**

score on MRI reports based on the RSI CI (Fig. 9C), as guided by data in Figure 8A. The reported RSI CI is determined by drawing an ROI that incorporates approximately half of the suspicious lesion, with care taken to avoid lesion margins. The RSI CI is tabulated from the top quartile cut-off within the ROI.

### Future Applications

As discussed above, there is great interest in developing robust, cost-effective, prostate cancer screening tools. The work by McCammack et al<sup>41</sup> (see Cancer Detection section) demonstrated that an abbreviated protocol combining RSI and T2w images alone is as sensitive in detecting prostate cancer as mpMRI. This protocol can be acquired in less than 10 min on a GE Signa HDx 3T scanner, with the potential for even faster times on more modern systems. One of the major critiques of using MRI as a screening tool is the cost. As a significant portion of the cost of MRI is attributable to the length of acquisitions, shorter protocols could lead to a decrease in the cost of an MRI. Moreover, limiting the number of sequences should increase the speed of interpretation, which may provide an additional source of cost savings. Future efforts will be needed to determine if this abbreviated RSI + T2w protocol can offer an alternative to current screening methods.

An added benefit of using MRI for screening is that images can subsequently be used for targeted biopsy. The above-described distortion correction techniques combined with improved diagnostic performance over conventional MRI tools suggest that RSI is well suited for image-guided biopsy and targeted therapy. Thus, fast acquisition RSI-based screening studies could subsequently be used for biopsy guidance with increased diagnostic yield and assist in

treatment plan development at no additional cost. Direct comparison of RSI-guided biopsy against current standard-of-care systematic biopsy will be needed.

Future studies should be aimed at vetting the association between Gleason grade and RSI CI. With further refinement there may be instances where imaging-based evaluation of tumors will obviate the need for biopsy altogether leading to additional cost savings while avoiding the small, but not inconsequential, risk of complications following biopsy.

DWI evaluation of prostatic lesions is sometimes complicated by hemorrhage and inflammation post biopsy.<sup>29</sup> However, as discussed previously, RSI is specific for areas of high cellularity (Figs. 3 and 5B) and should be less susceptible to the effects of extracellular edema or blood products. This concept was validated in a small study of patients with CNS neoplasms, wherein RSI was superior to DTI in delineating normal white matter tracts in the setting of peritumoral FLAIR hyperintensity,<sup>48</sup> demonstrating the ability of RSI to identify meaningful pathology despite regional inflammation. Early clinical experience suggests a similar trend in prostate cancer patients (unpublished data).

The principles that make diffusion-based techniques attractive in prostate cancer are readily applied to other neoplasms. DWI is now included in routine MR protocols for oncologic imaging at institutions around the world,<sup>63,64</sup> with a strong correlation to tissue cellularity<sup>65</sup> and prognosis<sup>36</sup> in many abdominal and pelvic malignancies in addition to PCa. Despite these results, ADC values remain difficult to apply in the clinical setting for reasons outlined above, namely overlapping reference ranges and variable reproducibility. RSI is currently being evaluated in several abdominal and pelvic cancers where ADC maps have demonstrated clinical utility: in cervical cancer to evaluate for parametrial invasion,<sup>66</sup> in rectal cancer to evaluate for extension through the mesorectal fascia,<sup>67</sup> and in several tumor types for identifying pathological lymph nodes.<sup>68</sup> RSI also has a potential role in evaluating suspicious renal lesions. Oncocytomas in particular, present an important diagnostic dilemma as these lesions can appear indistinguishable from renal cell carcinoma on CT<sup>69</sup> and anatomic MR<sup>70</sup> sequences, yet are benign lesions that generally do not require surgery.<sup>71</sup> Other areas of active research include early posttreatment assessment and whole body MRI.

## Limitations

Like all diffusion-based techniques, RSI suffers from low resolution and in most settings will be best used as an adjunct to high spatial resolution sequences. Additionally, some normal structures such as the spleen and spinal cord show inherently high signal on RSI cellularity maps (Fig. 10). Thus, RSI will be best applied as part of a multiparametric / multimodal imaging protocol.

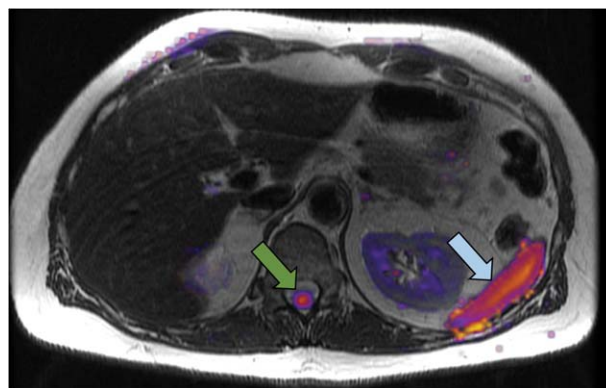


**FIGURE 10: Limitations of RSI: normal structures with high signal on the RSI cellularity map include the spinal cord (green arrow) and the spleen (blue arrow).**

The application of RSI to PCa has been designed to highlight the highly restricted isotropic water found in epithelial cells. The findings that RSI CI correlates with Gleason grade match segmentation studies wherein increasing epithelial cell number correlated positively with increasing Gleason grade.<sup>72</sup> However, other pathological changes such as decreased stromal tissue and decreased luminal space have also been shown to correlate with increasing Gleason grade,<sup>72</sup> highlighting the complex nature of the architectural changes that occur during neoplastic dedifferentiation. Thus, another limitation of RSI is that it may fail to identify some of the histopathologic features that characterize increasing Gleason grade.

While the strength of RSI comes from being able to isolate specific water fractions (e.g., intracellular water), other diffusion-based techniques may prove more powerful for certain pathological settings not focused on identifying highly cellular tissues. For example, conventional DWI proves to be better than RSI at identifying edema in patients with CNS malignancy.<sup>45</sup> Future studies will be needed to clarify the pathological questions best suited to each unique diffusion-based technique.

ADC values are technique and machine dependent.<sup>36,37</sup> This limits if not precludes the development of generalizable parameters and reference ranges, a critical step in the development of an effective imaging biomarker.<sup>34</sup> While partially addressed by the normalization steps used in calculating RSI cellularity maps, RSI techniques will need to be standardized to avoid the technique variability that has constrained comparison of ADC maps across sites.

Image distortion is a critical issue in the translation of imaging findings to clinically actionable information. Differences on the scale of a millimeter can result in changes in treatment plans. Thus the vetting and continued refinement of distortion correction tools will be vital to the implementation of RSI in guiding patient care.

Focused efforts should initially be aimed at those tumors where compelling data exists from the ADC literature, as some cancer patients may not benefit from RSI or other advanced diffusion-based techniques. For example,

evaluation of pulmonary nodules with DWI have had mixed results. One study demonstrated no difference in ADC values between 18 malignant pulmonary nodules and 10 benign nodules,<sup>73</sup> and a meta-analysis by Li et al raised questions about the clinical utility of DWI in evaluating pulmonary nodules.<sup>74</sup> While usage of DWI contrast ratios between the lesion in question and an internal control (for example, the spinal cord)<sup>73,75</sup> may help resolve some of these issues, it is important to keep in mind that no single tool will be adequate for all oncologic imaging.

In conclusion, diffusion-weighted imaging has proven utility in PCa. Results to date suggest that RSI can build upon the success of conventional DWI while addressing several known limitations. RSI isolates signal from isotropic restricted volumes of water to highlight regions of cellularity with high conspicuity making it a powerful tool in PCa detection and localization. An abbreviated protocol combining RSI and an anatomic T2-weighted image may offer a viable option for imaging-based PCa screening, using a decision tree developed on current PIRADSv2 recommendations. RSI CI strongly correlates with Gleason grade making imaging-based in vivo characterization a reality, while robust distortion correction techniques allow RSI data to be clinically applied in the setting of cancer staging, image-guided targeted biopsy or therapy. With the advent of RSI, combined with the continued development of other imaging techniques, new standards in the early detection of malignancy and improved therapeutic guidance are on the horizon.

## Acknowledgments

Contract grant sponsor: Department of Defense (DoD); contract grant number: W81XWH-13-1-0391; Contract grant sponsor: the American Cancer Society; contract grant number: 70-002; Contract grant sponsor: UCSD Clinician Scientist Program; contract grant number: 5T32EB005970-07; Contract grant sponsor: NINDS P30 core grant; contract grant number: NS047101; Contract grant sponsor: General Electric, Investigator Initiated Research Award; contract grant number: BOK92325

This study was funded by a Department of Defense (DoD) grant, Prostate Cancer Research Program, the American Cancer Society Institutional Research Grant, UCSD Clinician Scientist Program, UCSD School of Medicine Microscopy Core, and NINDS P30 core grant, and a General Electric, Investigator Initiated Research Award.

## References

1. American Cancer Society. Cancer facts and figures. Atlanta, GA: American Cancer Society; 2016.
2. SEER Stat Fact Sheet. Surveillance, epidemiology, and end results program. Bethesda, MD: National Cancer Institute.
3. Ueno Y, Tamada T, Bist V, et al. Multiparametric magnetic resonance imaging: Current role in prostate cancer management. *Int J Urol* 2016;23:550–557.
4. Oppenheimer DC, Weinberg EP, Hollenberg GM, Meyers SP. Multiparametric magnetic resonance imaging of recurrent prostate cancer. *J Clin Imaging Sci* 2016;6:18.
5. Felker ER, Margolis DJ, Nassiri N, Marks LS. Prostate cancer risk stratification with magnetic resonance imaging. *Urol Oncol* 2016;34:311–319.
6. Park JJ, Kim CK, Park SY, Park BK, Lee HM, Cho SW. Prostate cancer: role of pretreatment multiparametric 3-T MRI in predicting biochemical recurrence after radical prostatectomy. *AJR Am J Roentgenol* 2014;202:W459–W465.
7. Futterer JJ, Briganti A, De Visschere P, et al. Can clinically significant prostate cancer be detected with multiparametric magnetic resonance imaging? A systematic review of the literature. *Eur Urol* 2015;68:1045–1053.
8. Hegde JV, Mulkern RV, Panych LP, et al. Multiparametric MRI of prostate cancer: an update on state-of-the-art techniques and their performance in detecting and localizing prostate cancer. *J Magn Reson Imaging* 2013;37:1035–1054.
9. Isebaert S, Van den Bergh L, Haustermans K, et al. Multiparametric MRI for prostate cancer localization in correlation to whole-mount histopathology. *J Magn Reson Imaging* 2013;37:1392–1401.
10. Kitajima K, Kaji Y, Fukabori Y, Yoshida K, Suganuma N, Sugimura K. Prostate cancer detection with 3 T MRI: comparison of diffusion-weighted imaging and dynamic contrast-enhanced MRI in combination with T2-weighted imaging. *J Magn Reson Imaging* 2010;31:625–631.
11. Lim HK, Kim JK, Kim KA, Cho KS. Prostate cancer: apparent diffusion coefficient map with T2-weighted images for detection—a multireader study. *Radiology* 2009;250:145–151.
12. Haider MA, van der Kwast TH, Tanguay J, et al. Combined T2-weighted and diffusion-weighted MRI for localization of prostate cancer. *AJR Am J Roentgenol* 2007;189:323–328.
13. Donati OF, Jung SI, Vargas HA, et al. Multiparametric prostate MR imaging with T2-weighted, diffusion-weighted, and dynamic contrast-enhanced sequences: are all pulse sequences necessary to detect locally recurrent prostate cancer after radiation therapy? *Radiology* 2013;268:440–450.
14. Turkbey B, Pinto PA, Mani H, et al. Prostate cancer: value of multiparametric MR imaging at 3 T for detection—histopathologic correlation. *Radiology* 2010;255:89–99.
15. Giannarini G, Nguyen DP, Thalmann GN, Thoeny HC. Diffusion-weighted magnetic resonance imaging detects local recurrence after radical prostatectomy: initial experience. *Eur Urol* 2012;61:616–620.
16. Miao H, Fukatsu H, Ishigaki T. Prostate cancer detection with 3-T MRI: comparison of diffusion-weighted and T2-weighted imaging. *Eur J Radiol* 2007;61:297–302.
17. Tan CH, Wei W, Johnson V, Kundra V. Diffusion-weighted MRI in the detection of prostate cancer: meta-analysis. *AJR Am J Roentgenol* 2012;199:822–829.
18. Langer DL, van der Kwast TH, Evans AJ, Trachtenberg J, Wilson BC, Haider MA. Prostate cancer detection with multi-parametric MRI: logistic regression analysis of quantitative T2, diffusion-weighted imaging, and dynamic contrast-enhanced MRI. *J Magn Reson Imaging* 2009;30:327–334.
19. Peng Y, Jiang Y, Yang C, et al. Quantitative analysis of multiparametric prostate MR images: differentiation between prostate cancer and normal tissue and correlation with Gleason score—a computer-aided diagnosis development study. *Radiology* 2013;267:787–796.
20. Peng Y, Jiang Y, Antic T, Giger ML, Eggen SE, Oto A. Validation of quantitative analysis of multiparametric prostate MR images for



- prostate cancer detection and aggressiveness assessment: a cross-imager study. *Radiology* 2014;271:461–471.
21. Kozlowski P, Chang SD, Jones EC, Berean KW, Chen H, Goldenberg SL. Combined diffusion-weighted and dynamic contrast-enhanced MRI for prostate cancer diagnosis—correlation with biopsy and histopathology. *J Magn Reson Imaging* 2006;24:108–113.
22. Vargas HA, Hotker AM, Goldman DA, et al. Updated prostate imaging reporting and data system (PIRADS v2) recommendations for the detection of clinically significant prostate cancer using multiparametric MRI: critical evaluation using whole-mount pathology as standard of reference. *Eur Radiol* 2016;26:1606–1612.
23. Turkbey B, Choyke PL. PIRADS 2.0: what is new? *Diagn Interv Radiol* 2015;21:382–384.
24. White NS, Leergaard TB, D'Arceuil H, Bjaalie JG, Dale AM. Probing tissue microstructure with restriction spectrum imaging: Histological and theoretical validation. *Hum Brain Mapp* 2013;34:327–346.
25. Le Bihan D. Molecular diffusion, tissue microdynamics and microstructure. *NMR Biomed* 1995;8:375–386.
26. Le Bihan D, Mangin J-F, Poupon C, et al. Diffusion tensor imaging: Concepts and applications. *J Magn Reson Imaging* 2001;13:534–546.
27. Yamada K, Sakai K, Akazawa K, Yuen S, Nishimura T. MR tractography: a review of its clinical applications. *Magn Reson Med Sci* 2009;8:165–174.
28. Stejskal EO, Tanner JE. Spin diffusion measurement: spin echoes in the presence of a time dependent field gradient. *J Chem Phys* 1965;42:288–292.
29. Tamada T, Sone T, Jo Y, et al. Prostate cancer: relationships between postbiopsy hemorrhage and tumor detectability at MR diagnosis. *Radiology* 2008;248:531–539.
30. Donato F Jr, Costa DN, Yuan Q, Rofsky NM, Lenkinski RE, Pedrosa I. Geometric distortion in diffusion-weighted MR imaging of the prostate-contributing factors and strategies for improvement. *Acad Radiol* 2014;21:817–823.
31. White NS, Dale AM. Distinct effects of nuclear volume fraction and cell diameter on high b-value diffusion MRI contrast in tumors. *Magn Reson Med* 2014;72:1435–1443.
32. Rakow-Penner RA, White NS, Margolis DJ, et al. Prostate diffusion imaging with distortion correction. *Magn Reson Imaging* 2015;33:1178–1181.
33. White NS, McDonald C, Farid N, et al. Diffusion-weighted imaging in cancer: physical foundations and applications of restriction spectrum imaging. *Cancer Res* 2014;74:4638–4652.
34. Prescott JW. Quantitative imaging biomarkers: the application of advanced image processing and analysis to clinical and preclinical decision making. *J Digit Imaging* 2013;26:97–108.
35. Jung KH, Lee KH. Molecular imaging in the era of personalized medicine. *J Pathol Transl Med* 2015;49:5–12.
36. Heijmen L, Verstappen MC, Ter Voert EE, et al. Tumour response prediction by diffusion-weighted MR imaging: ready for clinical use? *Crit Rev Oncol Hematol* 2012;83:194–207.
37. Jie C, Rongbo L, Ping T. The value of diffusion-weighted imaging in the detection of prostate cancer: a meta-analysis. *Eur Radiol* 2014;24:1929–1941.
38. Schreuder SM, Lensing R, Stoker J, Bipat S. Monitoring treatment response in patients undergoing chemoradiotherapy for locally advanced uterine cervical cancer by additional diffusion-weighted imaging: A systematic review. *J Magn Reson Imaging* 2014;42:572–594.
39. Liss MA, White NS, Parsons JK, et al. MRI-derived restriction spectrum imaging cellularity index is associated with high grade prostate cancer on radical prostatectomy specimens. *Front Oncol* 2015;5:30.
40. McCammack KC, Kane CJ, Parsons JK, et al. In vivo prostate cancer detection and grading using restriction spectrum imaging-MRI. *Prostate Cancer Prostatic Dis* 2016;19:168–173.
41. McCammack KC, Schenker-Ahmed NM, White NS, et al. Restriction spectrum imaging improves MRI-based prostate cancer detection. *Abdom Radiol (NY)* 2016;41:946–953.
42. de Rooij M, Hamoen EH, Witjes JA, Barentsz JO, Rovers MM. Accuracy of magnetic resonance imaging for local staging of prostate cancer: a diagnostic meta-analysis. *Eur Urol* 2016;70:233–245.
43. Holland D, Kuperman JM, Dale AM. Efficient correction of inhomogeneous static magnetic field-induced distortion in Echo Planar Imaging. *Neuroimage* 2010;50:175–183.
44. Rakow-Penner RA, White NS, Parsons JK, et al. Novel technique for characterizing prostate cancer utilizing MRI restriction spectrum imaging: proof of principle and initial clinical experience with extraprostatic extension. *Prostate Cancer Prostatic Dis* 2015;18:81–85.
45. Farid N, Almeida-Freitas DB, White NS, et al. Combining diffusion and perfusion differentiates tumor from bevacizumab-related imaging abnormality (bria). *J Neurooncol* 2014;120:539–546.
46. Farid N, Almeida-Freitas DB, White NS, et al. Restriction-spectrum imaging of bevacizumab-related necrosis in a patient with GBM. *Front Oncol* 2013;3:258.
47. McDonald CR, Delfanti RL, Krishnan AP, et al. Restriction spectrum imaging predicts response to bevacizumab in patients with high-grade glioma. *Neuro Oncol* 2016 [Epub ahead of print].
48. McDonald CR, White NS, Farid N, et al. Recovery of white matter tracts in regions of peritumoral FLAIR hyperintensity with use of restriction spectrum imaging. *AJNR Am J Neuroradiol* 2013;34:1157–1163.
49. White NS, McDonald CR, Farid N, Kuperman JM, Kesari S, Dale AM. Improved conspicuity and delineation of high-grade primary and metastatic brain tumors using “restriction spectrum imaging”: quantitative comparison with high B-value DWI and ADC. *AJNR Am J Neuroradiol* 2013;34:958–964, S1.
50. Hygino da Cruz LC Jr, Rodriguez I, Domingues RC, Gasparetto EL, Sorensen AG. Pseudoprogression and pseudoresponse: imaging challenges in the assessment of posttreatment glioma. *AJNR Am J Neuroradiol* 2011;32:1978–1985.
51. Mong S, Ellingson BM, Nghiemphu PL, et al. Persistent diffusion-restricted lesions in bevacizumab-treated malignant gliomas are associated with improved survival compared with matched controls. *AJNR Am J Neuroradiol* 2012;33:1763–1770.
52. McDonald ML, Parsons JK. The case for tailored prostate cancer screening: an NCCN perspective. *J Natl Compr Canc Netw* 2015;13:1576–1583.
53. Donati OF, Mazaheri Y, Afaq A, et al. Prostate cancer aggressiveness: assessment with whole-lesion histogram analysis of the apparent diffusion coefficient. *Radiology* 2014;271:143–152.
54. Vargas HA, Akin O, Franiel T, et al. Diffusion-weighted endorectal MR imaging at 3T for prostate cancer: tumor detection and assessment of aggressiveness. *Radiology* 2011;259:775–784.
55. Yamin G, Schenker-Ahmed NM, Shabaik A, et al. Voxel level radiologic-pathologic validation of Restriction Spectrum Imaging cellularity index with Gleason grade in Prostate Cancer. *Clin Cancer Res* 2016;22:2668–2674.
56. Freedland SJ, Kane CJ, Amling CL, et al. Upgrading and downgrading of prostate needle biopsy specimens: risk factors and clinical implications. *Urology* 2007;69:495–499.
57. Murphy G, Haider M, Ghai S, Sreeharsha B. The expanding role of MRI in prostate cancer. *AJR Am J Roentgenol* 2013;201:1229–1238.
58. Siddiqui MM, Rais-Bahrami S, Turkbey B, et al. Comparison of MR/ultrasound fusion-guided biopsy with ultrasound-guided biopsy for the diagnosis of prostate cancer. *JAMA* 2015;313:390–397.
59. Siddiqui MM, Rais-Bahrami S, Truong H, et al. Magnetic resonance imaging/ultrasound-fusion biopsy significantly upgrades prostate cancer versus systematic 12-core transrectal ultrasound biopsy. *Eur Urol* 2013;64:713–719.
60. Vourganti S, Rastinehad A, Yerram NK, et al. Multiparametric magnetic resonance imaging and ultrasound fusion biopsy detect prostate

- cancer in patients with prior negative transrectal ultrasound biopsies. *J Urol* 2012;188:2152–2157.
61. Sonn GA, Chang E, Natarajan S, et al. Value of targeted prostate biopsy using magnetic resonance-ultrasound fusion in men with prior negative biopsy and elevated prostate-specific antigen. *Eur Urol* 2014;65:809–815.
62. Carroll PR, Parsons JK, Andriole G, et al. NCCN Guidelines insights: prostate cancer early detection, version 2.2016. *J Natl Compr Canc Netw* 2016;14:509–519.
63. Koh DM, Lee JM, Bittencourt LK, Blackledge M, Collins DJ. Body diffusion-weighted MR imaging in oncology: imaging at 3T. *Magn Reson Imaging Clin N Am* 2016;24:31–44.
64. Jafar MM, Parsai A, Miquel ME. Diffusion-weighted magnetic resonance imaging in cancer: Reported apparent diffusion coefficients, in-vitro and in-vivo reproducibility. *World J Radiol* 2016;8:21–49.
65. Chen L, Liu M, Bao J, et al. The correlation between apparent diffusion coefficient and tumor cellularity in patients: a meta-analysis. *PLoS One* 2013;8:e79008.
66. Dhanda S, Thakur M, Kerkar R, Jagmohan P. Diffusion-weighted imaging of gynecologic tumors: diagnostic pearls and potential pitfalls. *Radiographics* 2014;34:1393–1416.
67. Burdan F, Sudol-Szopinska I, Staroslawska E, et al. Magnetic resonance imaging and endorectal ultrasound for diagnosis of rectal lesions. *Eur J Med Res* 2015;20:4.
68. Bonekamp S, Corona-Villalobos CP, Kamel IR. Oncologic applications of diffusion-weighted MRI in the body. *J Magn Reson Imaging* 2012;35:257–279.
69. Choudhary S, Rajesh A, Mayer NJ, Mulcahy KA, Haroon A. Renal oncocytoma: CT features cannot reliably distinguish oncocytoma from other renal neoplasms. *Clin Radiol* 2009;64:517–522.
70. Rosenkrantz AB, Hindman N, Fitzgerald EF, Niver BE, Melamed J, Babb JS. MRI features of renal oncocytoma and chromophobe renal cell carcinoma. *AJR Am J Roentgenol* 2010;195:W421–W427.
71. Ng KL, Rajandram R, Morais C, et al. Differentiation of oncocytoma from chromophobe renal cell carcinoma (RCC): can novel molecular biomarkers help solve an old problem? *J Clin Pathol* 2014;67:97–104.
72. Chatterjee A, Watson G, Myint E, Sved P, McEntee M, Bourne R. Changes in epithelium, stroma, and lumen space correlate more strongly with Gleason pattern and are stronger predictors of prostate ADC changes than cellularity metrics. *Radiology* 2015;277:751–762.
73. Uto T, Takehara Y, Nakamura Y, et al. Higher sensitivity and specificity for diffusion-weighted imaging of malignant lung lesions without apparent diffusion coefficient quantification. *Radiology* 2009;252:247–254.
74. Li B, Li Q, Chen C, Guan Y, Liu S. A systematic review and meta-analysis of the accuracy of diffusion-weighted MRI in the detection of malignant pulmonary nodules and masses. *Acad Radiol* 2014;21:21–29.
75. Nomori H, Cong Y, Sugimura H, Kato Y. Comparing diffusion-weighted imaging and positron emission tomography for pulmonary nodules measuring from 1 to 3 cm in size. *Surg Today* 2015;45:1535–1541.